Journal of Research of the National Bureau of Standards Vol. 46, No. 5, May 1951 Research Paper 2205

Acidic Dissociation Constant and Related Thermodynamic Quantities for Monoethanolammonium Ion in Water From 0° to 50° C

Roger G. Bates and Gladys D. Pinching

Twenty-three buffer solutions composed of approximately equal molal amounts of monoethanolamine (2-aminoethanol) and monoethanolammonium chloride in water were studied by electromotive-force methods at 11 temperatures from 0° to 50° C. The values obtained for the acidic dissociation constant, K_{bA}, of the ethanolammonium ion are given in this range of temperatures by

$$-\log K_{bA} = 2677.91/T + 0.3869 + 0.0004277T,$$

where T is the temperature on the Kelvin scale. The changes of free energy, heat content, entropy, and heat capacity that accompany the dissociation of 1 mole of ethanolammonium ion in the standard state were calculated from the dissociation constant and its temperature coefficient. Dissociation of a mole of ethanolammonium ion results in a small decrease of heat capacity. In this respect ethanolammonium ion resembles ammonium ion rather than the methyl-substituted ammonium ions, for which rather large increases of heat capacity on dissociation have been found.

I. Introduction

During the past 20 years much attention has been given to the effect of temperature changes on the dissociation constants of neutral and negatively charged acids. These studies have given a precise knowledge of the thermodynamic quantities associated with the dissociation of acids of these types. Nevertheless, the strengths of only a few positively charged acids have been measured both with the precision attainable by modern techniques and over a sufficiently wide range of temperatures to warrant the computation of the changes of entropy, heat content, and heat capacity that accompany the dissociation process.

The dissociation of a monobasic cationic acid is an isoelectric reaction; a proton is shifted, but no new electrostatic charge is created. The electrostatic contribution to the change of heat capacity, ΔC_p°, should therefore be zero, and it has been predicted that ΔC_p° for these dissociative processes would itself be found to be small or zero [1, 2].[1] Although this prediction was confirmed for ammonium ion [3], later studies of the methylammonium ions gave values of ΔC_p° ranging from +33 j deg^{-1} mole^{-1} for monomethylammonium to +183 j deg^{-1} mole^{-1} for trimethylammonium [4]. This discovery led Everett and Wynne-Jones to the conclusion [4] that specific interactions of a chemical nature among the solvent and the dissolved ions and molecules often exert a more profound influence upon the heat capacity than expected.

Everett and Wynne-Jones attributed the positive values of ΔC_p° for the substituted ammonium ions to the strongly hydrophobic character of the alkyl groups. This hydrophobic property is reduced by substitution of hydroxyl on the alkyl group. Hence, it is of interest to compare the thermodynamic functions for the dissociation of ethanolammonium ion with those for ammonium and the methyl-substituted ammonium ions. The dissociation constant of monoethanolammonium ion and the basic strength of monoethanolamine were determined by the electromotive-force method from 0° to 50° C and the thermodynamic quantities for the dissociation processes calculated. The change of heat capacity for the dissociation of monoethanolammonium ion in the standard state at 25° was found to be −5 j deg^{-1} mole^{-1}, not greatly different from that for ammonium ion.

[1] Figures in brackets indicate the literature references at the end of this paper.

II. Method

The method used was essentially the same as that by which the dissociation constant of ammonium ion was determined [5]. Electromotive-force measurements of the cell

$$\text{Pt; } H_2 \text{ } (g, \text{ 1 atm}), \text{ } HOC_2H_4NH_3Cl \text{ } (m_1),$$
$$HOC_2H_4NH_2 \text{ } (m_2), \text{ AgCl } (s); \text{ Ag},$$

were made at intervals of 5 deg from 0° to 50°. The partial pressure of the amine from its aqueous solution was so low that no correction for volatility of the solute was necessary, and the extra saturator used in determining the dissociation constant of ammonium ion was not required. Furthermore, it was found that the correction for solubility of silver chloride in these buffer solutions is only about 0.0006 in log K_{bA} (0.00004 v in the emf) and can therefore be neglected.

The acidity function, pwH, was computed for each buffer solution at each temperature from the emf, E, the standard potential of the cell, E° [5],

and the appropriate value of $2.3026RT/\boldsymbol{F}$ [5] by the equation

$$\text{pwH} \equiv -\log\,(f_{\text{H}} f_{\text{Cl}} m_{\text{H}}) = (E - E^{\circ})\boldsymbol{F}/(2.3026RT) + \log\, m_{\text{Cl}}, \quad (1)$$

where m is molality and f is the molal activity coefficient. If the mass-law expression for the dissociation of ethanolammonium ion, (BH^+), into ethanolamine (B) and hydrogen ion, namely,

$$BH^+ = B + H^+ \quad (2)$$

is combined with eq 1, the following relationship between the dissociation constant for eq 2, namely K_{bh}, and pwH is obtained:

$$-\log K_{bh} = \text{pwH} + \log\,(m_{BH^+}/m_{\text{B}}) + \log\,(f_{BH^+} f_{Cl^-}/f_{\text{B}}). \quad (3)$$

1. The Molality Term

Inasmuch as the basic strength of ethanolamine is greater than the acidic strength of ethanolammonium ion, its conjugate acid, the solutions have an alkaline reaction. The basic dissociation is formulated as follows:

$$B + H_2O = BH^+ + OH^-; \quad (4)$$

and the basic dissociation constant is designated K_b. The concentration of hydroxyl ion evidently measures the amount of free amine that has been converted by reaction 4 into the ion BH^+. Hence, the equilibrium concentrations of B and BH^+ are

$$m_{BH^+} = m_1 + m_{OH^-}, \quad (5a)$$

and

$$m_{\text{B}} = m_2 - m_{OH^-} \quad (5b)$$

and the ionic strength, μ, is given by

$$\mu = m_1 + m_{OH^-}. \quad (6)$$

The concentration of hydroxyl ion is easily computed by the approximation

$$\log m_{OH^-} \approx \log K_w + \text{pwH}, \quad (7)$$

where K_w is the ionization constant of water [6].

2. The Activity-Coefficient Term

The last term of eq 3 approaches zero at high dilutions. However, it is not feasible to omit this term and simply to extrapolate the sum of the first two terms on the right to zero ionic strength, for the last term contributes nearly 0.1 to log K_{bh} at an ionic strength of 0.01, and accurate data are often unobtainable at ionic strengths below 0.01. The Hückel equation [7] offers a practical means of estimating the activity-coefficient correction. The complete expression for K_{bh} is obtained by combining eq 3 with the Hückel equation and with eq 5a and 5b

$$-\log K'_{bh} \equiv -\log K_{bh} - \beta\mu = \text{pwH} + \log \frac{m_1 + m_{OH}}{m_2 - m_{OH}} - \frac{2A\sqrt{\mu}}{1 + Ba^*\sqrt{\mu}} \quad (8)$$

In eq 8, K'_{bh} is the apparent value of K_{bh}, the thermodynamic dissociation constant; A and B are constants of the Debye-Hückel theory [8]; and a^* and β are adjustable parameters. When too large a value of the ion-size parameter, a^*, is used, a plot of the right side of eq 8 as a function of ionic strength is concave downward. For too small values of a^*, the curve is concave upward. At each temperature, the intermediate value of 1.0 furnished straight lines, which were easily extended to an ionic strength of zero. The data for five temperatures are plotted in figure 1.

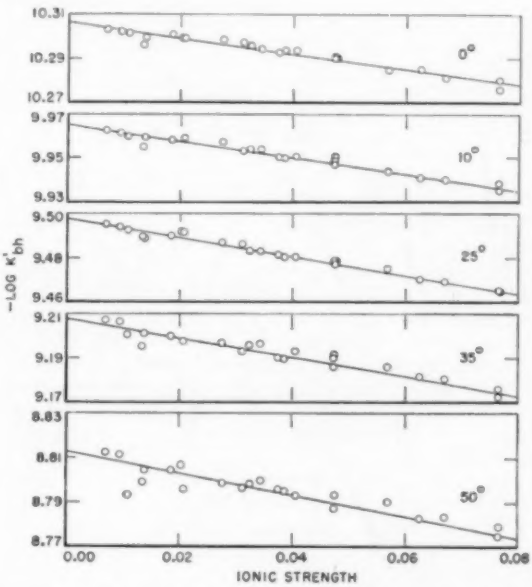

FIGURE 1. *Extrapolation of $-\log K'_{bh}$, the right side of eq 8, to zero ionic strength at 0°, 10°, 25°, 35°, and 50°.*

III. Experimental Procedures and Results

Monoethanolamine (2-aminoethanol) was distilled twice at atmospheric pressure and the middle third of the distillate collected. Two stock solutions of the amine in carbon dioxide-free water were used in preparing the 23 buffer solutions. These two solutions were stored in paraffin-lined flasks and were protected from contamination by atmospheric carbon dioxide and guarded from strong light. Each stock solution was standardized by weight titration with a solution of distilled hydrochloric acid which, in turn, had been standardized by weighing the chloride as silver chloride. The sodium salt of methyl red was chosen as indicator.

The buffer solutions were grouped into five series. The most concentrated solution of each series was prepared by mixing accurately weighed portions of amine solution and hydrochloric acid solution. Amine and acid were combined in the ratio of 2 moles to 1. The other solutions of each series were formed by weight dilution of the most concentrated solution with carbon dioxide-free water.

The two electrode compartments of the cells were separated by a stopcock of large bore [5], and air was excluded from the cells during the operations of rinsing and filling. The preparation of the hydrogen and silver-silver chloride electrodes has been described [9].

The solubility of silver chloride in a 0.1-M solution of the amine was determined in the following manner. Freshly precipitated silver chloride was digested overnight at about 90°, washed five times with water, and filtered. An excess of the product was added to 200 ml of the amine solution and the mixture shaken vigorously several times over a period of about 18 hr. A clear sample of the supernatant solution was withdrawn, acidified with nitric acid, and the precipitated silver chloride was collected, dried, and weighed. One liter of a 0.1-M solution of the amine was found to dissolve 0.0021 mole of silver chloride, or about one-third as much as a 0.1-M solution of ammonia. Hence, the correction for solubility could safely be omitted.

The values of pwH listed in table 1 were calculated by eq 1 from the measured emf and the chloride molality (m_1). With $a^*=1$ and m_{OH} obtained by eq 7, $-\log K'_{bh}$ was derived by eq 8 from each experimental measurement and plotted with respect to ionic strength as shown in figure 1. The slopes, $-\beta$, of these straight lines were measured at each temperature and used to compute $-\log K_{bh}$ for each solution (eq 8). The averages of these 22 or 23 values are summarized in the second column of table 2, together with the mean deviation from the average value at each temperature. The third column gives K_{bh}, whereas the last two columns list the negative logarithm of the basic dissociation constant of ethanolamine, $-\log K_b$ (compare eq 4), and K_b, respectively. The basic constant was obtained from K_{bh} and the ionization constant of water [6] by the equation

$$K_b=K_w/K_{bh}. \tag{9}$$

TABLE 1. pwH *for aqueous mixtures of ethanolammonium chloride* (m_1) *and ethanolamine* (m_2) *from 0° to 50°*

m_1	m_2	pwH at—										
		0°	5°	10°	15°	20°	25°	30°	35°	40°	45°	50°
0.07648	0.07533	10.5168	10.3459	10.1802	10.0195	9.8645	9.7160	9.5699	9.4315	9.2960	9.1670	9.0413
.07646	.07551	10.5222	10.3496	10.1817	10.0203	9.8627	9.7173	9.5685	9.4290	9.2938	9.1644	9.0382
.06999	.06599	10.5072	10.3360	10.1698	10.0093	9.8540	9.7051	9.5599	9.4202	9.2849	9.1554	9.0297
.06263	.06185	10.5053	10.3332	10.1646	10.0030	9.8471	9.6999	9.5541	9.4149	9.2793	9.1491	9.0226
.05690	.05605	10.4940	10.3222	10.1562	9.9963	9.8414	9.6921	9.5472	9.4074	9.2729	9.1437	9.0181
.04746	.04717	10.4880	10.3159	10.1498	9.9886	9.8328	9.6833	9.5376	9.3984	9.2322	9.1323	9.0058
.04741	.04732	10.4874	10.3140	10.1469	9.9855	9.8292	9.6836	9.5360	9.3943	9.2592	9.1301	9.0014
.04740	.04767	10.4911	10.3184	10.1520	9.9920	9.8365	9.6872	9.5409	9.4017	9.2663	9.1373	9.0110
.04055	.04005	10.4724	10.3001	10.1319	9.9724	9.8163	9.6663	9.5221	9.3820	9.2457	9.1151	8.9876
.03858	.03858	10.4724	10.2992	10.1310	9.9698	9.8133	9.6660	9.5193	9.3784	9.2444	9.1151	8.9890
.03746	.03700	10.4648	10.2929	10.1247	9.9614	9.8029	9.6601	9.5123	9.3720	9.2377	9.1083	8.9826
.03440	.03389	10.4584	10.2861	10.1200	9.9595	9.8043	9.6535	9.5099	9.3698	9.2340	9.1044	8.9782
.03253	.03232	10.4590	10.2861	10.1193	9.9578	9.8001	9.6525	9.5074	9.3681	9.2322	9.1031	8.9758
.03116	.03110	10.4586	10.2857	10.1170	9.9559	9.7996	9.6541	9.5036	9.3638	9.2279	9.1002	8.9717
.02765	.02780	10.4539	10.2817	10.1150	9.9546	9.7989	9.6482	9.5008	9.3609	9.2243	9.0947	8.9673
.02077	.02073	10.4316	10.2613	10.0936	9.9323	9.7770	9.6293	9.4802	9.3377	9.2006	9.0668	8.9398
.02032	.02002	10.4249	10.2530	-------	-------	-------	9.6219	-------	-------	9.1952	9.0648	8.9387
.018619	.018725	10.4296	10.2562	10.0889	9.9291	9.7736	9.6232	9.4751	9.3356	9.1990	9.0704	8.9435
.013871	.013700	10.4034	10.2310	10.0646	9.9028	9.7461	9.5964	9.4493	9.3104	9.1736	9.0427	8.9168
.013494	.013469	10.4033	10.2304	10.0635	9.9019	9.7463	9.6009	9.4491	9.3085	9.1744	9.0444	8.9155
.010944	.010877	10.3956	10.2230	10.0557	9.8925	9.7342	9.5900	9.4390	9.2997	9.1627	9.0330	8.9054
.009510	.009565	10.3946	10.2220	10.0549	9.8945	9.7384	9.5884	9.4426	9.3031	9.1672	9.0372	8.9105
.007042	.006998	10.3768	10.2043	10.0373	9.8759	9.7175	9.5710	9.4239	9.2843	9.1477	9.0185	8.8913

TABLE 2. *Summary of the dissociation constants of ethanolammonium ion and ethanolamine from 0° to 50°*

Temperature	$-\log K_{bh}$	$K_{bh}\times10^{10}$	$-\log K_b$	$K_b\times10^5$
°C				
0	10.3064 ±0.0014	0.494	4.637	2.31
5	10.1341 ±0.0013	.734	4.600	2.51
10	9.9654 ±0.0011	1.083	4.570	2.69
15	9.8037 ±0.0016	1.571	4.542	2.87
20	9.6467 ±0.0027	2.26	4.520	3.02
25	9.4980 ±0.0009	3.18	4.498	3.18
30	9.3485 ±0.0018	4.48	4.484	3.28
35	9.2082 ±0.0020	6.19	4.472	3.37
40	9.0702 ±0.0021	8.51	4.465	3.43
45	8.9401 ±0.0021	11.48	4.456	3.50
50	8.8130 ±0.0031	15.38	4.449	3.56

The dissociation constants given in the second column of table 2 may be expressed by the following equation, valid from 0° to 50°:

$$-\log K_{bh}=2677.91/T+0.3869+0.0004277T, \tag{10}$$

where T is the temperature on the absolute (Kelvin) scale: $T=°C+273.16$. The constants of eq 10 were determined by the method of least squares. The average difference at the 11 temperatures between the observed log K_{bh} and the calculated value was 0.0010.

Simms [10] found 9.470 for $-\log K_{bh}$ at 25° from the emf of cells with hydrogen and calomel electrodes,

whereas Glasstone and Schram [11] obtained 9.45 from measurements made with the glass electrode. Bruehlman and Verhoek [12] determined $-\log K_{bh}$ in a 0.5-M solution of potassium nitrate from data obtained with the glass electrode, and reported values of 9.74 at 25° and 9.51 at 35°. Apparently the most precise and extensive of the earlier investigations of the dissociation of ethanolamine is that of Sivertz, Reitmeier, and Tartar [13], who determined K_b at 25° from measurements of the electrolytic conductance of aqueous solutions of ethanolamine and ethanolammonium chloride. Their result leads to a value of 9.500 for $-\log K_{bh}$, in excellent agreement with 9.498 given in table 2.

Several factors combine to determine the effect of substituents on the strength of organic bases. Some of the most important are polar (inductive) effects, resonance, electrical repulsion, solvation, and steric effects [14 to 19]. As a result of their electron-donating or electron-attracting powers, substituent groups increase or decrease the base strength, in the Lewis sense, of the nitrogen atom of ammonia. This nitrogen atom is itself so strongly electron-attracting that each hydrogen atom of ammonia acquires a definite positive charge. Their combined repulsions make ammonia a weak base. On the other hand, the basic strength of ethylamine is 26 times as great as that of ammonia. Not only does the ethyl group have a small electron-donating effect, but substitution also reduces considerably the net repulsions of the hydrogens. The electron-attracting power of the hydroxyl group is relatively large, however, and consequently ethanolamine is only one-fourteenth as strong a base as ethylamine, or about twice as strong as ammonia.

IV. Thermodynamic Quantities

The thermodynamic quantities for the dissociation of ethanolammonium ion (eq 2) in the standard state were computed from the constants of eq 10 by application of the usual formulas [5]. The results are summarized in table 3. The thermodynamic functions at 25° for the basic dissociation of ethanolamine in water (eq 4) are obtained by subtracting the values given in table 3 from the corresponding quanties for the ionization of water at 25°. The latter are listed in calories by Harned and Owen [6] and are converted to joules by multiplying each figure by 4.1840. For the basic dissociation, $\Delta F°$ is found to be 25,675 j mole^{-1}, $\Delta H°$ is 6,023 j mole^{-1}, $\Delta S°$ is -65.9 j deg^{-1} mole^{-1}, and $\Delta C_p°$ is -190 j deg^{-1} mole^{-1}. These values do not differ greatly from those for the basic dissociation of ammonia [5].[2]

[2] For ammonia, $\Delta H° = 4{,}345$ j mole^{-1}, $\Delta S° = -76.4$ j deg^{-1} mole^{-1}, and $\Delta C_p° = -195$ j deg^{-1} mole^{-1}. The negative sign has been omitted from $\Delta C_p°$ in table 7 of [5].

TABLE 3. *Thermodynamic quantities for the acidic dissociation of ethanolammonium ion*

Temperature	$\Delta F°$	$\Delta H°$	$\Delta S°$	$\Delta C_p°$
°C	j mole^{-1}	j mole^{-1}	j deg^{-1} mole^{-1}	j deg^{-1} mole^{-1}
0	53, 902	50, 657	−11. 88	−4. 5
5	53, 962	50, 634	−11. 96	−4. 6
10	54, 023	50, 611	−12. 04	−4. 6
15	54, 082	50, 588	−12. 13	−4. 7
20	54, 144	50, 564	−12. 21	−4. 8
25	54, 205	50, 540	−12. 29	−4. 9
30	54, 267	50, 515	−12. 37	−5. 0
35	54, 327	50, 492	−12. 45	−5. 0
40	54, 391	50, 465	−12. 54	−5. 1
45	54, 454	50, 439	−12. 62	−5. 2
50	54, 517	50, 413	−12. 70	−5. 3

The change of heat capacity that accompanies the dissociation of ethanolammonium ion is found to be small and negative, in contrast to the rather large positive values for the methyl-substituted ammonium ions [4]. This difference can be attributed to differences in the chemical properties of the two amines. Widely different values of $\Delta C_p°$ are often found for a series of neutral acids or for negatively charged acids, even though the individual dissociation reactions are of the same electric type. The close correspondence between the heat-capacity changes for the dissociation of ammonium and ethanolammonium ions may signify a reduction, by the OH substituent, of the hydrophobic character of the alkyl group to which Everett and Wynne-Jones ascribe the positive values found for the methyl-substituted ammonium ions.

V. References

[1] R. W. Gurney, J. Chem. Phys. **6,** 499 (1938).
[2] E. C. Baughan, J. Chem. Phys. **7,** 951 (1939).
[3] D. H. Everett and W. F. K. Wynne-Jones, Proc. Roy Soc. (London) **169A,** 190 (1938).
[4] D. H. Everett and W. F. K. Wynne-Jones, Proc. Roy. Soc. (London) **177A,** 499 (1941).
[5] R. G. Bates and G. D. Pinching, J. Research NBS **42,** 419 (1949) RP1982.
[6] H. S. Harned and B. B. Owen, The physical chemistry of electrolytic solutions, 2d ed., p. 485, 514 (Reinhold Publishing Corp., New York, N. Y., 1950).
[7] E. Hückel, Physik. Z. **26,** 93 (1925).
[8] G. G. Manov, R. G. Bates, W. J. Hamer, and S. F. Acree, J. Am. Chem. Soc. **65,** 1765 (1943).
[9] R. G. Bates, G. D. Pinching, and E. R. Smith, J. Research NBS **45,** 418 (1950) RP2153.
[10] H. S. Simms, J. Phys. Chem. **32,** 1121 (1928).
[11] S. Glasstone and A. F. Schram, J. Am. Chem. Soc. **69,** 1213 (1947).
[12] R. J. Bruehlman and F. H. Verhoek, J. Am. Chem. Soc. **70,** 1401 (1948).
[13] V. Sivertz, R. E. Reitmeier, and H. V. Tartar, J. Am. Chem. Soc. **62,** 1379 (1940).
[14] S. R. Palit, J. Indian Chem. Soc. **25,** 127 (1948).
[15] H. C. Brown, H. Bartholomay, Jr., and M. D. Taylor, J. Am. Chem. Soc. **66,** 435 (1944).
[16] H. C. Brown, J. Am. Chem. Soc. **67,** 378 (1945).
[17] H. C. Brown, J. Am. Chem. Soc. **67,** 1452 (1945).
[18] G. E. K. Branch and M. Calvin, The theory of organic chemistry, chapter VI (Prentice-Hall, Inc., New York, N. Y., 1946).
[19] A. F. Trotman-Dickenson, J. Chem. Soc., 1293 (1949).

WASHINGTON, November 28, 1950.

Journal of Research of the National Bureau of Standards Vol. 46, No. 5, May 1951 Research Paper 2206

Ultraviolet Spectral Distribution of Radiant Energy From the Sun

Ralph Stair

This paper gives the results of some preliminary measurements on the ultraviolet spectral energy distribution of direct solar radiation at Washington, D. C. Data are given for wavelengths extending below 300 millimicrons for air masses approximating $M=1.4$. The new equipment and method employed in this work permit the rapid acquirement of a prismatic ultraviolet spectral energy curve at sea level showing greater Fraunhofer structure than previously obtained even at desert and mountain stations.

Other applications of this equipment, for example, in the study of total ozone and in sky-light spectral-energy distributions are suggested.

I. Introduction

The determination of the ultraviolet spectral radiant energy of sunlight has long been a subject of considerable interest. Nevertheless, but few measurements for wavelength regions shorter than about 330 or 340 mμ have been recorded in the literature [1 to 7].[1] This is easily understandable, since double quartz prism spectrometers suitable for the automatic and rapid recording of low spectral intensities have not been generally available until quite recently. The best radiometric data previously published, extending to wavelengths shorter than 300 mμ, are those of Pettit [1]. Although they were obtained at high altitudes the low sensitivity of the radiometer necessitated the use of wide optical slits (spectral width usually 5.0 to 10.0 mμ) and long response times.

The solar spectrum, when photographed with a good grating spectrograph, shows a continuous spectral energy distribution on which are superimposed thousands of Fraunhofer lines and bands [8, 9]. These features are much too numerous to be detected separately by a prism spectrometer. The prism averages the spectral energy over a wavelength interval corresponding to the effective slit width of the instrument. Hence in spectral regions in which the Fraunhofer lines are numerous and have intense absorption, depressions will occur in the energy curve observed with a prism spectrometer. The character of the observed curve will be significantly affected by the slit width employed. In general, the narrower the slit width the more detailed will be the structural character of the observed spectrum.

The data on the ultraviolet solar energy curve recorded in this paper were obtained between 10:00 a. m. and 12:00 noon during October 1950, when the sun was shining through clear atmosphere associated with high-pressure conditions. Since the purpose of this investigation was primarily to determine the possibilities of the available equipment in work of this type rather than to acquire extensive data, the instruments have not been removed to a location having day-long clear access to direct solar rays.

[1] Figures in brackets indicate the literature references at the end of this paper

II. Instruments and Methods

The apparatus employed in this investigation consists of a Farrand double quartz prism spectrometer, RCA type 935 phototube, 510-cycle light modulator, tuned amplifier and auxiliary meters, and recording apparatus (see fig. 1), set up and calibrated as described elsewhere [19], except that a heliostat was employed for keeping sunlight reflected into the entrance slit of the instrument. For this purpose the entrance slit of the instrument was placed toward the south and the heliostat arranged so that a beam of direct sunlight reflected from a plane chrom-aluminized mirror fell upon the center of the first lithium-fluoride-quartz collimating lens of the instrument. The spectral energy response characteristic of the complete instrument, including the heliostat mirror and phototube, were determined by using a standard tungsten-filament-in-quartz lamp [19, 20] calibrated for color temperature [11] and evaluated for spectral emission in the ultraviolet with the application of spectral emissivity data for tungsten [12 to 15] (see table 1). In this calibration the radiant energy from the standard lamp was reflected into the spectrometer by the heliostat mirror. The lamp distance was arranged so that the illuminated area of the collimating lens approximated that illuminated by direct sunlight.

No refracting lens or mirror was employed to produce an image of the sun on the entrance slit of the spectrometer because an integrated solar energy spectrum was desired. Although a small area of the sky surrounding the sun contributed to the total energy response, its effect is necessarily small since it probably did not at any time exceed 1 percent of the total and did not differ radically in spectral quality from sunlight as observed in check measurements on the sky only, near the sun.

In the present investigation the high sensitivity of the detecting and recording apparatus permitted the use of relatively narrow slit widths (spectral width 2 to 3 mμ), with noise levels less than 1 percent, to about 305 mμ. Hence, with this equipment somewhat narrower spectral slit widths could be practically employed at the altitude of the Bureau's

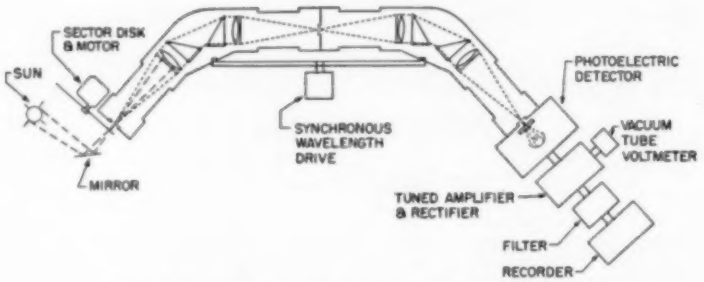

FIGURE 1. *Block diagram showing instrumental lay-out.*

TABLE 1. *Black-body data and emissivity factors for tungsten at operation temperature of standard tungsten-filament-in-quartz lamp; relative spectral energy emission of standard lamp, based on tabulated values of tungsten emissivity; relative spectral transmissive factor (response factor) of Farrand spectrometer, including heliostat mirror, phototube and all other components of the instrument; transmission coefficients of 0.18 cm of ozone per unit air mass through an air mass of M-1.43; and the calculated Rayleigh scattering spectral transmission coefficients for air mass, M=1.43, at Washington (approximately sea level, 355 ft)*

Wavelength	Relative energy black body, 2,945° K, c_2=1.438	Emissivity of tungsten	Relative energy tungsten lamp, 2,945° K	Relative spectral response factor of spectrometer, 0.25-mm slits	Transmission coefficient of 0.18-cm ozone, *ntp* M=1.43	Rayleigh scatter-coefficient, M=1.43
mμ						
300	100	0.422	422	48	0.060	0.197
305	.....	.425	509	59	.217	.219
310	143	.4275	611	82	.457	.242
315	.....	.430	728	96	.653	.265
320	199	.433	862	139	.814	.287
325	.....	.436	1,007	169	.903	.310
330	269	.4385	1,180	199	.953	.332
335	.....	.441	1,367	241	.980	.354
340	358	.443	1,586	271	.997	.376
345	.....	.4445	1,825	307	.998	.399
350	469	.446	2,092	335	.999	.421
355	.....	.447	2,369	405	.999	.444
360	598	.448	2,679	407	1.000	.466
365	.....	.449	3,017	444	.....	.....
370	752	.450	3,384	458	.....	.....
375	.....	.4505	3,776	479	.....	.....
380	931	.451	4,199	507	.....	.....
385	.....	.451	4,605	549	.....	.....
390	1,137	.4515	5,134	579	.....	.....
400	1,369	.452	6,188	630	.....	.....

Radiometry Laboratory (355 ft) and much narrower ones at mountain elevations. The rapid spectral scanning rate (300 to 400 mμ in about 3 min) permits the completion of an ultraviolet spectrogram before a significant change occurs in the air mass [2] even for air masses M=2.0 to M=3.0.

Within the wavelength range extending from about 299 to 330 mμ the spectral intensities increase so rapidly with wavelength that in order to evaluate the data properly the instrumental sensitivity must be changed at intervals of 10 to 30 mμ. For example, below about 304 mμ for an air mass M=1.4 an increase of 1 mμ in wavelength results in nearly 100-percent change in the intensity of solar radiant energy reaching the earth's surface. This rapid increase of intensity with wavelength made difficult the accurate interpretation of recorder records below 320 or 330 mμ. Hence, within this spectral region, supplementary readings were usually made by manual operation of the wavelength drive of the instrument and by recording the energy values as indicated on a Ballantine alternating-current VTVM or by the Leeds & Northrup recorder.

III. Ultraviolet Solar Energy Curve

The data on which the solar energy curves displayed in figures 2 and 3 and in table 2 are based were obtained in the Radiometry Laboratory at this Bureau, which is located in the northwest section of Washington away from a large part of the city smoke. The air mass penetrated by the direct solar rays ranged from approximately M=1.35 to M=1.50 during the course of the mesasurements. Representative data for specific air masses are given for a few days during the early part of October. On some of the days on which 10 to 20 spectral determinations were rapidly made within the spectral range from 299 to 315 (or 320) mμ considerable variation was noted in the shorter wavelength intensities relative to that at 315 or 320 mμ. As the Rayleigh scattering factor is not greatly different (see table 1) between the limits of this wavelength interval, it is to be concluded that the greater fluctuations at the shorter wavelengths must be primarily associated with rapid changes in the amount of ozone penetrated. The data in table 2, and for the shorter wavelengths in figures 2 and 3, are the averages of three to seven sets of measurements at air masses approximating the values applied to the curves.

The solar energy curves displayed contain numerous absorption bands varying in magnitude both in spectral width and in intensity of absorption. If reference is made to the Rowland maps and wavelength data [8] and to the Utrecht photometric atlas of the solar spectrum [9], it is found that each band

[2] In this paper air mass, represented by M, refers to the amount of air between the observer and the sun; air mass, M=1, being assigned to a single thickness of atmosphere above the particular station. For any solar position air mass is nearly proportional to the cosecant of the angle the sun's rays make with the earth's surface. For sunlight outside the earth's atmosphere, air mass, M=0. The reader must not confuse this use of the term, air mass, with the same term used to designate air of a particular origin, temperature, or other property.

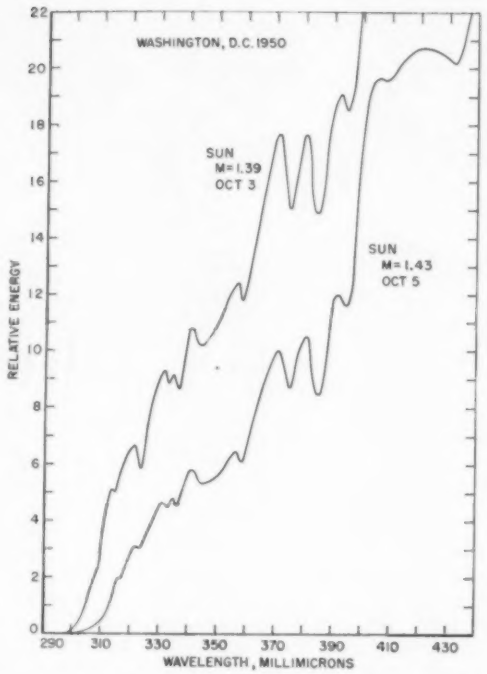

FIGURE 2. *Spectral distribution of radiant energy at Washington, D. C., from the sun for 2 days in October 1950; ordinates arbitrary.*

results from one or more groups of intense Fraunhofer lines. Some of these result mainly from one or two elements in the solar atmosphere—others from several elements. For example, in the spectral region of 309 mμ the principal absorbing elements are the neutral metals, Ni, Mn, Al, and Fe, accompanied by OH, while at 315 to 316 mμ, Cr, Fe, Ti and others are present. Again at 322 to 323 mμ Fe and several other metals have strong absorption lines, while at 335 to 337 mμ NH shows additional absorption. At 345 to 348 mμ Fe is the principal absorbing element, although many lines of Mn, Ni, and other elements are present. At 358 to 359 mμ and at 375 to 376 mμ the absorption bands result mainly from many strong Fe lines. The strong CN band (at 388 mμ) accompanied by many strong Fe lines (around 385 mμ), together with Mg absorption results in the strong band centered at about 386 mμ. The band at 395 mμ is a combination of the intense H and K Fraunhofer lines located at about 393.5 and 396.8 mμ and results primarily from absorption by ionized Ca and H atoms in the solar atmosphere. At 408 mμ and again at 432 mμ Fe and H are primarily responsible in producing two of the important absorption bands of the visible spectrum of the sun. Two relatively weak bands occurring at 465 and 489 mμ are caused principally by Fe and H, respectively, while the strong band between 520 and 530 mμ results mainly from Mg absorption in the solar atmosphere. A more detailed listing of the principal

TABLE 2. *Observed relative spectral-energy distribution of direct sunlight at Washington, D. C. on 3 days in October 1950*

Wavelength	October 3 $M=1.37$	October 6 $M=1.43$	October 6 $M=1.41$	October 11 $M=1.51$
mμ				
299.2	5	---	3	4
300.2	10	4	7	8
301.2	18	9	13	15
302.2	35	20	29	30
303.2	59	37	45	51
304.2	89	60	74	74
305.2	109	82	99	98
306.2	131	105	120	121
307.2	172	145	156	161
308.2	201	181	192	179
309.2	223	202	210	224
310.2	286	280	283	280
311.2	374	361	359	352
312.2	431	430	421	411
313.2	473	460	461	435
314.2	502	502	510	478
315.2	498	507	519	497
316.2	534	---	---	534
317.2	572	---	---	---
318.2	605	---	---	---
319.2	629	---	---	---
320.2	646	---	---	---
Number of settings	3	4	6	7

Fraunhofer lines responsible for the observed absorption spectrum is given in table 3. The wavelength position of the absorption bands is found to be in close agreement with that of the main concentrations of the winged lines [10] in the solar spectrum.

The large drop in solar radiant energy intensity at about 390 mμ, previously noted by Pettit [1], is very interesting.

When consideration is given to the winged lines [10] of the solar spectrum and their effect upon the observed intensity as vividly displayed on the Utrecht

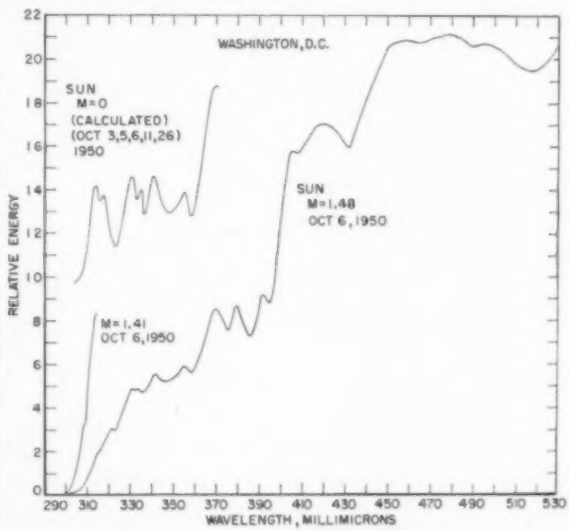

FIGURE 3. *Spectral distribution of radiant energy at Washington, D. C., for 1 day in October 1950; and calculated mean outside the atmosphere for several days; ordinates arbitrary.*

TABLE 3. *Relationship between the location of winged and other strong Fraunhofer lines and the observed minima in the spectral solar energy curve*

Very strong lines result from absorption by the italicized elements

Wavelength Rowland and Utrecht maps	Principal absorbing elements	Observed absorption band
mμ		mμ
308 to 310	Fe, Ni, Mn, Al, OH	308 to 309
316 to 317	Fe I and II, Cr II, Ni, Ti II, OH	315 to 316
323	Fe I and II, Ti II, Ni	322 to 323
331.5	Fe, Zr II, Na I, Ti II, Fe II	...
334	Mg, Ti I, Ti II, Fe, Cr II	335 to 337
336	NH, Ti II, Ni, Cr II	...
344	Fe, Mn II, Ti II, Ni, Co	345 to 348
358	*Fe*, Ni, V II, Sc II, Co, Ti II, Cr II	358 to 359
374	*Fe*, Ni, Ti, Ti II	375 to 376
385	*Fe*, Mg, *CN*	386
394	Ca II, Al, H_ϵ	395
410	H_δ	408
427	Fe	...
434	H_γ	432
476	Mn, Fe, Ti II, Ni	465
490	H_β, Fe	489
520	Mg	520 to 530

maps [9], the drop is adequately explained. As a matter of fact the other intensity depressions and resulting plateaus, for example in the regions of 315 to 360 mμ, 370 to 390 mμ, and 405 to 435 mμ simply represent departures from what would otherwise be a smooth approximate black body curve representative of the mean solar surface temperature, and result primarily from absorption by the winged lines of Fe, Mg, Ca, Ni, H, Ti and Al [9, 10].

The large calculated decrease in solar energy outside the earth's atmosphere for wavelengths shorter than about 310 mμ is probably not entirely real. At least an absorption band occurs at about 304 mμ, as can be detected by the inflection in the observed data at this wavelength. Its magnitude may be overrated in the calculated curve. Pettit's data also indicate a sharp decrease in solar radiant energy for wavelengths below about 310 mμ and probably for the same reason; namely, a lack of correct knowledge of the ozone absorption coefficients for these wavelengths. Data obtained by personnel of the Naval Research Laboratory [6] with apparatus transported by rockets into the stratosphere show no sharp decrease in solar energy at this wavelength except for a strong absorption band near 300 mμ. It is readily understandable that in these calculations, wherein small energy values are divided by extremely low ozone transmittance coefficients, errors in the ozone transmittance are greatly magnified in the short wavelength solar energy curve.

IV. Conclusions

As previously noted the data recorded herein on the solar energy curve, principally in the ultraviolet spectrum, are based on a few measurements made on a few days under similar air mass conditions, both as to time of day (similar values of air mass) and as to type of pressure pattern. Although these data were carefully obtained, their value lies principally in illustration of the use of new equipment and of the method employed in their acquirement, especially in view of the fact that at sea level solar radiant energy intensity values are extremely low at the shorter ultraviolet wavelengths. The quality of these data indicate the practicability of using much narrower spectral slit widths if the apparatus were installed at mountain or desert locations. At suitable stations much valuable solar spectral data should be obtainable.

Data of the type obtained with this instrument have long been urgently needed for use in ozone determinations by means of the phototube and filter method [16 to 18]. Previously a smooth curve best representing the filter measurements has been employed. The limited data recorded herein should serve to permit the use, in future phototube-filter ozone work, of a solar energy curve closely approximating in shape the true spectral energy curve outside the earth's atmosphere.

The use of spectroradiometric equipment of the type employed in the present investigation appears highly promising of producing precise data in total ozone determinations. The presence of numerous Fraunhofer absorption lines in the solar spectrum, resulting in a number of plateaus or inflections in the prismatic curve, furnish wavelength calibration indices that acquire significant importance in ascertaining the correct wavelength positions in the ultraviolet spectrum for use in the ozone calculations. Proper instrumental temperature corrections for use with double monochromator ozone meters ordinarily require unusual precautions. Often outdoor conditions of wind, varying sunlight, etc., render temperature correction next to impossible. With this equipment a solar curve covering the spectral region of the two or three wavelengths necessary for use in the ozone calculation may be made within a few minutes and it will include, on the same chart, the correct wavelength indices in the form of the Fraunhofer bands.

Tests on sky-light indicate a sensitivity of the equipment, as used on direct sunlight, sufficient to observe the spectral energy distribution down to about 310 mμ before noise becomes excessive. For practical use the full aperture can be employed. The small mirror employed with the sun (3 by 5 in.) and situated at a distance of about 6 ft from the spectrometer allowed use of only a small part of the total instrumental aperture in the tests to which reference is made. Wider spectral slit widths might also be employed. Hence, it would appear to be feasible to employ this equipment in the study of the spectral quality of the scattered radiant energy present in small areas of sky light.

V. References

[1] Edison Pettit, Spectral energy-curve of the sun in the ultraviolet, Astrophys. J. **91,** 159 (1940).

[2] C. G. Abbot, F. E. Fowle, and L. B. Aldrich, The distribution of energy in the spectra of the sun and stars, Smithsonian Misc. Collections **74,** No. 7 (1923).

[3] Paul Hess, Untersuchungen über die spektrale Energieverteilung im Sonnenspektrum von 350 mμ bis 500 mμ, Inaugural-Dissertation, Universität Frankfurt a. M. (1938).

[4] C. Fabry and M. Buisson, Etude de l'extrémité ultraviolete du Spectre solaire, J. Phys. radium **2,** 197 (1921).
[5] F. W. Paul Götz and Ernst Schönmann, Die spektrale Energieverteilung von Himmels- und Sonnenstrahlung, Helv. Phys. Acta **21,** 151 (1948).
[6] E. O. Hulburt, The Upper Atmosphere of the Earth, J. Opt. Soc. Am. **37,** 405 (1947).
[7] Heinz Reiner, Die Struktur des Sonnenspektrums zwischen 400 und 600 mμ, Gerlands Beitr. Geophys. **55,** Heft 2, 234 (1939).
[8] Rowland's Map of the solar spectrum. For Rowland's wavelengths see Astrophys. J. **1, 2, 3, 4, 5** (1895–97). For revised wavelengths see Revision of preliminary table of solar spectrum wavelengths, etc. by Charles E. St. John, et al, Carnegie Publication No. 396 (1928).
[9] M. Minnaert, G. F. W. Mulders, and J. Houtgast, The Utrecht photometric atlas of the solar spectrum (J. Schnabel, Amsterdam, 1940).
[10] Charlotte E. Moore and Henry Norris Russell, On the winged lines in the solar spectrum, Astrophys. J. **63,** 1 (1926).
[11] Deane B. Judd, The 1949 scale of color temperature, J. Research NBS **44,** 1 (1950) RP2053.
[12] F. Hoffman and H. Willenberg, Das Emissionsvermögen des Wolframs im ultraviolett bei hohen Temperaturen, Physik. Z. **35,** 1, 711 (1934).
[13] H. C. Hamaker, Reflectivity and emissivity of tungsten, Inaug. Diss. (Utrecht, Holland, 1934).
[14] W. E. Forsythe and A. G. Worthing, The properties of tungsten and the characteristics of tungsten lamps, Astrophys. J. **61,** 146 (1925).
[15] L. S. Ornstein, Tables of the emissivity of tungsten as a function of wavelength from 0.23-2.0 μ in the region of temperature 1600° to 3000° K, Physica **3,** 561 (1936).
[16] R. Stair and I. F. Hand, Methods and results of ozone measurements over Mount Evans, Colo., Mo. Weather Rev. **67,** 331 (1939).
[17] Ralph Stair, Measurements of ozone over the Organ Mountains, New Mexico, J. Research NBS **40,** 9 (1948) RP1851.
[18] Ralph Stair, Seasonal variations of ozone at Washington, D. C., J. Research NBS **43,** 209 (1949) RP2022.
[19] Ralph Stair, Photoelectric spectroradiometry and its application to the measurement of fluorescent lamps, J. Research NBS **46** 437 (1951) RP2212.
[20] Ralph Stair and W. O. Smith, A tungsten-in-quartz lamp and its applications in photoelectric radiometry, J. Research NBS **30,** 449 (1943) RP1543.

WASHINGTON, November 27, 1950.

Journal of Research of the National Bureau of Standards Vol. 46, No. 5, May 1951 Research Paper 2207

Wind Tides in Small Closed Channels

Garbis H. Keulegan

In addition to the generation of waves, a wind produces a mass transport in a body of water resulting in the lowering of the level at the windward side and rise at the leeward side, which is called wind tide or set-up. Two effects of the wind are involved: the surface traction on the water, and the form resistance of the waves. This paper presents the theoretical background of the subject and experimental results. It was discovered that formation of waves in an experimental channel could be inhibited by adding small amounts of soap or detergent to the water. This made it possible to study the surface traction effect separately. The effect was studied for both laminar and turbulent motion of the drift and gravity currents produced by the wind. The set-up computed from measured wind and water surface velocities agreed with theory. Regardless of the flow regime, the set-up was unaffected by viscosity and independent of the depth-length ratio of the channel. The additional set-up due to presence of waves could be correlated only by introducing a characteristic velocity. This additional set-up appears to vary as the square root of the depth-length ratio. The relation of the characteristic velocity to the critical velocity for wind generation is discussed. The derived empirical formula for set-up is compared with observations in Lake Erie.

I. Introduction

Early in the course of a comprehensive investigation of density currents now under way, the question arose as to what phenomena might have a probable bearing, no matter how remote, on the general problem of density currents and especially on the stability of the interface between two fluids of different densities. Among such phenomena are the disturbances that may be introduced by wind-generated surface waves on the interface between two layers of different densities such as occur in lakes and in the lower reaches of rivers emptying into the ocean.

At least two ways in which surface wind waves may affect the interface may be imagined. The first possibility is that internal waves will be generated as a response to the surface waves. This, however, is very unlikely to happen. It is well known that a two-layer system of liquids with a free surface is a system of two degrees of freedom. To one degree of freedom there corresponds the ordinary waves of a homogeneous liquid, and to the other the internal waves of the interface. The velocities of propagation of these two types of waves are unequal, and the particle motions are significantly different from each other. In ordinary waves of a homogeneous liquid, the particle motions along a given vertical line are in the same direction from the bottom to the free surface. With internal waves on the other hand, the particle motions are oppositely directed in the two layers of different densities. It follows that whatever may be the agency that causes the ordinary type of waves in a homogeneous liquid, the same agency cannot produce internal waves if the homogeneous system is replaced by a system of two layers of liquids. Wind waves are surface waves of ordinary type and therefore will not excite internal waves. If internal waves are to be created, they must be produced by displacements of the internal surface that will leave the free surface practically smooth.

The second possible effect of surface wind waves arises from their tendency to produce turbulence in the region occupied by the interface, which causes mixing of the two liquids. It is conceivable that this mixing is brought about in two ways. First, wind-generated waves are associated inherently with turbulence, and a progressive downward movement of turbulence may reach the level of the interface. If the density difference at the two sides of the interface is small, and if the turbulence fluctuations are sufficiently strong, a gradual mixing of the liquids obviously will take place.

The second and more significant way in which mixing at the interface might occur may be illustrated by the case of a lake subjected to wind wave where there is a considerable wind tide or set-up present. If there are two layers of liquids of different densities in the lake, the set-up will produce circulations of opposite directions in the two layers and thereby will cause mixing. If the density differences are small, a similar effect may also be expected to occur in the case of salt intrusion in a river when the wind is blowing in the upstream direction. The smaller the river velocity, the larger will be the mixing due to wind effects.

Before considering the effect on interfacial stability of surface disturbances caused by wind, it is necessary that sufficiently full information be obtained on the dynamical and geometrical characteristics of the wind waves and especially of wind waves in shallow and long channels. There appear to be no complete investigations, either theoretical or experimental, regarding such waves. Having in mind the excellent theoretical work of Sverdrup and Munk [1][1] on wind waves and swells originating in

[1] Figures in brackets indicate the literature references at the end of this paper

deep waters, it was thought that an experimental investigation relating to shallow waters would be a relatively simple matter. It was soon evident that there are many difficulties in the study of wind waves in a laboratory channel with shallow water that are absent in the case relating to deep water. An extensive program of investigation is practically unavoidable. As the subject is of much wider interest and practical importance than merely in its relation to density currents, a separate project was initiated. For convenience this project has been divided into three parts: (1) wind tides or set-up in small channels, (2) the dissipation characteristics of oscillatory progressive waves in long shallow channels, and (3) the growth of wind waves in height and length in long shallow channels.

The present paper deals with the first subject, that is, wind tides or set-up in small closed channels. This subject is of considerable practical importance in relation to wind effects on long shallow lakes and the feasibility of model tests. The problem of Lake Okeechobee falls into this category. Although a final solution of the question of model testing and of valid transference equations is not reached, nevertheless the results obtained represent a method of approach toward this solution.

II. Theoretical Developments

1. Generalized Surface Equation

The generalized surface equation is the differential equation involving the surface displacement of a limited body of water, the free surface being subjected to a tangential stress. We shall consider a channel closed at its ends with a constant width throughout and the bottom horizontal. The surface equation can be established very conveniently by considering the general equations of motion of the Navier type.

Selecting the origin of the axes at the bottom, with x along the channel axis and z vertical and drawn upwards as in figure 1, the equations of motion are:

$$\frac{\partial u}{\partial t}+u\frac{\partial u}{\partial x}+w\frac{\partial u}{\partial z}=-\frac{1}{\rho}\frac{\partial p}{\partial x}+\frac{1}{\rho}\left[\frac{\partial N_1}{\partial x}+\frac{\partial T_2}{\partial z}\right], \quad (1)$$

$$\frac{\partial w}{\partial t}+u\frac{\partial w}{\partial x}+w\frac{\partial w}{\partial z}=-\frac{1}{\rho}\frac{\partial p}{\partial z}-g+\frac{1}{\rho}\left[\frac{\partial T_2}{\partial x}+\frac{\partial N_3}{\partial z}\right]. \quad (2)$$

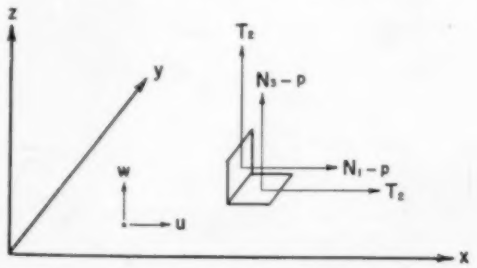

FIGURE 1. *Coordinate axes and stresses.*

Here u and w are the velocity components parallel to the x and z axes, respectively, p is the pressure, g the acceleration of gravity, and ρ the density of the liquid. The quantities N_1, N_3, T_2, are the tractional stresses as shown in figure 1. In the notation of Lamb, $N_1=p+p_{xx}$, $N_3=p+p_{zz}$, and $T_2=p_{xz}$.

The equations in the form given are too general and too difficult to integrate. In the case of a long shallow channel some simplifying assumptions may be adopted. These assumptions are commonly resorted to in solutions of boundary layer flow problems and are well known. As the surface curvature is small, the vertical acceleration and the normal traction N_3 will be neglected. As the surface displacement is small, the normal traction N_1 will be neglected. The variation of T_2 with respect to x is negligible since the channel is very long. Accordingly, the simplified forms of the equations of motion, writing τ for T_2 are

$$\frac{\partial u}{\partial t}+u\frac{\partial u}{\partial x}+w\frac{\partial u}{\partial z}=-\frac{1}{\rho}\frac{\partial p}{\partial x}+\frac{1}{\rho}\frac{\partial \tau}{\partial z}, \quad (3)$$

$$0=-\frac{1}{\rho}\frac{\partial p}{\partial z}-g. \quad (4)$$

It is to be noted that one consequence of the assumptions is to regard the pressures as hydrostatic. For the long central portion of the channel, these forms of the equations are sufficiently valid. They fail, however, to represent the conditions of flow at the ends of the channel.

Denoting the undisturbed depth of the water by H, as in figure 2, the surface displacement as measured from the initial level by h, and the atmospheric pressure by p_a, eq 4 yields

$$p=\rho g\,(H+h-z)+p_a. \quad (5)$$

Substituting in eq 3,

$$\frac{\partial u}{\partial t}+u\frac{\partial u}{\partial x}+w\frac{\partial u}{\partial z}=-g\frac{\partial h}{\partial x}-\frac{1}{\rho}\frac{\partial p_a}{\partial x}+\frac{1}{\rho}\frac{\partial \tau}{\partial z}. \quad (6)$$

Now, since the liquid is incompressible,

$$\frac{\partial u}{\partial x}+\frac{\partial w}{\partial z}=0. \quad (7)$$

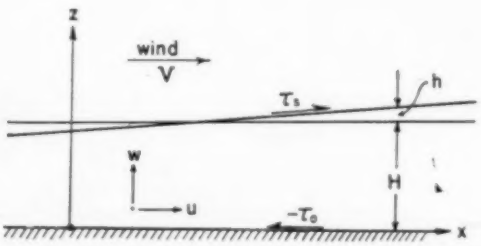

FIGURE 2. *Water levels and surface shears*

The rule

$$w\frac{\partial u}{\partial z}=\frac{\partial}{\partial z}(wu)-u\frac{\partial w}{\partial z}, \tag{8}$$

combined with eq 7 yields

$$w\frac{\partial u}{\partial z}=\frac{\partial}{\partial z}(wu)+u\frac{\partial u}{\partial x}. \tag{9}$$

Substituting this in eq 6,

$$\frac{\partial u}{\partial t}+\frac{\partial u^2}{\partial x}+\frac{\partial}{\partial z}(wu)=-g\frac{\partial h}{\partial x}-\frac{1}{\rho}\frac{\partial p_a}{\partial x}+\frac{1}{\rho}\frac{\partial \tau}{\partial z}. \tag{10}$$

Multiplying the two sides of the equation by dz, integrating with respect to z between the limits 0 and $(H+h)$, and noting that $w=0$ at the bottom where $z=0$,

$$\left.\begin{aligned}&\int_0^{H+h}\frac{\partial u}{\partial t}\,dz+\int_0^{H+h}\frac{\partial u^2}{\partial x}\,dz+w_s u_s=\\&-\left(g\frac{\partial h}{\partial x}+\frac{1}{\rho}\frac{\partial p_a}{\partial x}\right)(H+h)+\frac{1}{\rho}(\tau_s+\tau_0),\end{aligned}\right\} \tag{11}$$

where w_s and u_s are the velocity components at the free surface, τ_s and $-\tau_0$ are the tangential stresses at the free surface and at the bottom (see fig. 2). We may express w_s in terms of u_s by considering the surface kinematic condition that a particle at the free surface remains on the surface. Symbolically,

$$w_s=\frac{\partial h}{\partial t}+u_s\frac{\partial h}{\partial x},\ z=H+h. \tag{12}$$

Introducing this in eq 11 and remembering Leibnitz's rule for differentiation under the integral sign, we have

$$\left.\begin{aligned}&\frac{\partial}{\partial t}\int_0^{H+h}u\,dz+\frac{\partial}{\partial x}\int_0^{H+h}u^2dz=\\&-\left(g\frac{\partial h}{\partial x}+\frac{1}{\rho}\frac{\partial p_a}{\partial x}\right)(H+h)+\frac{1}{\rho}(\tau_s+\tau_0).\end{aligned}\right\} \tag{13}$$

This is the generalized differential equation of the surface for a long body of water subjected to the surface tractions τ_s and $-\tau_0$. The terms on the left-hand side are the acceleration terms.

If the conditions are steady, as when the wind has acted with uniform intensity over the body of water for a long time, the equation reduces to

$$\frac{\partial}{\partial x}\int_0^{H+h}u^2dz=-\left(g\frac{\partial h}{\partial x}+\frac{1}{\rho}\frac{\partial p_a}{\partial x}\right)(H+h)+\frac{1}{\rho}(\tau_s+\tau_0). \tag{15}$$

Under certain assumptions, to be discussed later, the acceleration term on the left-hand side of the equation may be neglected. Thus, the surface equation reduces to

$$\frac{\partial h}{\partial x}+\frac{1}{\rho}\frac{\partial p_a}{\partial x}=\frac{1}{\rho}\frac{\tau_s+\tau_0}{g(H+h)}. \tag{16}$$

From this point on it will be supposed either that the atmospheric pressure or, more properly stated, the pressure on the free surface, does not vary with x; or that if it does vary, a correction is made so that h will denote the surface elevation after due account is made of the pressure effect. With this understanding, the basic simplified surface equation is

$$\frac{\partial h}{\partial x}=\frac{\tau_s+\tau_0}{\rho g(H+h)}. \tag{17}$$

A further simplification, based on assumptions relating to the relative values of τ_0 and τ_s, is needed. The flow in the channel is a combustion of a drift current at the surface and a gravity current at the bottom. The drift current is induced by the wind. The gravity current is induced by the inclination of the upper free surface, its direction being opposite to that of the drift current.

Denoting the mean velocity of the gravity current by u_0, the resistance of the channel bottom may be written as

$$\tau_0=k_0\rho u_0^2. \tag{18}$$

Similarly, if V is the wind velocity and ρ_a the density of the air, the surface traction may be expressed as

$$\tau_s=k_s\rho_a V^2. \tag{19}$$

Considering the ratio

$$\tau_0/\tau_s=\frac{k_0\rho u_0^2}{k_s\rho_a V^2}, \tag{20}$$

it is not obvious that τ_0 is negligible with respect to τ_s. The velocity u_0 may be small with respect to V, but since ρ is about one thousand times larger than ρ_a, the product ρu_0^2 may be a measurable portion of $\rho_a V^2$. Besides one must also consider the relative values of k_s and k_0, and at the moment it cannot be said that k_0 is smaller than k_s. For these reasons, it is better not to neglect τ_0 with respec to τ_s, but to incorporate it with τ_s. Writing

$$n=\frac{\tau_0}{\tau_s}+1, \tag{21}$$

eq 17 becomes

$$\frac{\partial h}{\partial x}=\frac{n\tau_s}{g\rho(H+h)}. \tag{22}$$

If a computation is made on the basis of pure viscous laminar motion, and this will be done in one of the following sections, it will be seen that $n=1.5$. The determination of n for turbulent motion requires some form of turbulent theory for the case under consideration. The value of n will then depend on the particular theory adopted. Hellström [2], after

adopting the Boussinesq theory for turbulent flow, finds that n varies between the values 1.15 and 1.80 for channels of moderate and very large depths. Temporarily we shall take $n=1.25$ for turbulent flow.

2. Surface Equation for Laminar Flow

From the viewpoint of theory it is important to consider the case of laminar flow. The chief interest, of course, rests on the fact that for this case a solution is easily available. In laboratory experiments, as will be shown later, this solution is of great value when the depths are small.

In viscous flow of the type envisaged

$$\tau=\mu\frac{\partial u}{\partial z}. \tag{23}$$

Substituting in eq 10, neglecting inertia terms, supposing the flow to be steady, the pressure over the surface uniform, and the surface displacements small with respect to the depth of water, there results

$$\frac{d^2u}{dz^2}=\frac{g}{\nu}\frac{dh}{dx}. \tag{24}$$

If the velocities are expressed in terms of the surface velocity, u_s, and the distances from the bottom in terms of the initial liquid depth, H, this equation may be made dimensionless. Thus, writing

$$\frac{u}{u_s}=\theta, \frac{z}{H}=\zeta, \tag{25}$$

and

$$\frac{gH^2}{\nu u_s}\frac{dh}{dx}=\alpha, \tag{26}$$

eq 24 becomes

$$\frac{d^2\theta}{d\zeta^2}=\alpha, \tag{27}$$

which is subject to the boundary conditions

$$\left.\begin{aligned} &\theta=0, && \zeta=0,\\ &\theta=1, && \zeta=1,\\ &\int_0^1\theta d\zeta=0. \end{aligned}\right\} \tag{28}$$

The first condition states that the velocity at the bottom is zero, the second that velocities are measured in terms of the surface velocity, and the third that the integrated flow in a vertical cross section vanishes.

The desired solution subject to the boundary conditions is

$$\theta=3\zeta^2-2\zeta, \tag{29}$$

and

$$\alpha=6. \tag{30}$$

Equation 29 gives the law of velocity distribution. In the horizontal plane at a distance of $H/3$ below the liquid surface the velocities vanish. All the particles above this plane move in the direction of the wind, and the particles below this plane move in the opposite direction. The former represents the drift current, and the latter the gravity current. Equation 30 gives the surface equation; for, using eq 26,

$$\frac{dh}{dx}=\frac{6\nu u_s}{gH^2}, \tag{31}$$

which relates the surface inclination to the depth of liquid, the surface velocity, and the kinematic viscosity of the liquid in the channel.

Now, from eq 23 and 25,

$$\tau=\frac{\mu u_s}{H}\frac{d\theta}{d\zeta}. \tag{32}$$

The surface shear and the shear at the bottom correspond to $\zeta=1$ and $\zeta=0$, respectively, and we have for these shears

$$\tau_s=4\frac{\mu u_s}{H}, \tag{33}$$

and

$$-\tau_0=-2\frac{\mu u_s}{H}; \tag{34}$$

that is, the surface shear is twice as large as the shear at bottom. The surface equation may be written also as

$$\frac{dh}{dx}=1.5\frac{\tau_s}{\rho gH}. \tag{35}$$

It is apparent that ignoring the bottom shear results in a 50-percent error.

III. Characteristics of the Experimental Channel

1. Apparatus

The apparatus, shown diagrammatically in figure 3, consisted of three parts: the entrance assemblage, the experimental channel, and the terminal assemblage.

The upstream blower in the entrance assemblage was driven by a constant speed motor. The air volume, and hence the air velocity in the experimental channel, was controlled by a damper at the intake end of the blower by means of which the intake area could be varied. The control of air velocities by this method was very satisfactory.

At the discharge end of the blower was a rectangular duct of the same dimensions as the blower discharge opening connected to a duct converging in plan to the width of the experimental channel. This was followed by a Venturi nozzle of constant

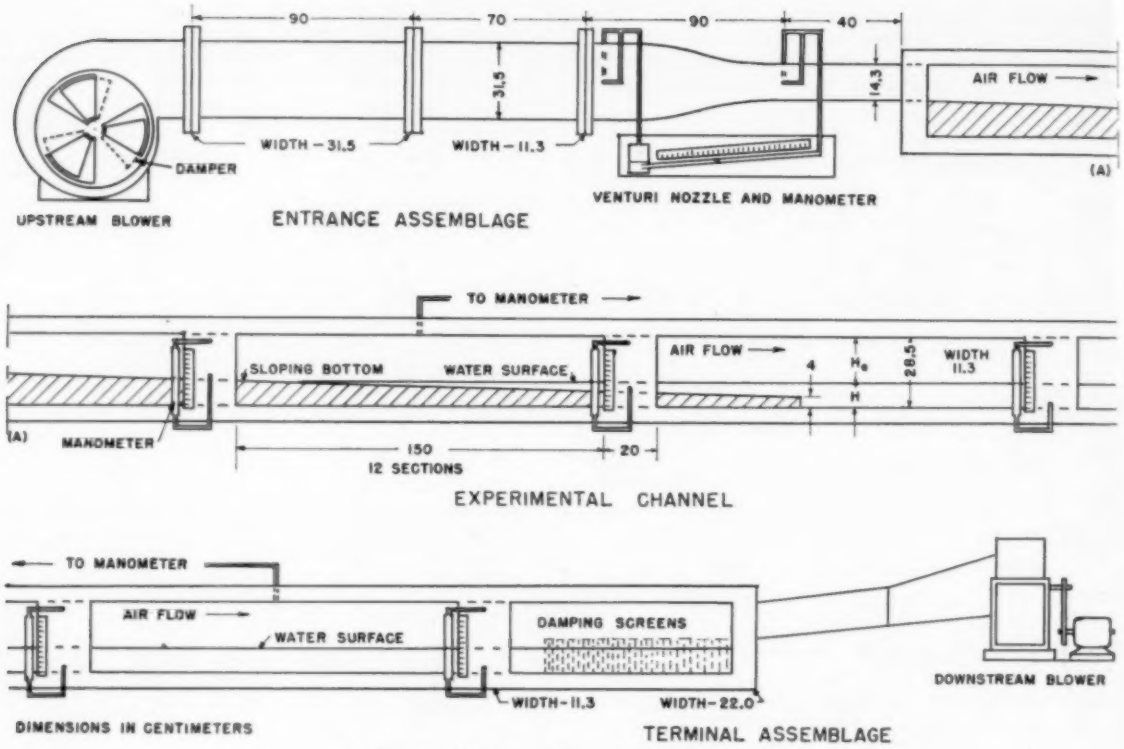

FIGURE 3. *Diagram of experimental apparatus.*

width and converging in the vertical dimension to half the height of the experimental channel. Piezometer openings in the side walls of the Venturi nozzle were connected to an inclined manometer. The Venturi was connected by a short duct to the upper half of the experimental channel. It was thought that the length of the assemblage and the lateral and vertical contractions would even out most of the irregularities in flow produced by the blower.

The experimental channel, shown in figure 3, was a closed conduit of uniform rectangular cross section, 28.5 cm deep, 11.3 cm wide, and about 20 m long. It consisted of 12 sections constructed of wood with sides of glass. The glass sections were connected by short sections made of wood. Piezometers, opening to the inside air at the top and to water at the bottom of the channel were installed in the walls of the wooden sections. The piezometer openings were connected to glass manometer wells. The average water levels in the channel were measured by the water levels in the manometers.

It was desired to make tests with different depths of water. As it was not practicable to change the elevation of the Venturi nozzle, a sloping floor was set in the upstream end of the channel. The rate of variation of the air cross section was quite small, thus assuring a nearly uniform air velocity distribution vertically.

In the top of each channel section at the center was placed a piezometer opening, and the drop in air pressure between any pair of these could be measured by connecting them to an inclined manometer. During observations of set-up, those two piezometers were used that were nearest to the ends of the fetch over which measurements were being made.

The terminal assemblage, also shown in figure 3, began at the end of the experimental channel with a section expanding in width. A succession of screens was placed at the lower end for damping of the waves. The screens were spaced about 2 cm apart initially and the spacing decreased to about ½ cm at the downstream end. The arrangement proved to be quite satisfactory. The damping was gradual and effective, there being no appreciable reflection of the waves. Downstream from this section was a duct sloping slightly upward and expanding to the size of the intake opening of the downstream blower. This blower was used in addition to the upstream one whenever high air velocities were required.

2. Calibration of the Venturi Nozzle

The mean velocity of the air stream over the water in the channel was chosen as the significant velocity to be associated with the growth of waves or with the development of wind set-up. The depth

of the channel being small, the height of the air passage over the water decreased continually in the leeward direction because of the set-up and of the increase in wave heights. Therefor it was not very practical to measure the local mean air velocity at any chosen cross section. Instead, the air velocity was deduced from the velocity at the discharge end of the Venturi nozzle. Thus if V_1 is the velocity and A_1 the area of the nozzle exit, and V is the mean air velocity in the channel for an air passage of cross-sectional area A, then $V=V_1A_1/A$. The area, A, represents the mean value of the area averaged along the entire length of the channel. Obviously, A is also the area of the air passage cross section when the water in the channel is not disturbed. In the measurements of set-up, however, the decrease of the cross section of the air passage with distance was considerable, and hence corrections were devised, as will be explained later, to obtain the value of the effective wind velocities.

The differential head reading of the inclined manometer was an indication of the velocity at the discharge end of the Venturi nozzle. The calibration was made in the following manner. The terminal assemblage at the lower end of the experimental channel was removed, and the velocities at the end section of the channel were measured. These were associated with the simultaneous readings of the Venturi manometer. The velocities at the channel end were measured by two instruments. One was a propeller-type anemometer of current manufacture that was calibrated in a wind tunnel by the Aerodynamics Section of the National Bureau of Standards. The second instrument was a small Ott current meter. Although this instrument is used ordinarily for flowing water and the calibration is likewise made in water, it can, nevertheless, be used for flowing air provided the calibration of the instrument is expressed in the form

$$N/U=f(U\sqrt{\rho}), \tag{36}$$

where N is the number of revolutions per second corresponding to the velocity, U. [3] To be sure that this relationship applied to the Ott meter to be used, it was calibrated both in water and in air. In the range where the calibration results with air and with water overlapped, the results fell on the same curve.

The Ott meter, being the smaller of the two, was set in six different positions in the channel cross section. The other instrument was set in three positions on the vertical center line. The average of the mean velocities determined in these two ways was taken to be the mean velocity of the air stream at the end cross section of the channel. Comparing the cross-sectional areas, the velocity at the nozzle was obtained in relation to the manometer reading. Following this, a second calibration was obtained after attaching to the end of the main channel an additional closed rectangular conduit of a larger cross section. In the second channel both instruments were set in six different positions.

It was gratifying to note that the Venturi nozzle velocities as observed during the calibrations could be very well represented by the theoretical expression.

$$2\rho g\Delta h=\rho_a V_1^2\left[1-\left(\frac{A_1}{A_2}\right)^2\right], \tag{37}$$

where Δh is the reading of the inclined manometer in feet of water, and A_2 is the area at the entrance of the nozzle. The final calibration chart was made by using the above formula and taking $\rho_a/\rho=1.16\times10^{-3}$, a value corresponding to an atmospheric pressure of 740 mm Hg and an air temperature of 23° C.

3. Air Velocity Distribution in Channel

In studies of the growth of waves with distance and of the development of wind set-up under natural conditions the proper selection of the elevations for the measurement of wind velocities is a difficult matter. If one could assign an operative roughness length, k, independent of the dimensions of waves excited by the wind, it would be sufficient to measure the wind velocity at a constant elevation, z_a, independent of the wind velocity. The investigations of Roll [4] concerning the wind field over the seas show that an operative constant roughness in the above sense does not exist and the roughness is dependent on the wind velocity. This naturally introduces a complication if results of investigations in the open seas are to be compared with results obtained under laboratory conditions.

Because of the limited channel dimensions there is little latitude in selecting the location for the wind velocity measurements in laboratory tests. The velocity of the wind may be taken either as the velocity at the center of the area above the water or as the mean velocity all over the area. In the present investigation the second choice was preferred. This procedure would be free of any objection provided the air velocity distributions in the channel remain always affine to each other for varying velocities and varying water depths. This matter was examined for a water surface free of waves.

One additional point that needed examination was the assumed effectiveness of the expansion caused by the sloping bottom at the entrance of the main channel (see fig. 3) in establishing uniform air velocities at the leeward end of the expansion. For this purpose two sections were chosen, one at the windward end and the other at the leeward end of the channel, and vertical air velocity traverses were made along the vertical median plane. One group of such determinations is shown in figure 4, where V represents the velocity at a distance, z_a, from the water surface, V_m the average velocity along the vertical, and H_a the height of the air gap. In this case the water depth was 4.0 cm, the air space height 24.5 cm, and the average velocity along the vertical 1,008 cm/sec. The velocity distributions at the two ends of the experimental channel are practically alike. For the same air

space similar determinations were carried out for two other velocities, namely 700 and 480 cm/sec, with results very similar to those shown in figure 4. The measurements were repeated for other air gaps, namely H_a=20.5, 17.5, 14.0 cm, with three air velocities not greatly different from those mentioned above. It was noted in every case, regardless of the air space or the magnitude of the mean air velocity, that the median vertical velocity distributions were alike in the extreme end cross sections. Thus for the comparison of the velocity distributions in each air space it should suffice to consider the averages from the measurements with a chosen air space. Such mean values are shown in figure 5. From the curve drawn in the figure we make two deductions. First, central wind velocities are about 1.1 times as large as the mean air velocity. Second, there are no large differences between the air velocities near the rigid top of the channel and those near the water surface. If anything, the air velocities near the water surface are slightly higher, as might be expected.

Next, the horizontal velocity distribution close to the water surface was examined. The results of a few traverses are shown in figure 6. The plotting is V/V_{max} versus y/B, where V_{max} is the velocity at the median plane, V the velocity at a distance, y, from one of the vertical walls, and B the width of the channel. The liquid in the channel was of large viscosity so that for large air velocities the surface would be free of waves. Three series of traverses were obtained for the surface of the liquid thus unmodified by waves corresponding to settings of the pitot tube at successive elevations, z_a, of 0.4, 0.9, and 1.7 cm above the water surface. The results are shown in the figure by the open symbols. Only one measurement of velocities was made with the liquid surface covered with waves. In these measurements the pitot tube aperture was almost at the level of the crests of the waves. The data for these tests are shown by black circles. It is important to note that for the lateral traverses the distributions of the velocities are more uniform than in the vertical traverses. The presence of the waves hardly modifies this comparison.

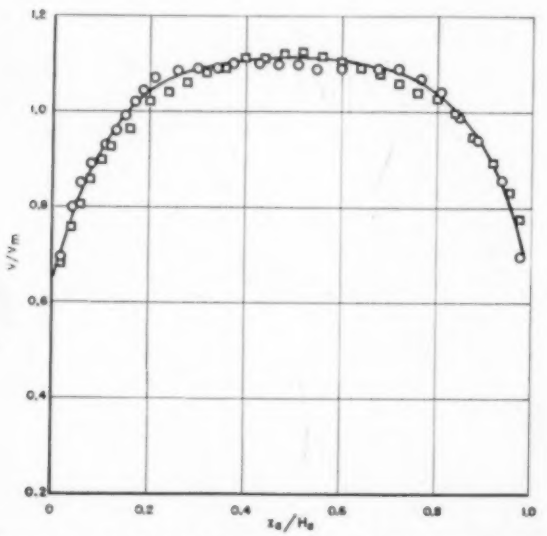

FIGURE 4. *Vertical distributions of air velocities at the ends of the channel.*

Circles, velocities at windward end; squares, velocities at leeward end.

IV. Wind Set-Up in the Absence of Waves

1. Effect of Soapy Waters on the Start of Waves

It was discovered accidentally during the conduct of the routine experiments that the addition of soap to the water inhibited the formation of waves by wind action. Ordinarily when the water in the channel was free of foreign matter, a wind with velocity of 300 to 400 cm/sec caused waves to be formed. An increase in the wind velocity above this value increased the height and length of the waves. On the other hand, when soap was introduced in the water and the wind velocity was increased gradually from zero value, it was found that no matter how great the wind velocity, the surface of the liquid resisted the formation of waves. Even at a wind velocity of 1,200 cm/sec, which was the limiting capacity of the apparatus, the soapy liquid surface was free of waves. This peculiar phenomenon could be repeated for all depths of liquid from 4 to 14.5 cm. The same condition could also be reproduced by introducing a detergent of the type sold for cleansing kitchen utensils, instead of soap.

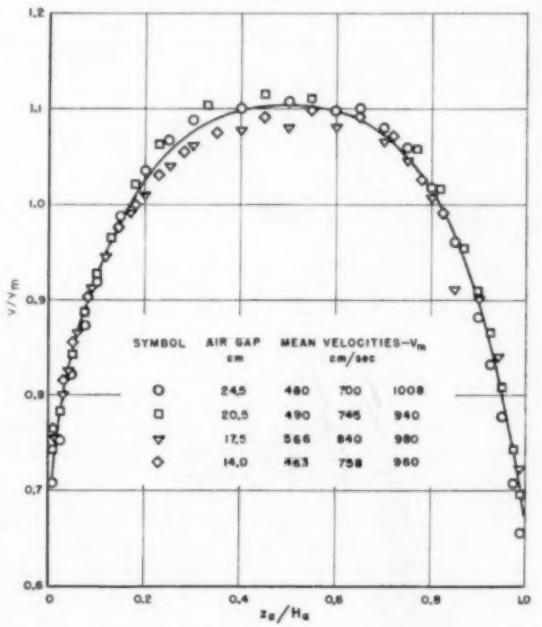

FIGURE 5. *Vertical distributions of air velocities at center-line of channel.*

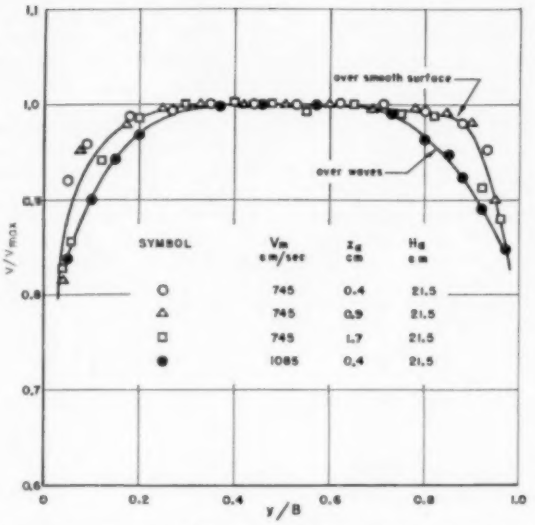

FIGURE 6. *Horizontal distributions of air velocities near liquid surface.*

It must not be inferred from the above that in contaminated waters of the kind described all wave motions are impossible. If, by a special manipulation, waves of substantial dimensions are once produced, these continue to grow in size and multiply in number after traveling long distances under the action of the wind. We have had a very significant experience demonstrating this fact which deserves a brief mention here.

The soapy water in the channel was about 10 or 11 cm deep, the two blowers were in action and, owing to the large air velocity, the water surface was considerably inclined, the greater depth, of course, being at the leeward end of the channel. The surface was smooth and free of waves. The windward edge of the water was located on the solid sloping surface at the channel entrance. To see what effect a sudden reduction of the air velocity would produce, one of the blowers was stopped quickly. Immediately a surge from the leeward end of the channel started to travel toward the windward end. At the instant that the surge reached the windward end and the water commenced to pile up on the sloping surface there, the idle blower was started again. Under the impact of the increasing wind two joining intumescenses were seen to develop at the windward water edge which moved in the leeward direction. In the movement the number of the waves continually increased and the crests became higher. Thus a limited line of waves, so to speak, was moving downstream, the length of the line increasing continually. Waves in the front of the line would be pressing forward, while at the rear new waves appeared. Finally, a long line of waves was filling the last quarter of the channel whereas the water in the rest of the channel was smooth and undisturbed. This line of waves would be seen to enter the wave dampers, and after a while the last wave of the line would be lost. Following this a new surge started moving toward the windward end. The cause of the surge was the sudden decrease of the wave friction concommitant with the disappearance of the waves. The surge reaching the windward end of the channel, a new pair of waves was seen to be formed and the entire process of wave group motion described above was repeated. The phenomenon appeared to reproduce itself periodically and uniformly. Obviously, here was a special case involving the principle of group waves and their generation under the action of wind forces. It is regrettable that, due to the pressure of the main problems of the investigation, additional time could not be devoted to the study of this unusual phenomenon.

Thus the inhibitive action of the soapy water or water containing detergent is to be associated with water surfaces initially undisturbed and therefore free of local elevations occurring over short lengths. Under these conditions, no matter how strong the wind may be, the action of the flowing air fails to start those tremors of the water surface that are always present when the water is pure and the formation of waves is impending. The action of the contaminated water cannot be explained. It would appear that neither viscosity nor surface tension have a bearing on the subject.

Once the fact became known that it was possible to operate with a smooth surface in the channel within the full capacity of the blowers even though the wind velocities were large, by merely adding soap or detergent to the water, it was decided to make full use of it. Numerous experiments were carried out under these conditions that are considered in the subsequent sections. It was felt at the time and also verified later that through these experiments a better understanding of the main problems of the investigation would result.

2. Formulation of Wind Set-Up for Smooth Water Surfaces

The term "set-up" may be defined to represent either the displacement of the water surface at the leeward end of the channel with respect to the undisturbed level of the water or the difference of the displacements of the water levels at the windward and the leeward ends of the channel, that at the windward end being negative. The displacements referred to are the values that remain after correcting for the fall of the air pressure in the channel. In this investigation the term will be used in the second sense. Thus denoting the windward and leeward displacements by h_1 and h_2, respectively, the set-up, S, is

$$S=h_2-h_1. \tag{38}$$

Observations of the set-up were made for depths of 14.5, 11, 8, 6, and 4 cm with smooth water surfaces. In every observation of the set-up for a given wind velocity the following quantities were observed. First, the reading of the Venturi nozzle manometer,

which gave the average wind velocity in the channel, was noted. Second, the elevations of the water levels in the two extreme manometer wells were observed, the distance between the wells being the nearest possible to the fetch, that is, the length of the water surface acted on by the wind. The diameters of the manometer glass tubes being 2 cm, the meniscii were hardly affected by surface tension. The meniscus positions were read by a telescope against a centimeter scale with millimeter divisions, which was placed near and parallel to the tubes. The elevations could be estimated with an accuracy of ± 0.1 mm. Third, the pressure fall in the channel air passage corresponding to the fetch was noted. This was done by connecting the extreme piezometer openings in the top of the channel to an inclined manometer, the pressure differences being read in heads of water.

Because of the inclined solid bottom at the channel entrance the fetch varied with the depth of water. The manometer well distances, L', approximating the fetches were: $L'=2{,}000$ cm for $H=14.5$ cm; $L'=1{,}850$ cm for $H=11$ and 10 cm; and $L'=1{,}725$ cm for $H=6$ and 4 cm. The set-up values observed with these lengths were reduced, after correcting for the pressure fall in the air space, to a common fetch of $L=1{,}900$ cm. As the curve of the surface displacements to a first approximation is linear, the reduction to a standard fetch is a matter of direct proportionality. That is, if S' is the set-up corresponding to L', and if the difference $L'-L$ is a small part of L, then

$$S=S'L/L'. \tag{39}$$

The results of the set-up observations, determined in this manner, for various depths of water are shown in figure 7. The set-ups observed with smooth surfaces will be denoted as S_1. In the figure S_1, expressed in centimeters, is plotted against V^2, the square of the average wind velocity, where V is expressed in centimeters per second. For a given depth of water and for a given fetch the set-up is proportional to the square of the wind velocity. From the data of figure 7 the values of S_1 for the different depths at a common wind velocity $V=1{,}000$ can be obtained. These are shown in figure 8. It is seen that the distribution of the data points is nearly linear, and the straight line drawn through the points has a slope of one to one. The interpretation, therefore, is that for a constant wind velocity and for a constant fetch the set-up is inversely proportional to the depth of water. Expressed mathematically,

$$S_1 \sim V^2/H. \tag{40}$$

Rendering the relation dimensionally correct we have, since the quantities g and L were constant in the tests,

$$\frac{S_1}{L}=A\frac{V^2}{gH}, \tag{41}$$

where A is a numerical constant having the value

$$A=3.30\times 10^{-6}. \tag{42}$$

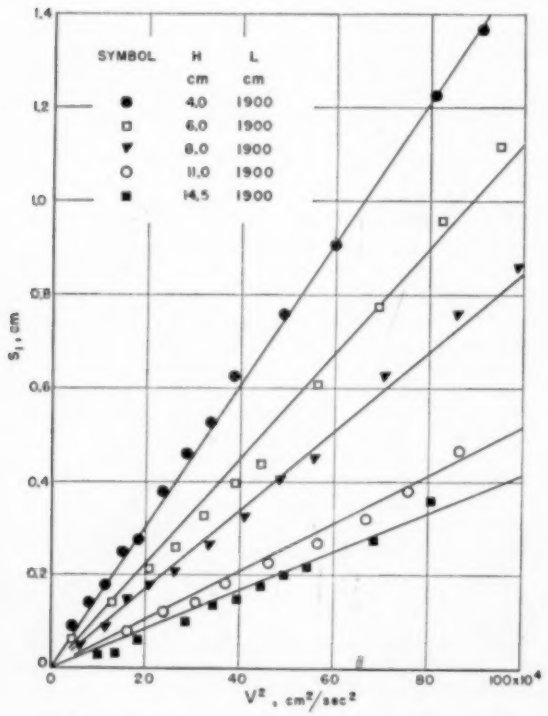

FIGURE 7. *Wind set-up in the absence of waves.*

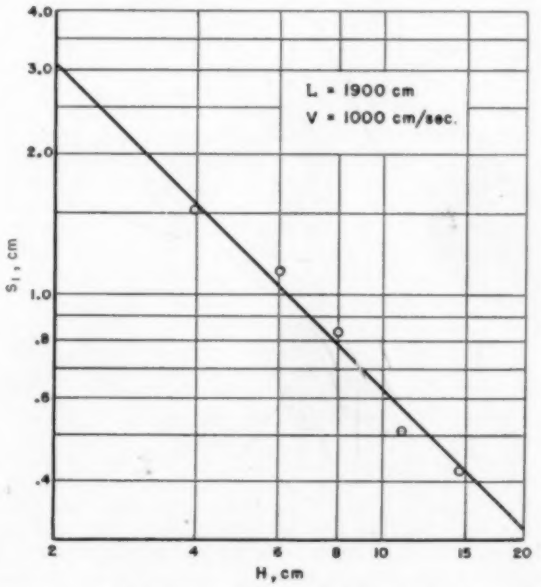

FIGURE 8. *Variation of set-up with depth in the absence of waves.*

These relations give the law of wind set-up where the wind is not of sufficient strength to excite waves and therefore the water surface is smooth.

3. Relation of Water Surface Velocities to Wind Velocities

The argument regarding the development of the final formula of the preceding section is not complete. It remains to see whether the coefficient, A, of the wind velocity term is in every respect a numerical constant unaffected by the viscosity of the liquid. This aspect of the problem will be investigated later. For the present the inquiry will be facilitated by first establishing the relationship between the surface velocities of the water and the wind velocities.

An effort was made continually during the tests to measure the water surface velocity to see whether a relationship existed between this and the air velocity, as affected by the depth of liquid and the viscosity of liquid. It was also thought desirable to see if the relationship was modified by the fact that the liquid surface was smooth or covered by waves. The change in the viscosities was brought about invariably by using sugar solutions of various concentrations.

To obtain the surface velocities, small paraffin particles were dropped from a perforation in the channel roof, and the movement of the particles along a given distance was timed by a stop watch. At the commencement of such observations, the velocities were measured over successive intervals covering the entire channel from the beginning to the end. It was found during numerous tests of this type that the surface velocities did not change with distance when the liquid depth was large and the viscosity of the liquid small. Only when the depths were small and the liquid viscosities large would the surface velocities vary with distance. Thus in the later experiments the surface velocity was measured over small lengths.

The velocity values for a given wind velocity were based on the average value of three to five individual determinations. Usually the floating particles did not maintain a constant distance from the wall during their travel. The meander of the particles, however, was such that it could be taken to be equivalent to the motion of a hypothetical particle keeping a constant midway position between the channel axis and the glass wall. A study of the lateral distribution of the surface velocities did show, and the evidence will be reproduced later in this section, that the motions of such particles give very nearly the average value of the surface velocities taken in the lateral distribution.

Representing the average surface velocity by u_s, the question to be examined is the dependence of u_s on the wind velocity V, on the liquid depth H, and on the kinematic viscosity ν of the liquid. Obviously, the relationship is of the type

$$\frac{u_s}{V}=f\left(\frac{u_sH}{\nu}\right). \tag{43}$$

For the establishment of the relationship the measurements obtained with water depths of 4, 6, 8, 11, and 14.5 cm were first considered. In some of the tests the water was charged with soap or with detergent. These observations, however, did not yield Reynolds numbers of sufficiently low values. To supplement the data other observations were undertaken with liquid depths of 8, 4, and 2 cm, using heavy sugar solutions.

The data accumulated from these extensive tests yielded the values of the parameters u_s/V and u_sH/ν, which are plotted in figure 9. Obviously, when the Reynolds number is small, the viscosity of the liquid has a very marked effect on the surface velocity. In the logarithmic plotting the distribution of the points of observation for low Reynolds numbers is linear, and the line drawn has the slope one in two. Accordingly the law for the surface velocities when the Reynolds number is small is

$$\frac{u_s}{V}=K\left(\frac{u_sH}{\nu}\right)^{\frac{1}{2}}, \tag{44}$$

where the coefficient K is a pure number having the value

$$K=7.6\times10^{-4}. \tag{45}$$

Starting with a Reynolds number of approximately 1,000 the ratio of the two velocities tends slowly to a constant value indicating that above this value the effect of kinematic viscosity is very slight.

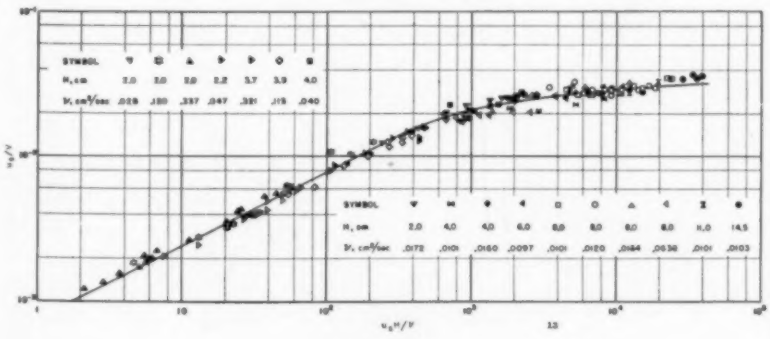

FIGURE 9. *Variation of water-surface velocities with Reynolds Number.*

Judging from the curve drawn in the figure the limiting value of the ratio is

$$\frac{u_s}{V}=0.033. \tag{46}$$

In establishing the part of the graph above a Reynolds number of 1000, test data were used without regard to the condition of the liquid surface that happened to prevail. That is, some of the data are from runs where the surface was covered with waves and other data are from runs where the surface was smooth. Where waves were present, the surface velocities used were mean values from the crests and from the troughs. Due to the close grouping of points the inference is that the surface velocities are not affected by the presence of the waves. This surely was an unexpected result, and due to its importance the question was further investigated in two additional series of experiments. In one of the series the water of the channel was treated with detergent. During the measurement of the surface velocities the surfaces were smooth and calm. The data from this series of tests are shown in figure 10. For the second series the channel water was clean, and the observations were made with air velocities yielding substantial wave formations. The data from the latter series are shown in figure 11. In the figure are drawn two straight lines; the broken line represents the average values from the tests with water surface remaining calm; the continuous line represents the average values of the individual data shown in the figure. The disparity between the two curves is less than the scatter of the individual observations, and it may be stated on this basis that the presence of waves does not appreciably affect the relation between the surface velocities and the wind velocities.

In the above discussion, the ratio of the two velocities is treated as a function of the Reynolds number based on the surface velocities. It is equally feasible to take the Reynolds number based on wind velocities. This is especially useful for comparison with prototype data. The data for this case are given in figure 12. Accordingly for Reynolds numbers below 30,000 the ratio u_s/V varies inversely with Reynolds number; for higher Reynolds numbers the ratio tends to a constant value of 0.033, roughly.

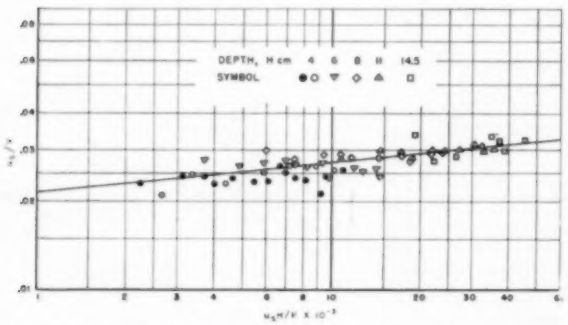

FIGURE 10. *Water-surface velocities for large wind velocities in the absence of waves.*

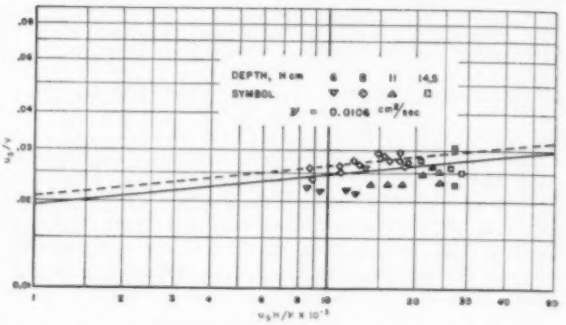

FIGURE 11. *Water-surface velocities for large wind velocities in the presence of waves.*

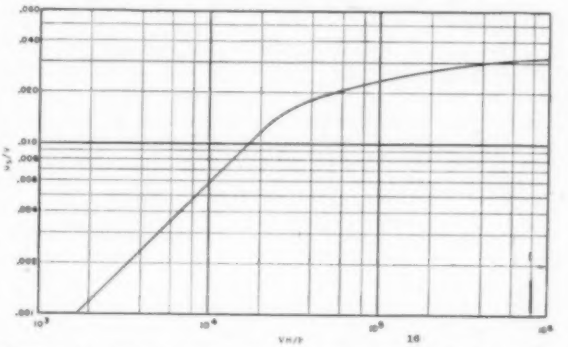

FIGURE 12. *Variation of water-surface velocities with Reynolds Number based on wind velocities.*

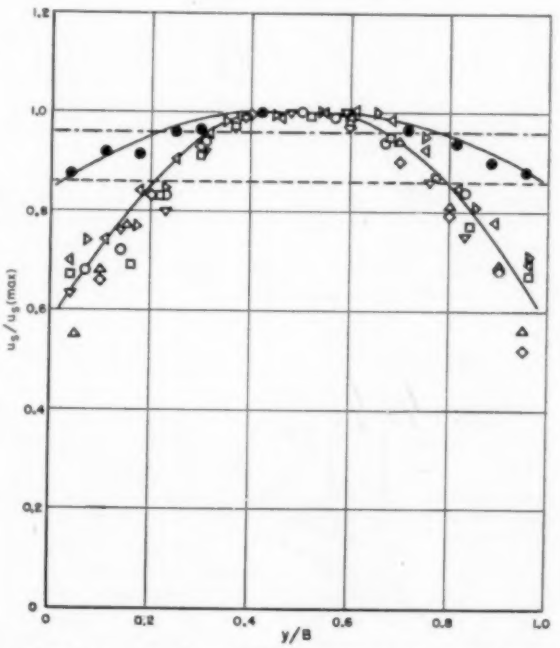

FIGURE 13. *Lateral distribution of water-surface velocities.*

Before closing the matter of the present section, the evidence that the measured surface velocities equal the averages taken across the width of the channel must be shown. The establishment of the lateral distribution of the surface velocities proved to be a very difficult task. Much time was spent and the observations were repeated many times until some assurance about the results was obtained, working always with statistical averages. Without attempting a description of the methods used, the final results are shown in the form of graphs in figure 13. The lower group of points represents test data for the case where the liquid surface was smooth and free of waves. The data points are differently indicated and correspond to liquid depths varying from 2 to 8 cm and to velocities varying from 350 to 700 cm/sec. As the points group so closely among themselves for a given distance from the walls, it did not seem necessary to indicate the velocities and the depths corresponding to specific symbols. The broken line gives the coordinate coinciding with the average velocity. According to these results a particle on the water surface at a distance of 2.2 cm from the nearest wall moves with a velocity equal to the average of the velocities in the lateral traverse. The upper group of points in the figure was obtained for a liquid surface covered with waves. The number of observations was as large as for the points below; the observations being made with various depths and with various wind velocities. In order not to confuse the appearance of the graph, only averaged values are shown since no systematic variations could be discerned in the data with respect to depth of liquid or to wind velocity. It appears as though the surface velocities vary less in a lateral traverse when waves are present. In this case also the surface velocity at a distance of about 2.2 cm away from the nearest wall represents practically the average velocity of a lateral traverse.

4. General Law of the Surface Gradient in the Absence of Waves

The regularity seen in the relationship of the surface velocities with the Reynolds numbers based either on the surface velocities or on the wind velocities suggests that perhaps a similar relationship should exist for the surface gradient.

It was remarked in the theoretical analysis of purely viscous conditions that the surface gradient may be expressed as

$$\frac{dh}{dx}=\frac{6\nu u_s}{gH^2}. \tag{31a}$$

This might be generalized to include the case of turbulent flow by writing

$$\frac{dh}{dx}=\phi_s\frac{u_s^2}{gH}, \tag{47}$$

where

$$\phi_s=\phi_s\left(\frac{u_sH}{\nu}\right). \tag{48}$$

The quantity ϕ_s may be referred to as the surface coefficient. Accordingly, the surface coefficient for the case of purely viscous flow is

$$\phi_s=6\Big/\frac{u_sH}{\nu}. \tag{49}$$

The set-up observations that were made with water

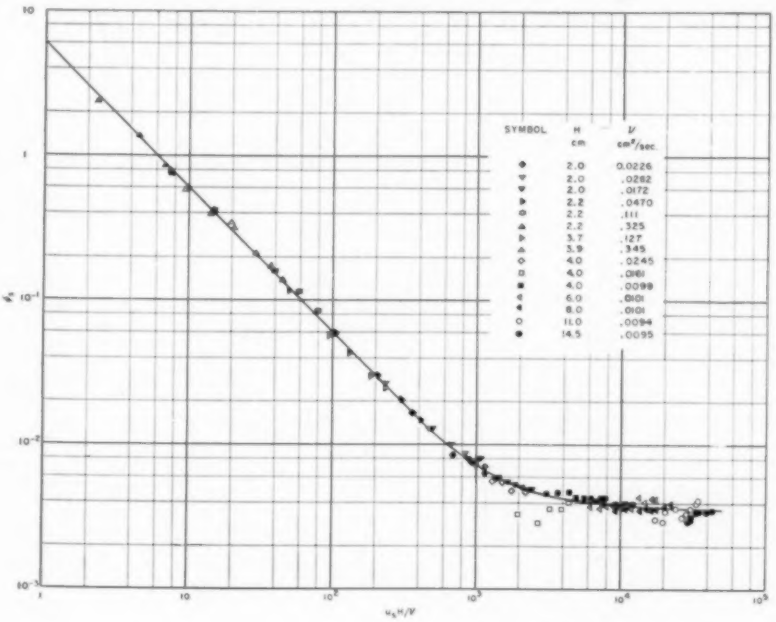

FIGURE 14. *Coefficient of surface slope in the absence of waves as a function of Reynolds Number.*

charged with soap or detergent may be used for evaluating ϕ_s corresponding to large Reynolds numbers, for in this case the surface gradient can be written also as

$$\frac{dh}{dx}=\frac{S_1}{L}. \tag{50}$$

The relation between the wind velocities and the surface velocities is given by the graph in figure 12. As regards ϕ_s for small Reynolds numbers, set-up observations were made with small depths (2 and 4 cm) and with sugar solutions of various concentrations. In these latter tests, owing to the large viscosities of the solutions, waves could be excited only with winds of large velocities and therefore there was a range of velocities that left the liquid surface calm and smooth. As an illustration, the set-up observations made with a liquid of kinematic viscosity $\nu=0.111$, a water depth $H=2.0$ cm, and a fetch $L=1{,}760$ cm, are shown in figure 18.

The determination of the surface gradient coefficient as a function of the Reynolds number is shown in figure 14. It is apparent for low Reynolds numbers, that if the coefficient be defined as in eq 47, its value is affected very markedly by the Reynolds number. The distribution of the data points is sufficiently linear to allow the drawing of a straight line through them. The line actually drawn conforms to the theoretical expression given by eq 49, and since the line represents the positions of the observed points quite accurately the theory is verified satisfactorily. There was another deduction of the theory that appeared from limited observations to be verified. According to eq 29 the particle velocity is zero at a point two-thirds of the total depth measured from the bottom. Observations of small particles that had accumulated in the channel for one reason or another indicated this deduction to be substantially true.

For high Reynolds numbers, as may be observed from the data of figure 14, the effect of Reynolds number is small and the coefficient tends to a constant value. The deduction from the data presented is that the surface velocities define completely the regime of flow in the liquid below, the flow assuming either the character of a viscous flow or a turbulent flow. The passage from one type of flow to the other type does not show the sharp and sudden transition ordinarily seen in fluid motion phenomena.

For practical applications it is desired to define the coefficient of the surface gradient in terms of the wind velocities instead of the liquid surface velocities. In this new representation

$$\frac{dh}{dx}=\phi_a\frac{V^2}{gH}, \tag{51}$$

and

$$\phi_a=\phi_a\left(\frac{VH}{\nu}\right), \tag{52}$$

where ϕ_a is the coefficient of the surface gradient in relation to wind velocity. The transfer from ϕ_s to ϕ_a is readily made by using the data in figures 9 and 14. The determinations of ϕ_a thus made are shown in figure 15. The surface gradient coefficient ϕ_a is independent of the Reynolds number VH/ν. Specifically

$$\frac{dh}{dx}=3.35\times10^{-6}\frac{V^2}{gH}. \tag{53}$$

This value of $\phi_a=3.35\times10^{-6}$ is to be compared with the value of $A=3.30\times10^{-6}$ appearing in eq 42. This then completes the argument that the coefficient, A, appearing in eq 41 is actually a numerical constant and in particular is independent of liquid viscosity.

The result shown above is one of remarkable simplicity. In terms of the shear acting on the water surface, the gradient is

$$\frac{dh}{dx}=\frac{n\tau_s}{\rho gH}, \tag{22a}$$

and comparison with eq 53, using the average value of ϕ_a from eq 42 and eq 53 yields,

$$n\tau_s=3.32\times10^{-6}\rho V^2, \tag{54}$$

where ρ is the density of the liquid. Replacing ρ with the moist air density ρ_a by using the relation,

$$\rho_a=1.169\times10^{-3}\rho, \tag{55}$$

the expression for the surface stress is

$$n\tau_s=0.0028\rho_a V^2. \tag{56}$$

If the value 1.5 be assigned to n, the value of the surface stress, using the ordinary form of the formula for such stresses, is

$$\tau_s=0.0037\frac{\rho_a V^2}{2}. \tag{57}$$

If it is supposed that the height of the air passage in the present experiments has no effect on the stresses developed on the surface of the liquid, then the shear obtained might be compared with the shear evaluated according to some boundary layer theory applicable to the case of a moving liquid surface. Such a theory is not yet available, and the next best

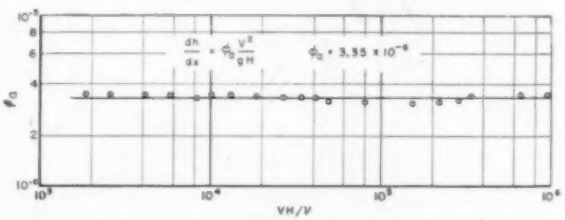

FIGURE 15. *Coefficient of surface slope in the absence of waves as a function of Reynolds Number based on wind velocities.*

choice is therefore to compare our results with the well-known theory of the resistance of smooth plates. In terms of the drag coefficient C_d,

$$\tau_s = C_d \rho_a V^2/2, \tag{58}$$

where

$$C_d = C_d\left(\frac{VL}{\nu_a}\right), \tag{59}$$

and ν_a is the kinematic viscosity of air. In the tests, the results of which are now being examined, the Reynolds number VL/ν_a ranged from 10^6 to 10^7. The drag coefficient for this range as determined by Gebers [5] and by Kempf and Kloess [6] is

$$C_d = 0.0032, \tag{60}$$

and this agrees very well with the corresponding coefficient in eq 57.

It would thus appear that the stress developed over the smooth surface of water under the action of flowing air could be determined with sufficient accuracy by using the ordinary theory of smooth plate resistance.

For emphasis, the foregoing results will be summarized. Shear acting on the liquid surface in the absence of waves is independent of the depth of liquid and the kinematic viscosity of the liquid. The magnitude of the shear is almost identical with the shear that may be associated with the skin friction of smooth plates. In this comparison one may assume that the ratios of the surface shear to the bottom shear is two; that is, $n=1.5$. The value of the ratio is exact in the case of viscous flow; it is not known precisely for the case of turbulent flow. The prevailing flow in the liquid below the surface is determined solely on the basis of the surface velocities, the depth, and the kinematic viscosity of the liquid. For purely viscous flow, the flow is in accordance with the simple one-dimensional theory. The exact conditions and the details of the mechanism of flow in the case of turbulent flow are not known. These could be made the object of a fruitful and a promising special study.

V. Wind Set-Up in the Presence of Waves

1. Effective Air Velocities

In the observations of set-up with smooth water surfaces the variations in the value of the air velocities with distance along the channel axis proved to be small, and they were ignored. On the other hand the corresponding variations were large when the surface of the liquid was covered with waves and due account was taken during the reduction of data. Two causes were operative in producing the variations of the air velocities with distance. First, waves induced comparatively large stresses over the water surface and thus a greater rise in water level in the leeward end of the channel. Second, as the heights of the waves increased with distance, the elevated crests caused a further decrease in the height of the air passage. The air velocity variations with distance were especially marked for the larger depths of water because of the small depth of the channel.

Under these conditions the air velocity values derived from the Venturi nozzle are only nominal velocities, and these had to be modified or corrected to obtain the effective air velocities. The basis of the corrections is as follows:

The local surface gradient at the point x may be written as

$$\frac{dh}{dx} = C\frac{V^2}{gH}, \tag{61}$$

where the coefficient is

$$C = C\left(\frac{x}{L}, \frac{V}{gH}, \frac{H}{L}, \frac{VH}{\nu}\right), \tag{62}$$

which is an assumption of the most general application. If V be constant, the integration of eq 61 yields

$$S = h_2 - h_1 = \frac{V^2}{gH}\int_0^L C\,dx = C_m L\frac{V^2}{gH}. \tag{63}$$

Supposing that V is not constant but $V = V_n + \Delta V$, where ΔV is a small fraction of V_n, the same integration gives

$$S = \frac{V_n^2}{gH}\left[\int_0^L C\,dx + 2\int_0^L C\frac{\Delta V}{V_n}dx\right],$$

or expressed in a different manner

$$S = \frac{V_n^2}{gH}\left[C_m L + 2\eta C_m \int_0^L \frac{\Delta V}{V_n}dx\right], \tag{64}$$

where η is a quantity larger than unity. Comparing with eq 63,

$$V^2 = \left[1 + 2\eta\int_0^L \frac{\Delta V}{V_n}\frac{dx}{L}\right]V_n^2, \tag{65}$$

which gives the effective wind velocity, V, in terms of the nominal wind velocity, V_n. What the exact value of the coefficient η should be is questionable. We have assumed $\eta = 1.5$ as a plausible value for present applications.

To apply the correction to those measurements of set-up that showed considerable restrictions in the air space above the waves it became necessary to observe the variations of $\Delta V/V_n$ along the channel axis for the different depths of water and for the different air velocities. To give an idea of the variations noted, the data for a depth of 11 cm are shown in figure 16. Using these data and also similar data for other depths, the relationship between the effective wind velocity and the nominal velocity was established as shown in figure 17.

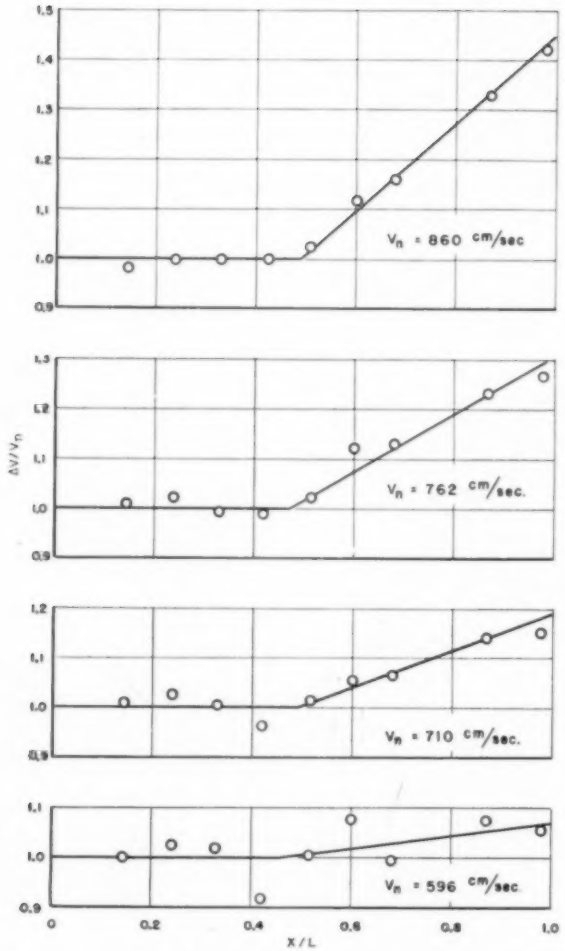

FIGURE 16. *Variation of mean air velocities along the channel axis. Water depth = 11.4 cm.*

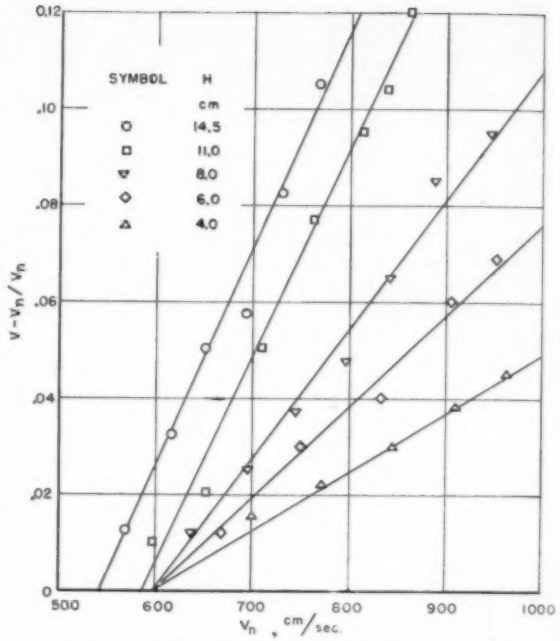

FIGURE 17. *Effective wind velocities in terms of the nominal wind velocities.*

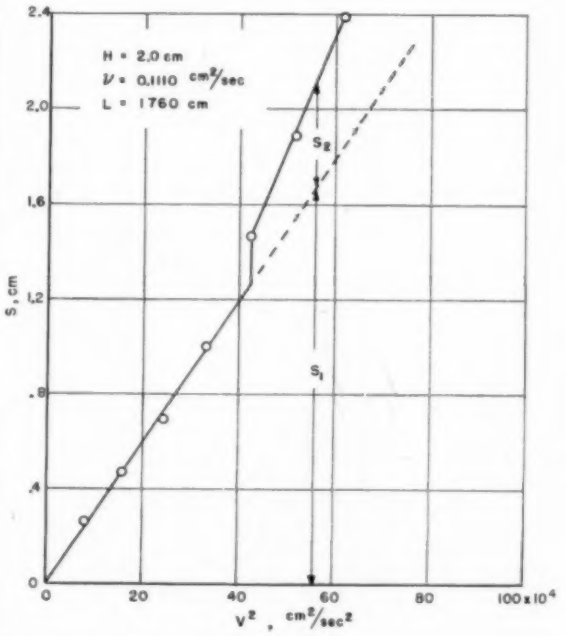

FIGURE 18. *The partitioning of set-up when waves are present.*

2. Dependence of Set-Up on Depth of Water When Waves Are Present

Great difficulty was experienced in the beginning when an attempt was made to establish the relationship between set-up and the depth of water for the case where waves were present. The difficulty was overcome partly by supposing that it is permissible to break the observed set-up into two parts, S_1 and S_2, the first being due to skin friction alone and the second part due to form resistance of the wave crests. It was supposed further that the magnitude of S_1 is not affected by the presence of waves, and indeed that it would be the value that would have been obtained for the prevailing air velocities with a smooth water surface. Thus, if S is the observed total set-up, the part S_2 due to the waves is simply

$$S_2 = S - S_1, \tag{66}$$

where

$$S_1 = 3.30 \times 10^{-6} \frac{V^2}{gH} L. \tag{41a}$$

The latter relationship was fully discussed in the previous sections.

At the moment the dynamical significance of the procedure of partitioning is not clear. The only justification that may be mentioned now is the consistency and the reasonableness of the results obtained. The idea was suggested by the fact that the relationship between the water surface velocities and the wind velocities is not affected by the presence of waves. Eventually, of course, we wish to consider the dynamical aspects of the phenomenon of total resistance in a future investigation. For the present, however, our main interest is in the parametric representation of measured quantities and the validity of these representations for the quantitative evaluations of the set-up.

As an example of partitioning the set-up into parts, the data in figure 18 are presented. The data were obtained with a sugar solution of kinematic viscosity $\nu = 0.111$ cm²/sec. The surface length was $L = 1760$ cm, and the depth of water was $H = 2$ cm. Due to the high value of viscosity, the surface remained smooth for an appreciably large range of wind velocities, as can be seen from the curve. For this range the set-up varies with the square of the wind velocity as it should. Waves were initiated when the wind velocity exceeded 650 cm/sec. The curve indicates that the increase in the value of the set-up starts with a jump. The projection of the straight line passing through the points of observation corresponding to small wind velocities is indicated by dashes. The quantity S_2 shown in the diagram, which is the excess over the dashed line, is taken to represent that part of the set-up due to waves.

The same method of graphic partitioning was employed in the results of the tests made with water depths of 14.5, 11, 8, 6, and 4 cm. As the tap water used in the tests was relatively pure, waves of substantial size were obtained. The data are given in figures 19 and 20. The straight lines represent the magnitudes of S_1, whereas the curves drawn through

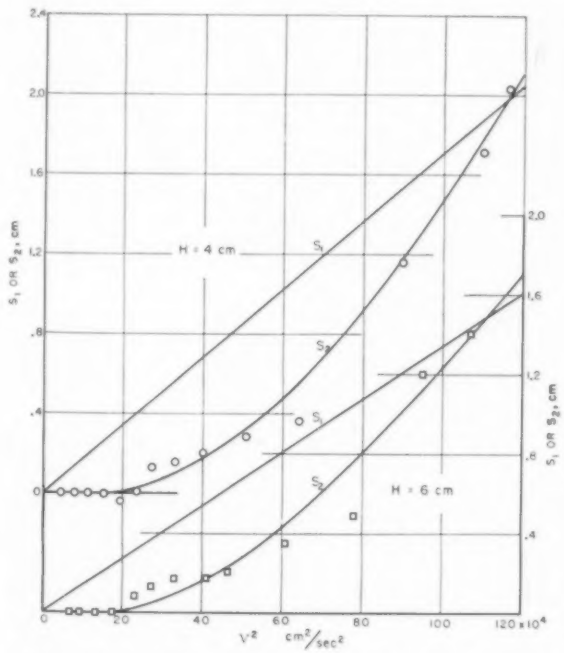

FIGURE 19. *Partial set-up due to waves in tests with small water depths.*

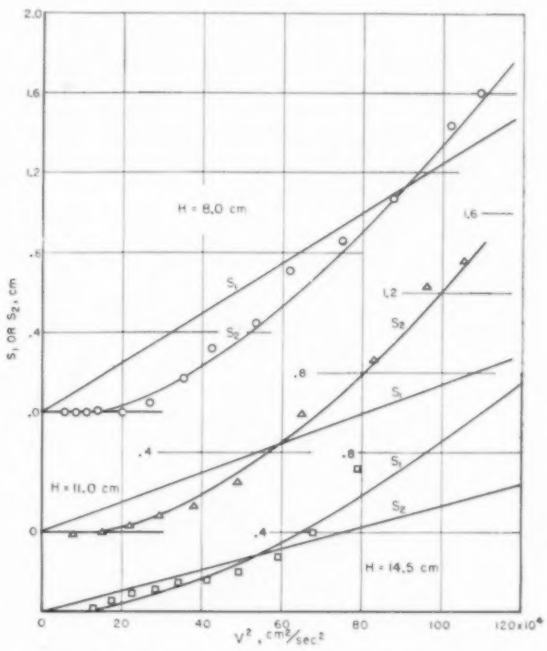

FIGURE 20. *Partial set-up due to waves in tests with large water depths.*

the symbols show the excess of the observed set-up with respect to S_1. These two quantities, S_1 and S_2, are expressed as functions of the squares of the wind velocities. As is seen from the figures, S_2 commences to increase after V has exceeded a certain critical wind velocity, V_0. The figures suggest that the increase starts with a jump. This fact will be ignored, and it will be assumed that the increase is from a null value and the changes are gradual. The curves representing S_2 are drawn accordingly.

On the basis of dimensional reasoning it is to be expected that

$$\frac{S_2}{L}=f_1\left(\frac{V}{\sqrt{gH}},\frac{(g\nu)^{1/3}}{\sqrt{gH}},\frac{\rho}{\rho_a},\frac{H}{L}\right), \tag{67}$$

and as to the identification of V_0,

$$\frac{V_0}{\sqrt{gH}}=f_2\left(\frac{(g\nu)^{1/3}}{\sqrt{gH}},\frac{\rho}{\rho_a},\frac{H}{L}\right). \tag{68}$$

Eliminating the parameter containing the kinematic viscosity,

$$\frac{S_2}{L}=f_3\left(\frac{V}{\sqrt{gH}},\frac{V_0}{\sqrt{gH}},\frac{\rho}{\rho_a},\frac{H}{L}\right). \tag{69}$$

Now, if we take V_0 as 350, 360, 380, 420, and 440 cm/sec, corresponding to water depths of 14.5, 11, 8, 6, and 4 cm, respectively, then the additional set-up S^2 due to the waves may be represented as

$$S_2=C(V-V_0)^2. \tag{70}$$

The evidence for the statement is shown in figure 21. Since in this group of data the quantities L, g, μ are not changed, the factor C may involve the depth H. To determine the nature of dependence on the depth, the values of S_2 corresponding to $(V-V_0)^2=50\times10^4$ are first read from the lines in figure 21 and are then transferred to the logarithmic plot of figure 22. The disposition of the points definitely lacks the even regularity of alinement that one naturally wishes to find. The points may be approximated by a straight line; but there is considerable latitude in the selection of the slope of the line. If one adopts the straight line drawn in the figure, then the equation for the partial set-up due to waves is

$$\frac{S_2}{L}=B\,\frac{(V-V_0)^2}{gH}\left(\frac{H}{L}\right)^{1/2}, \tag{71}$$

where $B=2.08\times10^{-4}$, and V_0 has the values mentioned above. If we disregard the small variations of V_0 for the different depths, the mean $V_0=390$ cm/sec is a suitable value. Adding to this the part due to skin friction, the expression for the set-up in the presence of waves is

$$\frac{S}{L}=A\,\frac{V^2}{gH}+B\,\frac{(V-V_0)^2}{gH}\left(\frac{H}{L}\right)^{1/2}, \tag{72}$$

where

$$A=33.0\times10^{-6}, \qquad B=2{,}08\times10^{-4},$$

It is understandable that the expression represents with sufficient accuracy the data that were observed. Yet, neither the reality nor the dynamical significance of the quantity V_0 appearing in the formula can be discussed at the moment in a manner satisfactory to us. For this reason the quantity V_0 will be referred to as the formula characteristic velocity.

3. Effect of Viscosity on Partial Set-Up Due To Waves

It was shown previously, working with the data for smooth water surfaces, that the partial set-up S_1 is independent of viscosity. It now remains to investigate what effect, if any, viscosity will have on the partial set-up due to waves, that is on S_2.

To consider this matter, a series of tests was carried out with a constant liquid depth of 8 cm. In addition to water, sugar solutions of four different concentrations were used, thus making altogether five experimental liquids of unequal kinematic viscosities. The setups observed with these liquids for an effective surface length of 1,900 cm are shown in figure 23. The two components, S_1 and S_2, of the total setup are plotted as functions of the squares of the wind velocities. It is to be noted that the S_1 line is common to all the liquids and is independent of viscosity. After drawing the curves through the S_2 points of observation, values of S_2 were read from these curves, the square roots of which are plotted in figure 24 against the wind velocity. The disposition of the points is linear. This would mean that the form of the expression in eq 70 is valid for liquids of varying viscosity. The lines have practically the same inclination independent of viscosity, and thus the value of C in eq 70, and hence the value of B appearing in eq 71, is not affected by viscosity. The intersections of the lines with the axis of velocities give the formula characteristic velocity, V_0, which varies with the viscosity. Specifically, corresponding to the successive viscosities $\mu=0.0092$, 0.0154, 0.0217, 0.0351, 0.0600 cm²/sec, the formula velocities are $V_0=380$, 630, 680, 720, 900 cm/sec, respectively.

Summarizing, the only effect of the increased viscosities is to increase the formula characteristic velocity. As a result, then, the total setup observed for a given wind velocity decreases when the kinematic viscosity of the liquid is increased.

4. An Analysis of Hellström's Data on Setup

In deriving the law of setup expressed by eq 72, the assumption was made tacitly that the limited height of the air passage over the surface of the water in these experiments does not substantially modify the magnitude of the resulting setups. Had it not been for the fixed construction of the channel, this circumstance would have been studied experimentally by varying the height of the air passage for a given depth of water. Fortunately

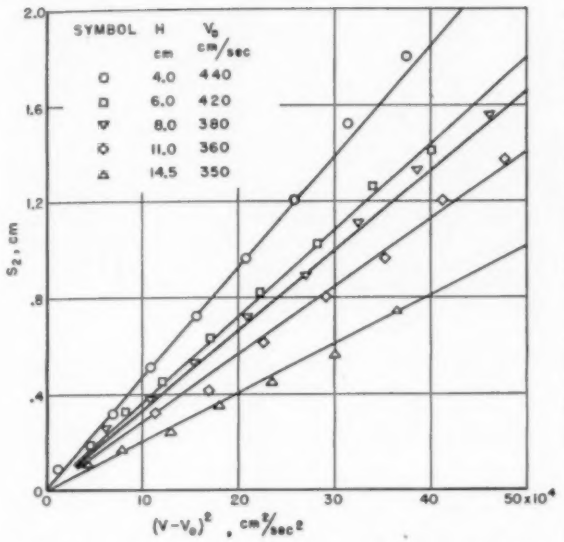

FIGURE 21. *The relation of the formula characteristic velocity to the partial set-up due to waves.*

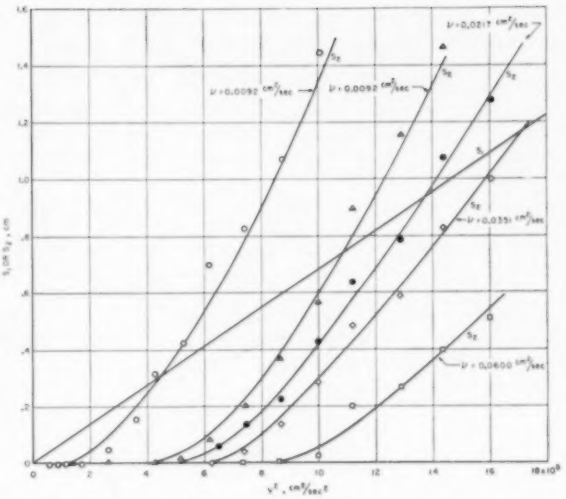

FIGURE 23. *Effect of viscosity on partial set-up due to waves.*

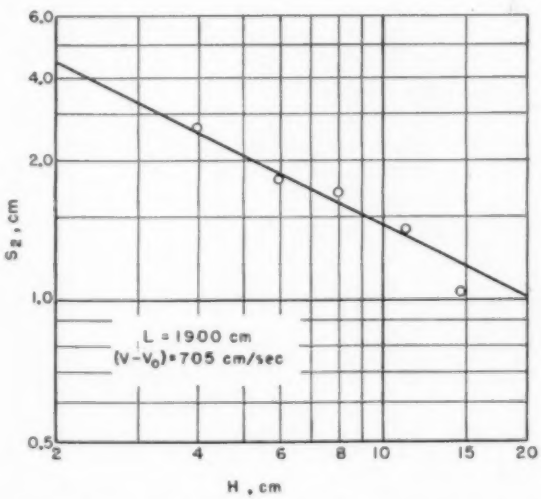

FIGURE 22. *Effect of depth on partial set-up due to waves.*

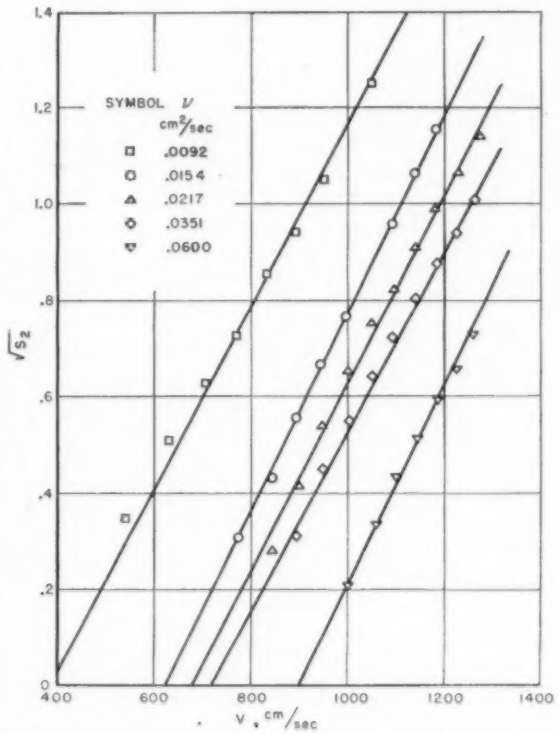

FIGURE 24. *The determination of formula characteristic velocities.*

the experiments of Hellström are of value in discussing the effect of size of air passage by comparison of results, as the channel used by Hellström had an air passage of relatively large depth.

The data in figure 25 give the relationship between surface shear and depth of water for various wind velocities as found by Hellström. One modification was made on our part; that is, to conform to our results channel central velocities were changed to mean velocities in the channel cross section. The data in this figure may be made the basis on which to deduce the set-up magnitudes in the Hellström channel. The channel had a length of 300 cm and a depth of 50 cm. The average depth of the water in the experiments appeared to have been varied between the limits of approximately 2 and 4 cm.

From the relation

$$\frac{dh}{dx}=\frac{n\tau_s}{\rho g H}, \tag{22b}$$

if the set-up is small, can be derived the expression

$$S=\frac{n\tau_s L}{\rho g H}, \tag{73}$$

which connects the set-up with the effective average wind force over the entire fetch. Since Hellström has assigned to n the value 1.50, the proper relation to be used in deducing the set-up in his experiments is

$$S=\frac{1.5\,\tau_s L}{\rho g H}. \tag{74}$$

Taking the data from figure 25, sequences of set-up values were obtained for the depths of 2, 3, and 4 cm. These computed values are given by the points plotted in figure 26.

To compare these with the results of the present investigation it suffices to determine similar values of set-up, using eq 72. Now, it will be remembered that for water the formula characteristic velocity showed slight variations from the mean, V_0=390 cm/sec, as the water depths where changed. We wish to assign a similar tendency to be valid in the Hellström tests. Accordingly we assign to V_0 the magnitudes 410, 390, and 370 cm/sec to apply to the depths of 2, 3, and 4 cm, respectively. The computed values of the set-ups on this basis, using our general formula, are shown likewise in figure 26. The curves of the computed set-up values form a band, and the Hellström values are within this band. Moreover, the sequence of the curves is the same as the sequence of the Hellström set-up values as the depths are changed. This shows that there is quite a satisfactory agreement between the general formula and the results from the Hellström channel. Accordingly, we are permitted to infer that the restrictive effect of the small air passage in our experiments, if present, must have been small indeed.

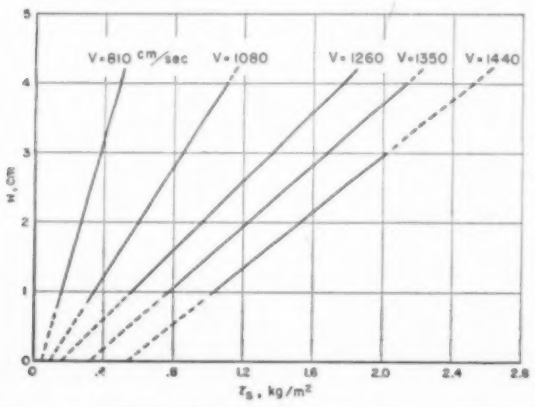

FIGURE 25. *The relation between wind velocity and depth of water in Hellström's experiments.*

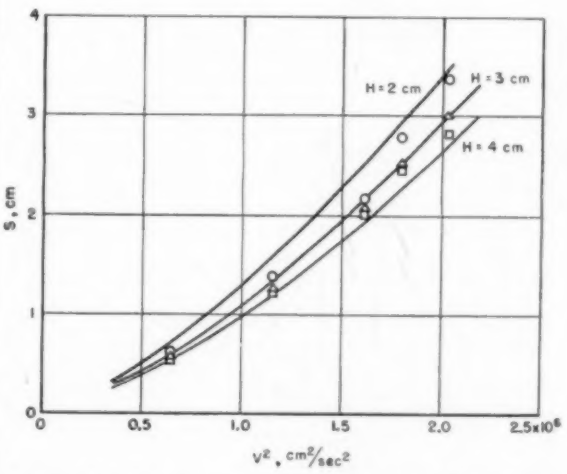

FIGURE 26. *Comparison of set-ups from the Hellström experiments with values obtained from equation 72.*

VII. The Probable Meaning of the Formula Characteristic Velocity

1. Dimensional Requirements of the Monomial Set-Up Formulas

Before we consider various topics related to the question of the formula characteristic velocities, it becomes necessary to see if the total set-up in association with waves can admit representation by a single term. The general formula developed in this investigation is at variance with this possibility, whereas a monomial formula is implied in the work of Hellström.

Hellström proposes that the relation between the wind force and the wind velocity be of the form

$$\tau_s \sim HV^2. \tag{75}$$

In view of the relation

$$\frac{dh}{dx}=\frac{n\tau_s}{\rho g H}, \tag{22c}$$

one must now infer that the corresponding expression for set-up is

$$\frac{S}{L}=A'V^3, \tag{76}$$

where A' is independent of the depth of water.

The set-up values that were deduced previously and considered during the analysis of the Hellström data are reproduced in figure 27. There are reproduced also the set-up values observed in the tests of the present investigation with water for the region of high wind velocities. The graph representation is logarithmic and the observation points of the two groups of tests, one from Hellström's channel which was 300 cm long and the other from our channel, which was 1,900 cm long, aline themselves linearly. In both cases the inclination of the lines representing the points may be taken to be approximately 3 to 1. Thus the formula of eq 76, applies equally well to the two groups of data from water surfaces covered with waves.

Now in order that eq 76 may represent the physical law of set-up in laboratory channels, the right-hand member must be a dimensionless expression since the left-hand member is a dimensionless ratio. It will

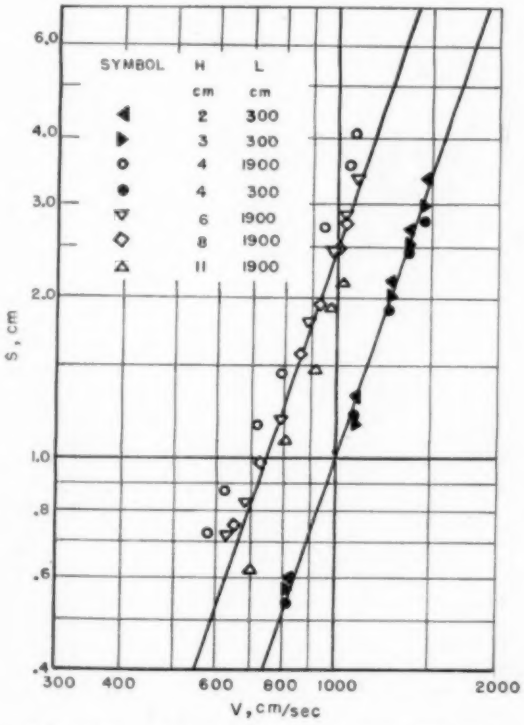

FIGURE 27. *Monomial formula of set-up with waves.*
ν=0.009 to 0.010 cm²/sec.

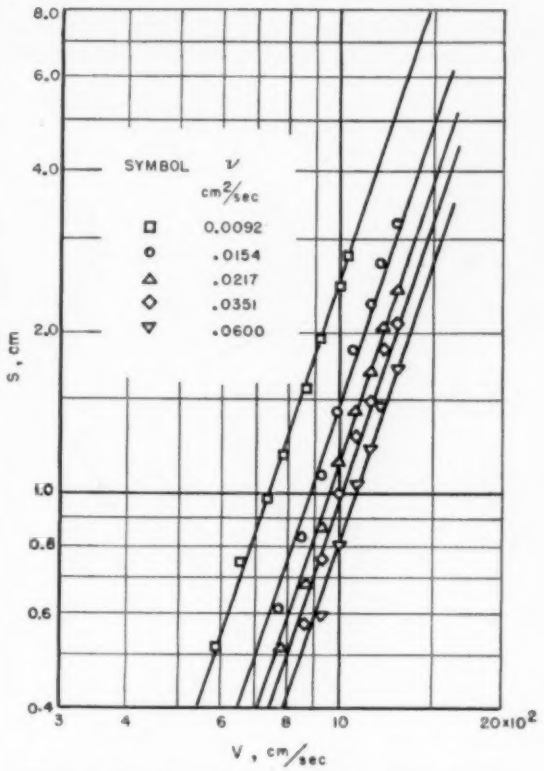

FIGURE 28. *Monomial formula for variable viscosities.*
L=1900 cm. H=8.0 cm.

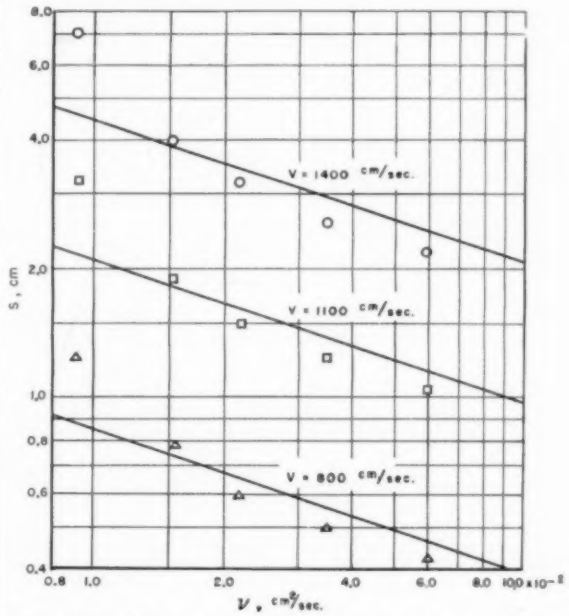

FIGURE 29. *Monomial formula of set-up formulating the effect of velocity.*

be remembered that the data now being considered are from two groups of tests where the kinematic viscosities were the same. Accordingly, the general law could be

$$\frac{S}{L}=A'\left(\frac{V}{\sqrt{gL}}\right)^3 f\left(\frac{\sqrt{gL}L}{\nu}\right). \tag{77}$$

The right member contains a factor involving the kinematic viscosity. The influence of this factor may be determined by considering the set-up data obtained with highly viscous sugar solutions subjected to large wind velocities. These data are shown in a separate logarithmic plotting in figure 28. The distribution of the points for a given viscosity are linear, and furthermore the inclination of the lines are in agreement with the expression in eq 77.

If the S values for the velocities V=1,400, 1,000, and 800 cm/sec be considered, as in figure 29, it is seen that these may be approximated by straight lines with a slope of $-\frac{1}{3}$. Accordingly, if the expression in eq 76 does represent a physical law, it must be of the form

$$\frac{S}{L}=A'\left(\frac{V}{\sqrt{gL}}\right)^3\left(\frac{\sqrt{gL}L}{\nu}\right)^{1/3}. \tag{78}$$

It now remains to be seen if this is actually the physical law for the set-ups observed in the laboratory channels. Owing to the manner of the derivation, the separate exponents represent the effects of velocity and kinematic viscosity. To examine the contingency that these exponents represent likewise the effect of channel length, the last expression will be written in the form

$$S=A'\frac{V^3}{g^{4/3}\nu^{1/3}}. \tag{79}$$

Accordingly, wind velocities and kinematic viscosities remaining the same, the set-up observed is independent of the length of channel. As this deduction is contrary to observation, it is to be inferred that the monomial form for expressing the set-up is invalid when set-ups are observed in laboratory channels with the wind velocities sufficiently high to produce waves.

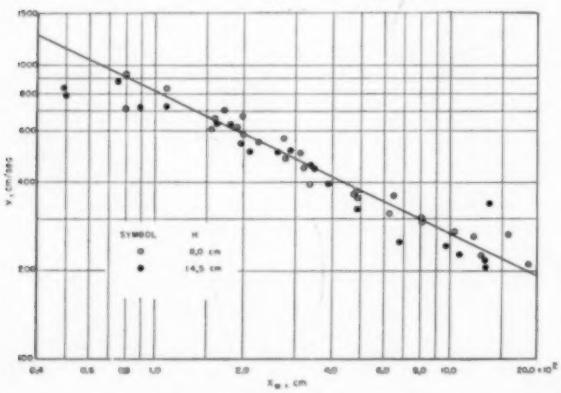

FIGURE 30. *Variation of initial fetch for the start of waves with wind velocity.*

2. Critical Wind Velocity for Wave Formation

It was noted during the preparation of data for analysis that almost invariably the formula characteristic velocity exceeded the critical wind velocity for generating waves. It may prove to be of some significance if a relationship can be established between these two velocities. This in turn requires that the law giving the critical wind velocity for wave formation be first established.

At very low wind velocities the surface of the water remained calm. In fact if one studied the images of the vertical and the horizontal bars of windows reflected from the water surface, they appeared as even bands extending laterally and longitudinally over the water surface. On increasing the wind velocity, a tremor of the water surface was noticed, and the reflections of the bars now had the appearance of sinusoidal bands. This condition extended from one end of the channel to the other, except that there was a tendency for the amplitudes of the irregularities to increase somewhat with distance. With a further increase of the wind velocity the tremor of the water surface was considerably augmented until finally the reflected shadows were confused. Experience showed that this state of the water surface was precedent to the appearance of waves, and in fact only a slight further increase in the wind velocity would be sufficient for the formation of waves.

The waves first formed were two dimensional, their length being estimated to be close to 4 cm. The wave heights were less than 2 mm, but this value could not be definitely determined since it was effected by the meniscus at the glass wall. Initially when the waves were formed, they did not cover the entire area of the water surface but were seen first in the leeward part of the channel. This would mean that an initial fetch of length, X_w, is necessary for the waves to appear, or more precisely to be visible to the eye. With increasing wind velocities the length of the initial fetch gradually decreased. To examine the magnitude of the decrease a few observations were made at water depths of 14.5 and 8 cm. The data from these observations are shown in figure 30. It is obvious that for these observations the initial fetch is inversely proportional to the square root of the velocity of the wind. When the initial fetch decreased to a length of about 1 or 1½ m, a new condition of the surface was manifested. The area between the windward water edge and the locality where the initial two-dimensional waves of the wavelength of 4 cm were first noted was covered with ripples. These ripples were three-dimensional and were about 2 cm long. One noticed with amazement the sharp and distinct issuing of the initial two-dimensional waves of wavelength of 4 cm at the lower end of the area of the ripples. With

greater wind velocities the initial area of the ripples was somewhat decreased; but in these investigations the length of the area never fell below 60 cm.

When the initial fetch for the startof the waves was small, which occurred at high wind velocities, wave height and wavelength increased with distance. With some exceptions, the increase of the wave height was proportional to the square root of distance, whereas the increase of wavelength was proportional to the distance. When the initial fetch was large, which corresponded to small velocities, it was observed at times that the waves once formed would be damped out, but reappeared near the leeward end of the channel.

The condition of variable fetch at the start of the waves and the tendency of waves to damp out when the wind velocity was small made it difficult to determine the particular wind velocity to be associated with the formation of waves. The matter of observation of the critical wind velocities for wave genesis was resolved as follows. Three initial fetches, of lengths 1,000, 800, and 600 cm were selected and the corresponding wind velocities determined. The average value of the three velocities was taken to represent the critical wind velocity, V_c, for the wave formation. When using water alone, the critical wind velocities were determined for depths of 14.5, 11, 8, 6, and 4 cm. When using more viscous solutions, the depths were 8, 4, and 2 cm.

In the presentation of data we follow the procedure of dimensional analysis. If it be assumed that the critical wind velocity is independent of fetch, then the dependence can be on the depth of water, the kinematic viscosity of the liquid, and the densities of the air and the liquid. Accordingly,

$$\frac{V_c}{\sqrt{gH}} = f([g\nu\rho/\rho_a]^{1/3}/\sqrt{gH}). \tag{80}$$

Conforming with this, the observed data are presented in the logarithmic plotting in figure 31. Despite the difficulty encountered in the observation of the critical wind velocities, the distribution of the points is sufficiently regular to allow the drawing of a straight line to represent them. Since the slope of the line drawn is unity, the critical wind velocity is independent of depth of liquid. Accordingly the desired form of the law is, very simply,

$$V_c = 16.2(g\rho\nu/\rho_a)^{1/3}. \tag{81}$$

Interestingly enough the form of the criterion accords well with the form that Harold Jeffreys [7] has derived theoretically. The only disagreement is in the numerical values of observation. The observations made by Jeffreys in open lakes and rivers suggest that the numerical value of the coefficient is about one-third as great as that given in eq 81. The cause of the disagreement may be the possibility that the critical value in reality depends also on the fetch of the initial waves noted. This aspect of the question deserves an examination in channels of variable lengths.

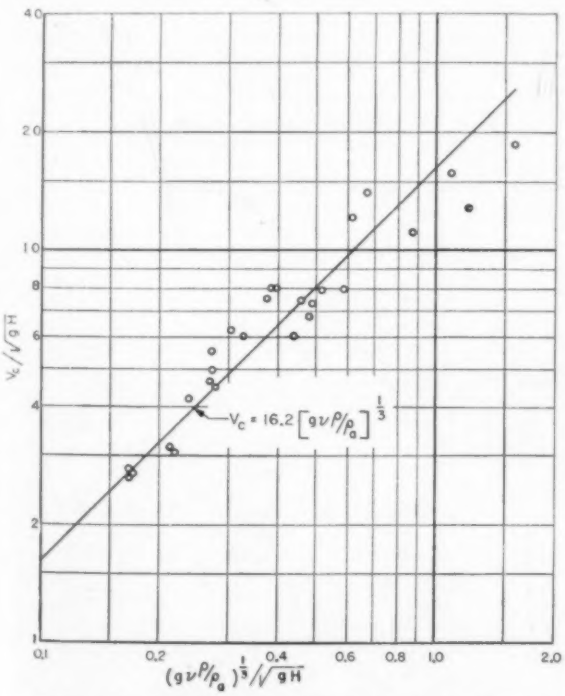

FIGURE 31. *Critical wind velocity for the start of waves.*

3. Correlation Between the Critical Wind Velocity and the Formula Characteristic velocity

As mentioned previously, it was noted during the work of data reduction that a correlation may exist between the critical wind velocity and the formula characteristic velocity. Since, as shown above, the factors affecting the critical wind velocity assume a very simple relationship, it would likewise seem sufficient to consider the dependence of the formula characteristic velocity on the kinematic viscosity and the channel length in the manner carried out in figure 32. The open circles in the figure are the values obtained during the analysis of the set-up due to waves, and the values of the associated formula characteristic velocity were indicated previously. The values corresponding to the black

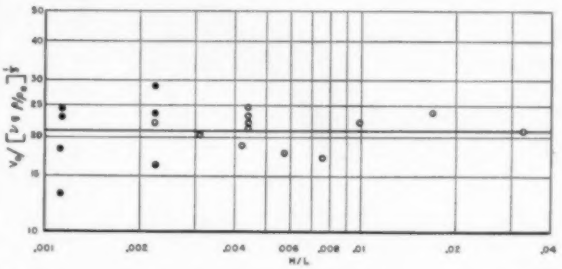

FIGURE 32. *Variation of the formula characteristic velocity with viscosity.*

circles were obtained in a different manner. The method is suggested from the graph in figure 18. The velocity concurrent with the sudden increase in the set-up values due to the presence of waves is interpreted as a value close to V_0. The full circles are from tests with small liquid depths and with high viscosities.

The distribution of the points suggests that it should suffice to represent the data by a horizontal line. Thus the formula characteristic velocity is independent of channel length and is proportional to critical wind velocity for the generation of waves. More specifically

$$V_0=21.0(g\rho\nu/\rho_a)^{1/3}. \tag{82}$$

The reader unquestionably will suspect, and this very justly, that we have tended to an over-simplification in this representation. Although the use of the formula characteristic velocity has caused a simpler representation of the set-up relationship in the general formula, this velocity by itself must have reference to various hydrodynamic elements involving dissipation and relative velocities such as the velocity of the waves with respect to the velocity of wind and also the velocity of the drift current at the surface of the water. At the moment the author is not prepared to discuss these matters satisfactorily. If dissipation really plays a large part in forming the formula characteristic velocity, then the opinion may be expressed that with greater liquid depths the magnitude of the formula characteristic velocity decreases.

4. A Possible Mathematical Basis for the Law of Partial Set-up Due To Waves

As mentioned before, between the points representing S_2 values and the curves intended to represent the course of the data, there exist small disparities. This fact no doubt has a bearing on the accuracy of the determinations, first of the formula velocity, V_0, and second of the exponent of H/L occurring in the formula for the partial set-up S_2, that is in the expression of eq 71. Accordingly, if one can formulate a mathematical basis that will justify the form of the law for S_2, independent of the actual methods of reductions used, this should prove to be very illuminating.

Pursuant to our original ideas and opinions we will suppose that when waves are present each crest contributes an additional resistance, and the resistance, in its major part at least, is due to form resistance. Let R be the resistance. The length of waves being λ, the added shear due to waves is

$$\tau_{s2}=R/\lambda. \tag{83}$$

As for the law relating to R we may suppose that

$$R=c\rho_a(V-V_0)^2a, \tag{84}$$

where a is the half value of wave height. At the moment nothing will be said as to the cause or the origin of V_0. Thus, the added shear is

$$\tau_{s2}=c\rho_a(V-V_0)^2a/\lambda. \tag{85}$$

Substituting in the expression

$$\left(\frac{dh}{dx}\right)_2=\frac{\tau_{s2}}{\rho gH}, \tag{22c}$$

and integrating with respect to x, there is obtained

$$S_2=c_1\frac{(V-V_0)^2}{gH}\int_0^L\frac{a}{\lambda}\,dx. \tag{86}$$

If the variation of a/λ with respect to x be known for the waves generated in shallow channels by the action of wind, the integration required above will lead to an expression for the set-up S_2 due to waves only.

Next it shall be supposed that the law of growth of waves in shallow waters is virtually

$$a\sim V^{1/2}Hx^{1/2}, \tag{87}$$

and

$$\lambda\sim V^{1/2}H^{1/2}x, \tag{88}$$

for sufficiently large values of V. Hence, we have

$$\frac{a}{\lambda}=c_2\left(\frac{H}{x}\right)^{1/2}. \tag{89}$$

That is, the steepness of wind waves in shallow water decreases with distance in the leeward direction. Since

$$\int_0^L\frac{a}{\lambda}\,dx=c_3H^{1/2}L^{1/2}, \tag{90}$$

there results, by substituting in eq 86

$$\frac{S_2}{L}=B\frac{(V-V_0)^2}{gH}\left(\frac{H}{L}\right)^{1/2}, \tag{91}$$

which in fact is the form that was adopted in the analysis of the set-up due to waves.

In the above derivation three separate assumptions are used. These are represented by eq 85, 87, and 88. Each of these assumptions is amenable to experimental examination. This work is now under way.

VIII. An Application to Natural Conditions

In his fine treatise Hellström gives some data on the wind effects of storms on Lake Erie. It will be interesting to compare the magnitudes of the set-ups occurring during these storms with the computed values to be obtained with the general formula of the present investigation. The observed set-ups at Lake Erie are shown in figure 33 by the plotted points.

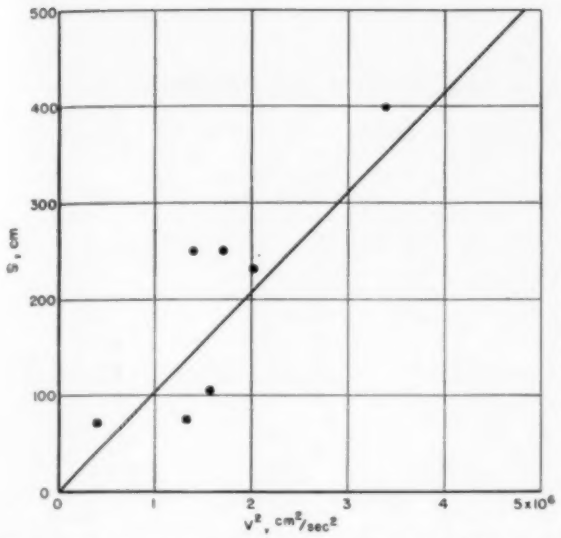

FIGURE 33. *Comparison of observed set-up in Lake Erie during storms with equation 87.*

In applying the general formula, eq 72, a statement is necessary regarding the value of the formula characteristic velocity appropriate for natural conditions. As was mentioned previously, the critical wind velocity for the genesis of waves on large bodies of water is about one-third as great as the corresponding value obtained in our laboratory channel. Furthermore, it was also shown that the formula characteristic velocity is about 1.3 times larger than the critical wind velocity. Thus it is to be expected, as the formula characteristic velocity is of the order of 100 cm/sec for large bodies of water, that only a minor error will be made if this velocity is omitted. With this understanding the set-up expression for natural conditions may be given in the form

$$\frac{S}{L}=3.30\times10^{-6}\left[1+63\left(\frac{H}{L}\right)^{1/2}\right]\frac{V^2}{gH}, \qquad (87)$$

and this should apply to large bodies of water, the confinement approximating the shape of a rectangular channel of a uniform cross section.

The average depth of Lake Erie being 17.7 m and the length 377 km, computations on the basis of the above formula gave a set of values of the expected set-up shown by the heavy straight line in figure 33. It will be remembered that the difference between the surface elevations at the extreme ends of the lake is defined as the set-up.

The agreement between the laboratory results and the observed set-up during storms may be deemed satisfactory. However, this relationship can neither be elaborated on nor discussed with a sense of finality. In order to make a definite evaluation of the rigor of the general formula proposed on the basis of the tests of the present investigation, it is necessary to have reliable observational data from numerous lakes or reservoirs with different depth/length ratios. Such data are not known to us at the present.

IX. The Need of New Experiments

One of the most significant deductions from the general set-up formula developed from these tests is in relation to the effective stresses at the surface of the water. Ordinarily it is supposed that the stress or the wind force is independent of the length of channel. The tests of the present investigation, however, show that the stress depends on the length of the channel. If this result holds in general, model experimentation on wind effects to simulate prototype conditions and effects will be out of the question.

Regarding this effect of channel length, two possibilities may be imagined. First, the effect of the length on the effective magnitude of the wind force may continue indefinitely when the channel length is increased keeping the water depth constant. Second, the effect may become gradually less important with increased length and less than that required by the general formula now given.

These matters can be studied within certain limitations in a new series of tests with channels much longer than the channel used in the present investigation. At the National Hydraulic Laboratory there are now available channels of sufficient length, and it is our intention to resume experiments when opportunity permits.

The author expresses his appreciation for the careful and thorough experimental work of his assistants, Marion R. Brockman and Victor Brame, without which it would have been impossible to complete this investigation.

X. References

[1] H. U. Sverdrup and W. H. Munk, Wind, sea and swell: Theory of relations for forecasting, Hydrographic Office, United States Navy Department, H. O. Pub. No. 601 (March 1947).

[2] B. Hellström, Wind effects on lakes and rivers, Handlingar, Ingeniörs Vetenskaps Akademien; Nr. 158 (Stockholm, 1941).

[3] G. B. Schubauer and M. A. Mason, Performance characteristics of water current meters in water and in air, J. Research NBS **18,** 351 (1937) RP981.

[4] U. Roll, Das Windfeld über den Meerswellen, Naturwissenschaften **35,** 230 (1948).

[5] Gebers, Das Ähnlichkeitsgesetz für den Flächenwiderstand im Wasser geradlinig fortbewegter, politierter Platten, Schiffbau **22,** 687 (1919).

[6] Kempf und Kloess, Widerstand kurzer Flächen, Werft, Reederei, Hafen **6,** 435 (1925).

[7] H. Jeffreys, Formation of water waves by wind, Proc. Roy. Soc. [A] **110,** 241 (1926).

WASHINGTON, November 3, 1950.

Journal of Research of the National Bureau of Standards Vol. 46, No. 5, May 1951 Research Paper 2208

Infrared Spectrum of Bromochlorofluoromethane

Earle K. Plyler and Mary A. Lamb

The spectrum of bromochlorofluoromethane has been measured in order to compare the wave numbers of the fundamental bands with those of other substituted methanes containing the halogens. The positions of the absorption bands have been determined for the liquid and vapor states and all fundamental bands except one at 220 cm^{-1} have been observed. The position of this band has been predicted from other bands that are classified as combinations of two fundamental bands, one of which was the 220 cm^{-1} band. Many of the bands of low or medium intensity have been classified as combinations or overtones of the nine fundamentals.

The spectra of many substituted methanes have been measured in the infrared, and normal coordinate calculations have been made on the fundamental modes of vibration of these molecules.[1] Good agreement has been found between the experimental and theoretical values assigned to the fundamental vibrations.

The number of different fundamental vibrations can be determined from the symmetry of the molecule. For example, molecules like methane or tetrafluoromethane have four different vibrations, molecules of the type of chloroform and fluoroform have six different fundamental frequencies, and molecules of the type of methylene chloride and bromochlorofluoromethane have nine separate fundamental frequencies. When the hydrogens of methane are substituted by the different halogen atoms, the number of molecular constants increases, and it is more difficult to obtain good agreement between the observed and calculated positions for the bands. Methods for carrying out the calculations with some simplifications have been described by Decius.[2] The compound bromochlorofluoromethane is of interest for it does not have a center or axis of symmetry.

The purpose of this investigation was to study the spectrum of bromochlorofluoromethane and to assign the fundamental bands. A comparison of the spectrum of bromochlorofluoromethane with the assigned vibrations in the spectra of related halogen-substituted methanes is helpful in making the assignments and in attributing them to motions of particular atoms. The dichlorofluoromethane assignments are also helpful in making the identification of the C-Cl and C-F bending and stretching vibrations in bromochlorofluoromethane. The identification of the C-Br bending and stretching vibrations were made by comparison of the spectrum with the assigned spectrum of dibromochloromethane.

The bromochlorofluoromethane was obtained from Halogen Chemicals Inc., where it was repurified so that it was suitable for spectroscopic measurements. The compound was redistilled into three fractions by W. Harold Smith, of the Bureau's Organic Chemistry Section. Tests of the purity of two of the fractions were made in the Mass Spectrometry Section of this Bureau, and the results showed that the distilled fraction with the intermediate boiling point, 37° C, was 98 percent of bromochlorofluoromethane. The principal impurities were probably dichlorobromomethane and dichlorofluoromethane. The fraction with the lower boiling point, 29.5° to 35.8° C, showed 95.1 percent of bromochlorofluoromethane, and the most likely impurities were dibromofluoromethane, dichlorofluoromethane, and dichlorobromomethane. The spectra of the three fractions were essentially the same. Some slight differences in the intensity of weak bands were noted; these coincided in position with the strongest bands in the spectra of the most likely impurities and are attributed to those molecules. These are discussed later.

The infrared absorption spectrum of bromochlorofluoromethane has been measured in both the liquid and vapor states. Although all three distillation fractions were measured, only the spectrum of the fraction with the intermediate boiling point, 37° C, will be presented since this was the fraction of highest purity. In figure 1, A, is shown the region from 2 to 15 μ of the spectrum of the compound in the liquid state as measured by a Perkin-Elmer spectrometer with the lithium fluoride and sodium chloride prisms. The broken line portions of the curve represent the weak bands, which are probably due to the impurities present in the fraction, and they also represent regions of atmospheric water absorption where the shapes and positions of the bands were difficult to determine accurately. These regions have been plotted using the spectrum measured on a Baird infrared spectrophotometer. Five of the nine fundamental vibrations are present in this region, and most of the other bands have been assigned as combination or overtone bands. A list of the bands with their assignments is included in table 1. The region from 15 to 23 μ, as measured with a potassium bromide prism, and the region from 23 to 38 μ, as measured with a thallium bromide-iodide prism, are shown in figure 1, B. Three of the remaining four fundamental bands have been assigned to bands in this region. The ninth fundamental vibration has not been observed directly, but may be a value of 220 cm^{-1} on the basis of observed combination and difference bands. This band is beyond the range of the thallium bromide-iodide prism.

[1] G. Herzberg, Infrared and Raman spectra of polyatomic molecules (D. Van Nostrand Co., Inc., New York, N. Y., 1945).
[2] J. C. Decius, J. Chem. Phys. **16**, 214 (1948).

In figure 1, C, are shown the more intense bands in the vapor spectrum in the region from 2 to 23 μ. Most of these bands show evidence of P, Q, and R branches. The C-H stretching vibration at 3,023 cm^{-1} is shown on an enlarged scale so that the detail of the band can be seen more clearly. The bands shown are of the same relative intensities as they were in the measurements of the liquid state. There is noted, however, a slight shift to larger wave numbers of not more than 10 cm^{-1} for the vapor state from the wave numbers observed in the liquid state spectrum.

In table 1 are listed all of the observed bands as observed in the liquid state of appreciable intensity with their intensities denoted by abbreviations for very weak, weak, medium, strong, or very strong. The assignments of the bands have also been given as fundamental, combination, overtone, or difference bands. All of the intense bands are classified and fall into a consistent array based on the nine fundamental vibrations. Several of the assignments for weaker bands may not be correct, and eight observed weak bands have not been assigned in the table. It is possible that these weak bands arise from the small quantities of impurities in the compound. For example, the bands observed at 605, 721, and 1,168 cm^{-1} may be due to the dichlorobromomethane fundamental frequencies ν_3, ν_7, and ν_8 respectively, also the observed band at 848 cm^{-1} may arise from trichlorofluoromethane. The unassigned band at 790 cm^{-1} possibly may be explained as a combination band of dichlorobromomethane, $\nu_3+\nu_5$. To an approximation the bands may be considered as arising from stretching and bending vibrations of each peripheral atom (H, Br, Cl, F) with respect to the carbon atom. This would account for eight fundamental modes of vibration. The ninth fundamental band could be considered as a torsional motion of the molecule, but since the hydrogen atom is so much lighter than the halogens, the motion in this mode may equally well be considered a second degree of freedom of bending of the CH bond.

The spectrum of bromochlorofluoromethane should be similar to that of dichlorofluoromethane except for the modes of motion primarily involving the C-Br group, which should occur at lower frequencies for bromochlorofluoromethane than the corresponding C-Cl group in dichlorofluoromethane. Thus, for example, the band with the wave number of 3,023 cm^{-1} is identified as the C-H stretching, ν_1, vibration and the bands with wave numbers of 1,202 and 1,299 cm^{-1} are classified as the two bending vibrations of CH. These two types of vibrations are referred to as ν^{CH} and δ^{CH}, respectively, in table 1, and the same type of symbols are used to designate the other bands. Similar relationships hold between the unsymmetrical CHBrClF and the other kindred methane derivatives.

A comparison of the fundamentals of all four related molecules is shown in table 2. The assignments of the observed bands of the three latter methanes have been made and will be published later with a group of substituted methane derivatives.

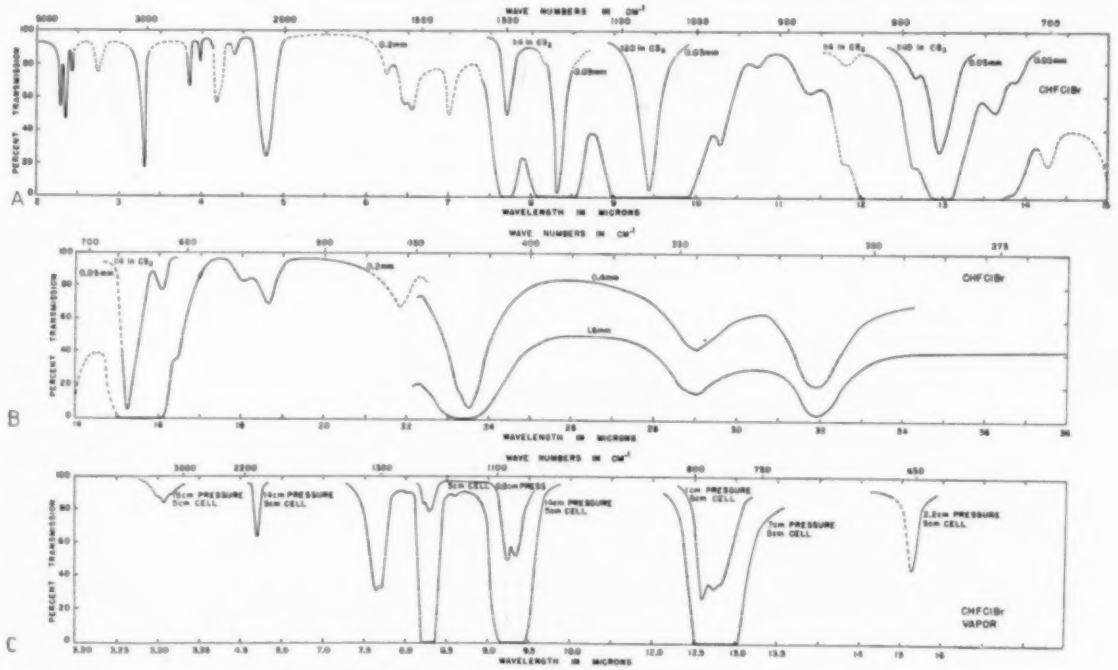

FIGURE 1. *Infrared spectrum of bromochlorofluoromethane.*

A, Liquid state from 2 to 15 μ; B, liquid state from 14 to 38 μ; C, intense bands, vapor state from 3 to 16 μ.

TABLE 1. *Classification of the observed bands of bromochlorofluoromethane*

Type	Assignment	Intensity	Wavelength	Wave number
			μ	cm^{-1}
δCBr	ν_2	.....	45.5	[a] 220
δCCl	ν_5	W	31.9	313
	$\nu_3-\nu_5$	VW	29.0	345
δCF	ν_6	M	23.5	426
	$\nu_3-\nu_2$	W	23.3	429
	$\nu_7-\nu_5$	W	21.83	458
	$\nu_2+\nu_5$	W	18.64	536
	$\nu_7-\nu_2$	VW	18.05	554
		W	16.78	596
		M	16.53	605
	$2\nu_5$	M	16.07	622
νCBr	ν_2	VS	15.26	655
		W	13.87	721
	$\nu_4+\nu_5$	M	13.62	734
νCCl	ν_7	VS	12.95	772
		M	12.65	790
	$2\nu_4$	W	11.79	848
	$\nu_3+\nu_2$	W	11.37	880
	$3\nu_5$	VVW	10.73	932
	$\nu_3+\nu_5$	W	10.29	972
νCF	ν_8	VS	9.43	1060
	$2\nu_5-\nu_5$	VW	8.56	1168
δCH	ν_9	VS	8.32	1202
		VW	8.04	1243
δCH	ν_4	S	7.69	1299
	$\nu_5+\nu_7$	W	7.0	[b] 1429
	$2\nu_7$	W	6.5	[b] 1538
		VW	6.4	[b] 1563
	$\nu_5+\nu_8$	VVW	6.2	[b] 1613
	$2\nu_5$	M	4.75	2105
		VW	4.40	2273
	$2\nu_8$	VW	4.182	2391
	$2\nu_9+\nu_5$	W	4.132	2420
	$\nu_8+\nu_9$	VW	3.979	2513
	$2\nu_6$	W	3.847	2599
νCH	ν_1	M	3.308	3023
	$\nu_1+\nu_5$	VW	2.75	3636
	$\nu_1+\nu_9$	VW	2.426	4122
	$\nu_1+\nu_8$	W	2.348	4259
	$\nu_1+\nu_6$	W	2.290	4367

[a] Predicted value.
[b] Value from Baird spectrophotometer.

The bands of bromofluorochloromethane have slightly smaller wave numbers than those of the corresponding dichlorofluoromethane bands. However the C-H stretching vibration is about equal for both compounds.

TABLE 2. *Comparison of the fundamental frequencies of dichlorofluoromethane, bromochlorofluoromethane, bromodichlorofluoromethane, and dibromochloromethane*

Assignment	Wave number (cm^{-1})			
	$CHCl_2F$	CHBrClF	$CHBrCl_2$	$CHBr_2Cl$
ν_2	276	220	220	168
ν_5	338	313	215	201
ν_6	458	426	330	278
ν_3	742	655	604	570
ν_7	804	772	719	746
ν_9	1079	1060	760	657
ν_8	1242	1202	1211	1144
ν_4	1304	1299	1168	1189
ν_1	3023	3023	3040	3034

The Raman spectrum of bromochlorofluoromethane has been measured by Glockler and Leader.[3] They found Raman lines that check well in wave number with the fundamentals assigned in the present work. Except for the CH stretching vibration the Raman values were not assigned to different types of vibrations of the molecules.

[3] G. Glockler and G. R. Leader, J. Chem Phys **8**, 669 (1940).

WASHINGTON, October 23, 1950

Journal of Research of the National Bureau of Standards Vol. 46, No. 5, May 1951 Research Paper 2209

Surface Tension of Molten Alkali Silicates

Leo Shartsis and Sam Spinner

The surface tensions of a series of lithium, sodium, and potassium silicate melts were measured by a maximum-pull-on-cylinder method. The order Li>Na>K was established for surface tension as well as for the algebraic value of the temperature coefficient of surface tension. Lithia and soda raised the surface tension, and potash lowered it. The surface tension curves of different alkali content converged with increasing temperature for lithium and sodium, but diverged for potassium silicates. Liquids containing less than 33 mole percent of lithia had positive temperature coefficients of surface tension. Correlation was observed between alkali content, volume expansivity, and temperature coefficient of surface tension.

I. Introduction

One of the fundamental aims of the scientific study of glass-forming systems is to find relationships between composition and properties that will lead to a better understanding of the glassy state. For this purpose, studies of the change in properties resulting from systematic variations in composition of simple glass-forming systems are necessary. In planning such experiments, it is neither necessary nor desirable to limit the composition range to formulations where glasses are readily formed on cooling. In many such systems, the glass-forming region shades off gradually into the non-glass-forming region, and useful information may be obtained by extending the formulations range beyond the glass-forming region.

Surface tension is one of the physical properties of glass-forming materials that is related to certain working properties of glasses. These properties include the fining of glass (removal of bubbles), healing of glass blisters, the adhesion of hot glass to hot glass and other heated solids, the fire polishing of rough edges and surfaces, etc.

The common constituent of practical glasses is SiO_2. Unfortunately, there are not many oxides that can be conveniently added alone to SiO_2 to form glasses. However, the alkaline oxides, Li_2O, Na_2O, and K_2O, are among those that form binary glasses with SiO_2, and a study of these systems was undertaken. The objectives of this investigation were to determine (1) how the surface tension varied with composition and temperature, (2) how the temperature coefficient of surface tension varied with composition, and (3) how the temperature coefficient of surface tension varied with expansivity.

II. Preparation of Melts and Methods of Tests

1. Preparation of Melts

The liquids investigated were made by melting in platinum crucibles the requisite amounts of raw materials of the purity [1] used for optical glasses. The melts, weighing approximately 500 g, were stirred with a motor-driven (propellor-type) platinum stirrer. When they seemed homogeneous, they were poured into iron molds.

2. Chemical Analysis

Samples from each melt were analyzed for alkali oxide content by evaporation to dryness on a steam bath with HF to the corresponding fluosilicate and followed by drying at 135° C to constant weight. With higher alkali content better reproducibility of the analyses was obtained by evaporation with HF and H_2SO_4 to the sulphate, followed by heating to constant weight at approximately 600° C. Analyses were made also of many of the samples remaining from the individual determinations of surface tension.

3. Measurement of Surface Tension

The method for measuring surface tension in use in this laboratory [1] [2] was that of determining the maximum pull exerted on a thin-walled platinum cylinder when its lower edge was in contact with the test liquid. In general the first determination of surface tension of any melt was made at 1,400° C. Subsequent measurements were made at 100-deg C intervals, decreasing the temperature until the glass was too viscous to yield in a reasonable time, or until crystallization occurred.

4. Measurement of Density

In order to obtain accurate values of surface tension with the method used, it was necessary to know the density of the liquid at the temperature of test. These densities were determined by a counter-balanced-sphere method [2]. Expansivities were calculated from the change of density with temperature.

[1] A typical analysis of silica is SiO_2-99.71, Fe_2O_3-0.01, R_2O_3-0.11; HF residue-0.20 ignition loss-0.09. Potash is required to contain over 98% of K_2CO_3, negligible amounts of coloring oxides (Mn, Cr, Ni, Fe) and be completely soluble in water. Soda ash is required to contain at least 58% of Na_2O, same negligible amounts of coloring oxides and be completely soluble.

[2] Figures in brackets indicate the literature references at the end of this paper.

III. Results and Discussion

1. The System Li_2O-SiO_2

Table 1 gives the surface tension values obtained, and figure 1 shows the data in graphical form. Below 16 percent of lithia, surface tension measurements could not be made at temperatures less than 1,300° C because of crystallization. Above 20 percent of lithia the lowest temperatures at which surface tensions could be measured rose from 1,000° C to about 1,200° C. The curves of surface tension versus temperature appear to converge with increasing temperature. It will be noted (fig. 1) that the surface tension values of liquids containing less than 20 percent of lithia increases with rise in temperature, which means that in this case the temperature coefficient of surface tension ($d\sigma/dt$) has a positive sign. This result can be contrasted with familiar liquids whose surface tension decreases with rise in temperature, that is, $d\sigma/dt$ has a negative sign. In discussing changes in the magnitude of $d\sigma/dt$ of ordinary liquids it has been tacitly assumed in the literature that the sign is always negative and only the absolute values are of concern. However, in the present study liquids exhibiting both positive and negative temperature coefficients are encountered, and the algebraic sign as well as the magnitude must be kept in mind.

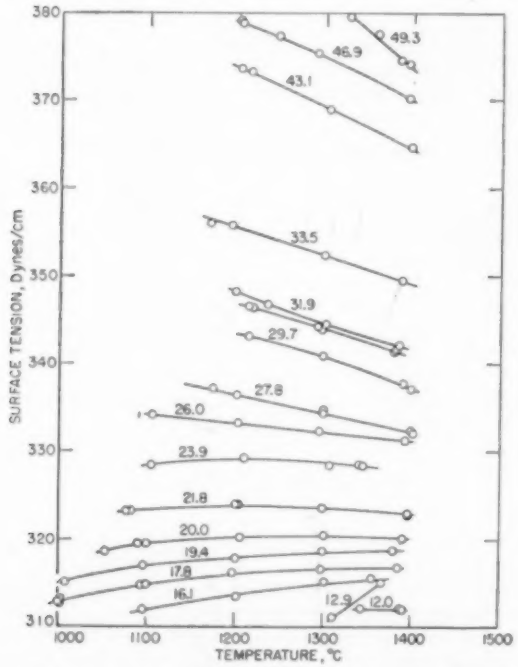

FIGURE 1. *Surface tension of liquids in the system* Li_2O-SiO_2 *as a function of temperature.*

The percentage of Li_2O is shown just above each curve.

The upper part of figure 5 shows a plot of the surface tensions of lithia-silica liquids at 1,300° C as a function of composition. The surface tension goes up with increasing lithia content. The value found by Jaeger [3] for the metasilicate composition (cross in fig. 5) is about 10 dynes/cm higher (2.8 %) than that obtained in this investigation. The lower portion of figure 5 shows a plot of the temperature coefficient of surface tension at 1,300° C versus composition. The temperature coefficient becomes more negative with increasing amounts of lithia. Liquids containing less than 33.4 mole percent of lithia have positive temperature coefficients.

These data permit inferences regarding the properties of vitreous silica. Unless the curve (fig. 5) has a minimum in the region below 21.5 mole percent of lithia or shows other unusual dependence on lithia content, the surface tension of vitreous silica at 1,300° C is of the order of 300 dynes/cm. With the same reservations a parallel inference that the temperature coefficient of surface tension is positive may be made.

2. The System Na_2O-SiO_2

Table 2 gives the results obtained with liquids in the soda-silica system, and figure 2 shows the results in graphical form. The effect of increasing temperature is to decrease the surface tension for a given composition and to decrease the magnitude

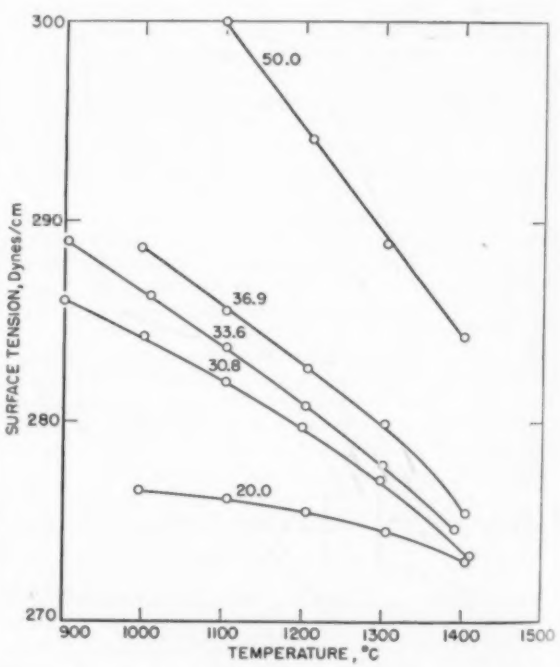

FIGURE 2. *Surface tension of liquids in the system* Na_2O-SiO_2 *as a function of temperature.*

The percentage of Na_2O is shown just above each curve.

TABLE 1. *Surface tension, temperature coefficient of surface tension, and expansivity of liquids in the system* Li_2O-SiO_2

Weight percent of Li_2O	Mole percent Li_2O	Surface tension at— 1,400° C.	1,300° C.	1,200° C.	1,100° C.	1,000° C.	$\Delta\sigma/\Delta t$ at 1,300° C.	Volume expansivity
		Dynes/cm	*Dynes/cm*	*Dynes/cm*	*Dynes/cm*	*Dynes/cm*	*(Dynes/cm)° C.*	*ppm/° C.*
12.0	21.5	312.1	.....	.....	.....	.....	.....	.....
12.9	22.9	316.3	310.8	.....	.....	.....	.....	46.5
16.1	28.6	316.5	315.1	313.5	311.9	.....	+0.015	60.7
17.8	30.3	316.8	316.7	316.2	314.7	312.8	+.003	45.5
19.4	32.6	318.8	318.4	317.8	316.9	314.8	+.005	76.8
20.0	33.4	320.1	320.2	320.0	319.4	.....	0	76.0
21.8	35.9	322.7	323.5	323.9	323.3	.....	−0.006	87.7
23.9	38.7	327.9	328.4	329.1	328.3	.....	−.006	81.3
25.9	41.3	331.1	332.1	333.1	334.1	.....	−.010	97.2
27.8	43.6	332.2	334.2	336.3	338.4	.....	−.020	91.8
29.7	45.9	337.1	340.8	343.4	.....	.....	−.032	103.9
31.9	48.5	341.8	344.5	348.1	.....	.....	−.032	112.3
		341.0	343.9	346.9	.....	.....	−.030	
33.5	50.3	349.1	352.3	355.5	.....	.....	−.032	.....
43.1	60.4	364.4	369.1	373.9	.....	.....	−.048	.....
46.9	64.0	370.0	374.9	379.1	.....	.....	−.046	.....
49.3	66.2	373.6	[381.3]	.....	.....	.....	−.08	.....

* Figures in brackets are extrapolated values.

TABLE 2. *Surface tension, temperature coefficient of surface tension, and volume expansivity of some liquids in the system* Na_2O-SiO_2

Weight percent of Na_2O	Mole percent of Na_2O	Surface tension at— 1,400°C	1,300°C	1,200°C	1,100°C	1,000°C	900°C	$\Delta\sigma/\Delta t$ at 1,300°C	Volume expansivity
		Dynes/cm	*Dynes/cm*	*Dynes/cm*	*Dynes/cm*	*Dynes/cm*	*Dynes/cm*	*(Dynes/cm)/°C*	*ppm/°C*
20.0	19.5	273.1	274.6	275.6	276.2	276.6	.....	−0.008	54
30.8	30.1	373.7	277.0	279.7	282.1	284.3	286.0	−.026	66
33.6	32.9	274.4	277.9	280.9	283.8	286.4	289.0	−.030	82
36.9	36.2	275.6	279.9	282.8	285.6	288.5	.....	−.035	88
50.0	49.2	284.3	289.0	294.6	300.0	.....	.....	−.052	112

of the difference in the surface tensions of the different compositions.

The upper part of figure 3 shows the effect of varying the soda content on the surface tension at 1,300° C. The straight line was drawn through the data of other investigators, while the curved line was drawn through the data of the present investigation. Three of the other investigators [4, 5, 6] used a maximum pressure method and one [7] used a modified drop-weight method. All the data are agreed in showing that the surface tension increases about 10 to 15 dynes/cm as the soda content increases from 20 to 50 percent by weight. The values in the present investigation are lower by approximately 6 dynes/cm (2.1%) than the average of the other investigators. In a previous investigation of the PbO-SiO_2 [8] system it was found that the maximum pull-on-cylinder method was higher than the drop-weight method [7] by about 9 dynes/cm. This suggests that differences between methods may be influenced by the compositions of the materials tested. The lower part of figure 3 shows a plot of the temperature coefficient of surface tension versus composition. Nearly all the available data indicate that the temperature coefficient becomes increasingly negative with increasing soda content.

As in the lithia-silica system the inference that vitreous silica at 1,300° C has a surface tension value of the order of 300 dynes/cm may be drawn unless the curve starts upward again as the silica content is increased. The data of Parmelee et al. [4] (hollow circles) suggest that this is indeed the case. The inference that $d\sigma/dt$ for vitreous silica is positive may also be drawn from its relation to soda content. Parmelee's [4] data (hollow circles) show, however, some evidence of a decrease or even a reversal of the tendency for the temperature coefficient to become more positive with decreasing soda content in the region below 25 percent of soda.

3. The System K_2O-SiO_2

Table 3 gives the results of two sets of determinations on eight liquids of different K_2O content, and figure 4 shows the data of the second set of determinations in graphical form. It may be seen that the effect on surface tension of differences in potash content is very small at 1,000° C but increases with increasing temperature. This divergence of the curves with increasing temperature is contrary to the experience with the lithia and soda silicates (figs. 1 and 2) where the different composition curves converge with increasing temperature. These contrasts in behavior correlate with the fact that both lithia and soda raise the surface tension of SiO_2, whereas potash lowers it.

Some conclusions may be drawn regarding changes in surface concentration of potash by applying the Gibbs adsorption isotherm [9]. The divergence of the curves with increasing temperature means that the

TABLE 3. *Surface tension, temperature coefficient of surface tension, and volume expansivity of some liquids in the system* K_2O-SiO_2

Weight percent of K_2O	Mole percent of K_2O	Determination number	Surface tension at—					$\Delta s/\Delta t$ at 1,300° C	Volume expansivity
			1,400° C	1,300° C	1,200° C	1,100° C	1,000° C		
			Dynes/cm	*Dynes/cm*	*Dynes/cm*	*Dynes/cm*	*Dynes/cm*	*(Dynes/cm)/°C*	*ppm/°C*
43.6	33.0	1	207.7	212.1	216.1	221.1	223.0	----------	119.4
		2	204.7	209.5	214.6	219.6	----------	−0.050	------
		Avg	206.2	210.8	215.4	220.3	----------	−.046	------
41.6	31.2	1	209.0	214.1	218.2	221.8	226.2	----------	102.0
		2	207.3	211.8	216.1	220.5	224.8	−.044	------
		Avg	208.9	213.0	217.2	221.2	225.5	−.045	------
38.7	28.7	1	211.4	213.1	218.7	221.9	226.2	----------	112.1
		2	208.7	212.8	216.6	220.7	224.6	−.040	------
		Avg	210.0	213.0	217.6	221.3	225.4	−.038	------
36.6	26.9	1	211.0	212.8	216.7	220.9	225.2	----------	86.3
		2	209.3	213.2	217.1	221.4	225.3	−.039	------
		Avg	210.2	213.0	216.9	221.2	225.2	−.034	------
32.9	23.8	1	213.9	216.5	218.6	221.4	227.6	----------	95.1
		2	213.4	216.1	219.8	222.6	226.2	−.032	------
		Avg	213.6	216.3	219.2	222.0	226.9	−.028	------
29.9	21.4	1	216.3	219.0	220.0	222.5	225.8	----------	74.1
		2	216.6	218.5	220.5	224.1	227.4	−.020	------
		Avg	216.4	218.8	220.2	223.3	226.6	−.019	------
26.7	18.8	1	218.8	220.4	224.2	224.6	226.8	----------	79.5
		2	218.2	220.2	222.6	225.0	227.6	−.022	------
		Avg	218.5	220.3	223.4	224.8	227.2	−.024	------
23.9	16.7	1	217.9	220.1	220.8	224.0	228.4	----------	70.4
		2	219.9	222.0	223.9	225.5	----------	−.020	------
		Avg	218.9	221.0	222.4	224.8	----------	−.018	------

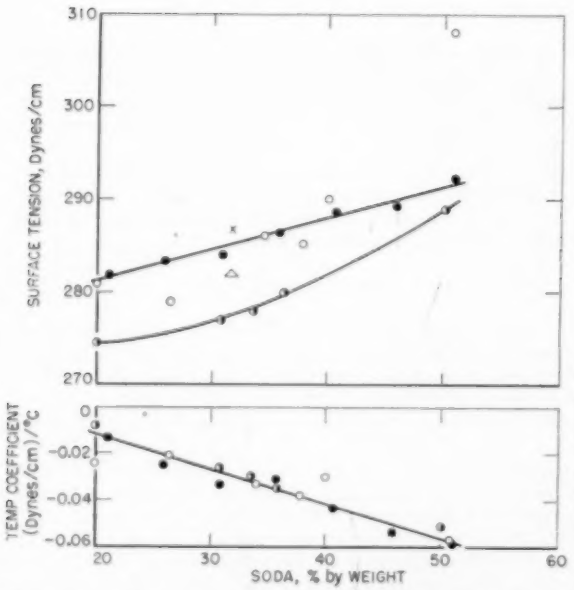

FIGURE 3. *Surface tension and temperature coefficient of surface tension of liquids in the system* Na_2O-SiO_2 *at 1,300° C.*

Hollow circles represent data of Parmelee et al. [4] with a bubble pressure method, filled circles represent data of Appen [7] with a modified drop-weight method, half-filled circles represent data of the present investigation, the cross represents datum of Williams and Simpson [6] with a bubble pressure method, and the triangle represents the datum of Amberg [5] with a bubble pressure method.

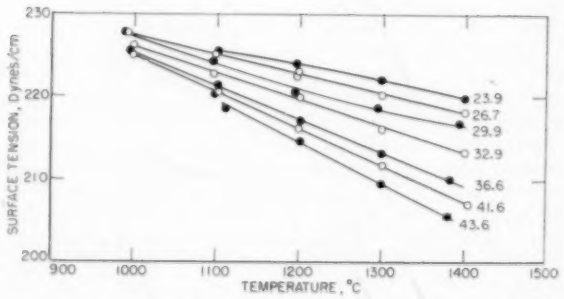

FIGURE 4. *Surface tension of liquids in the system* K_2O-SiO_2 *as a function of temperature.*

Second set of determinations. The percentage of K_2O is shown to the right of each curve.

change of surface tension with change in concentration of potash, $\Delta\sigma/\Delta c$ which may be called the concentration coefficient for convenience, increases in absolute magnitude with temperature. Since $\Delta\sigma/\Delta c$ is negative, the concentration of potash in the surface is greater than in the interior of the liquid according to the Gibbs adsorption isotherm. The increase in negative magnitude of $\Delta\sigma/\Delta c$ with increase in temperature means that the excess potash in the surface becomes greater as the temperature is raised. In the lithia and soda systems, the concentration coefficients are positive and become smaller as the temperature is raised. As there is less of these alkalies in the surface than in the interior and since this deficiency becomes less as the temperature is raised, the concentration of alkali in the surface increases with temperature.

In the above considerations, concentrations have been used instead of activities. A recent publication of Callow [10] has given the order of magnitude of the activity coefficients to be associated with the alkali concentrations. As the activity coefficients are always positive, they cannot change the algebraic sign of the concentration coefficients. Therefore, the general conclusions drawn here will not be affected.

The upper part of figure 5 shows a plot of the surface tension at 1,300° C as a function of the potash content. The effect of increasing the potash content is to lower the surface tension. There is a reason for not expecting a linear extrapolation of this curve to 0 percent of potash to yield a correct value for the surface tension of pure silica at 1,300° C. When a substance lowers the surface tension of the liquid, the effect of the initial additions is usually much greater than that of the succeeding additions [9]. Therefore, linear extrapolation to 0 percent of K_2O would be expected to give too low a value for the surface tension of pure silica at 1,300° C.

The lower part of figure 5 shows the effect of composition on the temperature coefficient of surface tension at 1,300° C. The general trend is for the temperature coefficients to become more negative with increasing K_2O content. Linear extrapolation of the temperature coefficient to 0 percent of potash indicates a positive temperature coefficient of surface tension for pure silica at 1,300° C, in agreement with the measurements of the Li_2O-SiO_2 and Na_2O-SiO_2 systems.

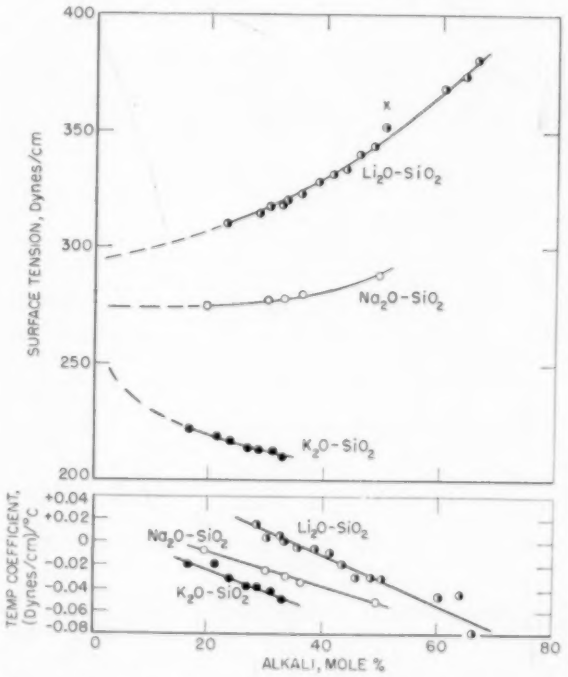

FIGURE 5. *Comparison of the surface tension and temperature coefficient of surface tension at 1,300° C of alkali silicate liquids as a function of the mole percent of alkali.*

Cross was obtained by linear extrapolation of Jaegers [3] data above 1,380° C.

4. Comparison of the Surface Tensions of the Alkali Silicates

The upper part of figure 5 shows a plot of the surface tension at 1,300° C of the systems investigated versus the mole percent of alkali. The order Li>Na>K found is the same as that observed by Jaeger [3] for molten salts and by Badger [11] for equal molar alkali additions to a soda-lime-silica base glass.

The lower part of figure 5 shows a plot of the temperature coefficient of surface tension at 1,300° C versus mole percent of alkali. Comparing the values of the coefficient (at the disilicate composition) the order Li>Na>K is found to hold in the sense that Li gives more positive coefficients than Na and Na gives more positive ones than K.

5. Temperature Coefficients and Expansivity

The normal process tending to lower the surface tension as the temperature is raised is generally con-

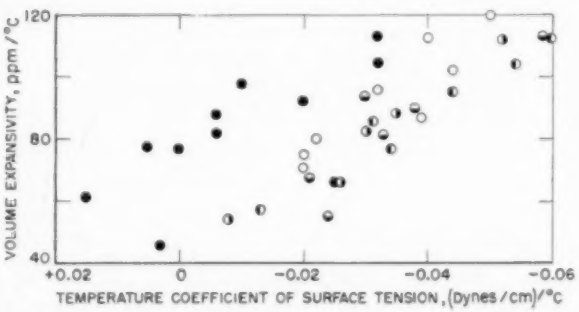

FIGURE 6. *Volume expansivity at 1,300° C versus temperature coefficient of surface tension at 1,300° C of alkali silicate liquids.*

Filled circles represent Li_2O liquids, hollow circles represent K_2O liquids, and half-filled circles represent Na_2O liquids. Circles whose right half is darkened represent data of the present investigation, those whose left half is darkened represent Appens [7] data, and those whose lower half is darkened represent data of Parmelee et al. [4]

sidered to be associated with the decrease in the force of attraction between adjacent molecules as their average distance of separation increases with rising temperature. This suggests that the mechanism leading to negative temperature coefficients should have some relation to the expansivity. It has been deduced from theoretical considerations [9] that the ratio of the temperature coefficient [3] of surface tension to that of cubical expansion should be constant. This deduction is based on the assumption that the liquids discussed are strictly homogeneous, that is, they each contain only one kind of molecule. Obviously, constancy of the ratio cannot be expected in solutions where different kinds of molecules exist and where the surface composition is generally different from that of the interior. Nevertheless, in a series of liquids containing one solute in different concentrations in the same solvent, one may expect some systematic relation between the two coefficients. The tendency for the temperature coefficient to increase in negative magnitude with increasing expansivity may be expected.

Figure 6 shows a plot of the volume expansivity versus the temperature coefficient of surface tension. In the case of the system Na_2O-SiO_2, expansivity data were calculated from density data in the literature [12] combined with the data of the sphere method [2]. The general trend for the temperature coefficient of surface tension to become more negative as the expansivity increases is quite marked.

The authors invite attention to the large scatter in the temperature-coefficient data as well as the volume-expansivity data. The precision of such measurements is necessarily low because each value is derived from a small difference between two relatively large quantities. The differences between the two large quantities are often not much greater than the reproducibility of the method used so that a large scatter in the coefficients is to be expected. No exact laws can be deduced from such data; instead, only general trends may be observed.

In a previous publication [8] where the relation between temperature coefficient of surface tension and expansivity was discussed, the expansion data used were not in the same temperature region as that at which the surface tension was measured, principally because suitable data were not available. It was tacitly assumed that the expansivities in the liquid region would parallel those in the solid range. Recent experience [2] in measuring densities has shown that such an assumption is not valid. The comparison of different properties must be based on measurements made over the same temperature range.

[3] The temperature coefficient referred to in the literature [9] is $1\ (1/\sigma)\ (d\sigma/dt)$, whereas the one used in this paper is $\Delta\sigma/\Delta t$, where σ is the surface tension and t the temperature.

IV. Summary and Conclusions

The surface tensions of a series of lithium, sodium, and potassium silicates have been measured. Increasing the lithia and soda content was found to raise the surface tension, whereas increasing the potash caused a lowering in surface tension. The order Li>Na>K was established for surface tension as well as for the temperature coefficient of surface tension. The surface tension-versus-temperature curves of differing alkali content were found to converge with increasing temperature in the case of the lithium and sodium silicates and to diverge in the case of the potassium silicates. Liquids containing less than 33 mole percent of lithia had positive temperature coefficients of surface tensions. Correlation was observed between alkali content, volume expansivity, and temperature coefficient of surface tension.

V. References

[1] L. Shartsis and A. W. Smock, J. Research NBS **38,** 41 (1947) RP1771.
[2] L. Shartsis and S. Spinner, J. Research NBS **46,** 176 (1951) RP2190.
[3] F. M. Jaeger, *Z.* fur Anorg Chemie **101,** 179 (1917).
[4] Cullen W. Parmelee, Kenneth C. Lyon, and Cameron G. Harman, U. Ill. Bull. **36,** No. 81 (June 6, 1939).
[5] C. R. Amberg, Thesis, Penn. State College (1948).
[6] R. M. Williams and H. E. Simpson, private communication.
[7] A. A. Appen, Optiko-Mekh Prom. **6** [3], 7 to 12; [12], 17f (1936); Ceram. Abs. **16** [2], 242 (1937).
[8] L. Shartsis, S. Spinner, and A. W. Smock, J. Research NBS **40,** 61 (1948) RP1855.
[9] H. Freundlich, Colloid and Capillary Chemistry, p. 53 to 55 (E. P. Dutton and Co., New York, N. Y., 1922).
[10] R. J. Callow, Trans. Faraday Soc. **46,** 663 (1950).
[11] A. E. Badger, C. W. Parmelee, and A. W. Williams, J. Am. Ceram. Soc. **20,** 325 (1937).
[12] G. Heidtkamp and K. Endell, Glastech. Ber. **14,** 89 (1936).

WASHINGTON, October 26, 1950.

Journal of Research of the National Bureau of Standards Vol. 46, No. 5, May 1951 Research Paper 2210

Mechanism of the Degradation of Polyamides

Bernard G. Achhammer, Frank W. Reinhart, and Gordon M. Kline

Films of polyamides were exposed to heat, ultraviolet radiant energy, and different atmospheric conditions. The degradation products were collected in some cases and analyzed by mass spectrometric techniques. The unexposed and exposed specimens were examined by the following techniques to obtain information concerning the changes in chemical and physical structure of the polymer: infrared absorption, ultraviolet absorption, viscosity of solutions, measurement of dielectric constant and dissipation factor, photomicrography, X-ray diffraction, electron microscopy, electron diffraction, and effect of organic liquids. In addition, pyrolysis studies were made and some physical properties were determined. The results of the investigation show clearly that no single method gives a complete picture but that the results from several of the methods give an insight into the mechanism of degradation of polyamides.

Polyamide molecules are relatively unaffected by exposure to moderate temperature (60° C). However, loss of water and other volatile materials may cause changes in physcial properties. The effects of exposure to ultraviolet radiant energy are more pronounced, and degradation of the polyamide molecule occurs with accompanying loss of water and other volatile materials that act as plasticizers.

The results of this investigation show that the general course of the degradation of polyamides is as follows:

1. The polymer molecules break at the C—N bond of the peptide group creating smaller polymer molecules with the same unit of chemical structure. The fragments broken out are evolved as carbon dioxide, carbon monoxide, water, and hydrocarbons.
2. The degree of crystallinity or local order changes, including alterations in hydrocarbon packing, dipole rearrangement, and hydrogen bridging.
3. The amount of strongly bound water and/or organic liquids changes. These materials are probably bound by hydrogen bridging to the oxygen of the peptide group. They act as plasticizers for the polyamides.

I. Introduction

One of the major problems facing the plastics industry is the degradation of some plastics when exposed to certain service conditions. This problem has been investigated extensively by accelerated tests involving one or more physical properties. While empirical investigations of this type give information of value, they yield little or no information on the basic changes in the material. As a result, the value of the information now available is not only limited, but in too many instances the information cannot be used to predict behavior in actual service [1].[1] The physical changes observed during degradation may result from (1) changes in the chemical structure of the plastic material, and (2) loss or changes in the compounding ingredients. The logical method of attack is to determine the specific chemical reactions involved in the degradation of the plastic and how these reactions are affected by the intensity of the conditions encountered.

The degradation of the plastic type of polyamides was investigated as part of a general research program to determine the mechanism or fundamental chemical reactions that occur when organic high polymeric materials are exposed to degrading forces such as heat, ultraviolet radiant energy, and constituents of the ambient atmosphere. The term degradation is used in this paper to describe irreversible changes in the chemical structure of the polymer as a result of exposure to external forces.

[1] Figures in brackets indicate the literature references at the end of this paper.

Boulton and Jackson [2, 3] found that treatment with sulfuric acid, exposure to ultraviolet radiant energy from a carbon arc, and exposure to sunlight, degrade nylon. The degradation was followed by measurement of tensile strength and the viscosity of solutions in *m*-cresol and formic acid. They found that a loss of over 50 percent in tensile strength is accompanied by a relatively small change in relative viscosity. A smaller decrease in viscosity for a given loss in tensile strength was observed for the materials degraded photochemically than for those degraded by the acid.

Hosino [4] reported that heating nylon with concentrated hydrochloric acid for 12 hr causes almost complete hydrolysis of the polymer into adipic acid and hexamethylenediamine.

Taylor [5] reported that ammonia is produced during the degradation of nylon. Peterson [6] depolymerized polyamides by heating them with an equal amount of water in an autoclave at 200° to 210° C and 300 psi.

Fuller [7] found that heating linear polyamides for a short period of time to a suitable temperature in the presence of air or oxygen increases their toughness, flexibility, and resistance to embrittlement on aging. The temperature used, which must be above the melting point of the polyamide but below the decomposition temperature, may vary from 125° to 450° C, depending on the chemical structure of the polyamide. To obtain this effect the polyamide must be in the form of thin cross sections; otherwise the oxygen reacts with the material on the surface, leaving the interior unaffected.

TABLE 1. *Description of polyamides*

Sample designation	Chemical composition	Code designation for chemical composition	Nominal thickness	Approximate melting point in air	Approximate discoloration point in air.
			in.	*° C*	*° C*
4405	Hexamethylenediamine-adipic acid salt, 50%; ε-caprolactam, 50%	66/6–50:50	0.002	179 to 180	172
4406	Hexamethylenediamine-adipic acid salt, 50%; ε-caprolactam, 50%	66/6–50:50	.004	179 to 180	174
4407	Hexamethylenediamine-adipic acid salt, 60%; ε-caprolactam, 40%	66/6–60:40	.002	188 to 190	177
4408	Hexamethylenediamine-adipic acid salt, 60%; ε-caprolactam, 40%	66/6–60:40	.003	186 to 190	177
4409	Hexamethylenediamine-adipic acid salt; hexamethylenediamine-sebacic acid salt; ε-caprolactam [a]	66/610/6A	.002	165 to 167	160
4410	Hexamethylenediamine-adipic acid salt; hexamethylenediamine-sebacic acid salt; ε-caprolactam (more than in 4409)	66/610/6B	.002	161 to 163	158

[a] The percentage composition of sample 4409 is estimated to be 60% of 66 salt, 20% of 610 salt, and 20% of caprolactam.

II. Materials

The polyamide materials used in this investigation were copolymers of nylon salts with ε-caprolactam and are described in table 1. The samples were obtained in the form of commercial films, 0.002 to 0.004 in. thick, which were presumably cast from hot ethanol solutions. There were some differences among the samples in transparency, attributable to differences in rates of cooling.

The discoloration and melting points reported in table 1 were determined in air by the following procedure: The nylon film was cut into very small squares with a razor blade and the small pieces placed in a glass melting point tube. The tube was attached in the usual manner to a thermometer and the assembly placed in an agitated bath of silicone oil, which was heated by an electric coil heater. The temperature of the bath was raised at a fairly rapid rate to about 150° C and then at 1 deg C/min. The behavior of the nylon specimen was observed with a magnifying glass. Duplicate tests were made with all samples.

The thickness of the films was measured with a Mikrokator gage, which has a scale range of 0.0014 in. with graduations of 0.00002 in. The film was placed between gage blocks, 1 in. square, for measurement. The total force on the film was about 11 oz. Particular care must be taken to prevent contamination with grease, dirt, and dust in order to measure the thickness of the films to ± 0.00001 in.

It was necessary for some experiments to have thinner films. The following procedure was used for recasting the films: The nylon was dissolved in warm (above 45° C) ethanol. The warm solution, 2 to 4 percent, was poured on to a warm glass plate and spread to a uniform thickness with a doctor blade. In an alternate procedure the solution was poured into a brass ring on a warm glass plate and allowed to spread to a uniform thickness. This assembly was placed in a closed vessel with an ethanol-air atmosphere and maintained at 45° C for 1 hr. At the end of this time the vessel was opened and the ethanol was allowed to evaporate. The films were then washed in running water to free them of ethanol and dried over calcium chloride. The nylon films produced were clear and nearly free of surface defects. The film thickness was controlled by varying the concentration and depth of the solution. The films ranged in thickness from 0.0001 to 0.0008 in.

A dipping technique was developed to recast the films for the work with the electron microscope, since films for this purpose must be less than 0.00004 in. (1 μ) thick to permit sufficient transmission of the electron beam. The films were made by heating a 1.5-percent solution of the polyamide in 95-percent ethanol to 50° to 60° C and immersing a warm glass microscope slide in the solution. The glass slide was removed, held vertically for a couple of seconds, and then placed under a bell jar in an atmosphere of ethanol. The thin polyamide film on one side of the glass slide was removed by rubbing with a damp cloth after the film had dried. The glass slide, bearing the thin film on one side, was partially immersed in a dish of water. The immersed portion of the film was freed from the glass by the water and allowed to float free. Five 200-mesh stainless-steel specimen-supporting screens (⅛ in. in diameter) were placed on the submerged portion of the glass slide, so that upon removal from the water the free floating portion of the film fell back in place over the screens on the glass slide. This procedure made it unnecessary to apply tension on the film to remove it from the glass and place it on the screens as would be the case in the usual stripping and transfer technique.

III. Apparatus and Procedures

1. Apparatus to Produce Controlled Degradation

The apparatus designed to degrade polymeric materials by exposure to controlled conditions of heat, ultraviolet radiant energy, and ambient atmosphere is shown in figures 1 and 2. It consists of three integrated units: (1) a gas purification train, (2) an exposure chamber suitable for exposing polymer films to ultraviolet radiant energy at controlled temperatures, and (3) a gas-collection trap suitable for collecting samples for mass spectrometric analysis of the gaseous degradation products. Equipment of a somewhat similar nature was used successfully by Stillings and Van Nostrand [8] in a study of the action of ultraviolet radiant energy on cellulose.

The atmosphere in the exposure chamber was conditioned by the purification train, 1–9, shown schematically in figure 1. Any gas that is cylinder-packed could be used as the atmosphere. The gas

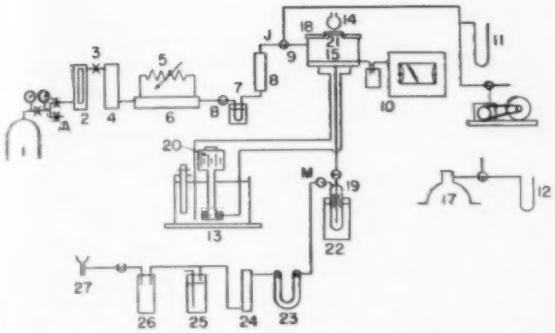

FIGURE 1. *Apparatus to produce controlled degradation.*

1, Gas cylinder; 2, flowmeter; 3, needle valve; 4, drying tube; 5, rheostat; 6, copper gauze furnace; 7, cold trap (−78° C); 8, carbon dioxide absorption tube; 9, three-way stopcock; 10, automatic temperature recorder with thermocouple cold junction; 11, manometer; 12, manometer; 13, constant-temperature bath; 14, source of ultraviolet radiant energy; 15, heating platen; 16, Pyrex ring (shown in fig. 2) used to hold film flat on heating platen; 15; 17, desiccator lid placed on 18 during evacuation to protect thin glass, 21, by evacuating both sides simultaneously; 18, Pyrex plate; 19, gas collection trap; 20, immersion pump; 21, ultraviolet transmitting glass; 22, cooling Dewar; 23, carbon dioxide absorbent; 24, drying tube; 25, reverse bubbler for pressure regulation; 26, water trap; 27, aspirator; A-B, bypass valve; J, end of purification train and start of exposure chamber unit; M, beginning of water aspirator and flow control apparatus.

was passed from the cylinder, 1, through a flow meter, 2. A flow of approximately 20 ml/min was maintained by manipulation of a needle valve. The outlet pressure on the gage attached to the gas cylinder was kept at about 2 psi. The gas passed from the flow meter through a needle valve, 3, which was used to close the system during evacuation. The gas then passed through a calcium chloride–copper sulfate tower, 4, to remove water, a copper gauze furnace, 6, to remove oxygen, a cold trap, 7, an ascarite-anhydrone tower, 8, to remove carbon dioxide, and finally into the exposure chamber through a three-way stopcock, 9. The temperature of the copper gauze furnace was controlled by a rheostat, 5. The furnace was removable from the train for regeneration of the copper. Sections of the purification train could be bypassed by attachment of rubber tubing from the gas cylinder at A to the three-way stopcocks B or 9. The gas used determined the type and amount of purification required. The mercury manometer, 11, connected to three-way stopcock 9, showed the pressure in the exposure chamber. The other manometer, 12, was used to maintain a pressure differential, which will be described subsequently.

A Brown potentiometer, 10, recorded the temperature of the platen on which the film was supported. The Dewar flask alongside the potentiometer was the cold junction for the copper constantan thermocouple embedded in the platen of the exposure chamber. The temperature of this platen was controlled by circulating silicone oil (DC–500) from the bath, 13, with an immersion pump, 20. The oil was circulated through a series of baffles and returned to the bath.

The exposure chamber 15 is shown in figures 1 and 2. It consists of an open-top brass cylinder 10 in. in diameter and 4 in. in height. The inside of the chamber was gold plated because most other metals

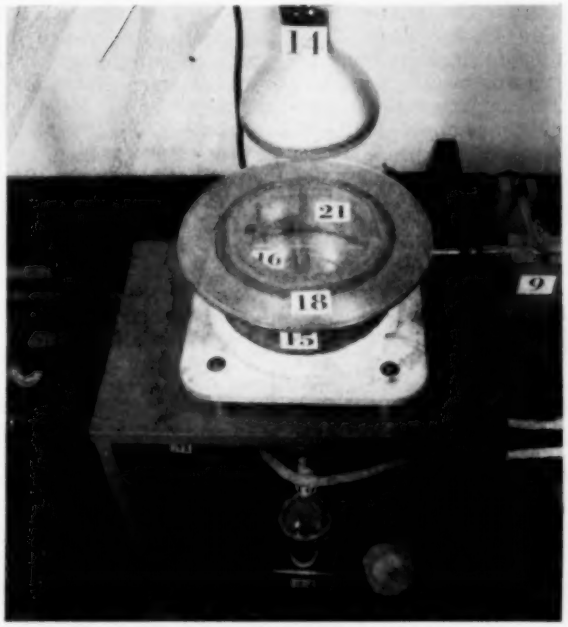

FIGURE 2. *Exposure chamber, vertical view, assembled for operation.*

act as catalysts and might cause reactions between the degradation products formed. Concentric grooves, 0.02 in. deep and 0.04 in. wide, on the floor of the exposure chamber are connected by radial grooves of the same dimensions to the outlet tube. A glass ring, 16, placed on the edge of the film to be studied prevented curling of the film. A Pyrex plate, 18, with a 5-in. aperture supported the Corex D window, 21, which was 2 mm thick and 6 in. in diameter. This Pyrex plate was sealed to the exposure chamber by a ground glass to ground brass seal and silicone stopcock grease. The Corex D window was sealed to the Pyrex glass with beeswax-rosin mixture or with silicone grease. An RS sunlamp, 14, was supported about 8 in. from the film to be studied. This type of sunlamp was convenient to use as a source of ultraviolet radiant energy. A blower (not shown) kept the temperature of the sunlamp, Corex D, and Pyrex sections down during irradiation.

The following assembly was used during evacuation of the system: A desiccator lid, 17, was placed on the ground surface of the Pyrex plate, 18. Because the Corex D window was so thin, it was necessary to evacuate both sides of the window simultaneously. A pressure differential was obtained by manipulation of suitably placed stopcocks. One manometer, 12, was used to read the pressure in the lid, 17, while another manometer, 11, gave the pressure in the chamber. By keeping the pressure slightly greater in the top section it was possible to maintain a good vacuum seal.

Gaseous products of the treatment were collected in a trap, 19, designed for simple attachment to the

mass spectrometer by means of spherical joints. The Dewar flask, 22, filled with acetone-carbon dioxide slush or liquid air, was used to condense the gaseous products in the collection trap. A U-tube, 23, containing ascarite-anhydrone and calcium chloride-copper sulfate was used to trap carbon dioxide that passed through the collection trap, 19. The calcium chloride-copper sulfate column, 24, prevented water vapor from entering the system. The inverse bubbler, 25, regulated the water supply so that a constant suction could be applied to the system. A trap, 26, was inserted to collect the water that might flow back into the apparatus if the water aspirator, 27, should not function properly.

The following procedure is representative of that used to make a typical exposure: The polyamide film, which was previously dried at room temperature in a desiccator and weighed, was placed in the exposure chamber. For study in an inert atmosphere, such as nitrogen, the exposure chamber was sealed and the system evacuated with a vacuum pump from point M to point 3. The system was then filled with purified nitrogen. This cycle was repeated several times. The entire system was then flushed with purified nitrogen at a rate of 500 ml/min for about ½ hr. The collection trap was then cooled; the sunlamp was turned on and the nitrogen flow was adjusted to 200 ml/min.

On completion of an exposure of a specimen to heat, to ultraviolet radiant energy, or to a combination of those factors, either of two procedures was followed: (1) The entire system was evacuated through the cold collection trap, 19, to point 3, and the evacuated collection trap was removed; or (2) the system was flushed with nitrogen and the collection trap removed under a slight positive pressure of nitrogen. The gaseous products were analyzed with a mass spectrometer. The treated film was examined by suitable analytical methods to detect changes.

The mass spectrometer is so sensitive that the presence of small amounts of volatile compounds is readily detected. This made it necessary to ensure that the experiments were made under conditions such that no volatile compounds were introduced from any source other than the degradation of the specimen. Blank tests were made with the degradation equipment. In one experiment an excess of silicone grease was used to seal the glass plates (18 and 21 in fig. 2) to the top of the exposure chamber and the chamber (15 in fig. 2) was exposed to radiation from an RS sunlamp for 6 hr while nitrogen gas was passed through the equipment. The mass spectrometric analysis of the material in the collection trap (19 in fig. 1) indicated the presence of no gases other than nitrogen. The results were also satisfactory in another blank experiment made at 25° C for 6 hr while nitrogen was passed through the equipment with a silicone grease seal at 18 in figure 2 and a beeswax-rosin seal at 21 in figure 2.

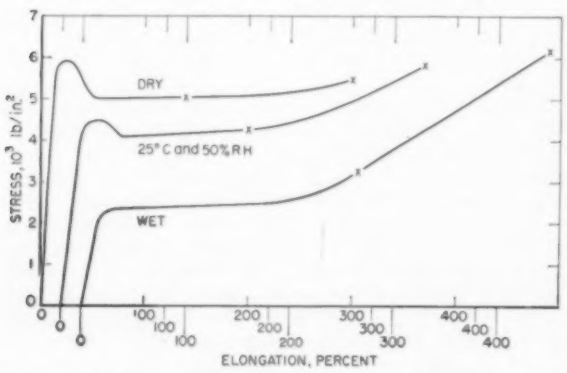

FIGURE 3. *Typical tensile stress-strain characteristics of polyamide sample 4409.*

2. Accelerated Weathering and Outdoor Exposure

Accelerated weathering was conducted in accordance with Method No. 6021 of Federal Specification L–P–406a [9], involving cyclic exposure to the radiant energy from an S–1 sunlamp and to fog. The total period of exposure to these two conditions is divided into multiples of 20 hr of sunlamp radiation to 4 hr of fog.

Outdoor exposure was accomplished by placing specimens fastened to glass frames on outdoor racks at 45° facing south from Feb. 17 to Apr. 18, 1947. During this period of 61 days there were 12 clear, 23 partly cloudy, and 26 cloudy days. The precipitation was 4.36 in. The temperature varied from 15° to 86° F and the relative humidity from 22 to 100 percent. The total sunshine was 530 hr.

IV. Mechanical Properties and Weathering Resistance

With J. J. Lamb, B. A. Hall, and C. Brown

The tensile strength, elongation at failure in the tensile tests, tearing strength, resistance to accelerated weathering, and resistance to exposure outdoors of the six polyamide samples were determined.

Tensile strength and elongation were determined at various temperatures and humidities after conditioning the specimens. The test specimens were cut with die D [10]. The results obtained utilizing two different machines are described in tables 2 and 3. A typical stress-strain curve obtained with an autographic strain gage system is shown in figure 3.

No significant differences were observed in tensile strength and elongation between the two orientations of the specimens of each sample, or between the various samples at 25° C and 50-percent relative humidity. At −29° C and 100-percent relative humidity, the differences between the samples are significant; the tensile strengths of samples 4405 and 4406 are slightly lower than those of samples 4407 and 4408 and higher than those of samples 4409 and 4410; the scatter in the elongation values as indicated by the coefficient of variation is so great that the differences are apparently not significant. The tensile strengths at −29° C are higher than

TABLE 2. *Tensile properties[a] of polyamides*

Sample designation[d]	Tests at 25° C and 50-percent relative humidity[b]						Tests at −29° C and 100-percent relative humidity[c]					
	Tensile strength			Elongation			Tensile strength			Elongation		
	Average	SE[e]	CV[f]	Average	SE[e]	CV[f]	Average	SE[e]	CV[f]	Average	SE[e]	CV[f]
	lb/in.²	*lb/in.²*	*%*	*%*	*%*	*%*	*lb/in.²*	*lb/in.²*	*%*	*%*	*%*	*%*
4405 C	8,400	240	8	440	8	5	13,500	340	8	10	0	0
4405 L	7,700	120	4	440	6	4	12,800	230	6	16	2	36
4406 C	7,800	150	6	440	6	4	11,300	130	4	10	2	70
4406 L	8,400	170	6	430	7	5	13,100	100	2	7	1	30
4407 C	8,500	310	12	390	10	8	14,100	200	4	10	1	17
4407 L	9,400	330	11	380	9	7	15,300	380	8	10	1	29
4408 C	7,400	190	8	430	10	7	11,700	350	10	10	1	40
4408 L	7,900	120	5	430	6	4	13,200	190	4	5	1	40
4409 C	9,400	150	5	440	5	4	10,800	480	14	10	2	80
4409 L	9,200	320	11	430	5	4	9,400	580	20	18	6	100
4410 C	7,200	500	22	390	21	17	10,500	460	13	7	1	37
4410 L	8,700	290	11	460	9	6	10,700	230	6	12	1	22

[a] Determined on a constant-speed spring-balance testing machine, 20-lb range, in accordance with Federal Specification ZZ-R-601a, Section II-5. Each average value was obtained with 10 specimens.
[b] Specimens conditioned for at least 48 hr.
[c] Specimens conditioned for at least 0.5 hr.
[d] Code for orientation of specimens: C=crosswise; L=lengthwise.
[e] Standard error.
[f] Coefficient of variation.

TABLE 3. *Tensile properties[a] of polyamides at 25° C*

Sample designation	Tensile strength			Elongation		
	Average	SE[b]	CV[c]	Average	SE[b]	CV[c]
CONDITIONED AT 50-PERCENT RELATIVE HUMIDITY[d]						
	lb/in.²	*lb/in.²*	*%*	*%*	*%*	*%*
4408	7,000	170	6	350	4	2
4409	6,000	330	13	280	25	20
WET (IMMERSED IN WATER)[e]						
4408	3,700	530	34	330	45	30
4409	5,400	640	29	360	24	15
DRY (DRIED OVER CALCIUM CHLORIDE)[f]						
4408	8,300	430	14	36	24	147
4409	6,600	660	24	136	52	84

[a] Determined on a Baldwin MTE testing machine, 50-lb range, in accordance with Federal Specification ZZ-R-601a, Section II-5. Each average value reported was obtained with 6 specimens.
[b] Standard error.
[c] Coefficient of variation.
[d] Specimens conditioned for at least 96 hr.
[e] Tests made immediately after removal of specimens from water at 25° C in which they were immersed for 24 hr.
[f] Tests made immediately on removal of the specimens from a desiccator charged with dry calcium chloride in which they were stored for 1 week.

those observed at 25° C; the increase on going to the low temperature is greater for samples 4405, 4406, 4407, and 4408 than for samples 4409 and 4410. The elongation values are much lower at −29° C than they are at 25° C. The tensile strengths of the samples were reduced by exposure outdoors for 2 months. Except for sample 4410, the elongations at break were also reduced by the exposure outdoors.

The tensile strength of sample 4408 increases with a decrease in water content. Although a similar trend is apparent for sample 4409, it is not statistically significant. The elongations at break for samples 4408 and 4409 wet and at 50-percent relative humidity are not statistically different. The elongations of the dry specimens are much lower than those of the wet specimens of both samples. Thus it appears that water acts as a plasticizer. The stressed specimens of sample 4408 became cloudy, but those of 4409 remained clear.

The tensile stress-strain curves show marked differences in characteristics between the wet and dry specimens. As the water content is reduced, the modulus of elasticity is reduced and the elongation at break is decreased. The failures were quick brittle breaks, particularly for the dry specimens. The shape of the stresss-strain curves is typical of materials that undergo an instantaneous elastic response when stressed and that also work-harden when stressed beyond the yield point [11 and 12]. The character of the yield point is also different for the wet and dry specimens. A comparison of the curves for the wet and dry specimens suggests that the crystalline order is different for the different conditions near the breaking point, but the character of this difference is not known. The curves for samples 4408 and 4409 indicate that these materials probably have different degrees of crystallinity.

The tearing strengths [13] of the polyamides at 25° C and 50-percent relative humidity and at −29° C and 100-percent relative humidity are reported in table 4. There is no difference in the tearing strengths of the crosswise and lengthwise directions of samples 4405, 4407, 4409, and 4410 at 25° C and 50-percent relative humidity, and of all the samples at −29° C and about 100-percent relative humidity. There is a significant difference between the crosswise and lengthwise directions for samples 4406 and 4408 at 25° C and 50-percent relative humidity. The tearing strengths at −29° C are markedly less than those at 25° C. As the thicknesses of samples 4405, 4407, 4409, and 4410 are approximately the same, the results of the tear-strength tests show that samples 4405 and 4410 are inherently stronger in tearing strength at ordinary temperatures than samples 4406 and 4409.

TABLE 4. *Tearing strength of polyamides*

Sample designation [b]		Elmendorf tearing strength per sheet [a]					
		Tests at 25° C and 50-percent relative humidity			Tests at −29° C and 100-percent relative humidity		
		Average	SE [c]	CV [d]	Average	SE [c]	CV [d]
		g	g	%	g	g	%
4405	C	[e] 90	11	27	40	6	38
		320	69	47	.....	.....	.....
	L	[e] 170	30	38	80	2	10
		220	27	24	.....	.....	.....
4406	C	220	37	37	70	19	63
	L	380	33	19	60	25	97
4407	C	65	14	46	40	2	12
	L	60	3	10	35	10	49
4408	C	[e] 130	10	16	60	25	55
		210	50	53	.....	.....	.....
	L	[e] 200	30	26	35	8	52
		440	10	5	.....	.....	.....
4409	C	150	18	28	45	0	0
	L	130	17	29	40	4	18
4410	C	[e] 250	40	34	35	1	8
		800	50	12	.....	.....	.....
	L	[e] 290	29	22	35	1	6
		750	85	25	.....	.....	.....

[a] Tests made with Elmendorf Tear Tester in accordance with ASTM Method of Test D 689-44 [13]. Each average value reported was obtained with 5 specimens.
[b] Code for orientation of specimens: C = crosswise; L = lengthwise.
[c] Standard error.
[d] Coefficient of variation.
[e] These values for samples 4405, 4408, and 4410 were obtained by placing the specimens in the grips of the Elmendorf Tear Tester and folding the free end to the left. All the other values for these samples were obtained with the free end folded to the right. The values for samples 4406, 4407, and 4409 did not depend on the way the test specimens were folded over in the test grips.

TABLE 5. *Effects of sunlamp-fog accelerated weathering test on the properties of polyamides*

Sample designation	Effects of accelerated weathering test [a]		
	Change in—		Condition (after 240 hr, unless otherwise noted)
	Width	Length	
	%	%	
4405	.....	.....	Very brittle and weak; fell apart at 180 hr.
4406	−3.4	−2.6	Slightly brittle; edges curled.
4407	.....	.....	Very brittle and weak; fell apart.
4408	−1.3	−1.7	Slightly brittle along edges nearest to sunlamp.
4409	.....	.....	Very brittle and weak; fell apart.
4410	.....	.....	Do.

[a] Three specimens of each sample were tested.

TABLE 6. *Tensile properties [a] of polyamides [b] at 25° C and 50-percent relative humidity after exposure outdoors for 2 months*

Sample designation	Orientation of specimens	Tensile strength		Elongation	
		Average	Range	Average	Range
		lb/in.²	lb/in.²	%	%
4406	Crosswise	5,700	4,600 to 7,000	350	290 to 450
	Lengthwise	5,000	4,300 to 7,200	240	50 to 450
4407	Crosswise	5,400	5,200 to 5,800	200	50 to 325
	Lengthwise	5,300	4,400 to 6,700	280	200 to 360
4408	Crosswise	5,400	5,000 to 5,600	280	140 to 350
	Lengthwise	4,800	4,600 to 5,000	190	110 to 300
4410	Lengthwise	6,200	4,400 to 7,400	400	300 to 470

[a] Determined on a constant-speed spring-balance testing machine, 20-lb range, in accordance with Federal Specification ZZ-R-601a, Section 11-5. Each average value reported was obtained with 5 specimens.
[b] Specimens of samples 4405 and 4409 were not in satisfactory condition to make tensile tests.

The effects of accelerated weathering and outdoor exposure on some properties on polyamide films are shown in tables 5 and 6. The accelerated weathering test conditions caused all the polamide samples to become more brittle. The outdoor exposure tests show that the resistance to weathering of samples 4406 and 4408 is superior to that of the other samples. The greater resistance of samples 4406 and 4408 to the action of the ultraviolet radiant energy is attributed to their greater thickness, and infers a surface degradation that may retard further degradation in the interior of the films.

Marked differences in the strength properties of the various polyamides are indicated in the results reported in this section. Various techniques were utilized to obtain data relating the observed changes in physical properties with changes in chemical structure of the polyamides. The results of these studies are described in the subsequent sections of this report.

V. Mass Spectrometry

With C. E. Wise, R. M. Reese, and L. M. Williamson

Polyamide samples 4406, 4407, and 4409 were exposed to controlled conditions of heat, ultraviolet radiant energy, and ambient atmosphere in the apparatus described previously in section III. The gaseous products were analyzed with a model 21–102 Consolidated Engineering mass spectrometer.

The experimental procedure is described in section III. Some of the experiments were made with the nylon samples in the film form in which they were received and others with recast films. Most of these films were dried in a vacuum at room temperature for 16 hr prior to use in the experiments.

The results of the experiments with the nylon samples are presented in table 7. Only water, carbon dioxide, and ethanol were found in the volatile products obtained from specimens of sample 4406 at 30° C with and without exposure to ultraviolet radiant energy (experiments 1 and 2). In experiment 3, a specimen of sample 4406 was dried in vacuum and then exposed as in experiment 1; the loss in weight was markedly less (0.2%, compared to 2.6%). It is apparent that part of the changes in properties observed in experiments 1, 2, and 3 can be attributed to the loss of absorbed water. Loss of the absorbed water causes the films to become brittle and crack readily.

Specimens of sample 4406 were exposed to ultraviolet radiant energy at 35° and 50° C for 20 hr (experiments 4 and 5). Water, carbon dioxide, ethanol, and hydrocarbons were found in the volatile products from these experiments. Carbon dioxide, water, ethanol, and hydrocarbons were obtained in all the experiments with specimens of samples 4407 and 4409 (experiments 9 to 13).

Carbon monoxide was evolved in all the experiments in which the specimens were exposed at temperatures of 90° to 100° C. Hydrocarbons were found in all experiments in which carbon monoxide

TABLE 7. *Mass spectrometric analysis of volatile products obtained during exposure of polyamides to heat and ultraviolet radiant energy*

Experiment	Sample designation	Thickness of film	Pretreatment	Exposure conditions: Temperature	Exposure conditions: Ultraviolet radiant energy	Exposure conditions: Time	Exposure conditions: Atmosphere	Loss in weight	Results of analysis
		in.		°C		*hr*		%	
1	4406	0.0036	None	30	RS	7	N_2	2.6	Water, ethanol.
2	4406	.0036	do	30	None	7	N_2	2.7	Do.
3	4406	.0036	Vacuum dried	30	RS	7	N_2	0.2	Water, carbon dioxide, ethanol.
4	4406	.0036	do	35	RS	20	N_2	.4	Water, carbon dioxide, ethanol, hydrocarbons.
5	4406	.0036	do	50	RS	20	N_2	.....	Do.
6	4406	.0036	None	35	None	20	Vacuum	.....	Water, ethanol.
7	4406	.0036	do	60	do	20	do	.....	Water, carbon dioxide, ethanol.
8	4406	.0036	do	100	do	20	do	.....	Water, carbon dioxide, ethanol, carbon monoxide, hydrocarbons.
9	4407	.0016	Vacuum dried	100	RS	20	N_2	0.6	Do.
10	4407	.0016	do	100	None	20	N_2	1.0	Do.
11	4407	.00044	Recast from ethanol, washed in water, dried.	100	do	17	N_2	.....	Do.
12	4409	.00096	do	90	RS	20	N_2	.....	Do.
13	4409	.00102	do	95	None	20	N_2	.....	Do.

was detected and in experiments 4, 5, and 13, in which no carbon monoxide was found.

It is apparent that a large part of the water given off in experiments 1, 2, 6, 7, 8, 11, 12, and 13 is absorbed water. However, the results of experiments 3, 4, 5, 9, and 10 indicate that some of the water is bound more strongly than normally absorbed water, since it was not removed by vacuum drying; the amount appears to be slightly greater for sample 4407 than for sample 4406.

A more detailed analysis of two experiments, 12 and 13, is presented in table 8. More than 15 individual hydrocarbon compounds were detected in each case. The results also indicate that when the proportion of carbon dioxide is high, no detectable quantity of carbon monoxide was found. When carbon monoxide was found, the proportion of carbon dioxide was lower than in the former case. The principal component in the volatile products in all experiments was water. This compound reduces the sensitivity and accuracy of the mass spectrometric analysis markedly and for this reason the hydrocarbons are not reported separately.

TABLE 8. *Mass spectrometric analysis of volatile products obtained in experiments 12 and 13*

Component	Experiment 12, 20 hr ultraviolet	Experiment 13, 20 hr at 95° C
	Mole percent [a]	*Mole percent* [a]
Carbon dioxide	24	71
Ethanol	7	8
Carbon monoxide and nitrogen [b]	63	...
Nitrogen [b]	...	16
Organic compounds, mainly hydrocarbons	6	5

[a] On a water-free basis. The principal component in the volatile products was water.
[b] These experiments were performed in a nitrogen atmosphere.

VI. Pyrolysis

With S. L. Madorsky, S. Straus, and L. A. Wall

Polyamide samples 4407 and 4409 were pyrolyzed at 400° C, the products separated into fractions, and the gaseous products analyzed with the mass spectrometer. These experiments were made (a) to obtain reference patterns to assist in the interpretation of the mass spectrometric analysis patterns of the products obtained on exposure to heat and to ultraviolet radiant energy, and (b) to determine what bonds are broken when nylon molecules are ruptured by heat.

Specimens of nylon samples 4407 and 4409 weighing approximately 40 mg were conditioned at 150° C for 2 hr in a vacuum of about 10^{-6} mm Hg to remove sorbed water and gases. The specimens were then heated to 400° C for 30 min in a vacuum of about 10^{-6} mm Hg and the products fractionated in the apparatus shown schematically in figure 4. The material in the form of sections of thin film about 2 to 5 mm square, was placed on the platinum tray, H, shown in the bottom of the tube on the extreme right and heated by the platinum wire coil, K. A solid residue remaining in the tray was designated fraction I. Most of the volatile fractions condensed on the walls of the heating chamber and on the liquid air condenser, B. The material volatile at the temperature of liquid air (about −190° C) was collected in the gaseous fraction receiver and designated as fraction V. After the pyrolysis, the liquid air was removed from condenser B and replaced with a carbon dioxide–acetone mixture (about −78° C). The volatile fraction was collected at liquid air temperature and designated as fraction IIIA. The carbon dioxide–acetone mixture was then removed and the condenser allowed to come to room temperature (About 25° C). The volatile fraction was also collected at liquid air temperature and designated as fraction IIIB. The waxlike material remaining on the condenser and on the walls of the heating chamber was designated as fractions II and IV, respectively. The apparatus and the procedure are described in more detail in [14]. The results of the analyses are presented in table 9.

TABLE 9. *Results of pyrolyses of polyamides and mass spectrometric analyses of volatile fractions*

Fraction	Product	Weight percentage of original specimen [a]			
		Polyamide 4407		Polyamide 4409	
		Exp. 1	Exp. 2	Exp. 3	Exp. 4
I	Residue; dirty-brown flakes, slightly soluble in warm ethanol.	7.87	5.89	2.09	2.37
II and IV	Semiliquid resinous mass, fairly soluble in warm ethanol.	86.71	88.77	92.87	93.12
IIIA	Volatile at −75° C	1.72	1.80	0.19	0.59
	Carbon dioxide	1.67	1.75	.18	.56
	Hydrocarbons	0.05	0.05	.00	.02
	Methane	.00	.01	.00	.00
	Ethane	.00	.01	.00	.01
	Propane	.00	.01	.00	.00
	Butanes	.00	.00	.00	.01
	Ethylene	.00	.01	.00	.00
	Butenes	.00	.01	.00	.00
	Cyclopentanone	.00	.00	.01	.01
IIIB	Volatile at room temperature	3.48	3.34	4.56	[b] 3.69
	Carbon dioxide	1.48	1.89	4.38	----
	Hydrocarbons	0.39	0.30	0.18	----
	Methane	.00	.00	.02	----
	Ethane	.01	.00	.01	----
	Butanes	.03	.03	.00	----
	Pentanes	.00	.00	.02	----
	n-Hexane	.00	.00	.02	----
	Ethylene	.00	.00	.03	----
	Propene	.07	.05	.00	----
	Butenes	.12	.13	.03	----
	Pentenes	.03	.03	.01	----
	Cyclohexene	.02	.00	.00	----
	Pentadiene	.00	.03	.00	----
	Cyclopentadiene	.00	.02	.00	----
	Benzene	.11	.01	.00	----
	Cyclopentanone	1.61	1.15	.04	----
V	Gaseous fraction	0.22	0.20	[c] .29	.23
	Carbon monoxide	.09	.12	----	.00
	Carbon dioxide	.13	.07	----	.20
	Methane	.00	.01	----	.03
	Summary on dry basis:				
	Carbon monoxide	.09	.12	.00	.00
	Carbon dioxide	3.28	3.71	4.56	----
	Hydrocarbons	0.44	0.36	0.18	----
	Cyclopentanone	1.61	1.15	.05	----
	Water	1.67	1.66	<.1	<.1

[a] On a dry basis, except for percentage of water.
[b] Peaks on mass spectrometer off scale; detailed analysis not possible.
[c] Sample tube broken.

The total amount of products in fractions IIIA, IIIB, and V from nylon samples 4407 and 4409 is about the same, 5 percent (by weight) of the original sample. However, a comparison of the distribution of the amounts of the various compounds among the fractions shows that the degradation of the two types of nylons is not the same, although similar. It is interesting to note that the solid residue obtained with sample 4409 is much less than that obtained with sample 4407. The semiliquid resin obtained with sample 4409 is greater than that obtained with sample 4407. The total solid and semiliquid materials obtained with both samples are not very different.

Sample 4407 produced appreciable amounts of carbon dioxide and cyclopentanone, and smaller amounts of carbon monoxide and hydrocarbons. Sample 4409 produced an appreciable amount of carbon dioxide and no carbon monoxide. The amounts of hydrocarbon and particularly cyclopentanone produced by sample 4409 were appreciably less than those produced by sample 4407.

The production of the cyclopentanone on heating the nylon samples was not expected. However, it is well known [15] that cyclopentanone can be synthesized in high yields by the thermal decomposition of adipic acid in accordance with the following reaction:

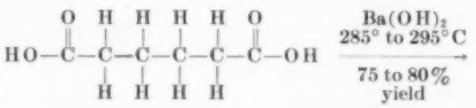

Adipic acid

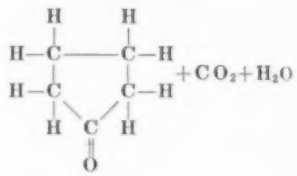

Cyclopentanone
(bp 130.6° C)

A sample of adipic acid was pyrolyzed, and the products formed were analyzed with the mass spectrometer. The pattern obtained matched the pattern of cyclopentanone obtained from the products of the pyrolysis of the nylon samples.

The distribution of the total oxygen in the gaseous products from both polyamide samples is shown in table 10. No significance should be attached to the agreement between the total figures, since it is observed from studying the data of the individual experiments that these results could not be duplicated this closely. The significant point is the difference in distribution of the oxygen between the two polymers.

TABLE 10. *Distribution of oxygen in gaseous products formed on pyrolysis of polyamides*

Source of oxygen	Amount of oxygen in—			
	Sample 4407		Sample 4409	
	Mole percent	*Percentage of total*	*Mole percent*	*Percentage of total*
Carbon dioxide	2.55	16.8	3.33	23.5
Carbon monoxide	0.06	0.4	0.00	0.0
Cyclopentanone	.30	2.0	.01	.0
Water	1.48	9.7	<.09	<.6
Total	4.39	28.9	3.43	24.1

The results of an elemental analysis of the nylon samples presented in table 11 shows that the amount of oxygen absorbed by this polymer is negligible. Consequently, all the oxygen in the volatile products must come from the polymer and water in the polymer.

It is interesting to note that there were no nitrogen compounds in the gaseous fractions as might be expected.

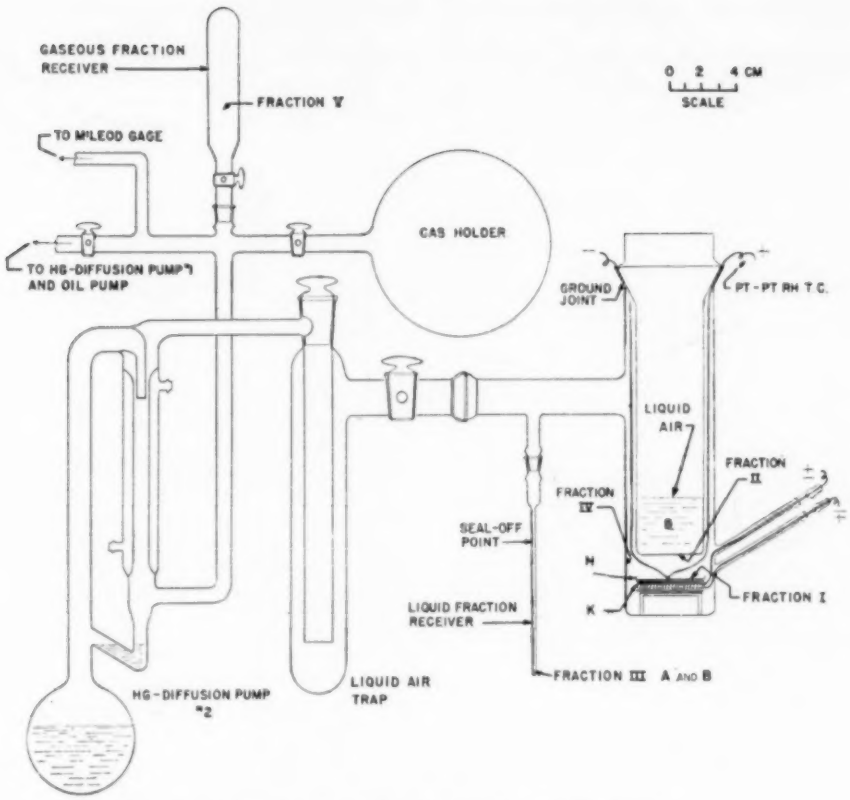

FIGURE 4.—*Molecular still for pyrolysis of high polymers.*

TABLE 11. *Elemental analysis of polyamides*

Sample designation	Source	Elemental analysis			
		Carbon	Hydrogen	Nitrogen	Oxygen
		Percent	*Percent*	*Percent*	*Percent*
4407	Chemical analysis	63.1	9.6	12.1	15.2
	Calculated dry	63.7	9.7	12.4	14.2
	Calculated conditioned [a]	62.1	9.7	12.1	16.1
4409 [b]	Chemical analysis	64.2	10.2	11.4	14.2
	Calculated dry	64.8	10.0	11.8	13.5
	Calculated conditioned [a]	63.2	10.0	11.5	15.4

[a] Water content at 25° C and 50-percent relative humidity assumed to be 2.5 percent of total weight.
[b] Composition estimated to be 60 percent of 66 salt, 20 percent of 610 salt, and 20 percent of caprolactam.

VII. Ultraviolet Spectrometry

With M. J. Reiney and L. A. Dunlap

The ultraviolet transmission characteristics of polyamides 4407 and 4409, subjected to various controlled conditions of heat, ultraviolet radiant energy, and ambient atmosphere, were determined with a model DU Beckman photoelectric quartz spectrophotometer, range 220 to 1,000 mμ.

A critical factor in comparative ultraviolet transmission measurements is the thickness of the specimens. The thicknesses of specimens of sample 4407 were measured; one set of the films was heated in air at 100° C for 20 hr, and another set was exposed to ultraviolet radiant energy from an RS sunlamp for 24 hr at 45° C in a nitrogen atmosphere. The changes in thickness were less than 0.00004 in. The maximum change in ultraviolet transmission that could be attributed to this change in thickness was calculated to be 2 percent at 280 mμ, which is considerably less than the observed changes in ultraviolet transmission.

The ultraviolet transmission curves of untreated films of the polyamides show an absorption band between wavelengths of 260 and 330 mμ with maximum absorption at approximately 280 mμ (figs. 5, 6, 7). Transmission in this region is increased by exposure to ultraviolet radiant energy, as shown by curve B of figures 5 and 6. The greater portion of the absorption band is eliminated during the first hour of exposure to the ultraviolet radiant energy and the band is entirely eliminated after exposure for 20 hr. Heat alone tends to decrease the over-all transmission of the films, although the shape of the

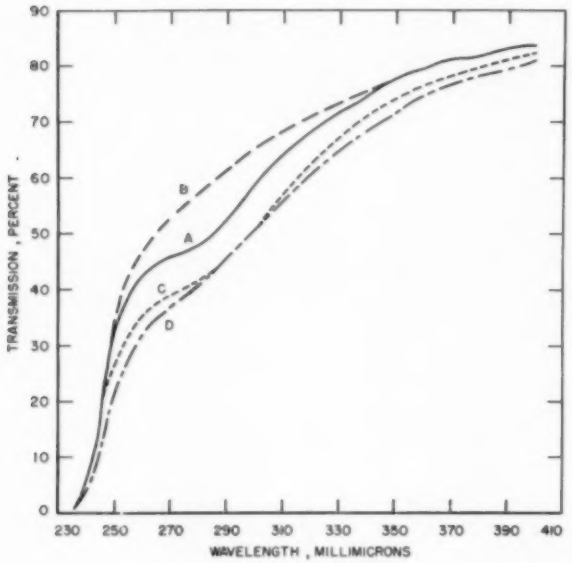

FIGURE 5. *Ultraviolet transmission of polyamide 4407 before and after exposure to ultraviolet radiant energy and/or heat.*

A, Untreated 4407; B, after 20-hr exposure to ultraviolet at 50° C in nitrogen; C, after 20 hr at 95° C in air oven; D, after 20-hr exposure to ultraviolet at 50° C in nitrogen and 20 hr at 95° C in air oven.

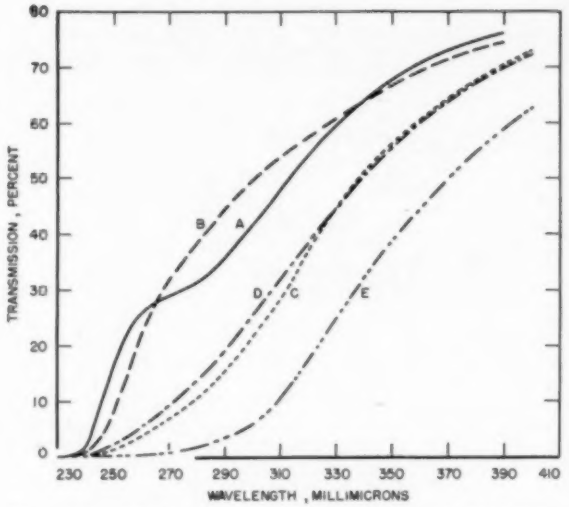

FIGURE 6. *Ultraviolet transmission of polyamide 4409 before and after exposure to ultraviolet radiant energy and/or heat.*

A, Untreated 4409; B, 25-hr exposure to ultraviolet at 40° C in nitrogen; C, after 20 hr at 100° C in air oven; D, after 25-hr exposure to ultraviolet radiant energy at 40° C in nitrogen and 20-hr heat at 100° C in air oven; E, after 95-hr heat at 100° C in air oven.

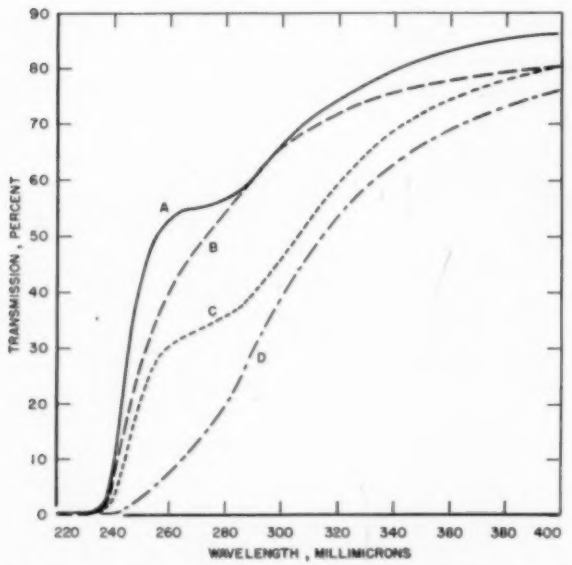

FIGURE 7. *Ultraviolet transmission of polyamides 4407 and 4409 before and after 120-hr accelerated weathering.*

A, Untreated 4407; B, 4407 after accelerated weathering; C, untreated 4409; D, 4409 after accelerated weathering.

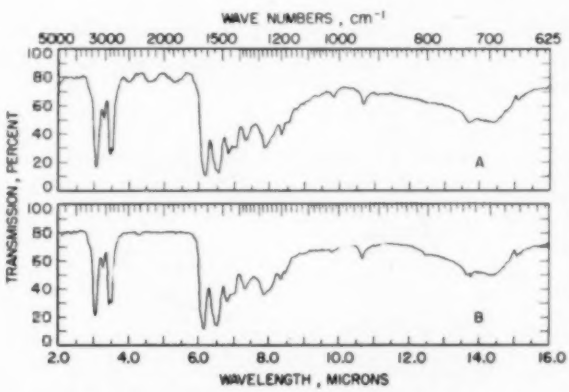

FIGURE 8. *Infrared transmission of untreated polyamides 4407 and 4409.*

A, 4407, 0.0008 in. thick; B, 4409, 0.0009 in. thick.

curve for sample 4407 is not changed, as shown in curve C of figure 5. Treatment with ultraviolet radiant energy followed by heating results in an ultraviolet curve representative of the effects of both treatments, as shown by curve D of figures 5 and 6.

Specimens of nylon samples were subjected to a 120-hr accelerated weathering test. The effects of this treatment, shown in figure 7, are similar to the combined effects of separate exposures to ultraviolet radiant energy and to heat. The decrease in transmission in sample 4409 is much greater than that in sample 4407.

After 3 weeks at room conditions, treated specimens of sample 4407 showed changes of less than 1 percent in ultraviolet transmission values from those made immediately after the treatments.

Experiments were made with samples 4407 and 4409 to determine the effect of absorbed water and ethanol on the ultraviolet transmission characteristics. Immersing specimens in water at 60° C for 72 hr caused the absorption band for sample 4407 to become stronger at approximately 280 mμ and had no appreciable effect on the absorption for sample 4409. The wet specimens were subjected to vacuum drying at 40° C for 22 hr, which caused a slight decrease in the transmission of both samples; the absorption band for sample 4407 became more pronounced and that for sample 4409 remained about the same shape. The dried specimens were next immersed in 95-percent ethanol for 17 hr, which resulted in a marked increase in transmission for both samples; the shape of the curve for sample 4407 remained about the same, and the absorption band for sample 4409 became more pronounced.

Exposure to ultraviolet radiant energy for 2.5 hr was nearly sufficient to remove the absorption band for both the untreated specimens of samples 4407 and 4409 and specimens soaked in water for 72 hr or in ethanol for 17 hr.

Specimens of samples 4407 and 4409 that had been exposed to 20 hr of ultraviolet radiant energy were immersed in water and in ethanol, respectively, for 72 hr. The absorption band in the curves for the untreated specimens did not return. Even films recast from ethanol solutions of specimens that had been exposed to 20 hr of ultraviolet radiant energy did not show the absorption band.

No differences were observed in the results of experiments conducted in oxygen and nitrogen, respectively.

VIII. Infrared Spectrometry

With M. J. Reiney and E. K. Plyler

Recast polyamide films were subjected to heat and to ultraviolet radiant energy and the infrared transmission characteristics measured before and after exposure to determine changes in chemical structure. A change of at least 2 percent in the amount of a chemical group is required for detection by the infrared spectrometers used in this investigation. Recast films were used for this phase of the investigation because the original films were too thick to distinguish individual characteristic transmission bands.

Typical infrared transmission curves obtained with a Baird recording spectrophotometer are shown in figure 8. Curves A and B show that polyamide samples 4407 and 4409 give essentially the same infrared transmission, although there is a difference in the number of methylene groups in the repeating units of the polymer chain.

Treatment of the polyamide films by heating and by exposure to RS sunlamp radiant energy for various periods up to 2 weeks in the presence of air and in nitrogen produced no extensive changes in the infrared spectrum of the films, that is, no new bands were created or former bands destroyed as a result of the treatments. Slight decrease in absorption at 3.2μ suggested possible changes in intermolecular bridging in some experiments; but the slight changes observed were considered to be within experimental error.

Specimens were exposed for periods of 120 hr and 217 hr to accelerated weathering. The 217-hr test consisted of 179 hr of exposure to ultraviolet radiant energy and 38 hr of exposure to fog. The test was stopped at 217 hr because the films were water spotted, had white spots of undetermined origin, and were split. No changes in appearance were observed in the 120-hr test. The infrared spectrum after 217-hr exposure showed that no appreciable changes in chemical structure occurred as a result of this treatment. The slight decrease in transmission observed between 2.8 and 16.0μ is attributed to experimental error.

Specimens of sample 4407 were exposed outdoors for 2 months (Feb. to Apr.). At the end of this period, the films were torn, the surfaces were badly scarred, and particles of dirt were imbedded in the film. The specimens were dissolved in warm ethanol, the solution centrifuged to remove the dirt particles, and recast films made by the usual technique. No appreciable changes occurred in chemical structure as a result of this treatment.

The results obtained with nylon sample 4409 parallel very closely those observed with nylon sample 4407. It was observed in the accelerated weathering treatment that the splitting of the films of sample 4409 was more severe than the splitting of the films of sample 4407.

Film specimens of the polyamide samples were soaked in ethanol, removed, and allowed to dry in air, and the infrared transmission characteristics measured. No appreciable changes from the original films were observed.

IX. Viscosity

With C. C. Chang, N. Dominguez, and S. G. Weissberg

Polyamide sample 4410 was subjected to controlled conditions of heat, ultraviolet radiant energy, and relative humidity, and to outdoor exposure and the degradation of the polymer chains determined from the measurement of the viscosities of dilute solutions of the exposed nylon specimens in *m*-cresol. This

procedure can be used to determine whether or not the polymer chains are broken or crosslinked but will not reveal any other changes in chemical structure [2, 5]. The viscosities of the solutions were measured at 30° C, using calibrated Ostwald-Fenske viscometers [16, 17]. Duplicate parallel runs were made, using the average of five efflux time measurements determined to the nearest 0.1 sec.

The viscosity data for the various nylon specimens are presented in table 12 and figures 9 to 11, inclusive. Not enough data were obtained on the treated nylon specimens to determine the curvatures of the plots of $(\ln \eta_r)/c$ versus c and of η_{sp}/c versus c. Since these plots for the untreated specimens show distinct curvature, the plots have been drawn as curved lines, as shown in figures 10 and 11, simply to indicate the general tendency, but they are by no means representative of the exact shape of the plots.

The relation between the intrinsic viscosity of polyamide sample 4410 and the time of exposure to heat and to ultraviolet radiant energy is shown in figure 12. This shows that the viscosity is decreased as the period of exposure to the degradation conditions is increased.

A study of the moisture sorption of nylon samples 4406, 4407, 4408, 4409, and 4410 showed that at 50-percent relative humidity the films contained 2 to 3 percent of water. The data observed for the materials used in this study do not show increased water sorption with decreased crystallinity. However, the levels of crystallinity were not determined experimentally, and these results may be indicative of a balancing factor in the changing total concentration of polar groups. It has been reported that for a given concentration of dipoles of a certain type increase in crystallinity markedly decreases moisture sorption in polyamides [18, 19]. As these types of nylon with varying compositions and degrees of crystallinity all contain between 2 and 3 percent of water in equilibrium with a relative humidity of 50 percent, and as a reduction in the water content of approximately 2 percent causes the film to become brittle, it is reasonable to assume that treated specimens that remain intact have water contents of the same order of magnitude.

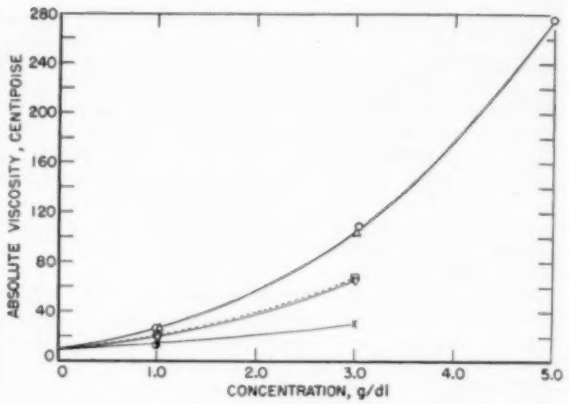

FIGURE 9. *Relation between absolute viscosity and concentration of solutions of polyamide 4410.*

△, A-1, Undegraded, specimen 1; ○, A-2, undegraded, specimen 2; ▽, B, 22-hr ultraviolet; ◑, C, 168-hr ultraviolet; □, D, 25 hr at 105° C; X, E, 169 hr at 105° C; □, F, 2 months outdoors; curves D and F are identical.

It is interesting to examine the consequences of a hypothesis that the lower relative viscosities of specimen B, as compared with solutions of specimen A, are due solely to an increase in water content of B, as compared with the water content of A. Calculation shows that specimen B would require 30-percent moisture to give the results obtained. Therefore, the hypothesis that the lowered viscosity is due only to an increase in water content of the degraded nylon requires an unreasonably high water content.

These results indicate that the effect of water content in the viscosity study is negligible and recalculation of the viscosity results to correct for moisture content is unnecessary.

TABLE 12. *Viscosity data for solutions of polyamide 4410 in m-cresol*

Specimen designation	Treatment	Concentration of solution	Absolute viscosity, η	Relative viscosity, η_r	Inherent viscosity, $\ln \eta_r/c$	Specific viscosity, η_{sp}	Reduced specific viscosity, η_{sp}/c	Intrinsic viscosity [a]		Viscosity average molecular weight, [b] $\overline{M}_v$
								$[\eta]$	Average $[\eta]$	
		g/dl	*cp*		*dl/g*		*dl/g*	*dl/g*	*dl/g*	
m-Cresol			8.67	1.00						
A-1	None	1.032	26.8	3.10	1.09	2.10	2.03	1.33		
		3.009	103.	11.8	0.821	10.8	3.60	1.28		
A-2	do	0.998	26.5	3.06	1.12	2.06	2.06	1.32		
		3.036	108.	12.5	0.831	11.5	3.78	1.30	1.31	16,300
		4.988	276.	31.8	.694	30.8	6.17	1.30		
B	Ultraviolet, 22 hr	1.006	20.3	2.34	.845	1.34	1.33	0.98	0.97	10,800
		3.001	66.1	7.62	.677	6.62	2.21	.97		
C	Ultraviolet, 168 hr	0.984	12.9	1.49	.403	0.486	0.495	.43	.43	3,500
D	105° C, 25 hr	1.014	21.2	2.44	.880	1.44	1.42	1.03	1.00	11,200
		3.005	67.6	7.80	.683	6.80	2.26	0.98		
E	105° C, 169 hr	1.020	14.8	1.71	.527	0.711	0.698	.58	0.56	5,000
		2.997	31.6	3.64	.432	2.64	.882	.54		
F	Outdoors, 2 mo	1.011	21.2	2.44	.884	1.44	1.43	1.03	1.01	11,400
		2.987	67.8	7.82	.689	6.82	2.28	0.99		

[a] The intrinsic viscosities were calculated as $3(\eta_r^{1/3}-1)/c$, where η_r is the relative viscosity and c is the concentration in g/dl.

[b] Estimated viscosity average molecular weight [66] based on the applicability of Taylor's equation and on the use of a different solvent, since the value for intrinsic viscosity depends on the solvent [67]

$\overline{M}_v = 13{,}000\ [\eta]^{1.39}$; $0.9[\eta]$ m-cresol $= [\eta]$ formic acid

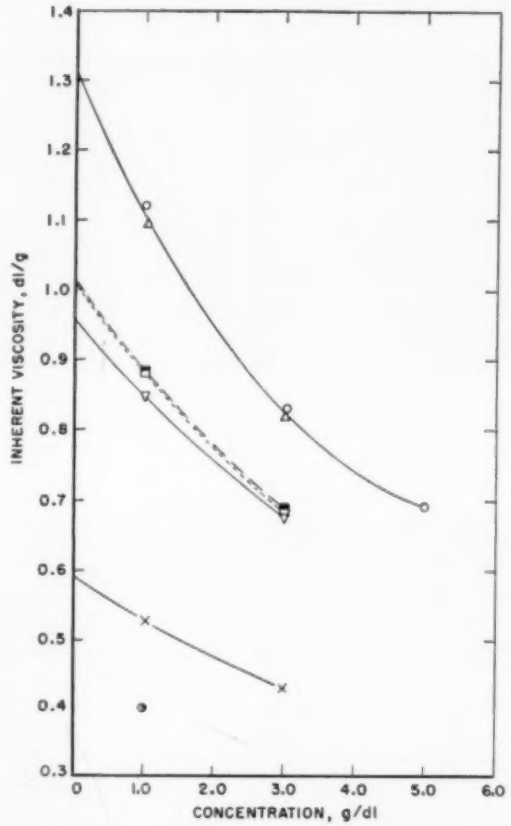

FIGURE 10. *Relation between inherent viscosity and concentration of solutions of polyamide 4410.*

△, A-1, Undegraded, specimen 1; ○, A-2, undegraded, specimen 2; ▽, B, 22-hr ultraviolet; ◑, C, 168-hr ultraviolet; □, D, 25 hr at 105° C; X, E, 169 hr at 105° C; ■, F, 2 months outdoors.

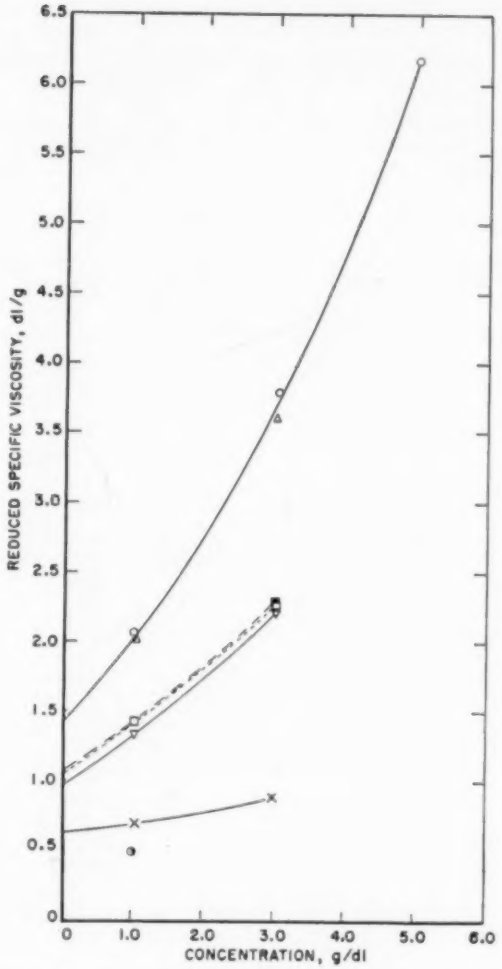

FIGURE 11. *Relation between reduced specific viscosity and concentration of solutions of polyamide 4410.*

△, A-1, Undegraded, specimen 1; ○, A-2, undegraded, specimen 2; ▽, B, 22-hr ultraviolet; ◑, C, 168-hr ultraviolet; □, D, 25 hr at 105° C; X, E, 169 hr at 105° C; ■, F, 2 months outdoors.

X. Light Microscopy

With C. P. Saylor

The changes in films of polyamides as a result of exposure to natural and accelerated weathering were studied with a microscopical technique. Photomicrographs of untreated and treated samples 4406, 4407, 4408, 4409, and 4410 were taken. Samples 4407 and 4409 were studied in greater detail to differentiate the two types and to compare their relative resistance to aging.

A petrographic microscope was used to examine the film specimens. Photomicrographs were taken under crossed nicols at magnifications of × 600 and × 950 (oil immersion lens), using a camera arrangement with a filament type lamp as the light source. Unless otherwise stated, a ground glass plate was used in the illuminator during the photographing. The heated specimens were exposed in a vacuum oven, "cracked" with dry air, at 87° C.

A series of photomicrographs of specimens of nylon samples 4407 and 4409 before and after exposure to an accelerated weathering treatment and outdoors is shown in figure 13. These photographs were taken at a magnification of × 600 with crossed nicols at extinction. No ground glass was used in the illuminator.

The photomicrograph of an unexposed specimen of sample 4407 is shown in plate A of figure 13. The grain structure of sample 4407 is smaller than that of sample 4409, as comparison of plates A and C shows. The specimen of sample 4407 that was exposed to the 120-hr accelerated weathering test is shown in plate B. The dark spots, in this case, are attributed to dirt particles attracted by static charge to the surface of the film, or imbedded in the film. These films develop considerable charge when rubbed

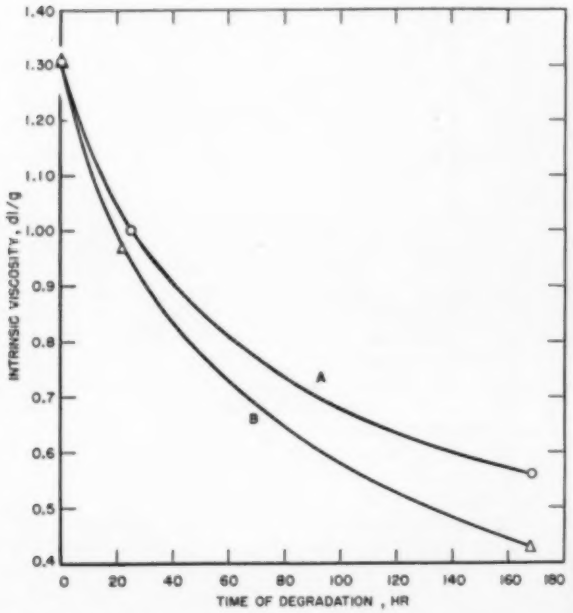

FIGURE 12. *Effect of degradation conditions on intrinsic viscosity of polyamide 4410.*

A, Heated in air oven at 105° C; B, irradiated with ultraviolet from S-1 in air at 60° C. Value of intrinsic viscosity of sample weathered outdoors for 2 months was 1.01 dl/g.

with a cloth. Both dark and bright lines are observed in plate B. This is a result of the orientation of the specimen under the crossed nicols. These lines become alternately dark and bright as the stage of the microscope is rotated, thus changing the orientation of the film under the crossed nicols.

Comparison of plates C and D in figure 13 shows the effect of exposure of specimens of sample 4409 to the 120-hr accelerated weathering test. The density differences in the photomicrographs are not relevant in this series. Bright lines are shown to be dominant in the exposed specimens, particularly after outdoor exposure. Photomicrographs of a specimen of sample 4409 that was exposed outdoors for 2 months are shown in plates E and F. Photomicrograph F was taken with a first-order retardation plate.

At first it was thought that the bright lines in plates E and F in figure 13 were caused by scratches on the surface resulting from dirt particles being blown across the surface. However, two later observations tend to throw doubt on this hypothesis: (1) Where samples have been cut by scissors, a bright band appears between crossed nicols. This brightness is much greater than appears at any unaltered part of the original film. It is caused by deformation and flow within the film so that the two directions parallel and perpendicular to the cut edge are no longer nearly equal in refractive index. The interference figures on these edge zones indicate extremely rapid changes in molecular orientation within short dis-

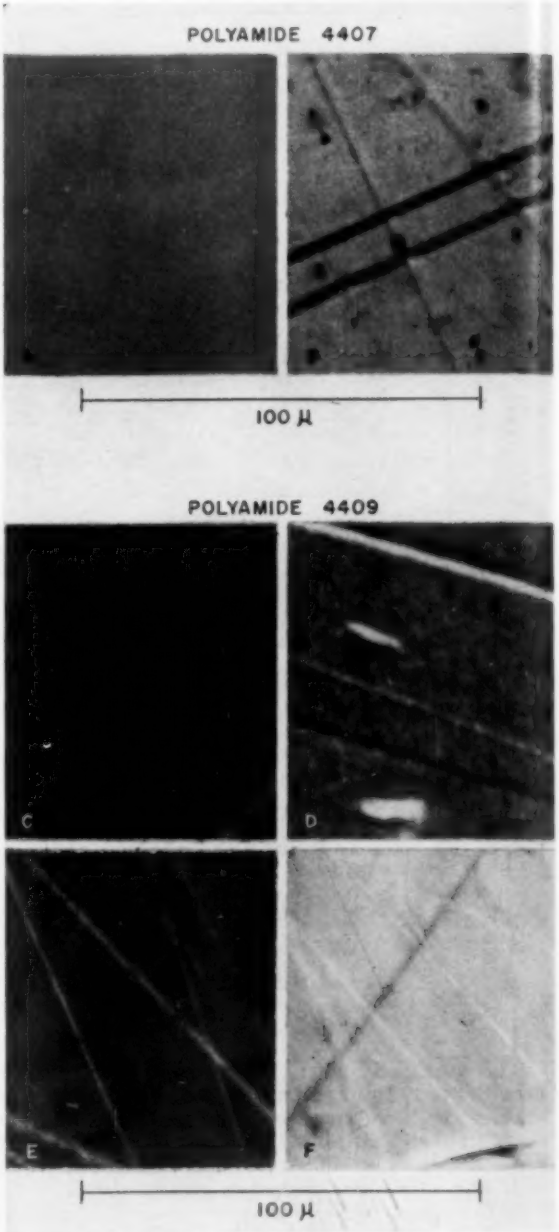

FIGURE 13. *Photomicrographs (×600, crossed nicols) of polyamides 4407 and 4409.*

4407: A, untreated film; B, after 120-hr accelerated weathering test. 4409: C, untreated film; D, after 120-hr accelerated weathering test; E, after 2 months' outdoor exposure; F, after 2 months' outdoor exposure (first-order retardation plate).

tances. A somewhat similar effect is shown in the specimen of 4409, which was exposed on the roof. There are stripes on the surface with apparently greater birefringence than the main area of film. This is particularly true when the objective has a small aperture. Interference figures show that these stripes are places where the orientation of the molecules within the plane of the film has been disturbed. (2) Similar bright lines were observed in photomicrographs of untreated specimens (see plate C), and in those which had been exposed to the accelerated weathering test. However, these bright lines appeared to be more dominant in the exposed specimens. These lines may have been caused by slight abrasion (and hence deformation) of the surface, by strains from shrinkage of the film, or by mechanical distortion.

It is stated in the literature [20] that when molten nylon 66 polymer is cooled slowly large spherulites are formed that are visible with a microscope. These spherulites show a characteristic cross shape under crossed nicols. An optically clear material is obtained when the molten polymer is cooled rapidly. The spherulites disappear when the polymer is heated above 250° C and are elongated into cylinders on drawing. No formations resembling spherulites as found in rubber [21] and in polyhexamethylene adipamide [22] were found in the nylon films, untreated or treated, used in this investigation.

Another series of photomicrographs of specimens of samples 4406, 4407, 4408, 4409, and 4410 is shown in figure 14. These photomicrographs were taken with an oil immersion lens at a magnification of ×950 under crossed nicols at maximum brightness. All variable factors such as light intensity, exposure time, temperature of the developer, etc., which would affect the apparent brightness of the final photomicrographs, were kept as constant as possible. No ground glass was used in the illuminator to take the photographs of samples 4409 and 4410 because

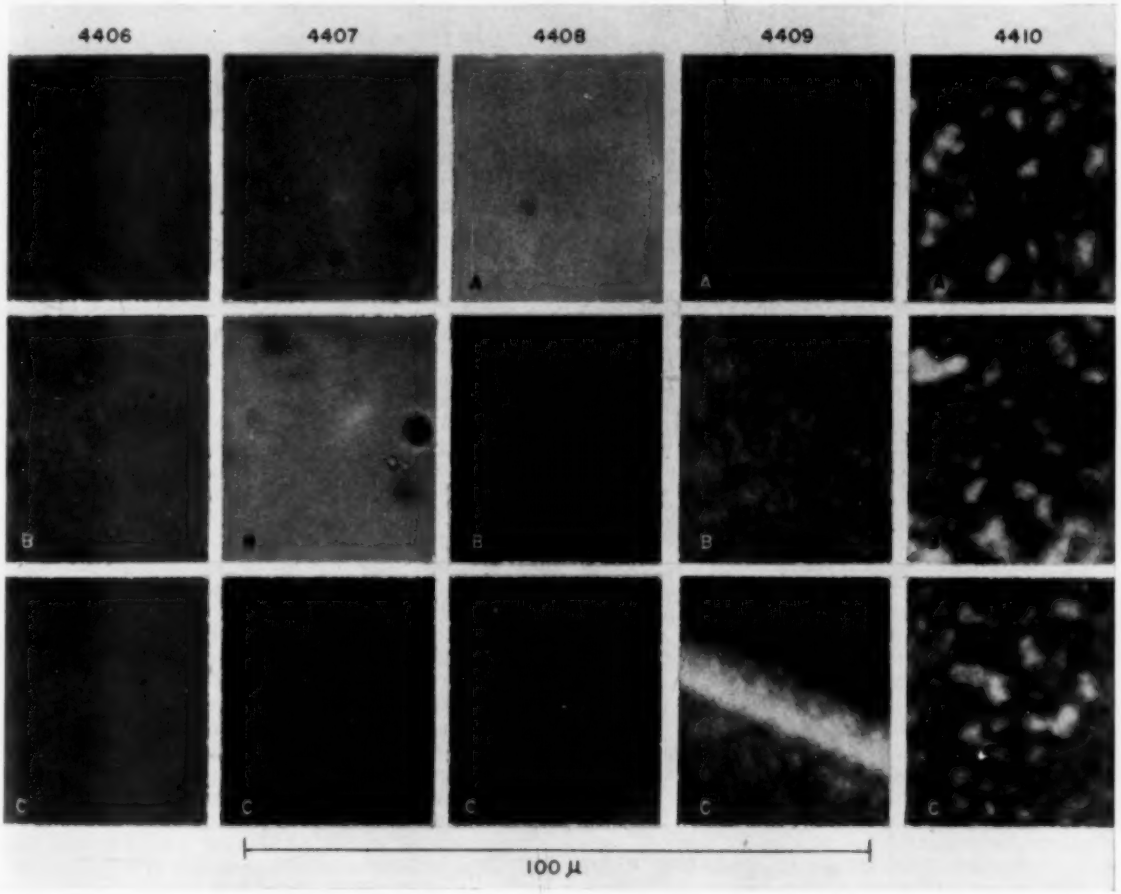

FIGURE 14. *Photomicrographs (× 950, crossed nicols) of polyamides.*

A Series, untreated film; B Series, after 2-months outdoor exposure; C Series, after exposure to S-1 sunlamp radiant energy.

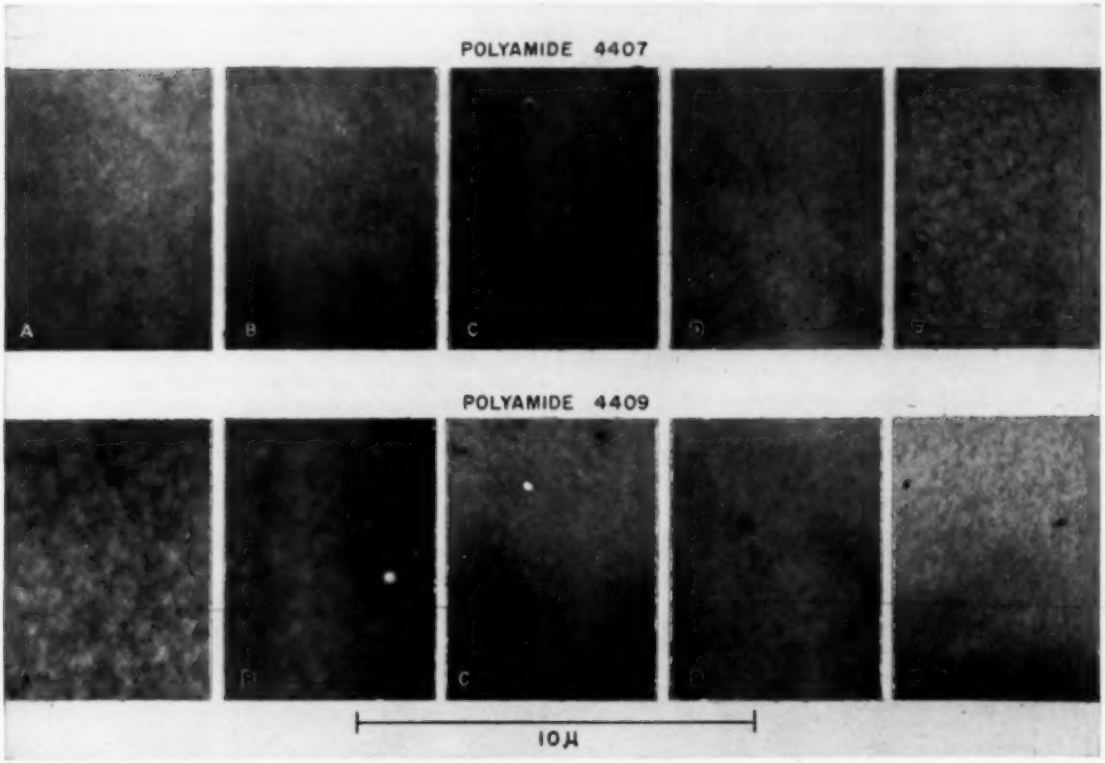

FIGURE 15. *Electron micrographs of unshadowed specimens of polyamides 4407 and 4409.*

A, Untreated; B, after 168-hr ultraviolet (S–1); C, after 336-hr ultraviolet (S–1); D, after 168 hr at 100° C in air oven; E, after 336 hr at 100° C in air oven.

these films were relatively quite dark even at maximum brightness. The exposure time for sample 4410 was 0.5 min instead of 1 min as used for the others. As more crystalline materials appear brighter under crossed nicols, it was hoped that the comparative brightness of the specimens in the photomicrographs would give some conception of the comparative degree of crystallinity.

The photomicrographs of the untreated specimens are shown in series A in figure 14. All the specimens of these samples are anisotropic. As the stage of the polarizing microscope was rotated, the dark areas changed to bright and vice versa. A marked difference in brightness is observed. Nylon sample 4408 is much brighter than 4409 by comparison. Nylon sample 4410 has no actual maximum brightness, as revolving the stage of the microscope merely reversed the dark and bright areas that are numerically almost equal.

Photomicrographs of the specimens exposed outdoors for 2 months are shown in series B of figure 14. Differences in maximum brightness are shown for nylon samples 4407 and 4408. Nylon sample 4408 appears much darker under crossed nicols, while sample 4407 appears somewhat brighter. The tendency toward generally increased brightness in samples 4406, 4409, and 4410, shown in the photomicrographs, is not great enough to warrant consideration. In nylon sample 4410, however, areas of increased brightness such as those that appear in the lower portion of the photomicrograph are observed. Dark spots are exhibited particularly in samples 4406 and 4407. Similar spots are observed in untreated specimens (see samples 4407 and 4408, series A of fig. 14) and appear to be present in greater quantity in exposed specimens.

Photomicrographs of the specimens exposed to radiant energy from an S–1 sunlamp at 60° C for 186 hr are shown in series C of figure 14. Samples 4406, 4407, and 4408 are much darker under crossed nicols. In general, sample 4409 appears darker as seen in the upper section of the photomicrograph. The bright line was photomicrographed to show the appearance of this type of area in nylon sample 4409. Nylon sample 4410 again shows no extensive change that is visible under the crossed nicols.

A closer comparative examination of nylon samples 4407 and 4409 was made with a petrographic microscope. Specimens of each sample, in the original condition, after exposure on the roof, after 68 hr at 87° C, and after 168 hr of exposure to ultraviolet radiant energy from an S–1 sunlamp at 60° C were

studied and the results compared. These specimens were stored at 50-percent relative humidity and 25° C after treatment. In all instances the specimens are optically negative with the acute bisectrix approximately normal to the film except in small areas. The significance of this is that the long axes of the molecules tend to be more or less parallel to the surface of the film. The orientation as between length and breadth of the film is slight as compared to the tendency to be parallel to the surface of the film. Sample 4407 exhibits a greater optic axial angle than sample 4409. Since the plane of the optic axes is parallel to neither of the edges of the film, this must be construed as accidental rather than as a result of strains introduced during formation of the film.

XI. Electron Microscopy

With M. Swerdlow and M. J. Reiney

Polyamide samples 4407 and 4409 were examined by an electron microscopic technique before and after exposure to ultraviolet radiant energy and to heat to determine any changes in structure resulting from these treatments. It was established that titanium dioxide, a delusterizing agent for nylon that would interfere with the electron microscope examination, was not present in these samples [23]. The film specimens were prepared by the dipping technique described in section II.

Four slides each of nylon samples 4407 and 4409 were selected on the basis of uniformity, thickness, and cleanliness with the aid of a light microscope. Two of the coated screens were removed from each slide, one for examination of the unexposed material and the other for electron diffraction work. The glass slides with the remaining three coated screens were exposed to ultraviolet radiant energy and to heat at 100° C. One slide of each sample was exposed to the ultraviolet radiant energy from an S–1 sunlamp for 168 hr and another set for 336 hr. The distance between the bulb and the specimens was 6 in., and the temperature of the specimens was about 60° C. The exposure to heat was made in a circulating-air oven at 100° C. One slide of each sample was exposed for 168 hr and another for 336 hr.

An RCA type EMU transmission electron microscope with an accelerating voltage of 50 kv and an operating pressure of less than 10^{-4} mm Hg was used to examine the specimens. Representative areas were selected and micrographs were taken at an exposure of about 10 sec. All the electron micrographs were taken at about 6,000 diameters under constant conditions except that the beam current intensity had to be altered slightly because of variation in film thickness between samples. Shadow casting was done in an RCA type EMV vacuum unit at a pressure not higher than 10^{-4} mm Hg.

Figure 15 shows a series of micrographs of the surfaces of nylon samples 4407 and 4409. These surfaces were not shadowed with chromium. Specimen A of each sample gives a view of the surface that is representative of the unexposed films. Specimens B and C are representative of the specimens exposed to the ultraviolet radiant energy. Specimens D and E are representative of the specimens exposed to heat in air at 100° C. A definite grain structure is shown in all the specimens. No definite changes in the structure of the surfaces of these specimens are observed.

The effect of shadowing in emphasizing the surface detail by increasing the contrast, resulting from the oblique deposition of a thin layer of chromium, is shown in figure 16. The small spherical pieces of dirt shown in these micrographs indicate the appearance of an elevated portion of the surface and its shadow.

Shadowed unexposed specimens of sample 4407 are shown in figure 16. The more crystalline appearance of specimens A and D may be a result of the film-making procedure. The slower the film cools, the greater the degree of molecular orientation. A comparison of the views of the specimens of sample 4407 before and after treatment with ultraviolet radiant energy and with heat shows that exposure to ultraviolet radiant energy appears to increase the degree of molecular orientation, whereas exposure to heat has very little effect.

The shadowed untreated and treated specimens of sample 4409 are also shown in figure 16. Sample 4409 appears to have a larger grain structure than sample 4407. However, the grain structure of the specimens of sample 4409 varies considerably. The exposure to ultraviolet radiant energy and to heat appears to have little effect on the surface structure of sample 4409 when examined with the electron microscope. The effect of shadow casting with chromium is shown quite markedly in view H′ of figure 16; the right-hand part of H′ was shielded by a large foreign particle and is unshadowed, while the left-hand part is shadowed with chromium.

The very thin films used in this part of the work did not develop the amount of splitting observed in the tests in which the original films were exposed to ultraviolet radiant energy. Splitting of the films of sample 4407 was observed with the electron microscope in a few isolated instances, but this was the exception and not the rule. The splitting observed with these thin films was in the top layer only; the film appeared to be laminated, with the top layer split and the bottom one intact. The splitting observed with the films in the original thickness was the usual type in which the split was completely through the film.

XII. Electron Diffraction

With M. Swerdlow and M. J. Reiney

Samples 4407 and 4409 were examined by electron diffraction technique to determine any changes that may have occurred as a result of exposure to ultraviolet radiant energy and to heat.

The diffraction stage of an RCA type EMU electron microscope was used to make transmission electron

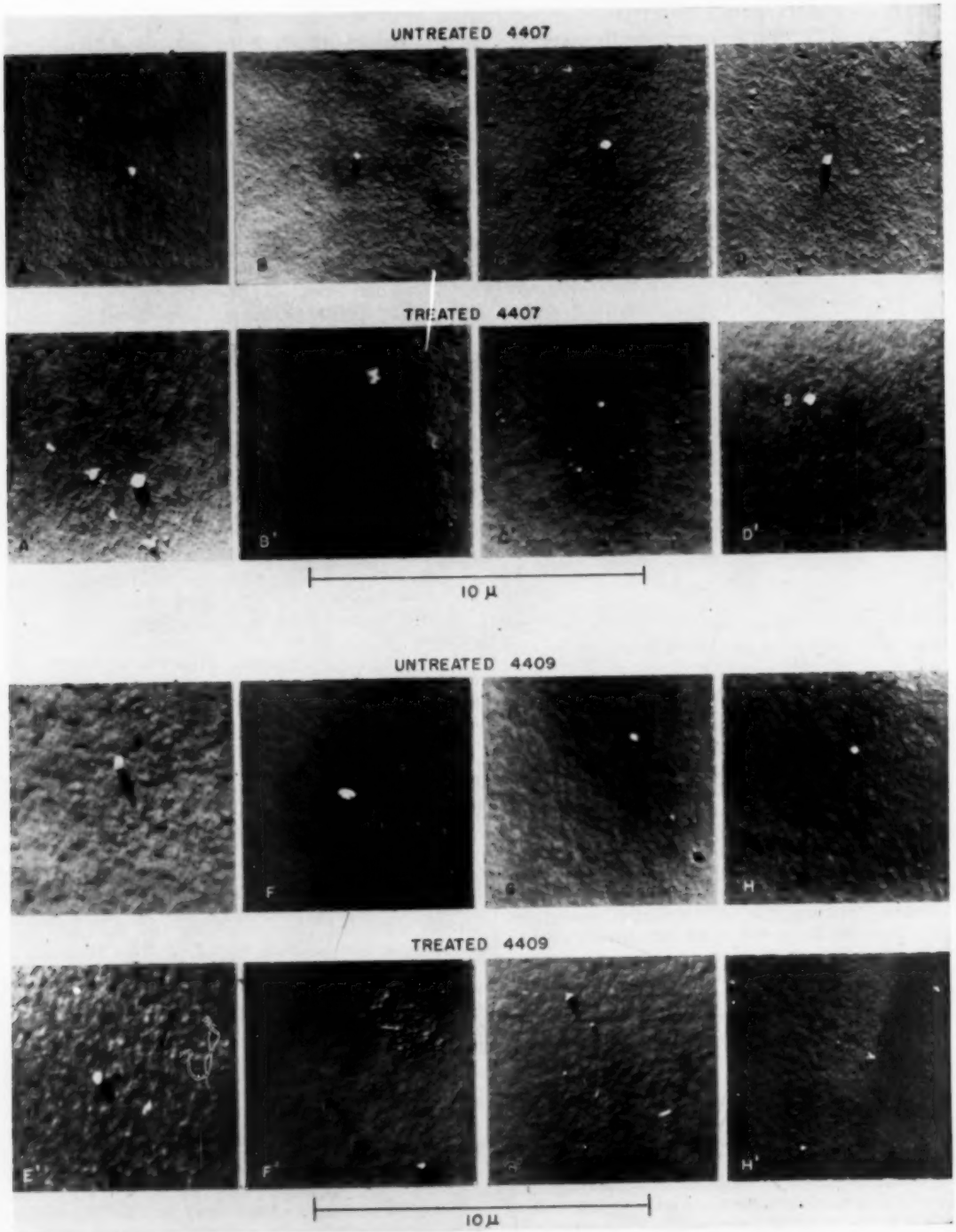

FIGURE 16. *Electron micrographs of chromium shadowed polyamides 4407 and 4409.*

A′ and E′, Sample of A and of E after 168-hr ultraviolet (S–1); B′ and F′, sample of B and of F after 336-hr ultraviolet (S–1); C′ and G′, sample of C and of G after 168 hr at 100° C in air oven; D′ and H′, sample of D and of H after 336 hr at 100° C in air oven.

diffraction patterns of unexposed and exposed specimens of the samples. Electron diffraction is especially suitable for the study of the structure of thin surface layers and films. The electrons are diffracted much the same way X-rays are by crystalline materials [24]. The thickness of films that can be used with this technique is limited because electrons are scattered a million times more effectively than X-rays. The average thickness of the nylon films used was 0.4 $\pm$0.1 μ as determined by an interferometer. The films were made and mounted on screens according to the procedure described in section II.

The electron diffraction patterns of samples 4407 and 4409 showed several diffuse rings. The interplanar spacings in angstrom units that were determined by comparison of the negative with a secondary standard are presented in table 13.

TABLE 13. *Electron diffraction spacings of polyamides* [a]

Sample	Diffraction ring	Interplanar spacings, in angstrom units				
		A	*B*	*C*	*D*	E_a
4407 (untreated)	1	25.15	23.89	11.95	11.95	25.15
	2	3.98	3.95	3.59	4.16	4.23
	3	2.09	2.13	2.06	1.97	2.02
	4	.....	.....	1.18	1.11	.....
		A'	*B'*	*C'*	*D'*	E'_a
4407 (treated)	1	9.75	12.91	9.19	11.38	10.86
	2	4.08	3.89	3.85	3.92	4.02
	3	1.95	1.99	2.03	2.06	1.97
	4	1.67	1.16	1.09	.....	1.16
		A	*B*	*C*	*D*	D_a
4409 (untreated)	1	13.65	11.95	10.86	9.18	10.84
	2	4.02	3.92	4.27	4.12	4.16
	3	2.07	1.97	1.88	2.16	2.11
	4	1.08	1.096	1.11	1.99	1.15
		A'	*B'*	*C'*	*D'*	D'_a
4409 (treated)	1	9.75	10.39	9.75	10.17	8.69
	3	3.95	3.82	3.79	3.73	4.12
	3	1.89	1.96	1.99	1.87	2.04
	4	1.12	1.10	1.12	1.13	1.12

[a] The patterns with a subscript *a* were made with an exposure of 7 sec; all other exposures were 15 sec.

XIII. X-Ray Diffraction

With H. E. Swanson

The X-ray diffraction patterns of samples 4407 and 4409 were obtained before and after specimens were exposed to outdoor and accelerated weathering treatments to determine whether or not these treatments cause any changes in structure that might be revealed by this techinque.

The X-ray patterns were obtained with a Philips X-ray spectrometer with various modifidations. $CuK_{\alpha 1}$ radiation at 40 kv and 15 ma was used. The spacings listed in table 14 were obtained by diffraction of the X-ray beam from the surface of the films. Penetration X-ray patterns were taken on photographic film 2 cm from the pinhole used to collimate the beam. The polyamide specimen was placed over the pinhole, which was 0.025 in. in diameter.

TABLE 14. *Spacings from X-ray reflection measurements with polyamides*

Nylon sample	Treatment	Film thickness	Observed spacings in X-ray measurements			
		in.	*A*	*A*	*A*	*A*
4407	None	0.0016	3.8	4.3	6.8	[c] 11.0
	Exposed outdoors	.0016	3.8	4.4	6.9	.....
	Exposed to 120-hr ultraviolet fog cyclic [b]	.0016	3.9	4.4	7.2	[c] 11.0
	Exposed to 217-hr ultraviolet-fog cyclic [b]	.0081	[c] 3.8	.....	.....	.....
4409	None	.0023	3.9	4.3	7.5	[c] 11.0
	Exposed outdoors	.0023	3.9	4.4	7.0	.....
	Exposed to 120-hr ultraviolet-fog cyclic [b]	.0023	3.9	4.4	7.1	[c] 11.0
	Exposed to 217-hr ultraviolet-fog cyclic [b]	.0092	3.8	[d] 4.4	.....	.....

[a] Very diffuse, low peak.
[b] Method No. 6021 of Federal Specification L–P–406a.
[c] Very weak, poor pattern.
[d] Poor pattern.

The X-ray patterns of samples 4407 and 4409 showed that there is a very slight molecular orientation in sample 4407 and none in sample 4409. Sample 4407 appeared to be more crystalline than sample 4409. No differences in degree of molecular orientation were observed in the unexposed and exposed specimens of either sample.

Four X-ray spacings were observed with the Geiger-counter spectrometer at approximately 3.8, 4.3, 7, and 11 A. A high concentration of polar bridges along the polyamide chains has been associated with extended chain configurations having the calculated length per repeating unit and side spacings of 3.7 and 4.4 A, respectively [25]. Even though the X-ray patterns showed no molecular orientation for sample 4409, the presence of the spacings at 3.8 and 4.3 A indicates that there is some degree of crystallinity [20].

The results of the tests indicate that the 4.3-A spacings are stronger when the nylon sample is penetrated at right angles by the X-rays. This indicates a perpendicular position to the plane of the film. The 3.8-A spacing appears to be more in the plane of the film.

If nylon sample 4409 were completely amorphous, a 4.18-A spacing observed by Baker and Fuller [25] in quenched polyamides would be expected. It appears that there is some crystallinity in both samples 4407 and 4409 and that sample 4407 is more crystalline than sample 4409.

XIV. Electrical Properties

With A. H. Scott

The dielectric constant and dissipation factor of nylon samples 4406 and 4407 were measured before and after exposure to ultraviolet radiant energy to determine whether or not these properties changed sufficiently to indicate the degradation of the materials.

The dielectric constant and dissipation factor of dry 610 nylon polymer have been reported as 3.5 and 0.02, respectively, at room temperature; at temperatures above 100° C, the values are much

greater and are similar to values of polar, hydrogen-bonded liquids such as alcohols [20]. Errera and Sack [26] have reported the following dielectric constant values for nylon, presumably the 66 type: 4.2 at 10 kc/s, 3.26 at 500 kc/s, 3.15 at 4 mc/s, and 3.15 at 10 mc/s.

The dielectric constant and dissipation factor measurements were made with a conjugate Schering bridge in accordance with ASTM Method of Test D 150–47T [27]. Tinfoil electrodes were applied to the film, using Vaseline as an adhesive. Measurements were made at 1,000 and 100,000 c/s. The measurements were made at 25° C and 50-percent relative humidity after the test specimens had been at these conditions for 24 hr. The ultraviolet treatment was made by exposing specimens of the films to radiant energy from an RS sunlamp for 20 hr in nitrogen at 100° C.

The tests were designed to determine the electrical uniformity of the nylon samples. Electrodes were placed on the specimens at three different positions, namely, in the center and at two positions off center. The latter two are designated as the second and third positions. The results are presented in table 15.

The films were found to be electrically nonuniform. The difference in the dielectric constant of different parts of the same specimen is as great as 50 percent. These large differences would tend to obscure changes resulting from exposure of specimens to heat, ultraviolet radiant energy, or other degrading forces. However, the results indicate that the dielectric constant of sample 4406 is not affected by the exposure to ultraviolet radiant energy and that the dielectric constant of sample 4407 is decreased markedly by the exposure to ultraviolet radiant energy. No particular trends are noted in the dissipation factor values.

The dielectric constant of both samples increased as the period of contact with Vaseline increased. The dissipation factor of sample 4406 increased, and that of sample 4407 decreased at the longer periods of contact with the Vaseline. The reason for these changes was not apparent since any swelling resulting from absorption of Vaseline by the polyamide would cause the dielectric constant to decrease.

XV. Effects of Water and Alcohols

With M. J. Reiney

The effects of water, methanol, and ethanol on the polyamide samples were investigated by immersing the films in these liquids before and after exposure to heat, ultraviolet radiant energy, and outdoor weathering. The effects of these particular liquids were investigated because in any actual use the polyamide films come into contact with water and in casting the films alcohols are probably used as the solvents.

The results of the tests made with original untreated specimens of the polyamide film samples are presented in table 16. Continuous immersion in 95-percent ethanol and methanol caused the polyamide films of the 66/6 and 66/610/6 types to split or disintegrate. Continuous immersion in water caused the 66/6 type films to disintegrate but caused only clouding of the water for the 66/610/6 type. Immersion in absolute ethanol had no effect on the 66/6 polymers and disintegrated the 66/610/6 polymers.

The effects of alcohol immersion on specimens of the polyamide samples that had been exposed to heat, ultraviolet radiant energy, and outdoor weathering are shown in table 17. Exposure to ultraviolet radiant energy causes an increase in the degree of attack by 95-percent ethanol and methanol. Immersion in 95-percent ethanol for 1 hr had no effect on any of the specimens that had been heated to 87° C for 68 hr. Exposure outdoors for 2 months had no

TABLE 15. *Electrical uniformity of polyamides*

Sample designation	Specimen number	Exposed to ultraviolet radiant energy	Time after electrodes were applied	Position of electrodes	Dielectric constant at—		Dissipation factor at—	
					10^3 c/s	10^5 c/s	10^3 c/s	10^5 c/s
			hr.					
4406	1	No	0	Center	6.5	4.2	0.17	0.27
			1	do	6.7		.17	
			96	do	6.8		.17	
			144	do	7.1		.17	
			312	do	7.1		.18	
			0	2	12.3	7.5	.18	.25
			0	3	11.7		.17	
	2	Yes	0	Center	6.4	4.3	.16	.10
			72	do	6.2		.15	
			264	do	6.2		.15	
			0	2	10.8	5.7	.23	.19
			24	2	11.7	5.9	.23	.20
			0	3	11.0	7.0	.25	.20
4407	1	No	0	Center	7.9	5.3	.15	.16
			1	do	7.9		.15	
			2	do	7.9		.15	
			120	do	8.3		.14	
			0	Center (reapplied)	8.4		.13	
			0	2	9.4	5.6	.17	.18
			24	2	10.1	5.9	.18	.20
			0	3	9.5	5.6	.17	.19
	2	Yes	0	Center	4.9	3.0	.13	.13
			336	do	4.8		.15	
			0	2	5.8	3.5	.16	.21
			2	2		3.8		.16
			24	2	6.0	3.5	.17	.17
			0	3	5.4	3.3	.17	.18

TABLE 16. *Effects of water and alcohol immersion on untreated polyamides* [a]

Immersion medium	Polyamide sample	Degree of attack [b] after immersion for—			
		18 days	31 days	7 months	18 months
Water, distilled	4405	P2	U2	U2	U2M; S5; V5
	4407	P2	U2	U2	U2; S5; V5
	4408	P2	U2	U2	U2M; S4; V5
	4409	P2	U2	U2	U2M; S2; V2
	4410	P2	U2	U2M	U2M; S2M; V2M
Ethanol, 95%	4406	U4	U4	U4	U4; S4; V4
	4407	P4	U4	U4	U4; S4; V4
	4408	P4	U4	U4	U4; S4; V4
	4409	P4	U4	U4	U5; S5; V5
	4410	P3	U3	U3	U3; S3; V3
		1 hour	24 hours	20 days	4 months; 15 months
Ethanol, absolute	4405	V1	V1	V1	U1; V1; V1
	4406	V1	V1	V1	U1; V1; V1
	4407	V1	V1	V1	U1; V1; V1
	4408	V1	V1	V1	U1; V1; V1
	4409	V1	V1	V1	U3; V3; V4
	4410	V1	V3	V3	U3; V3; V4
		5 min	30 min	3 days	1 month; 6 months; 16 months
Methanol, absolute	4405	U2	V4	V4	V4; V4; V4
	4406	U3	V4	V4	V4; V4; V4
	4407	U2	V3	V3	V3; V4; V4
	4408	U2	V3	V3	V3; V4; V4
	4409	U3	V5	V5	V5; V5; V5
	4410	U5; V5	V5	V5	V5; V5; V5

[a] Pieces of the films approximately 2 in.² in area were placed in a test tube or in a wide-mouthed bottle and covered with the test liquids. The containers were stoppered and allowed to stand at 21° to 26° C. The specimens were examined at various time intervals. The test specimens were all conditioned at 25° C and 50-percent relative humidity prior to immersion in the liquids. The films were examined by observing the changes in appearance after standing undisturbed, after shaking the container, and after probing the test films with a glass rod.

[b] Code for indicating degree of attack on film: U=undisturbed; P=probed gently with a glass rod; S=after gentle shaking; V=after vigorous shaking; 1=unaffected; 2=sediment or cloud in liquid, film intact; 3=cracks through film; 4=broken into large pieces; 5=broken into small pieces; 6=soluble; M=developed a green-mold growth.

effect on the degree of attack by methanol. Exposure to ultraviolet radiant energy increased the degree of attack by methanol.

The behavior of sample 4410, a 66/610/6 polymer, is different from that of the other polymers. Before exposure the specimens are more resistant to water and 95-percent ethanol, less resistant to absolute ethanol and methanol, and after exposure to ultraviolet radiant energy are affected more by absolute ethanol and methanol.

TABLE 17. *Effects of alcohol immersion on polyamides exposed to heat and ultraviolet radiant energy*

Immersion medium	Polyamide sample	Exposure prior to immersion [a]	Degree of attack [b] after immersion for—		
			5 min	30 min	60 min
Ethanol, 95%	4406	Ultraviolet; 168 hr	V1	V5	V5
	4407		V1	V5	V5
	4408		V1	V4	V4
	4409		V1	V5	V5
	4410		V6	V6	V6
	4406	87° C; 68 hr	V1	V1	V1
	4407		V1	V1	V1
	4408		V1	V1	V1
	4409		V1	V1	V1
	4410		V1	V1	V1
			5 min		10 months
Methanol, absolute	4406	Ultraviolet; 168 hr	U2; V5		V5
	4407		U3; V5		V5
	4408		U1; V4		V5
	4409		U3; V5		V5
	4410		U6; V6		V6
	4406	Outdoors; 2 months	U2; V4		V4
	4407		U1; V4		V4
	4408		U1; V4		V4
	4409		U1; V4		V5
	4410		U5; V5		V5

[a] The exposure to ultraviolet radiant energy was made with an S–1 sunlamp. The heating at 87° C was done in a vacuum oven.

[b] See table 16 for code indicating degree of attack.

XVI. Discussion of Results

1. Changes in Molecular Constitution

(a) Mass Spectrometry

The presence of the products detected by mass spectrometry, namely, water, carbon dioxide, ethanol, carbon monoxide, and hydrocarbons, may be explained as follows:

Most of the water was absorbed on the polymer molecules. A small part of the water may have resulted from a reaction of the type:

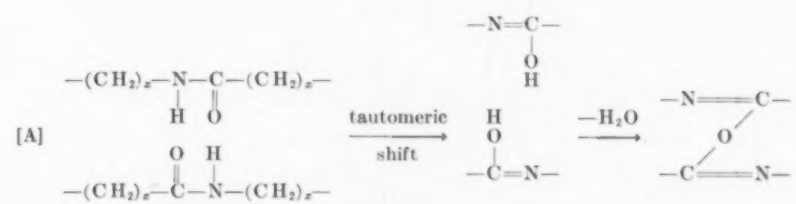

Such a reaction would result in cross linking of the polyamide chains. However, if cross linking did occur as a result of the treatments it was not sufficient to affect the solubility of the polymers in ethanol.

Carbon monoxide was evolved in all the experiments in which the specimens were exposed at temperatures of 90° to 100° C. Hydrocarbons were found in all experiments in which carbon monoxide was detected. A possible source of these two compounds is as follows:

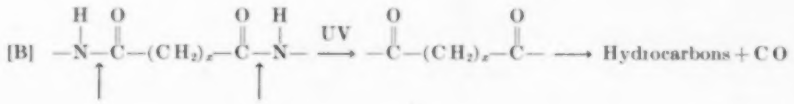

The arrows indicate the points of cleavage in the polymer chain. The carbonyl group of the peptide linkage absorbs energy at 280 mμ, and this energy apparently results in the scission of the bond between the imine group and the carbonyl group.

Presumably most of the carbon dioxide shown by the analysis was originally sorbed by the polymer. In the experiments made at the higher temperatures and/or with ultraviolet radiant energy, a small amount may be formed by the decarboxylation of the chain ends. Decarboxylation at temperatures of 100° C appears to be reasonable.

The ethanol evolved from these films is probably residual solvent. The specimens used in most of the experiments were studied in the condition in which they were received. The literature [28] indicates that sample 4406 is similar to the German Igamid 5A, which was made by casting the film from solution of the polyamide in ethanol. Residual ethanol could be attached at the peptide linkage during manufacture and act as a dipole associated plasticizer. The ethanol found in the products obtained at the milder conditions was evolved from the polyamide film when the apparatus was evacuated (see section III).

(b) Pyrolysis

Water was one of the gaseous degradation products resulting from pyrolysis of these polyamides. The conditioning period in which the films were heated for 2 hr at 150° C in vacuum should have removed sorbed water and gases. Water may be formed by reaction [A]. The probability of reaction [A] occurring in sample 4407, where there is the possibility of more peptide linkages in proximity to each other, is greater than in nylon sample 4409 where the formulation suggests a more dispersed dipole population. It is interesting to note that the water produced on pyrolysis of 4409 is almost insignificant. This water represents about 0.6 percent of the total oxygen of the polymer. With nylon 4407, 9.7 percent of the total oxygen of the polymer was evolved as water. The mechanism proposed above would lead to cross linking of the polymer. A relatively small percentage of cross linking leads to insolubility. The residues of these pyrolyses showed only partial solubility in ethanol; but no quantitative study of the relative solubility of samples 4407 and 4409 was made

The cyclopentanone formed in the pyrolysis experiments may be accounted for in two ways. The polymer molecule may break as follows:

[C]

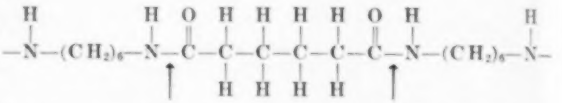

Scission at these places is logical since the C–N bond is weaker than the C–C bond, 66 kcal compared to 82.5 kcal [29]. The radical produced may split off carbon monoxide and form cyclopentanone:

[D]

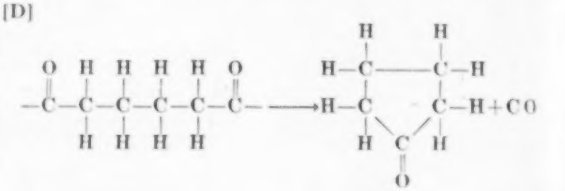

If this mechanism is correct and if it represents the only source of cyclopentanone, cyclopentanone and carbon monoxide should be produced in the molar ratio of 1:1, but the observed ratio was 4:1.

Another possible mechanism to explain formation of the cyclopentanone is as follows. If adipic acid terminated the polymer chain, a reaction of the following type may occur:

[E]

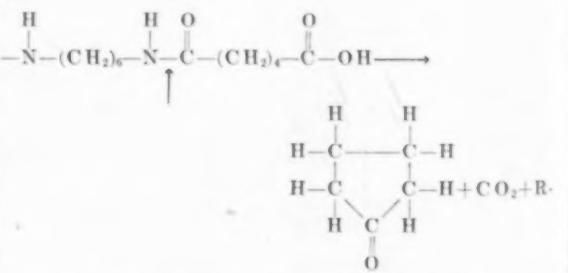

If a slight excess of adipic acid were used in the manufacture of the polymer, a large portion of the chain ends would be carboxyl groups.

It is possible that cyclopentanone is produced by both mechanisms described. There is sufficient carbon dioxide and carbon monoxide to account for these mechanisms. The moles of cyclopentanone, carbon dioxide, and carbon monoxide produced are about 0.017, 0.08, and 0.004, respectively, for sample 4407.

A very small amount of cyclopentanone was found in the products from sample 4409. This polymer contains some adipic acid salt. The ratio of cyclopentanone to adipic acid component for sample 4407 is about 40 times the same ratio for sample 4409. Evidently the sebacic acid component markedly affects the course of the reaction. If the ten carbon unit breaks out in a manner similar to the reaction in equation [C], the production of cyclopentanone would not be expected. If a ten carbon cyclic ketone formed, its existence would be transitory at the temperatures of the experiment considering the well-known weakness of ten carbon rings. It should be noted that no carbon monoxide was produced by sample 4409.

The carbon dioxide found is in excess of the maximum possible calculated on the basis of two carboxyl groups per molecular chain. If a molecular weight of 16,000 is assumed (table 12), the total possible mole percent of carbon dioxide that may be generated is about 0.3 percent; the mole percent of carbon dioxide found is about 3.5 and 4.6 percent for samples 4407 and 4409, respectively. This shows that a large part of the carbon dioxide was sorbed on the original material or comes from parts of the chains other than the ends.

The amounts of oxygen in samples 4407 and 4409 are 15.2 and 14.2 percent, respectively. The amounts of oxygen found in the gaseous fractions are about 2.9 and 3.3 percent, respectively. Although the gaseous fractions constituted only 5 percent of the weight of the polymer, these fractions contained 19 percent of the oxygen in sample 4407 and 23 percent of the oxygen in sample 4409. This can be explained on the basis that the C—N bonds break as indicated in equation [C] and that the fragment broken out decomposes as indicated in equation [B] or [D].

An obvious postulate to account for the large amount of carbon dioxide and hydrocarbons formed on the pyrolysis of these polyamides is that the C—N bonds break as indicated in equation [C] and that the fragment, of either six or ten carbon units, decomposes by some unknown mechanism to give carbon dioxide and hydrocarbons. In the case of the six carbon unit, part but not all of the fragment gives cyclopentanone and carbon monoxide as shown in equation [D].

(c) Ultraviolet Transmission

Nylon is a polypeptide, and absorption characteristics similar to polypeptides and proteins would be expected. A region of selective absorption at approximately 280 mμ has been attributed to the peptide group [30, 31] and more particularly to the carbonyl unit of this group [32]. Thus it seems probable that the absorption in the region of 280 mμ found in the polyamides is caused by the peptide group and more specifically by the carbonyl unit in this group.

The absorption band between 260 and 330 mμ with the polyamides may also be attributed in part to an associated structure between the peptide group and water or ethanol. The loss of the water and/or ethanol by the polyamides may cause an increase in the transmission in this region. The results obtained in this investigation show that exposure to ultraviolet radiant energy causes the disappearance of this absorption band; however, soaking the exposed specimens in water or ethanol does not cause it to return.

Anslow and Nassar [30] exposed solutions of egg albumin to ultraviolet radiant energy and found that the solutions first became rapidly more absorptive and after several hours of exposure to the radiation became less absorptive. They attributed this to breaking of the peptide linkage followed by recombinations producing hydrophobic molecules. About 4.4 electron-volts were required to break the peptide linkage. The effect of solvents such as aqueous sodium hydroxide and ethanol was to reduce the energy required to break the peptide linkage in egg albumin. In fact, exposure to sunlight through ordinary glass was sufficient to effect dissociation in such solutions.

Carpenter [33] exposed benzylstearylamine and β-phenylethylstearylamine to ultraviolet radiant energy and observed that both were decomposed. He found that peptide groups adjacent to side chains such as aromatic groups can be decomposed on exposure to ultraviolet radiant energy with the liberation of the absorbing amino acid from the molecule. Mitchell [34] states that exposure to ultraviolet radiant energy produces hydrolysis of peptide groups. The following reaction has been suggested [35] for the photochemical hydrolysis of stearic anilide:

[F] 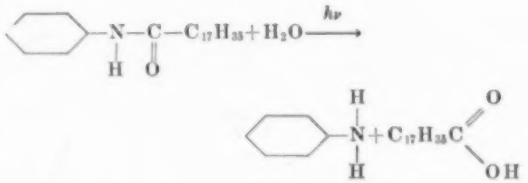

Peptones and proteins were found to yield aldehydes, ammonia, and carbon dioxide when exposed to ultraviolet radiant energy in the presence of oxygen. The decomposition of amino acids by ultraviolet radiant energy in the presence of oxygen was found to be as follows [36]:

[G] 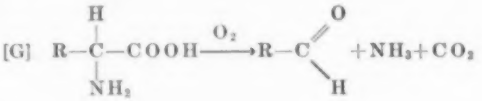

Exposure of a dilute solution of protein to ultraviolet radiant energy in the presence of oxygen resulted in the disappearance of the characteristic transmission minimum at 280 mμ [37]. The effect was considerably slower in nitrogen. The products resulting from the degradation of the protein caused an over-all decrease in the total transmission of the solution.

It is known that peptide groups form hydrogen bridges, possibly of the following nature:

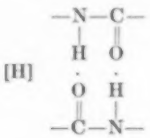

[H]

It is probable that denaturation by agents such as ethanol [38] causes these hydrogen bridges to be broken. The ethanol used to dissolve the nylon in making the film may break the hydrogen bridge and give a structure such as

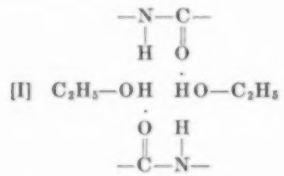

[I]

or some similar type of structure.

Exposure to heat and to ultraviolet radiant energy could eliminate the ethanol since the energy involved in a hydrogen bridge is only about 5 kcal [38]. However, if both these treatments remove ethanol, the structures left in the polyamide must be somewhat different; heating does not eliminate the absorption but does cause an over-all decrease in transmission, whereas ultraviolet radiant energy causes an increase in transmission so that the absorption band is removed. Water may be bound in a manner similar to that holding the ethanol.

The following hypothesis is suggested to explain the difference in the behavior of these polyamides on exposure to heat and to ultraviolet radiant energy. The heat may cause breakdown of the associated complex between the carbonyl group and the ethanol and/or water, resulting in an over-all decrease in transmission. If the absorption in the region of 280 mμ is attributed to the carbonyl group, it would not be appreciably affected by elimination of the complex. The ultraviolet radiant energy causes some reaction to take place that eliminates in part the absorption supposedly characteristic of the carbonyl and peptide groups. The greatest change in transmission in the region of 280 mμ, observed with sample 4407, was about 9 percent, that is, from 48 to 57 percent.

It may be that the characteristic dip can be attributed to structures such as that shown in [I] and that the structure shown in [H] has a somewhat greater transmission. The reaction in the presence of ultraviolet radiant energy could be as follows:

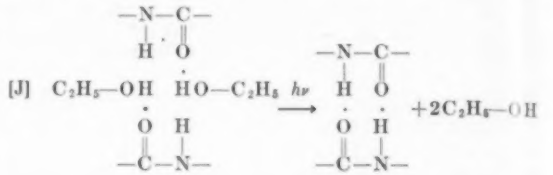

[J]

Another type of cross-linking reaction that eliminates the carbonyl group [39] has been suggested for proteins as follows:

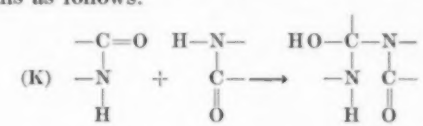

(K)

It has been found that the exposure of spread films of protein (the completely uncoiled form of the molecules) causes some degree of coiling, evident through collapse of the film [40]. The coagulation of proteins with ultraviolet radiant energy has been reported by many investigators [41]. This suggests another possible explanation for the splitting and brittleness of the polyamide films observed after exposure to sunlight.

The splitting of the C—N bond and removal of C=O as a result of ultraviolet exposure are possible and could be responsible for the changes in the ultraviolet spectra.

(d) Infrared Transmission

The infrared transmission curves of the polyamides are interpreted as follows: The absorption of the imine group (NH), which is ordinarily at 2.83 to 2.93 μ, is relatively weak. However, a shift to a longer wavelength with increased intensity of absorption occurs with bridging, indicating that the 3-μ band is probably caused by linear NH.O bridging [42 to 44]. Absorptions at 3.36 and 3.42 μ are usually a result of carbon-hydrogen bond stretching. The intense absorption at 6.1 μ is attributed to the carbonyl group, which usually absorbs at 5.76 to 5.84 microns but is displaced to longer wavelength in nylon 66 and amides in general probably as a result of interaction between the carbonyl and imine groups [42]. The intense absorption at 6.46 μ may result from N–H bending and could cause a harmonic effect at 3.2 μ.

The doublet band at 6.8 and 7.05 μ has been observed in diallyl adipate [45]. This pair of bands may be connected with CH_2 deformations, such as $-CH_2-$ and $=CH_2$ [42]. A band at 7.3 μ is attributed, in some cases, to $-CH_3$ deformation. Single bond stretching might absorb in this region, and the band has been observed in diallyl adipate [45]. Thompson and Torkington [42] claim that in polyamides "much of the absorption between 8.34 and 5.88 μ must be due to vibrations of the $-C-CO-NH-C-$ part of the structure".

The absorption at about 9.0 μ was attributed to the hydroxyl group in the case of polyvinyl alcohol by Thompson and Torkington [42]. From 14.3 μ to lower frequencies broad absorption has been observed with oxygenated hydrocarbons and some oxidized hydrocarbon polymers. Methyl alcohol has a broad absorption band here according to Thompson and Torkington.

In the present study no extensive changes were revealed by the infrared transmission measurements. In some cases, structural differences of significance for physical properties cannot be detected by infrared methods because the relative number of chemical linkages affected is too small [46]. Apparently the degradation of nylon under the conditions used in this study results in either a change in a small proportion of the chemical linkages or in alterations in chemical structure that are not accompanied by a change in infrared absorption, or both.

(e) Viscosity Measurements

It seems probable that some chain scission occurred during the treatments, as shown by the lowering of η, ln η_r/c, and η_{sp}/c (table 12 and figs. 9 to 12). The data obtained on solutions of specimens D and E show that the difference in degree of degradation is quite pronounced. No measurement was made with the 3-percent solution of specimen C since there was evidence of contamination. Nevertheless, by comparing the results obtained from the 1-percent solution of specimen C with those from the 1-percent solution of specimen B, it is evident that the degree of degradation exhibited by specimen C shows the same relationship to that of specimen B as that observed for specimens E and D.

The applicability of Baker's equation [47]

$$\eta_r=\left(1+\frac{[\eta]\,c}{z}\right)^z$$

to the polyamide solutions was examined. The value of $z=3$ was found to fit the data adequately. The values of intrinsic viscosity, $[\eta]$, calculated as

$$[\eta]=3\,(\eta_r^{1/3}-1)/c,$$

are tabulated in table 12. The agreement between values of $[\eta]$ obtained for the same specimen but with solutions of different concentrations is fair. Figure 12 is a plot of the values of $[\eta]$ versus the time of exposure to the degrading treatment.

Taylor [5] has expressed the relation between the intrinsic viscosity of nylon fractions in formic acid and the molecular weight as $\overline{M}_N=13{,}000\,[\eta]^{1.39}$, where $\overline{M}_N$ is the number-average molecular weight and $[\eta]$ is the intrinsic viscosity in formic acid. The measurements of intrinsic viscosity in this laboratory on sample 4410 were made in *m*-cresol. In 90-percent formic acid the intrinsic viscosity values are approximately 0.9 of those determined in *m*-cresol [20]. Application of Taylor's relation to the intrinsic viscosities of unfractionated polymers leads to a viscosity-average molecular weight ($\overline{M}_v$).

Calculations from the results presented in table 12 indicate that 0.4 percent of all chain bonds were broken in the specimen degraded by exposure to ultraviolet radiant energy for 168 hr, the treatment that resulted in the greatest decrease in intrinsic viscosity. Since the strength of the C—N bond is rather weak compared to the C—C bond, the chain break probably occurs at the peptide linkage. If this is the case, about 3.5 percent of the peptide linkages were broken in this specimen.

2. Changes in Molecular Orientation

Investigations were made to detect any changes in molecular orientation or crystallinity of the polyamides under study. The terms "molecular orientation" and "crystallinity" are used in this discussion to describe a condition or state in which sections of the macromolecules are more or less situated spatially in some definite pattern or alinement to one another. The development of crystallinity in films of polyamides would be expected to lead to increased brittleness and splitting with a corresponding limitation of plastic flow. A decrease in the water or alcohol content below a specific minimum value would also produce the same changes in physical properties.

There appear to be two types of molecular orientation possible in polyamides. One is hydrogen bridging through adjacent peptide groups. This is also referred to as intermolecular bridging and dipole association. The higher the degree of dipole association, the greater the degree of crystallinity attributable to hydrogen bridging. The other type is hydrocarbon packing or alinement of the polymethylenic sections between the peptide groups. It has been shown that smaller polymer molecules increase the possibility of more crystallinity or local order [48] and that molecular size has a determining effect on the uniformity of properties [49].

There are two other factors that may affect the degree of crystallinity. One is the association of molecules of water and alcohol by hydrogen bridges at the peptide groups. The other is the dispersion of liquids or gases in the form of minute spherical inclusions in the body of the polymer. The presence of molecules such as water and alcohol in any way in the matrix will reduce the potential for molecular orientation because of spatial factors.

On the basis of chemical constitution, the polyamides used in this investigation can be divided roughly into two classes as regards possibility of molecular orientation. Samples 4405, 4406, 4407, and 4408 would be expected to have or develop a higher degree of dipole association than samples 4409 and 4410 because of the regularity in the spacing of the peptides. The 10-carbon acid along with the 6-carbon acid in samples 4409 and 4410 creates an irregularity and causes the displacement of successive peptide groups along the chain. The caprolactam that is present in both classes also tends to create irregularity. This situation is analogous to the one

described by Baker and Fuller [18] for a 50:50 composition of a 66/610 polymer, which shows the effect of copolymerization in decreasing the concentration of polar groups in the average planes. The unequal polymethylene group spacings cause some of the polar peptide groups to fall along the polymer chain where they cannot contribute to dipole interaction.

(a) Miscroscopic Examination

As all of these samples exhibit relatively small optic axial angles, and since the acute bisectrix is approximately normal to the film, microscopical examinations made with crossed nicols, especially with objectives of small aperture, are extraordinarily sensitive to slight changes in optical directions. This is interpreted to be the reason for the large difference in brightness exhibited in the photomicrographs of figure 14.

The effect caused by cutting the film with scissors is noticeably less on the samples that were exposed to ultraviolet radiant energy. This is probably because the greater brittleness has limited plastic flow under the stress of the cutting edge.

Each of the samples exhibits dark spots with low-power lenses. With higher power lenses it can be seen that many of the spots are transparent and only appear dark because of the scattering of light that they have caused. The larger spots occur in the untreated film as nearly spherical liquid, or at least optically amorphous, inclusions. They have refractive indices noticeably but not greatly less than the rest of the films. With exposure these spherical inclusions shrink somewhat, with attendant strain in the surrounding plastic, and their refractive index becomes much less than that of the rest of the film. The most plausible explanation is that a dispersed liquid has diffused out and been replaced by air or vapor.

These polyamide films are anisotropic. Sample 4410 is apparently quite heterogeneous as compared to sample 4408, which appears to be very homogeneous. Sample 4410 shows less effects from the exposures to ultraviolet radiant energy than sample 4408.

The bright lines observed in both untreated and treated specimens are apparently places where the orientation of the molecules within the plane of the film has been disturbed. These lines may have been caused by slight abrasion (hence, deformation) of the surface, by strains from shrinkage of the film, or by mechanical distortion.

(b) Electron Miscroscopic Examination

The electron micrographs of the unshadowed surfaces of the untreated specimens and of those exposed to ultraviolet radiant energy and to heat show no appreciable differences as a result of the exposures. The examination of the shadowed surfaces was more fruitful.

The electron micrographs of the shadowed surfaces of the untreated samples and of those exposed to ultraviolet radiant energy show that the crystallinity of sample 4407 appears to be increased and that of sample 4409 not affected as a result of the treatment. Exposure to heat appears to have no effect on the crystallinity of samples 4407 and 4409. Exposure to ultraviolet radiant energy may permit rotation of a segment of the polymer chain into a more highly ordered state. If this is the situation, then sample 4407 would be affected more than sample 4409.

Some of the difference in grain structure between samples 4407 and 4409 may be caused by differences in rate of cooling.

(c) Electron Diffraction

Assuming that the spacing in the region of 4.0 A (see table 13) represents hydrogen-bridged peptide linkage, the intensity of this ring should be proportional to the degree of order in the molecular chains. Positive determination of the crystallinity from such criteria as the intensity and width of the lines could not be made even with such measuring devices as the recording densitometer and the comparator because of the diffuse background and halolike character of the patterns. Visual estimation of the intensity and width of the rings was made by several experienced observers. There was no correlation between their observations and the treatments to which the films were subjected.

These electron diffraction studies revealed no changes in the degree of molecular orientation of the polyamides as a result of exposure to heat and to ultraviolet radiant energy.

(d) X-Ray Diffraction

The results obtained with the X-ray penetration photographs show some correlation with those expected on the basis of chemical constitution. Sample 4407 appears to be more crystalline than sample 4409. The differences are sufficient to identify the samples.

Like proteins, the sorption of water has a marked effect on the physical properties of polyamides. The effect of water and of ethanol on samples 4407 and 4409 was studied with X-ray diffraction techniques. Specimens of each sample were subjected to the following treatments for 1 month: (1) dried over magnesium perchlorate, (2) conditioned at 50-percent relative humidity, (3) immersed in distilled water, and (4) immersed in 95-percent ethanol, respectively. The spacings and intensities obtained by measuring the X-ray reflections with a Geiger-counter spectrometer are so similar that no definite trends can be recognized. There appears to be a tendency for the 4.3-A spacing to decrease in intensity from the dry to the wet specimens.

It is possible that the 7-A spacing observed may be an identity period along the polymer chain. The increase in this spacing on exposure of sample 4407 to ultraviolet radiant energy may be attributed to the unkinking of the chain when dipole associated compounds, such as water, ethanol, or caprolactam, leave the polymer. This would permit bridging at the peptide groups and tend to extend the chain.

In the case of sample 4409, the chain may tend to kink on exposure to ultraviolet radiant energy. This may be explained by interference between the polar groups and by a tendency of the longer methylene chain to twist. As the polar linkages are broken, the longer hydrocarbon chain section may coil, thus causing a decrease in the spacing. These phenomena would be related to the action of any dipole associated plasticizer.

Spacings at 17.4 and 26 A were observed by Baker and Fuller [25] and were associated with the identity period spacings. These spacings were observed to change on retraction of the material. Sponsler, Bath, and Ellis [50] state that for gelatine the 11-A side chain spacing may be expected to disappear when the water content is great enough to make the side chain spacing so large that the layers become too distorted to form diffraction patterns.

There is evidence that the weakening of intermolecular forces may allow rotations to occur that would result in more complete lattice formations [25, 51]. The theory of rotation and further polymerization in the solid state may be explained by the "Segment theory of chain polymers" [51]. The probability of a given segment rotating is determined by the concentration of energy in the segment. This is shown in the annealing work done on linear polyamides by Fuller, Baker, and Pope [51]. Both amorphous and crystalline regions can exist in the film. Crystalline regions might be formed if sufficient energy is distributed along the molecular chain.

The splitting observed on exposure to heat and to ultraviolet radiant energy may be attributed to a rearrangement to a more crystalline state. In this case, evidence of increased crystallinity would be expected in the X-ray patterns; however, no increase in crystallinity was observed.

X-ray studies by Baker [52] and Brill [53] show that hydrogen bond rupture occurs on heating polyamides. A study of the rupture of intermolecular forces in molten nylon suggests that some of the intermolecular bonds rupture before melting, and thus permit "rotational movements and realinements inferred from X-ray diffraction data" [54].

(e) Electrical Measurements

The polyamides used in this investigation are electrically nonuniform to a high degree. This variation in electrical properties tends to obscure changes that might arise from alterations in molecular orientation due to exposure to heat, ultraviolet radiant energy, and other degrading forces. However, the results obtained indicate tentatively that exposure to ultraviolet radiant energy reduces the dielectric constant of sample 4406 slightly and that of sample 4407 markedly.

It seems highly probable that the nonuniform results reported here may be connected with local variations in the degree of dipole association. The change in dielectric constant with respect to time when the electrodes are not moved may be attributed to a change in the degree of dipole association under the influence of the electrical field. Changes in the degree of association of water at the free dipoles may also be a factor. Baker and Yager [55] have discussed the effect of hydrogen bridging in nylon on dielectric measurements.

(f) Effect of Water and Alcohols

The apparent relation between the degree of molecular orientation and degree of attack by liquid may be explained by the following hypothesis: Since the degree of intermolecular bridging in samples 4409 and 4410 is less than in the other samples, more unbridged carbonyl groups are available in samples 4409 and 4410 to associate with the liquid. The decreased degree of attack by the water in samples 4409 and 4410 is explained by the water molecules being sufficiently small to remain between the polymer chains without causing linear and lateral disorder sufficient to weaken the intermolecular forces holding them together. The alcohol molecules, on the other hand, are sufficiently large to cause enough disorder to weaken the intermolecular forces holding the polymer molecules together and permit further attack by the solvent.

The attack by water on samples 4406, 4407, and 4408 may be directly at peptides that are hydrogen bridged. Water being a very strong polar solvent may cause dissociation of the existing bridge and be held between the peptides causing a resultant strain on the molecular relations.

Ethanol, a larger molecule, apparently cannot interleave between chains of samples 4406, 4407, and 4408. Absolute ethanol does not show effects that indicate that it is breaking intermolecular bridges between adjacent peptides. In the case of samples 4409 and 4410, with more free dipoles and possibly less packing between the polymer chains, ethanol possibly can be absorbed. The size of the ethanol molecule, however, strains the chain configurations of these polymers.

The effects observed with 95-percent ethanol seem to indicate a preferential absorption of the water in samples 4406, 4407, and 4408. Samples 4409 and 4410 show effects similar to absolute ethanol. In general, cosolvent effects result.

Methanol represents a molecule of intermediate size. The data seem to indicate that the main attack by methanol is at unassociated dipoles. The association of a polar liquid at a free dipole may displace polymer chains with resultant strain that may make intermolecular bridging between the polymer chains more susceptible to attack by the polar solvent.

Methanol attack is greater after exposure of the films to ultraviolet radiant energy. Considering the immediate attack to be at free dipoles in the polymer, it seems logical to assume that exposure to ultraviolet radiant energy releases intermolecularly bridged peptides, thus causing a decrease in the degree of crystallinity. A decrease in molecular weight may also result in increased attack by methanol because of increased association at chain ends.

Hill and Walker [56] in their work on polymer constitution show that the melting point of a crystalline polymer depends on the arrangement of the molecules and the relative amount of intermolecular forces between the molecules in the crystal lattice. Polyamides with high melting points have peptide arrangements that permit a high degree of bonding between carbonyl and amino groups in adjacent molecules. The data obtained by Biggs, Frosch, and Erickson [57] on the effect of varying the degree of *N*-alkylation on the melting points of polyamides support the view that hydrogen bridging is the main cause of the high melting points observed. Additional information on the effect of hydrogen bonding on melting points is reported by Baker and Fuller [20, 25].

The relation between the melting points of the original polyamide samples used in this investigation and the final effects of the liquids are shown in table 18, in which the materials are arranged in order of decreasing melting point. If the melting points of these polyamides, which are similar in chemical constitution, are an indication of the intermolecular forces or the degree of crystallinity, the data in the above table indicate that the more crystalline polymers are more readily attacked by the water and the less crystalline polymers are more readily attacked by the absolute ethanol and methanol. The effect of the 95-percent ethanol is erratic, since the mixture exhibits cosolvent effects.

The relation between the effects of absolute methanol and the melting points of the original and exposed samples is shown in table 19. The effect of absolute methanol on the original untreated specimens is about the same as that on specimens exposed outdoors, and the melting points are practically the same. The melting points of the specimens exposed to ultraviolet radiant energy are less than those of unexposed specimens, and the effects of the absolute methanol are greater. If this is interpreted in terms of the hypothesis advanced above, it is indicated that there is little or no change in crystallinity in the specimens exposed outdoors and a decrease in crystallinity in the specimens exposed to ultraviolet radiant energy in the laboratory.

TABLE 18. *Relation between effects of liquids and the melting points of the polyamides*

Sample designation	Degree of attack [a]					
	Melting point	Water, 18 mo	95% ethanol, 18 mo	Ethanol, 15 mo	Methanol	
					30 min	16 mo
	°C					
4407	188 to 190	5	4	1	3	4
4408	186 to 191	5	4	1	3	4
4405	179 to 180	-----	-----	1	4	4
4406	179 to 180	5	4	1	4	4
4409	165 to 167	2	5	4	5	5
4410	161 to 163	2	3	4	5	5

[a] See table 16 for code indicating degree of attack.

TABLE 19. *Relation between effects of methanol immersion and melting points of original and exposed polyamides*

Polyamide sample	Untreated		Exposed to ultraviolet		Exposed outdoors 2 months	
	Melting point	Effect of methanol [a]	Melting point	Effect of methanol [a]	Melting point	Effect of methanol [a]
	°C		°C		°C	
4405	179 to 180	4	-----	-----	-----	-----
4406	179 to 180	4	163 to 170	5	180 to 183	4
4407	188 to 190	4	173 to 178	5	188 to 189	4
4408	186 to 191	4	180 to 182	5	190 to 191	4
4409	165 to 167	5	152 to 160	5	162 to 169	5
4410	161 to 163	5	145 to 151	6	164 to 166	5

[a] See table 16 for code indicating degree of attack.

3. Relative Effects of Environmental Conditions

The present study indicates that exposure of polyamides to ultraviolet radiant energy results in degradation. This is attributed to absorption of the short wavelengths by the carbonyl groups of the polymer with a resultant breaking of adjacent C—N bonds. Strongly bound water or organic liquids that act as a plasticizer are also removed. The net result is a decrease in strength and an increase in brittleness.

The viscosity, mass spectrometric, and ultraviolet transmission studies show that the polyamides are affected by exposure to heat. This effect is less pronounced than that caused by exposure to ultraviolet radiant energy and may be of a different type or order.

4. Relation Between Stability and Chemical Constitution

The 66/610/6 polyamides have compositions that should be favorable to less intermolecular bridging than the 66/6 polyamides. However, factors such as cooling rate from the molten state, which apparently has a considerable effect on the degree of association between chains, must be considered. It has been suggested [58] that a 66/610 (30:70) polymer is qualitatively less crystalline and consequently has a lower melting point than a 66 polymer. One can expect that the more heterogeneous the chemical composition of a polyamide is, the more resistance it will have to degradation.

The carbonyl groups in the polymer are a seat of ultraviolet absorption and consequently are detrimental to stability of the molecule. The adjacent, comparably weak, C—N bond is an arrangement that is susceptible to chain scission.

A superpolyamide with properties similar to the 66 polymer has been prepared from piperazine and dicarboxylic acids and is thought to contain no hydrogen bridges between molecules [59]. The resistance of polyamides to embrittlement on degradation increases when an amino hydrogen of an aromatic amine having at least two cyclic nuclei (e. g., β-naphthylamine or phenothiazine) is incorporated in the polymer molecule [60]. It is also reported

that the stability of polyamides to heat and light is increased by adding 0.5 to 4 mole percent of an amide-forming aromatic compound in the monomer mixture prior to condensation [61]. Plasticization of polyamides has also been suggested [62, 63]. Methylation of a fraction of the amide bonds results in polymer molecules with the same strength as the original ones but eliminates the possibility of the formation of hydrogen bridges [25, 64]. *N*-substituted polyamides obtained when mixtures of disecondary, secondary-primary, and diprimary amines are polymerized with dibasic acids have less hydrogen bridging and molecular interaction because of the lateral substituents [65]. The amount of *N*-substitution determines the properties of the polyamides; they can be varied from the hard tough polymers of the unsubstituted types to the soft tacky polymers of the 100-percent substituted types. Higher alkyl-*N*-substituted 610 polymers are less crystalline, have less potential crystallinity, and possess a higher degree of long-range elasticity than methyl-*N*-substituted 610 polymers. The basic idea involved in modifying these chemical structures is to prevent proximity of dipoles between the molecules.

5. Improvement of Service Life of Polyamides

The service life of polyamides could be extended by adding materials that will absorb the ultraviolet radiant energy instead of allowing the short wavelengths to be absorbed by the carbonyl group in the polyamide or by coating or covering with a material that would keep the ultraviolet radiant energy from getting to the carbonyl group. It appears unnecessary to protect from heat except under extraordinary circumstances. Maintaining the water content at a relatively high value would also extend the service life. Precautions should also be taken to prevent the loss of organic liquids or if they are lost to make certain that they are replaced with water or some other material capable of forming a similar associated complex. The absorption of excess amounts of water should be avoided since they cause a change in the strength properties. Water and organic liquids held in this manner act as volatile plasticizers. The use of less volatile water-insoluble materials that would be bound in a manner similar to the way water and alcohols are held is suggested.

The detrimental effects of changes in crystallinity or order on degradation may be remedied partially by changing the chemical constitution as mentioned in section XVI, 4. The changes in chemical constitution would need to be carefully controlled to retain the desirable physical characteristics. On the basis of our present limited knowledge of such effects, experimentation is the only method of determining how much of the problem can be solved by this method. It appears that as long as the peptide group is present, a definite focal point of attack for degradation exists. The addition of groups, such as phenyl, may only act as radiant energy absorbers and may be capable of transferring this absorbed energy to the weaker C—N bond causing it to break. The resulting smaller polymer molecules would be prevented from crystallizing by the presence of the large side groups. However, it is probable that any appreciable increases in stability by changes in chemical constitution would also produce soft tacky polymers.

XVII. Summary

The degradation of polyamides may involve the following: (1) change in chemical structure of the polymer molecule, (2) change in crystallinity (molecular orientation) including effects produced by hydrocarbon packing, dipole rearrangement, and hydrogen bridging, (3) change in the amount of molecularly associated materials that have a plasticizing effect, such as water and ethanol.

Infrared transmission studies of samples before and after exposure to heat and ultraviolet radiant energy show that there are no fundamental changes in the repeating unit of chemical structure of the polyamide molecule as a result of such treatment. Viscosity measurements show that the molecular weight decreases with the severity of the exposure conditions and with an increase in the period of exposure. The decreased resistance to immersion in water and alcohols as the material is degraded also indicates a decrease in molecular weight. It is concluded from these studies that the polymer molecule breaks into smaller molecules. The results of the mass spectrometric and pyrolysis studies show that the polymer molecule breaks at the C—N bond of the peptide group and that the nitrogen atom remains attached to the polymer molecule. From the nature of the products it is evident that C—N bonds in adjacent peptide groups of a molecule break, releasing a bicarbonyl polymethylene fragment. This bicarbonyl polymethylene fragment reacts to form water, carbon monoxide, carbon dioxide, hydrocarbons, and cyclopentanone, the particular products depending on the exposure conditions. The breaking of a very small proportion of the C—N bonds would result in an appreciable decrease in molecular weight and an appreciable change in physical characteristics.

The evidence for a change in crystallinity on exposure of the polyamides to heat and ultraviolet radiant energy is not as positive as that for a change in chemical structure and composition. The results of the light and electron microscopical studies suggest an increase in crystallinity particularly on exposure to ultraviolet radiant energy. The electron diffraction, X-ray diffraction, and electrical studies fail to reveal any changes in crystallinity. The increased degree of attack by alcohols after exposure to ultraviolet radiant energy may be attributed either to the reduction in molecular weight or to reduced crystallinity.

The loss of water, alcohols, or similarly dipole associated materials results in appreciable changes in physical characteristics. These small molecules are probably bound by hydrogen bridging to the oxygen

of the peptide group or some other associated molecular complex. They act as plasticizers for the polyamides. The results of the mass spectrometric, ultraviolet transmission, microscopic, and mechanical property studies show that sorbed water and ethanol are released on exposure to ultraviolet radiant energy. The loss of associated molecules as well as a decrease in the size of the polymer molecules will tend to foster an increase in crystallinity.

The results of the investigation show clearly that no single method gives a complete picture but that correlation of the results from several of the methods gives an insight into the mechanism of degradation of polyamides.

This investigation was sponsored by and conducted with the financial assistance of the Chemicals and Plastics Section, Research and Development Branch, Military Planning Division, Office of the Quartermaster General, Department of the Army. In particular, the efforts of Warren Stubblebine and Ladislav Boor are gratefully acknowledged.

Encouragement by the Committee on Plastics and Elastomers of the National Research Council Advisory Board on Quartermaster Research and Development (Robert Burns, Chairman, and Frank Y. Speight, Technical Aide) is acknowledged.

The help of many others at this Bureau is also appreciated. The assistance of Sanford B. Newman and Emil Borysko in taking the light photomicrographs and Leonardo Testa in the construction of the equipment used is acknowledged.

XVIII. References

[1] F. W. Reinhart, Degradation of plastics, SPE News **4,** No. 7, 3 (Sept. 1948).

[2] J. Boulton and D. L. C. Jackson, The fluidity of nylon solutions in *m*-cresol: measurement of chemical damage in nylon textiles, J. Soc. Dyers Colourists **59,** 21 (1943).

[3] J. Boulton and D. L. C. Jackson, The fluidity of nylon solutions in *m*-cresol: Part II, J. Soc, Dyers Colourists **61,** 40 (1945).

[4] K. Hosino, Studies of synthetic fibers. 1. Decomposition and synthesis of nylon, J. Chem. Soc. Japan **61,** 475 (1940).

[5] G. B. Taylor, The relation of the viscosity of nylon solutions in formic acid to molecular weight as determined by end-group measurements. J. Am. Chem. Soc. **69,** 635 (1947).

[6] W. R. Peterson, Degradation of synthetic linear polyamides, U. S. Patent 2,348,751 (May 16, 1944).

[7] C. S. Fuller, Heat-oxygen treatment of polyamides, U. S. Patent 2,364,204 (Dec. 5, 1944).

[8] R. A. Stillings and R. J. Van Nostrand, The action of ultraviolet light upon cellulose. I. Irradiation effects. II. Post-irradiation effects, J. Am. Chem. Soc. **66,** 753 (1944).

[9] Plastics, organic: general specifications, test methods, Federal Specification L–P–406a (Government Printing Office, Washington, D. C., Jan. 24, 1944).

[10] Rubber goods; general specifications (methods of physical tests and chemical analyses), Federal Specification ZZ–R–601a (Government Printing Office, Washington, D. C., June 25, 1940).

[11] T. Alfrey, Jr., Mechanical behavior of high polymers (Interscience Publishers, New York, N. Y., 1948).

[12] H. Leaderman, Proposed nomenclature for elastic and inelastic behavior of high polymers, J. Colloid Sc. **4,** 193 (1949).

[13] Standard method of test for internal tearing resistance of paper, D 689–44, ASTM Standards 1946, Part III–B (Am. Soc. Test. Mats., Philadelphia, Pa.).

[14] S. L. Madorsky and S. Straus, Pyrolytic fractionation of polystyrene in a high vacuum and mass spectrometer analysis of some of the fractions, Ind. Eng. Chem. **40,** 848 (1948); J. Research NBS **40,** 417 (1948) RP1886.

[15] L. F. Feiser and M. Feiser, Organic Chemistry (D. C. Health and Co., Boston, Mass., 1944).

[16] American Society for Testing Materials tentative method of test for kinematic viscosity D 445–46T.

[17] J. W. McElwain, Pump for volatile or toxic liquids in viscometers, Anal. Chem. **21,** 194 (Jan. 1949).

[18] W. O. Baker and C. S. Fuller, Macromolecular disorder in linear polyamides. Relation of structure to physical properties of copolyamides, J. Am. Chem. Soc. **64,** 2399 (1942).

[19] W. O. Baker and C. S. Fuller, Intermolecular forces and chain configuration in linear polymers—The effect of *N*-methylation on the *X*-ray structures and properties of linear polyamides, J. Am. Chem. Soc. **65,** 1120 (1943).

[20] J. B. Nichols, The colloid aspects of nylon. Published in Colloid Chemistry by J. Alexander **6,** 1077 (Reinhold Publishing Corp., New York, N. Y., 1946).

[21] W. H. Smith and C. P. Saylor, Optical and dimensional changes which accompany the freezing and melting of hevea rubber, J. Research NBS **21,** 257 (1938) RP1129.

[22] C. M. Langkammerer and W. E. Catlin, Spherulite formation in polyhexamethylene adipamide, J. Polymer Sci **3,** 305 (1948).

[23] J. B. Speakman and A. K. Saville, Some physical properties of nylon, J. Textile Inst. **37,** 271 (1946).

[24] G. P. Thomson, Electron diffraction, J. Inst. Metals **69,** 191 (1943).

[25] W. O. Baker and C. S. Fuller, Intermolecular forces and chain configuration in linear polymers. The effect of *N*-methylation on the *X*-ray structures and properties of linear polyamides. Annals of the New York Academy of Sciences **44,** Art. 4, 329 (Nov. 12, 1943).

[26] J. Errera and H. S. Sack, Dielectric properties of animal fibers, Ind. Eng. Chem. **35,** 712 (1943).

[27] American Society for Testing Materials tentative methods of test for power factor and dielectric constant of electrical insulating materials, D 150–47T.

[28] J. M. DeBell, W. C. Goggin, and W. E. Gloor, German plastics practice (DeBell & Richardson, Inc., Hazardville, Conn., 1946).

[29] F. O. Rice and K. Rice, The aliphatic free radicals (The Johns Hopkins University Press, Baltimore, Md., 1935).

[30] G. A. Anslow and S. C. Nassar, The absorption of ultraviolet energy by the peptide linkage, J. Opt. Soc. Am. **31,** 118 (1941).

[31] G. A. Anslow and E. R. Lyman, A. spectrophotometric study of glutathione, J. Opt. Soc. Am. **31,** 114 (1941).

[32] I. M. Klotz, Ultraviolet absorption spectroscopy, J. Chem. Education **22,** 328 (1945).

[33] D. C. Carpenter, Splitting the CONH linkage by means of ultraviolet light, J. Am. Chem. Soc. **62,** 289 (1940).

[34] J. S. Mitchell, Recent advances in the study of monolayers, Nature **137,** 502 (1936).

[35] E. K. Rideal and J. S. Mitchell Photochemical reactions in monolayers. I. Photochemical properties of the ketoimino linkage, Proc. Roy. Soc. (London) [A] **159,** 206 (1937).

[36] A. J. Allen, R. E. Steiger, M. A. Magill, and R. G. Franklin, XXIII, Amino-acids, acyl-amino-acids, dipeptides, acyl-dipeptides, and derivatives of these compounds. II. Effects of irradiation with cathode rays and ultraviolet light, J. Biochem. **31,** 195 (1937).

[37] J. P. Becher and P. Szendrö, Spectroscopic and chemical investigations of the degradation of proteins by ultraviolet rays, Pflügers Archiv für die Gesamte Physiologie des Menschen und der Tiere **228,** 755 (1931).

[38] A. E. Mirsky and Linus Pauling, On the structure of native, denatured, and coagulated proteins, Proc. Nat. Acad. Sci. **22,** 439 (1936).

[39] D. M. Wrinch, On the pattern of proteins, Proc. Roy. Soc. (London) [A] **160,** 59 (1937).
[40] H. Neurath, The influence of denaturation on the spreading of proteins on a water surface, J. Phys. Chem. **40,** 361 (1936).
[41] C. Ellis and A. A. Wells, The chemical action of ultraviolet rays (The Chem. Catalog Co., New York, N. Y., 1925).
[42] H. W. Thompson and P. Torkington, The infrared spectra of compounds of high molecular weight, Trans. Faraday Soc. **41,** 246 (1945).
[43] A. M. Buswell, Karl F. Krebs, and W. H. Rodebush, The infrared absorption of proteins in the 3μ region, J. Phys. Chem. **44,** 1126 (1940).
[44] S. E. Darmon and G. B. B. M. Sutherland, Infrared spectra and structure of natural and synthetic polypeptides, J. Am. Chem. Soc. **69,** 2074 (1947).
[45] R. B. Barnes, R. C. Gore, U. Liddel, and V. Z. Williams, Infrared spectroscopy (Reinhold Publishing Corp., New York, N. Y., 1944).
[46] J. E. Field, D. E. Woodford, and S. D. Gehman, Applications of infrared methods in the structural examination of synthetic rubber, J. Applied Phys. **17,** 386 (1946).
[47] Frank Baker, The viscosity of cellulose nitrate solutions, J. Chem. Soc. **103,** 1653 (1913).
[48] W. O. Baker and C. S. Fuller, Thermal evidence of crystallinity in linear polymers, Ind. Eng. Chem. **38,** 272 (1946).
[49] D. D. Coffman, G. J. Berchet, W. R. Peterson, and E. W. Spanagel, Polymeric amides from diamines and diabasic acids, J. Polymer Sci. **2,** 306 (1947).
[50] O. L. Sponsler, J. D. Bath, and J. W. Ellis, Water bound to gelatin as shown by molecular structure studies, J. Phys. Chem. **44,** 996 (1940).
[51] C. S. Fuller, W. O. Baker, and N. R. Pope, Crystalline behavior of linear polyamides. Effect of heat treatment, J. Am. Chem. Soc. **62,** 3275 (1940).
[52] W. O. Baker, Nature of the solid state of chain poly mers S. B. Twiss, Advancing fronts in chemistry, vol. I, High Polymers, chapter 8 (Reinhold Publishing Corp., New York, N. Y., 1945).
[53] R. Brill, Behavior of polyamides on heating, J. prakt. Chem. **161,** 49 (1942).
[54] Leonard Glatt and J. W. Ellis, Near infrared absorption of nylon films: dichroism and rupture of NH.O bonds on melting, J. Chem. Phys. **16,** 551 (1948).
[55] W. O. Baker and W. A. Yager, The relation of dielectric properties to structure of crystalline polymers. II. Linear polyamides, J. Am. Chem. Soc. **64,** 2171 (1942).
[56] R. Hill and E. E. Walker, Polymer constitution and fiber properties, J. Polymer Sci. **3,** 609 (1948).
[57] B. S. Biggs, C. J. Frosch, and R. H. Erickson, Melting points of *N*-substituted polyamides, Ind. Eng. Chem. **38,** 1016 (1946).
[58] W. E. Catlin, E. P. Czerwin, and R. H. Wiley, Multiingredient polyamides, J. Polymer Sci. **2,** 412 (1947).
[59] I. C. Funcke, Über die zwischen linearen Kettenmolekülen mit Peptidbindungen wirkenden intermolekularen Kräfte, Naturwissenschaften **29,** 517 (1941).
[60] E. I. du Pont de Nemours and Co. and G. D. Graves, Polymeric materials, Brit. Patent 549,370 (Nov. 18, 1942).
[61] G. B. Taylor, Improved polyamides, U. S. Patent 2,374,145 (April 17, 1945).
[62] C. Coolidge, Plasticizing synthetic linear polyamides for making sheets, filaments, etc., U. S. Patent 2,265,119 (Dec. 2, 1942).
[63] M. M. Brubaker, Plasticized polyamides, U. S. Patent 2,374,576 (April 24, 1945).
[64] H. Mark, The mechanical properties of high polymers, Trans. Faraday Soc. **43,** 451 (1947).
[65] E. L. Wittbecker, R. C. Houtz, and W. W. Watkins, Elastic *N*-substituted polyamides, Ind. Eng. Chem. **40,** 875 (May 1948).
[66] A. I. Goldberg, W. P. Hohenstein, and H. Mark, Intrinsic viscosity—molecular weight relationship for polystyrene, J. Polymer Sci. **2,** 503 (1947).
[67] P. J. Flory, Molecular weights and intrinsic viscosities of polyisobutylenes, J. Am. Chem. Soc. **65,** 372 (1943).

WASHINGTON, July 21, 1950.

Journal of Research of the National Bureau of Standards Vol. 46, No. 5, May 1951 Research Paper 2211

Radiation Properties of Spherical Antennas as a Function of the Location of the Driving Force[1]

Philip R. Karr

A theoretical analysis is made of the radiation properties of a perfectly conducting sphere excited as an antenna by a driving force that acts in the θ direction in a narrow strip around the circle of colatitude $\theta=\theta_0$ on the surface of the sphere. As the location θ_0 is varied, the radiation pattern, together with the current distribution and the input admittance, change. In the present paper some of these effects are analyzed, it is believed for the first time. In previous work only the case of center feed is treated.

Unless θ_0 equals 90 degrees, the radiation pattern is not symmetrical with respect to the equatorial plane. Some interesting features of this asymmetry are discovered in the course of the analysis that have also been found experimentally in certain classes of antennas driven asymmetrically. The radiation conductance, which is proportional to the amount of power radiated for a given applied voltage, varies in a complicated way with θ_0. However, for a sphere whose radius is not too large compared with the wavelength, this trend is approximately as $\sin^4\theta_0$. In some cases the radiation conductance is not a maximum for $\theta_0=90$ degrees, but is greater when the feeding strip is somewhat to one side of the equatorial plane. Other features of the radiation are analyzed. Reasons are given for believing that the idealization of the feed conditions does not prevent the theory from giving experimentally pertinent results for the radiation properties.

I. Introduction

The center-fed antenna in various shapes has been the subject of considerable theoretical and experimental research. On the other hand, the study of antennas not necessarily fed at the center has apparently received little attention in the theoretical literature. There has recently been a certain amount of systematic experimental work in this field [1, 2] [2], and there are a number of practical applications of such antennas [3, 4]. It therefore appears to be of some interest to attempt a theoretical study of asymmetrically fed antennas. In attempting such a study, it is necessary to find an idealization of the problem that can be solved mathematically and at the same time yields some physical insight into the nature of the results. In the present paper the spherical antenna is chosen for study. This form has the advantage that an idealized boundary value problem duplicating actual conditions to a certain extent can be set up and solved.

The spherical antenna, while not expected to be a popular type for applications, is in a number of respects not radically different from more conventional antennas, so that the results obtained can be of qualitative assistance in the study of such antennas. The problem of the prolate spheroid antenna with asymmetrical feed can in principle be solved as a boundary value problem in a manner similar to that presented here for the sphere, but tables of spheroidal wave functions are at present rather inadequate for any detailed study. The present report is in some respects an extension of the work of Stratton and Chu [5] on the spherical *center-fed* antenna. A number of the equations found are generalizations of corresponding equations already found for the center-fed antenna. The generalization of the location of the feed introduces some interesting effects. These, together with some other matters, are discussed in some detail. It is hoped that this paper will help to stimulate some further work on the subject.

[1] A dissertation submitted to the Faculty of the Graduate School of Arts and Sciences of the Catholic University of America in partial fulfillment of the requirements for the degree of Doctor of Philosophy.

[2] Figures in brackets indicate the literature references at the end of this paper.

II. Statement of the Problem and Its Formal Solution

We consider a conducting sphere, figure 1, of radius a, excited as an antenna by a driving emf, which acts in the θ direction in a narrow strip around the circle of colatitude $\theta=\theta_0$ on the surface of the sphere. The center of the sphere is the origin of a system of spherical coordinates, r, θ, ϕ. As the location θ_0 is varied, the radiation pattern, together with the current distribution and the input admittance, change. The purpose of this paper is to describe and, as far as possible, to "understand" some of these effects. Stating the boundary conditions more precisely, we are applying a field E' across a small zone of the conducting spherical surface. This causes a field E to appear in space. The value of the tangential component E_θ of E on the surface is such that $E_\theta+E'=0$ everywhere on the spherical surface since we shall assume perfect conductivity. The solution of the boundary value problem consists in finding wave solutions of Maxwell's equations, which on the surface of the antenna reduce to $E_\theta=-E'$.

We consider wave solutions of Maxwell's equations in the charge-free and current-free space around the sphere that will satisfy the correct boundary conditions on the sphere. The appropriate solutions (eq 4) will be in the form of rather well-known spherical fields. However, for the sake of completeness we shall derive these solutions. Let the medium be characterized by μ, ϵ, and let the time variation be as $e^{j\omega t}$. Then Maxwell's equations in mks rationalized units reduce to

$$\nabla \times \boldsymbol{E} = -j\omega\mu \boldsymbol{H}, \tag{1}$$

$$\nabla \times \boldsymbol{H} = j\omega\epsilon \boldsymbol{E}. \tag{2}$$

(The divergence equations are automatically satisfied in this case by solutions of (1) and (2), since the divergence of the curl of a vector is zero). In spherical coordinates, (1) and (2) become

$$\left.\begin{aligned} &\frac{1}{r\sin\theta}\left[\frac{\partial}{\partial\theta}(E_\phi \sin\theta) - \frac{\partial E_\theta}{\partial\phi}\right] = -j\omega\mu H_r \\ &\frac{1}{r}\left[\frac{1}{\sin\theta}\frac{\partial E_r}{\partial\phi} - \frac{\partial}{\partial r}(rE_\phi)\right] = -j\omega\mu H_\theta \\ &\frac{1}{r}\left[\frac{\partial}{\partial r}(rE_\theta) - \frac{\partial E_r}{\partial\theta}\right] = j\omega\mu H_\phi \end{aligned}\right\} \tag{1a}$$

$$\left.\begin{aligned} &\frac{1}{r\sin\theta}\left[\frac{\partial}{\partial\theta}(H_\phi \sin\theta - \frac{\partial H_\theta}{\partial\phi}\right] = j\omega\epsilon E_r \\ &\frac{1}{r}\left[\frac{1}{\sin\theta}\frac{\partial H_r}{\partial\phi} - \frac{\partial}{\partial r}(rH_\phi)\right] = j\omega\epsilon E_\theta \\ &\frac{1}{r}\left[\frac{\partial}{\partial r}(rH_\theta) - \frac{\partial H_r}{\partial\theta}\right] = j\omega\epsilon E_\phi \end{aligned}\right\} \tag{2a}$$

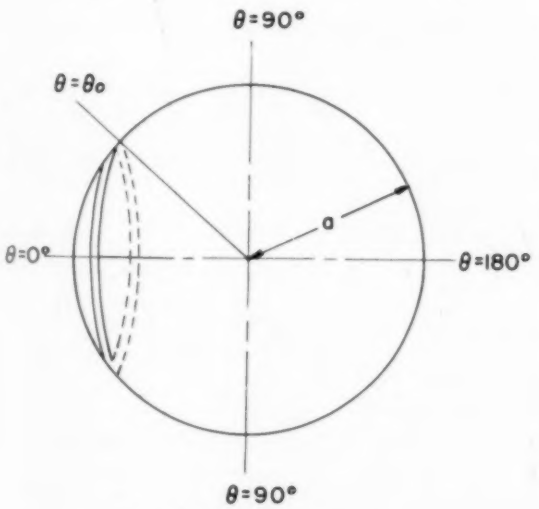

FIGURE 1. *Spherical antenna.*

The applied emf acts in the θ direction in a narrow zone around the sphere at $r=a$, $\theta=\theta_0$.

Now in the present problem it is clear that $\partial/\partial\phi = 0$. Using this relation in (1a) and (2a), we find immediately that the equations split into two sets of equations, one containing only H_ϕ, E_θ, and E_r, the other containing only E_ϕ, H_θ, and H_r. Solutions of these two sets are known as *TM* (transverse magnetic) and *TE* (transverse electric) solutions, respectively. In the present problem, it is clear that the *TE* solutions are inappropriate. We shall be able to satisfy our conditions with *TM* solutions; that is, solutions for which the magnetic lines are circles in planes perpendicular to the polar axis with their centers on this axis, and for which the electric lines lie in meridian planes.

Write the three equations containing H_ϕ, E_θ, E_r:

$$\frac{\partial}{\partial r}(rE_\theta) - \frac{\partial E_r}{\partial\theta} = -j\omega\mu(rH_\phi).$$

$$\frac{1}{r\sin\theta}\frac{\partial}{\partial\theta}(H_\phi \sin\theta) = j\omega\epsilon E_r,$$

$$-\frac{\partial}{\partial r}(rH_\phi) = j\omega\epsilon(rE_\theta).$$

When we differentiate the last two equations, with respect to θ and r, respectively, and substitute in the first, we obtain

$$\frac{\partial^2}{\partial r^2}(rH_\phi) + \frac{1}{r^2}\frac{\partial}{\partial\theta}\left[\frac{1}{\sin\theta}\frac{\partial}{\partial\theta}(rH_\phi \sin\theta)\right] + k^2(rH_\phi) = 0,$$

where

$$k = \omega\sqrt{\mu\epsilon} = \frac{2\pi}{\lambda}.$$

This equation is separable in the form $rH_\phi = R(r)\Theta(\theta)$. Calling the separation constant $n(n+1)$, we obtain

$$\frac{r^2}{R}\frac{\partial^2 R}{\partial r^2} + k^2r^2 = -\frac{1}{\Theta}\frac{d}{d\theta}\left[\frac{1}{\sin\theta}\frac{d}{d\theta}(\Theta\sin\theta)\right] = n(n+1).$$

Making the substitution $x = \cos\Theta$, the equation for Θ becomes

$$(1-x^2)\frac{d^2\Theta}{dx^2} - 2x\frac{\partial\Theta}{\partial x} + \left[n(n+1) - \frac{1}{1-x^2}\right]\Theta = 0,$$

which is the equation for the associated Legendre functions satisfied by the functions $P_n^1(x)$ and $Q_n^1(x)$ [6]. Only $P_n^1(x)$ can be used in our problem, because the function $Q_n^1(x)$ has singularities at $x = \pm 1$.

Returning to the r equation, we find that the substitution $P = R/\sqrt{r}$ yields

$$\frac{\partial^2 P}{\partial r^2} + \frac{1}{r}\frac{\partial P}{\partial r} + \left[k^2 - \frac{\left(n+\frac{1}{2}\right)^2}{r^2}\right]P = 0$$

which is Bessel's differential equation of order $n+\frac{1}{2}$,

whose general solution is of the form

$$P=C_n J_{n+\frac{1}{2}}(kr)+D_n N_{n+\frac{1}{2}}(kr).$$

Since we desire the solution to approach a travelling wave as $r\to\infty$, we use the linear combination (Hankel function),

$$H^{(2)}_{n+\frac{1}{2}}(kr)=J_{n+\frac{1}{2}}(kr)-jN_{n+\frac{1}{2}}(kr). \tag{3}$$

We then have as our generic *TM* solution, after some manipulation,

$$H_\phi=A_n r^{-1/2}P^1_n(\cos\theta)H^{(2)}_{n+\frac{1}{2}}(kr), \tag{4a}$$

$$E_\theta=\frac{A_n}{j\omega\epsilon}r^{-3/2}P^1_n(\cos\theta)[nH^{(2)}_{n+\frac{1}{2}}(kr)-krH^{(2)}_{n-\frac{1}{2}}(kr)], \tag{4b}$$

$$E_r=\frac{A_n}{j\omega\epsilon}\frac{r^{-3/2}}{\sin\theta}\frac{\partial}{\partial\theta}P^1_n(\cos\theta)[H^{(2)}_{n+\frac{1}{2}}(kr)]. \tag{4c}$$

These are the fields of electric dipoles, quadrupoles, and in general 2^n-poles. The *TE* solutions, not used here, represent the fields of magnetic 2^n-poles.

Our solution will be a superposition of *TM* waves (eq 4). To find the coefficients A_n we expand the applied field E' in a series of associated Legendre polynomials $P^1_n(\cos\theta)$:

$$E'(\theta)=\frac{V}{a}\sum_{n=1}^{\infty}a_n P^1_n(\cos\theta). \tag{5}$$

In (5) we have introduced the applied voltage V defined by

$$V=\int_0^\pi E'(\theta)a\,d\theta. \tag{6}$$

The letter a, it will be recalled, stands for the radius of the sphere. This normalization allows the a_n to be pure numbers, whereas $E'(\theta)$ will have the dimensions of field strength (volts per meter). Multiplying (5) by $P^1_n(\cos\theta)\sin\theta\,d\theta$, and integrating from 0 to π, we have, on account of the orthogonality and normalization properties of $P^1_n(\cos\theta)$, the following expression for a_n:

$$\frac{V}{a}a_n=\frac{2n+1}{2n(n+1)}\int_0^\pi E'(\theta)P^1_n(\cos\theta)\sin\theta\,d\theta \tag{7}$$

Now from (4),

$$E_\theta|_{r=a}=\frac{a^{-3/2}}{j\omega\epsilon}\sum_{n=1}^{\infty}A_n P^1_n\cos\theta\,[nH^{(2)}_{n+\frac{1}{2}}(ka)-kaH^{(2)}_{n+\frac{1}{2}}(ka)] \tag{8}$$

Comparing (8) and (5) and remembering that on the surface, $E_\theta=-E'$, we have for A_n:

$$\frac{a}{V}A_n=-j\omega\epsilon a^{3/2}a_n[nH^{(2)}_{n+\frac{1}{2}}(ka)-kaH^{(2)}_{n+\frac{1}{2}}(ka)]^{-1} \tag{9}$$

Thus the solution of our problem is a superposition of the waves given in eq 4, with the A_n given by eq 9. The manner of deriving the A_n guarantees that the boundary conditions are satisfied.

The values of the a_n and therefore of the A_n, depend upon the assumed form of $E'(\theta)$. In most of what follows we shall specialize by assuming $E'(\theta)$ takes the form of a "delta" function applied at the feed point $\theta=\theta_0$:

$$E'(\theta)=\frac{V}{a}\delta(\theta-\theta_0). \tag{10}$$

This means that

$$a_n=\frac{2n+1}{2n(n+1)}P^1_n(\cos\theta_0)\sin\theta_0. \tag{11}$$

It should be noted that if $E'(\theta)$ is applied over a small *finite* zone and does not vary wildly with θ over the zone, then the a_n found in such a case would be practically the same as in eq 11 except for high values of n (cf. eq 53 to 55). For this reason, results based upon (11), which are correct for an infinitesimal zone are almost correct for a small finite zone, except for those results that depend upon high values of n.

III. The Radiation Field

1. General Relations

Having written down the formal solution of our problem, we shall now investigate in more detail some of the important characteristics of our antenna. Let us first consider the "radiation field", (that part of the field that persists at large values of r). We note that as $r\to\infty$, the second term of (4b) dominates, and

$$E_{rad}=\sum_{n=1}^{\infty}\frac{A_n}{j\omega\epsilon}r^{-1/2}k\,P^1_n(\cos\theta)H^{(2)}_{n-\frac{1}{2}}(kr), \tag{12}$$

where E_{rad} denotes the radiation part of E_θ.

We see also, from (4b) and 4c) that as $r\to\infty$, $E_r/E_\theta\to 0$, so that the radiation field is purely transverse (as it should be). Now as r becomes very large, we have the well-known asymptotic expression for the Hankel function:

$$H^{(2)}_{n-\frac{1}{2}}(kr)\to\sqrt{\frac{2}{\pi kr}}e^{-jkr}e^{(jn\pi)/2}=j^n\sqrt{\frac{2}{\pi kr}}e^{-jkr}. \tag{13}$$

Combining (13), (12), and (9), we find

$$\frac{E_{rad}}{V}=\sqrt{\frac{2ka}{\pi}}\,\frac{e^{-jkr}}{r}\sum_{n=1}^{\infty}a(n,\theta_0)L(n,ka)P^1_n(\cos\theta), \tag{14}$$

where

$$a(n,\theta_0)\equiv a_n$$

$$=\frac{2n+1}{2n(n+1)}P^1_n(\cos\theta_0)\sin\theta_0,\ (\text{using (11)}), \tag{15}$$

and

$$L(n,ka)\equiv j^n\left[ka\,H_{n-\frac{1}{2}}^{(2)}(ka)-nH_{n-\frac{1}{2}}^{(2)}(ka)\right]^{-1}. \quad (16)$$

We find also, in the radiation region

$$H_\phi=\sqrt{\frac{\epsilon}{\mu}}\,E_\theta\equiv\frac{1}{Z_0}E_\theta. \quad (17)$$

Thus the radiation field decreases as $1/r$, as it should. Its θ variation is a superposition of the functions P_n^1 (cos θ). The contribution of each order n depends upon the nature and location of the excitation through $a(n,\theta_0)$ and upon the size of the sphere through $L(n,ka)$.

Before considering typical radiation patterns, it is useful to investigate the convergence of the series for E_{rad}. We have for $n\gg x$, the Debye asymptotic formula [7]

$$H_n^{(2)}(x)\sim\sqrt{\frac{2}{\pi x\,\sinh\alpha}}\exp\left[x(\alpha\cosh\alpha-\sinh\alpha)+j\frac{\pi}{2}\right],$$

where $n=x\cosh\alpha$.
Writing x/n=sech $\alpha=\zeta$, we obtain

$$H_n^{(2)}(x)=\sqrt{\frac{2}{\pi n\left(1-\frac{1}{\zeta^2}\right)^{1/2}}}\exp\left\{j\frac{\pi}{2}+n\sqrt{1-\zeta^2}\right.$$
$$\left.\left[\frac{1}{\zeta}\ln\left(\frac{1}{\zeta}+\sqrt{\frac{1}{\zeta^2}-1}\right)-\sqrt{\frac{1}{\zeta^2}-1}\right]\right\}$$

Disregarding small terms, the expression in braces becomes

$$\sim j\frac{\pi}{2}+n\left(\frac{1}{\zeta}\ln\frac{2}{\zeta}-\frac{1}{\zeta}\right),$$

so we find the approximate expression

$$H_n^{(2)}(x)\sim j\sqrt{\frac{2}{\pi n}}\left(\frac{2n}{xe}\right)^{n^2/x} \qquad x\ll n. \quad (18)$$

Substituting in (16) and disregarding small terms, we find

$$L(n,ka)\approx-j^{n-1}\sqrt{\frac{n}{2n}}\left(\frac{2n+1}{kae}\right)^{-\frac{\left(n+\frac{1}{2}\right)^2}{ka}}. \quad (19)$$

For the associated Legendre polynomial we have the asymptotic formula [8], for n large

$$P_n^1(\cos\theta)\approx\frac{2n^{1/2}}{\sqrt{2\pi\sin\theta}}\cos\left[\left(n+\frac{1}{2}\right)\theta+\frac{\pi}{4}\right]. \quad (20)$$

One sees then that on account of the factor

$$\left(\frac{2n+1}{kae}\right)^{-\frac{\left(n+\frac{1}{2}\right)^2}{ka}}=\left(\frac{2n+1}{kae}\right)^{-\frac{(2n+1)^2}{4ka}}$$

in (19), the series (14) for E_{rad} is convergent and that the terms fall off exceedingly rapidly as n becomes large. In physical terms, this means that the high-order modes contribute negligibly to the radiation. In practice we find that we may terminate the series around $n\approx 2ka$. This can be seen roughly by examining figures 2,a and 2,b, which show the real and imaginary parts of $L(n,ka)$ plotted versus ka.

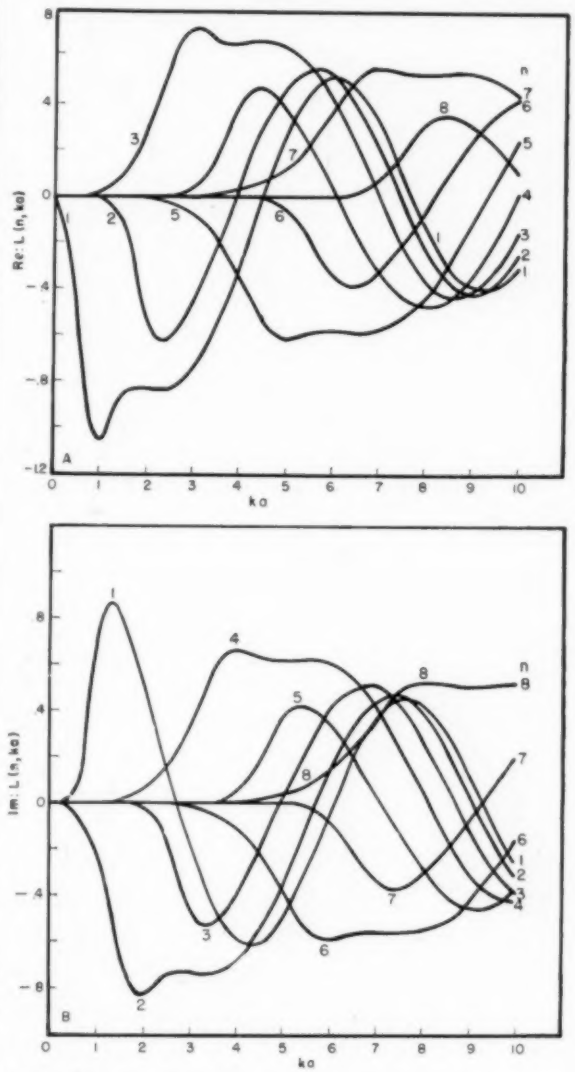

FIGURE 2. *L (n, ka) as a function of ka for several values of n.*
A, real part; B, imaginary part.

2. Small Spheres

It is of some interest to study the radiation from a small sphere ($ka \ll 1$). We expect on general grounds that as the radiating system becomes smaller (relative to the wavelength), the lowest (dipole) mode should become dominant. This is confirmed by an examination of figures 2,a and 2,b; as ka decreases considerably below 1, only 1 mode (represented by the real part of $L(1, ka)$) contributes appreciably.

We may find an explicit expression for the effective dipole moment of the small spherical antenna. We have

$$H^{(2)}_{1/2}(ka) = j\sqrt{\frac{2}{\pi ka}}\, e^{-jka}$$

$$H^{(2)}_{3/2}(ka) = \sqrt{\frac{2}{\pi ka}}\, e^{-jka}\left(\frac{j}{ka} - 1\right)$$

as $ka \to 0$, these become

$$H^{(2)}_{1/2}(ka) \approx j\sqrt{\frac{2}{\pi ka}},$$

$$H^{(2)}_{3/2}(ka) \approx \frac{j}{ka}\sqrt{\frac{2}{\pi ka}},$$

so that $L(1, ka) \equiv j\left[ka\, j\sqrt{\frac{2}{\pi ka}} - \frac{j}{ka}\sqrt{\frac{2}{\pi ka}}\right]^{-1}$

$$\approx -\sqrt{\frac{\pi}{2}}\,(ka)^{3/2} \qquad ka \ll 1. \tag{21}$$

One then finds, for the limiting case of small spheres,

$$\frac{E_{rad}}{V} \approx -(ka)^2\,\frac{e^{-jkr}}{r}\,\frac{3}{4}\,P^1_1(\cos\theta)\sin\theta_0 P^1_1(\cos\theta_0), \tag{22}$$

a radiation pattern like that for the Hertzian dipole. Since there is only one mode, the off-center feed does not introduce asymmetry in the radiation pattern, but merely reduces the field radiated for a given applied voltage in the ratio $P^1_1(\cos\theta_0)\sin\theta_0 : 1 = \sin^2\theta_0 : 1$.

The radiation field of a dipole of dipole moment M is

$$E_{rad} = \frac{-Mk^2}{4\pi\epsilon}\,\frac{e^{-jkr}}{r}\sin\theta \qquad [9]. \tag{23}$$

Comparing this with (22) we find that the effective dipole moment of the small sphere is

$$M = 3\pi\epsilon V a^2 \sin^2\theta_0. \tag{24}$$

3. Moderate-Sized Spheres

We now proceed to investigate the radiation patterns of spheres comparable in size to a wavelength. In figures 3, 4, and 5, we have plotted the power radiation patterns $|E_{rad}|^2$, all normalized to the same maximum value of $|E_{rad}|^2$, for $ka = 1$, $1\frac{1}{2}$, and 2, and several values of θ_0. An examination of these patterns discloses an interesting feature, which may be described roughly as follows: as the feedpoint θ_0 is moved towards 0°, the patterns become more asymmetrical and tend to lean more and more away from the feedpoint, into the hemispheres for which $90° \leq \theta \leq 180°$ (henceforth to be called the "forward" hemisphere). Upon computing the power radiated into the "forward" and "rear" ($0° \leq \theta \leq 90°$) hemispheres, by integrating the Poynting vector over the two hemispheres, we find that there is more power radiated into the forward hemisphere. This is equivalent to the statement that

$$\int_{\pi/2}^{\pi} |E_{rad}|^2 \sin\theta\, d\theta > \int_0^{\pi/2} |E_{rad}|^2 \sin\theta\, d\theta.$$

The effect of θ_0 upon the appearance of the radiation pattern is marked only when the antenna has appreciable size relative to a wavelength. This has already been implied in the discussion of small spheres.

The asymmetry we have found when $\theta_0 \neq 90°$ is due, mathematically speaking, to the fact that when $\theta_0 \neq 90°$, both the even-numbered and odd-numbered modes $P^1_n(\cos\theta)$ are excited, whereas when $\theta_0 = 90°$ only the odd-numbered modes are excited. The odd-numbered modes are symmetric about $\theta = 90°$, the even-numbered modes are antisymmetric, that is,

$$P^1_n(90° + \delta) = -P^1_n(90° - \delta),\ n \text{ even}$$

$$P^1_n(90° + \delta) = P^1_n(90° + \delta),\ n \text{ odd}$$

4. End Feed

In figures 3, 4, and 5, discussed above, there are radiation patterns purporting to have the driving force at $\theta_0 = 0°$. This calls for an explanation. Of course, as θ_0 approaches 0, the radiated power approaches zero for a finite applied voltage V. This is shown by our equations and agrees with the experience of experimental antenna workers who find that an antenna becomes a poor radiator as the feed point is moved toward the end. Some qualitative details on this point are given below. Although the radiation approaches zero, the radiation *pattern* approaches a stationary configuration. We are interested in obtaining this limiting pattern, which will serve as a good approximation for the patterns obtained when θ_0 is not quite zero; that is, when the antenna is fed near one pole.

To accomplish this we must see what form eq 14 takes as $\theta_0 \to 0$. The part containing θ_0 is

$$a(n, \theta_0) \equiv \frac{2n+1}{2n(n+1)}\,P^1_n(\cos\theta_0)\sin\theta_0. \tag{15}$$

We wish to express $P^1_n(\cos\theta_0)$ as a Taylor's series of the form

$$P_n^1(\cos\theta_0) = g(n)\theta_0 + h(n)\theta_0^2 + \ldots . \qquad (25)$$

Write the well-known formula [10]

$$P_n(\cos\theta_0) = \frac{1\cdot 3\cdot 5\ldots(2n-1)}{n!}\left[(\cos\theta_0)\right.$$
$$-\frac{n(n-1)(\cos\theta_0)^{n-2}}{(2n-1)2}$$
$$\left.+\frac{n(n-1)(n-2)(n-3)(\cos\theta_0)^{n-4}}{(2n-1)(2n-3)2\cdot 4}+\cdots\right] \qquad (26)$$

and

$$P_n^1(\cos\theta_0) = -\frac{d}{d\theta}P_n(\cos\theta_0)$$
$$= \frac{1\cdot 3\cdot 5\ldots(2n-1)}{n!}\sin\theta\left[n(\cos\theta_0)^{n-1}\right.$$
$$-\frac{n(n-1)(n-2)(\cos\theta_0)^{n-3}}{(2n-1)2}$$
$$\left.+\frac{n(n-1)(n-2)(n-3)(n-4)(\cos\theta_0)^{n-5}}{(2n-1)(2n-3)2\cdot 4}+\cdots\right] \qquad (27)$$

Then

$$g(n) = \frac{1\cdot 3\cdot 5\ldots(2n-1)}{n!}\left[n-\frac{n(n-1)(n-2)}{(2n-1)2}\right.$$
$$\left.+\frac{n(n-1)(n-2)(n-3)(n-4)}{(2n-1)(2n-3)2\cdot 4}+\cdots\right]$$

From this,

$$g(n+1)-g(n) = (n+1)\left[\frac{1\cdot 3\cdot 5\cdots(2n-1)}{n!}\right.$$
$$-\frac{1}{2}\frac{1\cdot 3\cdot 5\ldots 2n-3}{(n-2)!}$$
$$\left.+\frac{1}{2\cdot 4}\frac{1\cdot 3\cdot 5\ldots(2n-5)}{(n-4)!}+\cdots\right] \qquad (28)$$

But referring to eq 26, we see that the expression in square brackets in eq 28 is $P_n(1)\equiv 1$, so that

$$g(n+1)-g(n) = n+1,$$

or

$$g(n) = \frac{n(n+1)}{2}. \qquad (29)$$

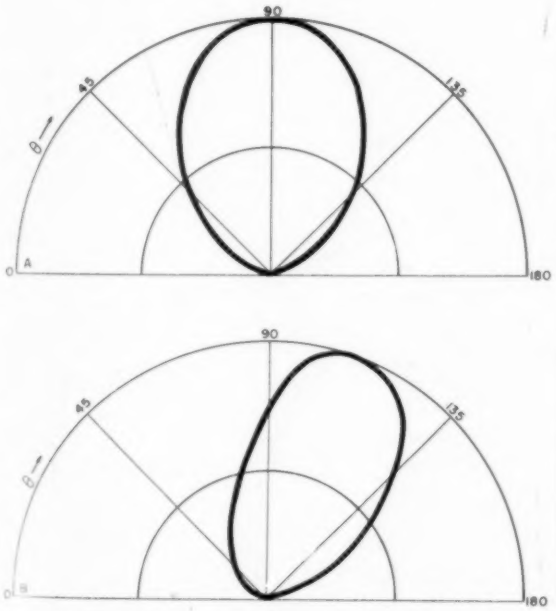

FIGURE 3. *Power radiation patterns for ka=1.*

The patterns show $|E_{rad}|^2$ as a function of θ. Both patterns are normalized to the same arbitrary maximum value of $|E_{rad}|^2$. A, $\theta_0=90°$; B, $\theta_0=0°$.

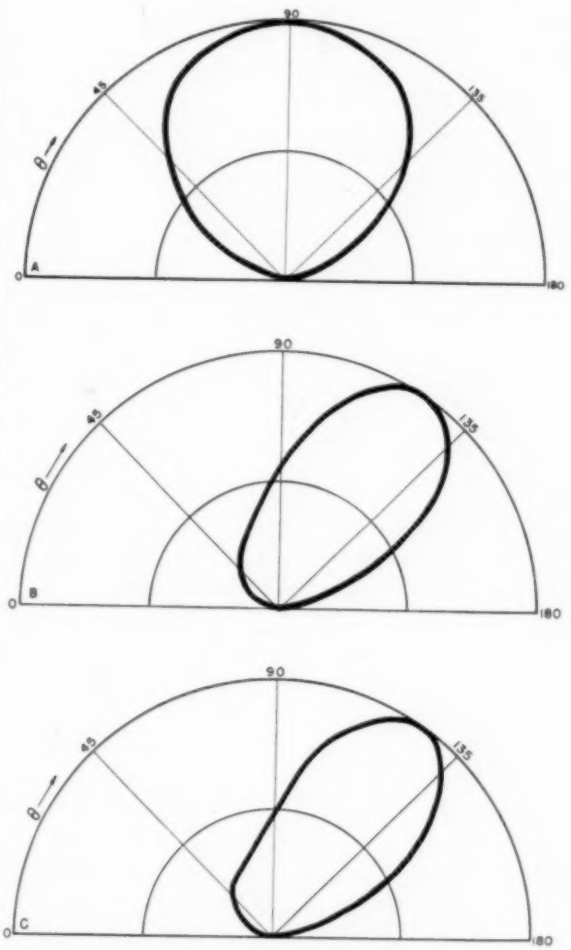

FIGURE 4. *Power radiation patterns for ka=1½.*

A, $\theta_0=90°$; B, $\theta_0=45°$; C, $\theta_0=0°$. The normalization is similar to that in figure 3.

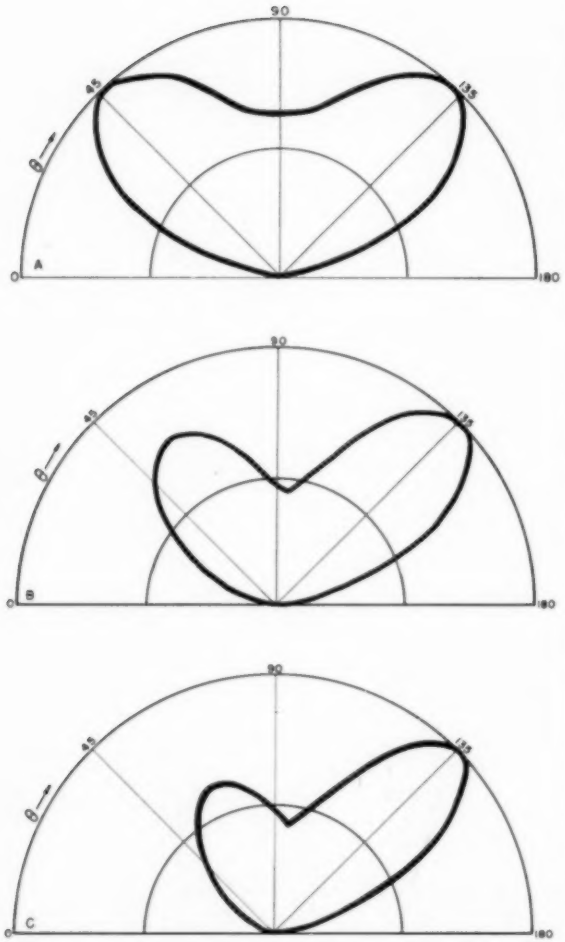

FIGURE 5. *Power radiation patterns for ka=2.*

A, $\theta_0=90°$; B, $\theta_0=45°$; C, $\theta_0=0°$. The normalization is similar to that in figure 3.

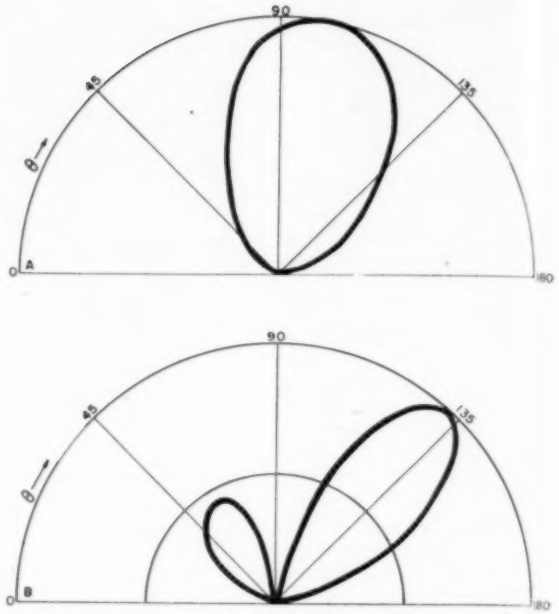

FIGURE 6. *Power radiation patterns for end-fed cylinders.*

Ratio of diameter to wavelength, 0.04. A, Ratio of length to wavelength, ½; B, ratio of length to wavelenth, 1. The normalization is similar to that in figure 3.

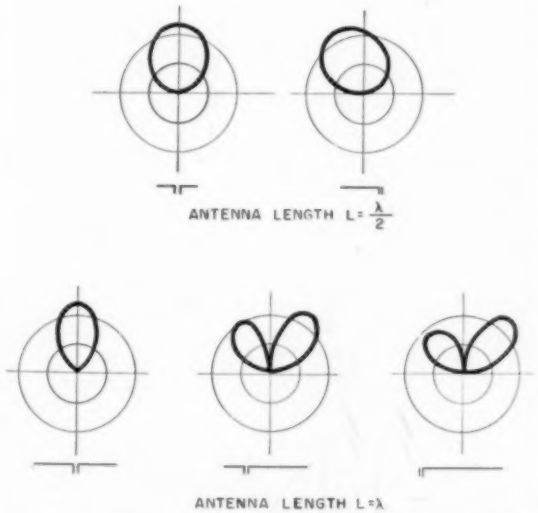

FIGURE 7. *Effect of feed point upon radiation patterns of wire antennas.*

Relative position of the feed point is shown under each pattern. Relative field strength $|E_{\tau\phi}|$ is shown. This material is adapted from figures 1 and 2 of reference [2] by permission of the McGraw-Hill Publishing Co.

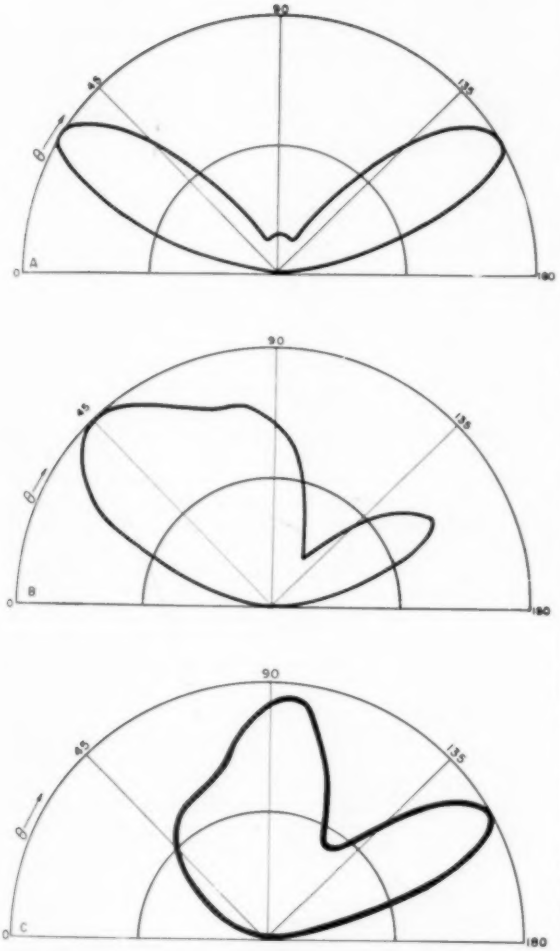

FIGURE 8. *Power radiation patterns for ka=3.*

A, $\theta_0=90°$; B, $\theta_0=45°$; C, $\theta_0=0°$. The normalization is similar to that in figure 3.

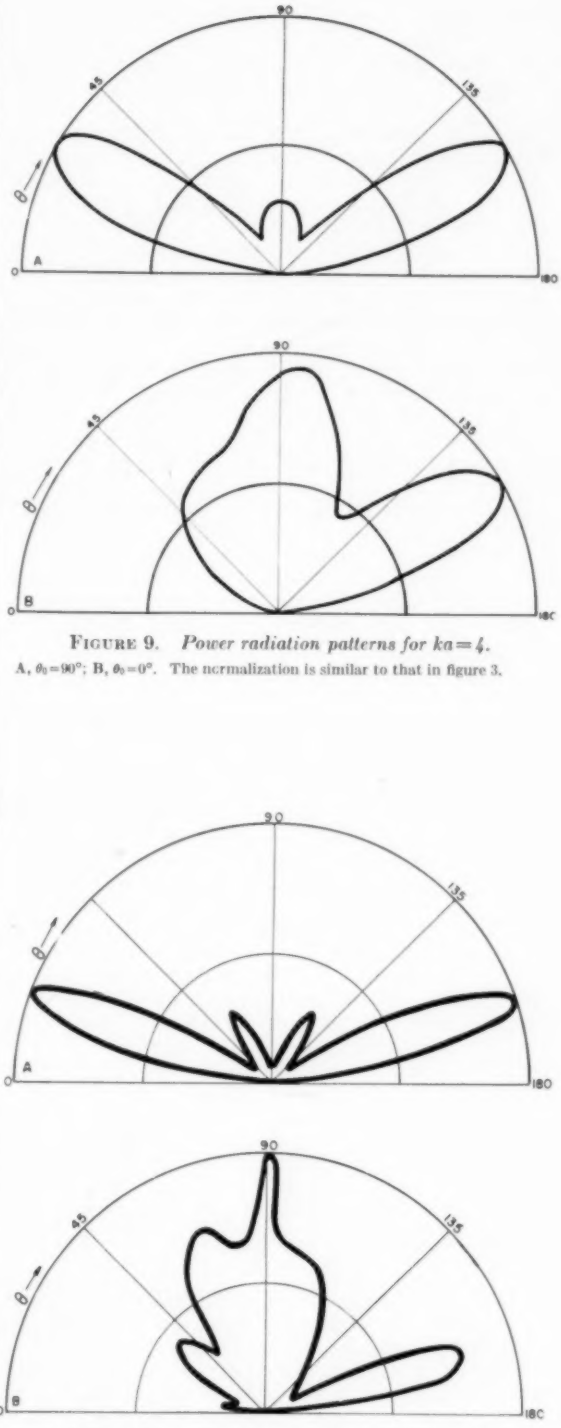

FIGURE 9. *Power radiation patterns for ka=4.*

A, $\theta_0=90°$; B, $\theta_0=0°$. The normalization is similar to that in figure 3.

FIGURE 10. *Power radiation patterns for ka=5.*

A, $\theta_0=90°$; B, $\theta_0=0°$. The normalization is similar to that in figure 3.

Using (15), we then have, as θ_0 approaches zero

$$a(n,\theta_0)=\frac{(2n+1)}{4}\theta_0^2+0(\theta_0)^3. \tag{30}$$

Thus the limiting shape $S(\theta)$ of the radiation pattern as $\theta\to 0$ is given by

$$S(\theta)=\sum_1^\infty (2n+1)L(n,ka)P_n^1(\cos\theta). \tag{31}$$

Looking back at eq 19 and 20, we see that $S(\theta)$ converges. These patterns for $\theta_0=0$ are close approximations to the patterns obtained when the feed is near $\theta_0=0°$. Among asymmetrically fed antennas, those having nearly end feed appear to be the most commonly used, so the results found for $\theta_0\approx 0$ are of especial interest.

5. Related Experimental Results

No experimental results for spherical antennas are known to the author. However, it is of considerable interest to note that the general type of behavior shown in figures 3, 4, and 5, as to the effect of θ_0 upon the pattern, has recently been found experimentally for wire antennas [2] and thick cylinders [1]. (Quantitatively, of course, we cannot compare such experiments with our theory). In those of the experiments in which the antenna lengths were of the order of a wavelength (so that the radiation patterns like those in figs. 3, 4, and 5 are relatively simple), the effect of moving θ_0 toward 0° was quite clearly reflected in the patterns; they have this characteristic lean with more than half the radiated power going into the forward hemisphere. For example, figure 6 shows radiation patterns found for two antennas consisting of cylindrical pipes for which the ratio of diameter d to wavelength λ was 0.04, and whose ratios of length L to λ were ½ and 1, respectively. Each pipe contained a small gap near one end, across which the generator was connected. The general similarity of the patterns to those of figures 3b and 5c is clear. Figure 7 shows some patterns obtained from figure 1 and figure 2 of reference [2], showing the same sort of effect for wires.

It is pleasing that our radiation pattern calculations for the asymmetrically fed spherical antenna show features that seem to be characteristic of a wide class of asymmetrically fed antennas and that have been experimentally observed.

6. Large Spheres

It is of interest to examine the radiation patterns for larger values of ka (figs. 8, 9, 10). Here we find, as expected, increasingly complicated, multilobed, patterns. We find also that the "leaning" trend that exists for smaller antennas is no longer clear. One can no longer say that in the case of asymmetric feed the radiation pattern leans away from the feed point—the patterns have too many lobes, large ones appearing in both hemispheres. One might suspect, however, that even though the pattern trends are more complicated, that here to, as in the case of the smaller antennas, there is more power radiated into the forward hemisphere. However, even this is no longer true; in several cases an integration of Poynting's vector shows that less than half of the energy is radiated into the forward hemisphere even for $\theta_0=0$. For the larger antennas there does not seem to be any definite trend for the radiated energy to favor either hemisphere. Thus except for the smaller spheres, the location of the feed point is not reflected in any clear-cut way in power distribution in the hemispheres. These statements appear also to be true in the case of the longer asymmetrically fed wire antennas (figs. 3, 4, and 5 of reference [2]).

7. Near-Polar Radiation

The question arises: is there a simple characteristic of the radiation pattern that indicates unambiguously which side of the antenna contains the feed point? For the smaller antennas there is a characteristic lean which renders such identification possible, but this effect becomes unclear as the antenna increases in size. The hypothesis that there is always more power radiated into the forward hemisphere has also been shown above to be false. The present investigation has, however, revealed one simple feature that appears to be correlated unambiguously with the location of the feed point. This is a characteristic, to be discussed below, of the radiation in the near-polar directions, that is, the radiation in the directions near $\theta=0°$ and $\theta=180°$.

We have seen that E_{rad} is a superposition of the Legendre functions $P_n^1(\cos\theta)$. All these functions are of the form $b(n)\theta$, for sufficiently small θ, where $b(n)$ is a constant depending upon n, so that E_{rad} is of the form $c_1\theta$ for small θ. At the other pole E_{rad} is of the form $c_2\psi$, where $\psi=\pi-\theta$. At $\theta=0$ and $\psi=0$, $E_{rad}=0$. In general, $|c_1|\neq|c_2|$ except when the excitation is symmetrical ($\theta_0=90°$).

We have seen that for $\theta_0=0$ the shape of the pattern is given by eq 31. Using eq 25 and 29 we find that for small θ this becomes

$$S(\theta)=\sum_{n=1}^\infty \frac{(2n+1)n(n+1)}{2}\theta L(n,ka)+0(\theta)^2.$$

Thus we have

$$\frac{|c_1|^2}{Q^2}=\left[\sum_{n=1}^\infty (2n+1)n(n+1)Re{:}\,L(n,ka)\right]^2+\left[\sum_{n=1}^\infty (2n+1)n(n+1)Im{:}\,L(n,ka)\right]^2, \tag{32}$$

where Q^2 is a constant immaterial to the present discussion, and Re and Im indicate the real and imaginary part, respectively. Also, recalling the symmetry and anti-symmetry properties of $P_n^1(\cos\theta)$,

$$\frac{|c_2|^2}{\mathcal{E}^2}=\left[\sum_{n=1}^{\infty}(-1)^{n+1}(2n+1)n(n+1)Re\colon L(n,ka)\right]^2+\left[\sum_{n=1}^{\infty}(-1)^{n+1}(2n+1)n(n+1)Im\colon L(n,ka)\right]^2 \quad (33)$$

These definitions of $|c_1|$ and $|c_2|$ are for $\theta_0=0$; for other values of θ_0 there are corresponding definitions.

The hypothesis here presented, with considerable evidence, is that if $\theta_0<90°$, $|c_2|>|c_1|$. This has been found to be true in all the spherical antenna patterns that have been computed. This can be seen, for example, in figures 3, 4, 5, 8, 9, and 10. (It has also been found in the experimental work on thick cylindrical antennas, and is also apparently true in the case of the 16 radiation patterns given in reference [2] for wire antennas.)

For the interesting case $\theta_0=0°$, we have calculated $|c_1|$ and $|c_2|$ from (32) and (33) for a considerable number of values of ka. The results are plotted in figure 11 as a function of ka. In this figure the points that have been computed have been clearly indicated. The dashed curve shown is suggested by the points. We see that $|c_2|/|c_1|$ has the value 1 at $ka=0$, and appears to have a generally increasing trend. Oscillations are superposed upon this trend, but there is no evidence that the curve dips down as far as the value 1 except at $ka=0$. Thus, particularly in the case of end feed, all the evidence so far seems to support our hypothesis that the smaller of the two quantities $|c_2|$ and $|c_1|$ indicates unambiguously which side of the antenna contains the feed point. However, on account of the complicated analytic form of $|c_1|$ and $|c_2|$, illustrated in eq 32 and 33, a complete proof of this statement has not yet been found.

8. Crude Model of an End-Fed Antenna

It is perhaps of some interest to mention that we have been able in the course of this investigation to prove that $|c_2|/|c_1|>1$ in the case of a very crude model of an end-fed antenna. Consider the radiation field of a linear current distribution

$$I=I_0e^{jkz}+RI_0e^{-jkz}, \quad (34)$$

whose length is L, and which is centered at the origin $z=0$. This distribution consists of a wave travelling in the negative z direction and a return wave that represents the original wave subjected at $-L/2$ to a complex reflection coefficient R. We shall restrict ourselves to the condition $|R|<1$. The time factor $e^{j\omega t}$ has been suppressed. Such a distribution may be expected on the basis of rough physical reasoning to give radiation patterns similar to those found for actual end-fed antennas. This can be seen in more detail by considering the well-known radiation pattern [11] obtained from the first term of (34), a pure travelling wave. A typical pattern is shown in figure 12. It will be seen that the main radiation is at an acute angle with the direction of the current flow. The distribution (34) may be said to give rise to *two* such radiation patterns of unequal magnitude, pointed in essentially opposite directions, and superposed (the complex values of E_{rad} are added). The resultant pattern may be expected to be very much like the actual patterns for end-fed antennas. In the case of the cylinders, for example, it was found some time ago [1] that the patterns can be quite closely duplicated by proper choice of R.

We shall now prove that for this simple model $|c_2|/|c_1|>1$. It is convenient here to derive $\boldsymbol{E}$ from the vector potential $\boldsymbol{A}$, according to the standard equations. Only a z component of $\boldsymbol{A}$ is present.

We have, since $\partial/\partial t=j\omega$

$$\boldsymbol{E}=-j\omega\mu\boldsymbol{A}+\frac{1}{j\omega\epsilon}\nabla(\nabla\cdot\boldsymbol{A}) \quad (35)$$

also

$$\boldsymbol{A}=A_z=\frac{1}{4\pi}\int_{-L/2}^{L/2}\frac{I(z)e^{-jkr}}{r}\,dz, \quad (36)$$

where r is the distance between the point P at which we are computing the field and the point z. If P is a remote point, $r\approx r_0-z\cos\theta$, where r_0 is the distance from P to the origin.

We may replace r in the denominator of the integrand by r_0 but must keep the more accurate expression in the exponential factor. We have then

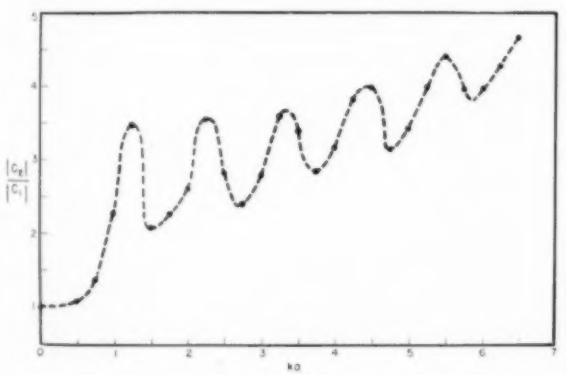

FIGURE 11. *$|c_2|/|c_1|$ as a function of ka for $\theta_0=0°$.*
Computed points are shown as dots.

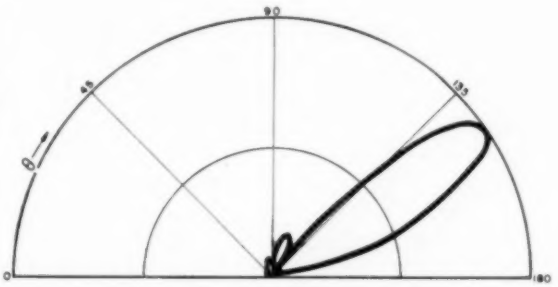

FIGURE 12. *Power radiation pattern of travelling wave of current.*
Length L of current distribution, 2λ. The wave is travelling toward the right.

$$A_z=\frac{I_0e^{-jkr_0}}{4\pi r_0}\int_{-L/2}^{L/2}[e^{jkz}+Re^{-jkz}]e^{jkz\cos\theta}\,dz,$$

$$=\frac{I_0e^{-jkr_0}}{4\pi r_0}\left\{\frac{e^{jk(L/2)(1+\cos\theta)}-e^{-jk(L/2)(1+\cos\theta)}}{jk(1+\cos\theta)}\right.$$

also

$$\left.+\frac{R[e^{jk(L/2)(\cos\theta-1)}-e^{-jk(L/2)(\cos\theta-1)}]}{jk(\cos\theta-1)}\right\}$$

$$=\frac{I_0e^{-jkr_0}}{2\pi r_0k}\left\{\frac{\sin(kL/2)(\cos\theta-1)}{\cos\theta+1}\right.$$

$$\left.+\frac{R\sin(kL/2)(\cos\theta-1)}{\cos\theta-1}\right\}.$$

The radiation field, it turns out, is found from the first term of (35):

$$E_{rad}=-j\omega\mu A_\theta=j\omega\mu A_z\sin\theta$$

so

$$E_{rad}=\frac{-\omega\mu I_0e^{-jkr_0}\sin\theta}{2\pi r_0jk}\left\{\frac{\sin\frac{kL}{2}(\cos\theta+1)}{\cos\theta+1}+\right.$$

$$\left.\frac{R\sin\frac{kL}{2}(\cos\theta-1)}{\cos\theta-1}\right\}.$$

The essential part of this is

$$\sin\theta\left\{\frac{\sin A(\cos\theta+1)}{\cos\theta+1}+\frac{R\sin A(\cos\theta-1)}{\cos\theta-1}\right\} \quad (37)$$

where $A\equiv kL/2$.

Now as $\theta\to0$, the expression in brackets becomes

$$\frac{\sin 2A}{2}+AR\equiv\frac{c_1}{Q_1},$$

and as $\theta\to\pi$, we have

$$A+R\frac{\sin 2A}{2}\equiv\frac{c_2}{Q_1}$$

where, as we see, c_1 and c_2 are defined as for the spherical antenna. Q_1 is a constant.

We shall now show that $|c_2|>|c_1|$. Since R is taken to be a complex number we write $R\equiv|R|e^{j\alpha}$. Then

$$\frac{|c_2|^2}{|Q_1|^2}=A^2+\frac{|R|^2\sin^2 2A}{4}+A|R|\cos\alpha\sin 2A \quad (38)$$

$$\frac{|c_1|^2}{|Q_1|^2}=A^2|R|^2+\frac{\sin^2 2A}{4}+A|R|\cos\alpha\sin 2A$$

$$\frac{|c_2|^2-|c_1|^2}{|Q_1|^2}=\left(A^2-\frac{\sin^2 2A}{4}\right)(1-|R|^2), \quad (39)$$

which is never negative and is zero only when $A=0$. Thus for this simple model $|c_2|>|c_1|$. It is also interesting to note that the general behavior of the quantity $|c_2|/|c_1|$ for this model is rather similar to that in the case of the spherical end-fed antenna. Consider the ratio

$$\delta^2\equiv\frac{|c_2|^2}{|c_1|^2}=\frac{A^2+(|R|^2/4)\sin^2 2A+A|R|\cos\alpha\sin 2A}{A^2|R|^2+\frac{\sin^2 2A}{4}+A|R|\cos\alpha\sin 2A}, \quad (40)$$

Examination of this expression shows that δ has the value 1 at $A=0$, begins to increase slowly with increasing A, then increases rapidly and begins to oscillate, always remaining greater than 1. If $|R|$ is a constant independent of A, δ approaches in an oscillating manner the asymptotic value $1/|R|$. If, however, $|R|$ decreases as A increases, δ has a continually increasing trend with superimposed oscillations. This is the type of behavior shown by $|c_2|/|c_1|$ for the sphere (and presumably for other types of end-fed antennas). It may be noted that if one wished to simulate an end-fed antenna by this crude model, it would be in keeping with general ideas on antenna radiation to have $|R|$ decrease with increasing length of the antenna. A better model would probably have the current wave attenuated gradually along the antenna, rather than suddenly at the end.

IV. Current and Admittance

Having discussed the radiation field in some detail, we now consider questions of admittance and current. The admittance presented to the applied voltage is determined by the value of the current at the feed point. Since we have postulated a perfectly conducting antenna, there will be at the surface a discontinuity in H_ϕ and a corresponding surface current density J_θ, related to H_ϕ at any point on the surface by

$$J_\theta=-H_\phi|_{r=a} \quad (41)$$

The direction of current flow is along meridian lines. The total current I_θ at colatitude θ is

$$I_\theta=2\pi a\sin\theta J_\theta=-2\pi a\sin H_\phi|_{r=a} \quad (42)$$

Using (4a) and (9), we find

$$I_\theta=2\pi a\sin\theta j\omega\epsilon V\sum_{n=1}^{\infty}a_n$$

$$\frac{H^{(2)}_{n+1/2}(ka)}{nH^{(2)}_{n+(1/2)}(ka)-kaH^{(2)}_{n+(1/2)}(ka)}P_n^1(\cos\theta) \quad (43)$$

$$=\sum_{n=1}^{\infty}I_\theta(n), \quad (44)$$

where $I_\theta(n)$ is the partial current associated with the nth mode. Rearranging (43) a bit, this takes the form

$$I_\theta(n)=2\pi a \sin\theta J_\theta(n)=$$

$$\frac{V\pi}{Z_0}\, a(n,\theta_0)K(n,ka)P_n^1(\cos\theta)\sin\theta, \tag{45}$$

where

$$\frac{1}{Z_0}\equiv\frac{\omega\epsilon}{k}\equiv\sqrt{\frac{\epsilon}{\mu}}$$

and

$$K(n,ka)\equiv\frac{j}{\dfrac{n}{ka}-\dfrac{H^{(2)}_{n-1/2}(ka)}{H^{(2)}_{n+1/2}(ka)}}. \tag{47}$$

The relation between each partial current and the corresponding partial radiation field $E_{rad}(n)$ is

$$J_\theta(n)=\frac{I_\theta(n)}{2\pi a\sin\theta}=\frac{-j^{n+1}kr\sqrt{\dfrac{\pi}{2ka}}}{2Z_0e^{-jkr}}H^{(2)}_{n+1/2}(ka)E_{rad}(n). \tag{48}$$

a relation that is independent of the excitation function $a(n,\theta_0)$. This relation means that the nth current mode is associated with or "causes" a corresponding nth radiation mode, independently of any other modes which, as a result of a particular form of excitation, may be present.

Defining the admittance Y as

$$Y\equiv\sum_{n=1}^{\infty}Y(n)\equiv\frac{I_{\theta_0}}{V},$$

we find

$$Y=\sum_{n=1}^{\infty}Y(n)=\sum_{n=1}^{\infty}\frac{I_{\theta_0}(n)}{V}=$$

$$\sum_{n=1}^{\infty}\frac{\pi}{Z_0}\,a(n,\theta_0)K(n,ka)P_n^1(\cos\theta_0)\sin\theta_0. \tag{49}$$

We see that the applied voltage "sees" an infinite number of partial admittances in parallel.

The real and imaginary parts of the function $K(n,ka)$, which represents the effect of the size of the sphere in the expressions for current and admittance are plotted in figure 13 for the first few modes. We note that for a given value of ka, values of n appreciably greater than ka all contribute only negligibly to $Re{:}K(n,ka)$, whereas in the case of $Im{:}K(n,ka)$ the contributions of the higher modes fall off only slowly with increasing n. This is related to the fact that, as we have seen, the radiation field is determined by only a relatively small number of modes; the part of Y that accounts for the radiation is the real part of conductance C. On the other hand, the part of the field that is reactive, rather than radiative, is associated with the imaginary part of Y, the susceptance S.

Upon examining the series (49) for current and admittance, it is found that this series is divergent. [Therefore for $\theta=\theta_0$ (44) is divergent]. Using for $a(n,\theta_0)$ the expression (15) referring to the delta-function excitation, we have

$$Y=\sum_{n=1}^{\infty}\frac{\pi}{Z_0}\frac{2n+1}{2n(n+1)}[P_n^1(\cos\theta_0)]\sin^2\theta_0\frac{j}{\dfrac{n}{ka}-\dfrac{H^{(2)}_{n-1/2}(ka)}{H^{(2)}_{n+1/2}(ka)}}. \tag{50}$$

Using the expressions (20) and (18), one finds that for sufficiently high n the general term of the series approaches

$$\frac{j(2n+1)ka}{Z_0n(n+1)}\cos^2\left[\left(n+\frac{1}{2}\right)\theta_0+\frac{\pi}{4}\right]\sin^2\theta_0. \tag{51}$$

Consider the series whose nth term is the expression (51). We shall show that for the infinite set of values of θ_0 given by

$$\theta_0=2\pi\frac{p}{q},\ (p,q \text{ integer},\ q>p),$$

the series diverges. For our purposes, this is a sufficient indication of divergence over the range of θ_0.

The $\cos^2$ factor, which is nonnegative, will repeat itself when n increases by q. Now choose $n=r$ such that

$$\cos^2\left[\left(r+\frac{1}{2}\right)\theta_0+\frac{n}{4}\right]=c>0.$$

Then, considering only the values of n given by

$$r,\ r+q,\ r+2q,\ \text{etc.},$$

we examine the series

$$c\left\{\frac{2r+1}{r(r+1)}+\frac{2(r+q)+1}{(r+q)(r+q+1)}+\frac{2(r+2q)+1}{(r+2q)(r+2q+1}+\cdots\right\}. \tag{52}$$

Dividing the nth term u_n of the series by u_{n+1} (Raabe's test [12]), we find

$$\frac{u_n}{u_n+1}=1+\frac{1}{n}+0\left(\frac{1}{n^2}\right),$$

showing that (52) is divergent. Therefore the series whose general term is (51) aiso diverges. The higher order terms in (20) and (18), which have been neglected in writing down (51), do not alter this conclusion. Thus the series for the admittance Y does not converge. It is to be noted, however, that it is the imaginary part of Y, the susceptance S, that diverges. The real part, the conductance C, converges rapidly, as implied above.

The nonconvergence of S is due to the delta-function excitation that has been assumed. The

susceptance becomes that of an infinite capacity, which is understandable; concentrating the applied force E' along a line at $\theta=\theta_0$ is equivalent to maintaining a potential difference across an infinitesimal gap at $\theta=\theta_0$. The infinitesimal gap has infinite capacity. (This gap terminology, represents, as J. C. Slater [13] has pointed out, another way of interpreting physically the type of boundary condition we are using, [explained in Part II]. In this approach, one considers that the driving field is applied tangentially across a small gap at the surface of the sphere and that solutions of the wave equation are being sought such that the tangential electric field will reduce to the applied field across the gap and to zero everywhere on the metallic surface.)

When the field E' is considered to be applied across a *finite* region, the high order terms in $a(n,\theta_0)$ decrease much more rapidly than in (11), which is for the infinitesimal case. For example if E' is constant $=V/a\Delta\theta$ over a small finite zone $\Delta\theta$ centered at θ_0, then our general expression (7) for $a(n,\theta_0)$ reduces to

$$a(n,\theta_0)=\frac{2n+1}{2n(n+1)\Delta\theta}\int_{\theta_0-(\Delta\theta/2)}^{\theta_0+(\Delta\theta/2)} P_n^1(\cos\theta)\sin\theta d\theta \tag{53}$$

$$=-\frac{2n+1}{2n(n+1)\Delta\theta}\int_{\theta_0-(\theta\Delta/2)}^{\theta_0+(\Delta\theta/2)} \frac{d}{d\theta}P_n(\cos\theta)\sin\theta d\theta \tag{54}$$

For small $\Delta\theta$, it will be sufficiently accurate in (54) to take sin θ outside of the integral sign and give it the value sin θ_0 (or some other average value). We then have

$$a(n,\theta_0)\approx\frac{(2n+1)\sin\theta_0}{2n(n+1)\Delta\theta}\left[P_n\cos\left(\theta_0-\frac{\Delta\theta}{2}\right)-P_n\cos\left(\theta_0+\frac{\Delta\theta}{2}\right)\right]. \tag{55}$$

For the first few values of n this reduces very closely to (11).

For high values of n, where the functions $P_n^1(\cos\theta)$ vary appreciably over the zone $\Delta\theta$, (55) begins to differ from (11). The asymptotic behavior of (55) for large n now makes the series (49) converge. We find [8] that the n dependence of $P_n(\cos\theta)$ for the large n is $n^{-1/2}$ instead of $n^{1/2}$ for $P_n^1(\cos\theta)$ as in (20). It is easily seen that this change will make the V series converge.

This discussion indicates that the theoretical results for radiation field and conductance obtained with the delta-function excitation will not differ appreciably from the results for a finite $\Delta\theta$. This important conclusion is paralleled in the experimental field, where it is rather well known that the radiation pattern and radiation conductance of an antenna are

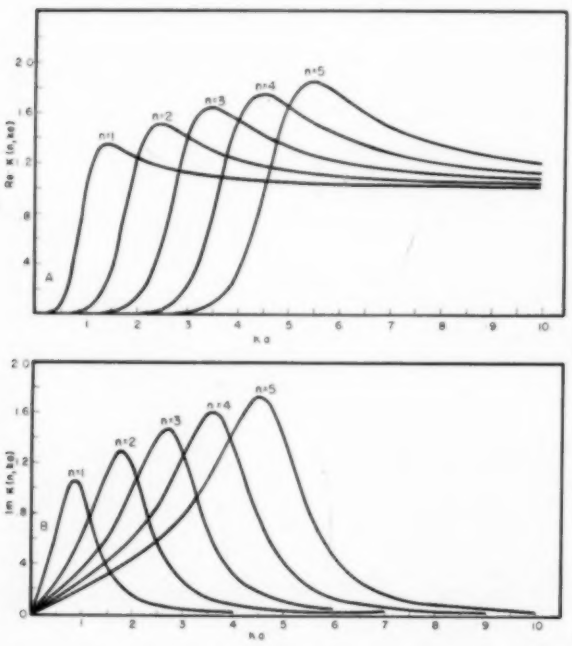

FIGURE 13. *$K(n,ka)$ as a function of ka for several values of n.* A, real part; B, imaginary part.

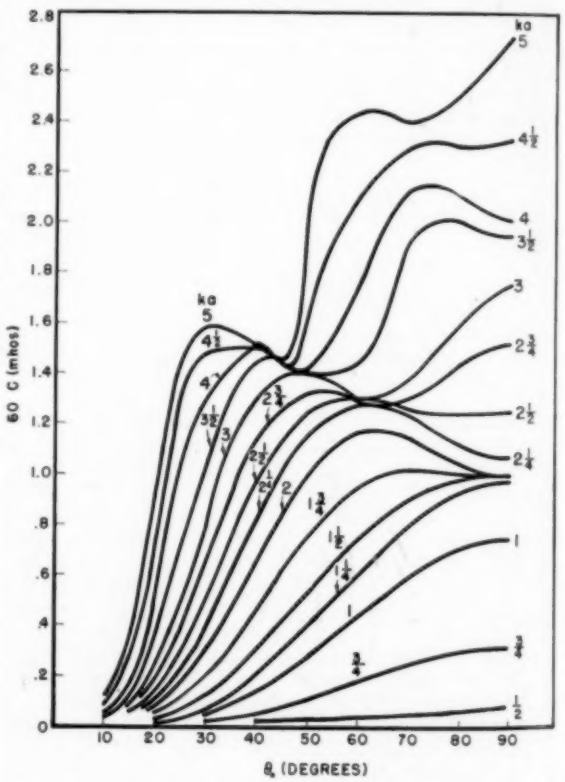

FIGURE 14. *Radiation conductance, C, as a function of θ_0, for several values of ka.*

very little affected by the size of the gap. The present work indicates in a sense the "reason" for this. It also tends to show that the idealized delta-function approach is capable of finding answers for radiation patterns and conductance that will agree with those found experimentally. On the other hand, the divergence of the imaginary part of the admittance indicates that these calculations do not throw too much light on the values of the susceptance that may be expected in practice. The values of this quantity, as is also well known experimentally, depend very much upon the details of the feed. Antenna calculations such as those in the present report severely schematize the feed conditions, so they cannot be expected to yield much information on susceptance.

As discussed above, we cannot plot the susceptance but confine ourselves to drawing graphs of the conductance, C, (fig. 14). We could, of course, attempt to plot the sum of the first m partial susceptances, where m is a number such that the contributions above m would not be appreciable when $\Delta\theta$ is finite, and so that the contributions below m would not be altered appreciably when $\Delta\theta$ is finite. This, however, is difficult because the high-order terms fall off extremely slowly. There are some qualitative conclusions about susceptance we can draw from the equations (47, 49, 50, and 55), and graphs (fig. 13). For ka considerably less than 1, the admittance will be primarily a capacitative susceptance, the conductance being small compared to the susceptance. For infinitesimal $\Delta\theta$ we see that the susceptance for a sphere of any size is always capacitative. For small but finite $\Delta\theta$, this will in general still be true, except possibly for ka very large.

The general trend of C, as disclosed in figure 14, is to start with the value zero at $ka=0$, rise rapidly, and then go through 0, 1, 2, or more secondary maxima (the number depending upon ka) before reaching its value at $\theta_0=90°$. The trend near $\theta_0=0$ is of interest. From eq 50 we find that this trend is as $\theta^4{}_0$. This is perhaps the first time in the literature that such a problem has received a clear-cut answer. The corresponding question for wire antennas has, it is believed, not yet been solved.

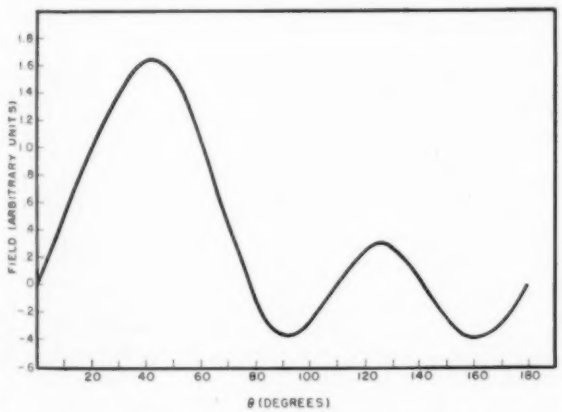

FIGURE 15. *Sum of lowest five modes of applied field, for $ka=2$ and $\theta_0=45°$.*

For relatively small spheres, $ka<1$, the trend of C is very closely as $\sin^4\theta_0$ for all positions of the feed point. The reason for this is that the first mode that gives $\sin^4\theta_0$ exactly, accounts for most of the conductance (and radiation).

The secondary maxima found for the larger antennas are of interest. Since for a given applied voltage $Ve^{j\omega t}$ the time-average power radiated is $1/2\ V^2C$, that is, proportional to C, we find in some cases that one gets more radiated power for a given voltage by feeding the antenna off center than for center feed. The local stationary regions on the C-vs-θ_0 curve indicate locations on the antenna where the value of C is not sensitive to the location of the feed point.

In general, we see that keeping θ_0 constant while increasing ka, increases C. There are several quite stationary spots on the C-vs-ka curve for given θ_0. For $\theta_0=90°$, C is very flat from $ka=1\ 1/4$ to $ka=2$. For $\theta_0=60°$, we find such a flat region for $ka=2$ to 3, and for $\theta_0=45°$, C is virtually constant for $ka=3$ to 5.

Some or all of the above features are probably to be found, qualitatively, even for nonspherical asymmetrically fed antennas. Experimentally (and theoretically), however, this seems to be a virtually unexplored field.

It may be noted that the first few modes into which the applied field is analyzed, which, as we have seen are primarily responsible for the form of the radiation pattern and the amount of radiated power, represent, when summed, a field that is very far from being localized at the "feed point". That is, we may say that this distributed applied field produces essentially the same radiation as the concentrated applied field. An example of this is shown in figure 15, which shows the sum of the first five modes of the applied field for $ka=2$ and $\theta_0=45°$. These modes account for practically all the radiation and determine the shape of the radiation pattern. The higher modes are associated with reactive components of the field that are localized near the antenna and whose importance is in meeting the boundary conditions at the antenna, including feed conditions. Similarly the current on the antenna that is associated with the first few modes and that may be considered "responsible" for the radiation, is very much different from the total current, which includes the higher reactive modes used in satisfying the local conditions.

V. Conclusions

An idealized treatment of the asymmetrically fed spherical antenna has been given that produces detailed results for the radiation properties as a function of size of antenna and location of the feed point. Reasons are given for believing that the idealization of the feed conditions does not prevent the theory from giving experimentally pertinent answers for the radiation properties. Some of the features show

qualitative agreement with experimental work on nonspherical antennas. The theory should be useful as a rough guide for experiments with other types of asymmetrically fed antennas, particularly those whose ratio of diameter to length is fairly large.

The author thanks K. F. Herzfeld, Head of the Physics Department of Catholic University of America, for his generous help and guidance throughout the course of this work. Gratitude is also expressed to C. H. Page, of this Bureau, for many stimulating and enlightening discussions and for much kind encouragement and help. The entire paper has been read with critical care and valuable suggestions by the above named, by J. Mendousse and D. Beard, of Catholic University, and by J. J. Freeman, of this Bureau. To all these deep appreciation is expressed. Thanks are also extended to A. V. Astin and W. S. Hinman, Jr., of this Bureau, for general encouragement and cooperation. The generous secretarial and other assistance of Marion B. Teele is gratefully acknowledged.

VI. References

[1] C. H. Page, R. D. Huntoon, and P. R. Karr, Radiation patterns of thick end-fed antennas; a talk presented at meetings of the Institute of Radio Engineers at Washington, D. C., May 1946, and New York, Feb. 1947.
[2] D. C. Cleckner, Effect of feed on patterns of wire antennas, Electronics **20**, 103 (1947).
[3] F. E. Terman, Radio engineer's handbook, first ed., chapter 11 (McGraw-Hill Book Co., New York, N. Y., 1943).
[4] W. S. Hinman and Cledo Brunetti, Radio proximity fuze design, J. Research NBS **37**, 1 (1946) RP1723; C. H. Page and A. V. Astin, Survey of proximity fuze development, Am. J. Phys. **15**, No. 2, 95 (1947).
[5] J. A. Stratton and L. J. Chu, Forced oscillations of a conducting sphere, J. Applied Phys. **13**, 236 (1941).
[6] E. T. Whittaker and G. N. Watson, A course of modern analysis, 4th ed., p. 324 (Cambridge Univ. Press, 1940).
[7] A. Sommerfeld, Partial differential equations of physics, p. 119 (Academic Press, New York, N. Y., 1949).
[8] E. W. Hobson, Spherical and ellipsoidal harmonics, p. 303 (Cambridge Univ. Press, 1931).
[9] J. A. Stratton, Electromagnetic theory, first ed., p. 436 (McGraw-Hill Book Co., New York, N. Y., 1941).
[10] T. M. MacRobert, Spherical harmonics, p. 86 (E. P. Dutton and Co., New York, N. Y., 1927).
[11] J. Aharoni, Antennae, p. 225 (Oxford Univ. Press, 1946).
[12] T. M. MacRobert, Functions of a complex variable, p. 77 (MacMillan and Co. Ltd., London, 1938).
[13] J. C. Slater, Microwave transmission, first ed., p. 221 (McGraw-Hill Book Co., New York, N. Y., 1942).

WASHINGTON, February 9, 1951.

U. S. GOVERNMENT PRINTING OFFICE: 1951